Rune Holmstad

Methods for paper structure characterisation by means of image analysis

Doktoravhandling
for graden doktor ingeniør

Trondheim, juli 2004

Norges teknisk-naturvitenskapelige universitet
Fakultet for naturvitenskap og teknologi
Institutt for kjemisk prosessteknologi

NTNU

Norwegian University of Science and Technology

Department of Chemical Engineering

Methods for paper structure characterisation by means of image analysis

by

Rune Holmstad

NTNU
Norwegian University of
Science and Technology

Thesis submitted in partial fulfilment of the doktor ingeniør degree

July 2004

ABSTRACT

Paper is a complex, disordered porous media. The complexity makes it difficult to obtain more than empirical knowledge of the relationship between papermaking variables and the resulting paper structural properties. It is known that the alteration of the paper structure is decisive for many paper properties, but the appropriate tools for visualising and assessing the changes to the paper structure after varying physical treatments of the paper have until recently not been available.

Scanning electron microscope in backscatter mode (SEM-BEI) and X-ray microtomography allows acquisition of respectively cross-sectional and 3D images of the detailed paper structure with sufficient contrast and resolution to clearly discern the structural constituents. The access to detailed images of the paper structure allows quantification of the changes made to the detailed paper structure through application of suitable image analysis routines. The microscopy techniques combined with image analysis thus provide the tools needed to improve the knowledge of how various papermaking variables may improve the paper properties through alteration of the paper structure. Improvement of the knowledge of the structural mechanisms governing the paper properties may help to give a more knowledge based operation of the paper machines and may be applied for process and product optimization.

This thesis work has considered different aspects of how the physics governing the SEM-BEI technique, image acquisition and sample preparation may affect the quality of the cross-sectional images of the paper structure with regard to the subsequent image analysis. The effect of the applied filtering and segmentation routines to obtain the binary representation needed for image analysis are also considered.

It was found that the applied methodology yielded realistic binary cross-sectional representations of the paper structure and thus representative structural assessments. However, to obtain assessments that are representative for the paper grade and not only the small cross section, at least 15 independent cross-sectional images were needed. The number of necessary replicates varied somewhat depending on the structural characteristics.

This study involved improvement of existing image analysis techniques. The main contribution from this work in this aspect is the application of the rolling ball algorithm for an objective surface definition of the physically small and often uneven paper cross sections. The objective surface definition enables the division of the structure into locally uniformly thick layers, for which the material distribution in the z-direction of the paper can be determined. The material distributions that may be determined include solid/void fractions, fillers and fines content. The improved image analysis routines also include measurement of local thickness, density and basis weight, pore chords and specific surface area.

The practical application of the SEM technique for obtaining new knowledge of paper making variables:paper structure:paper properties relationships included assessment of the pore geometry and the material distribution in the z-direction. The z-directional material distribution was determined in order to assess the effect of temperature gradient calendering on a SC-paper grade. The results obtained for the z-directional material distributions combined with surface topography techniques revealed that the temperature gradient effect was concentrated to the very few outermost micrometers of the paper structure.

The pore geometry was assessed by both the 2D and 3D techniques. The determined pore chord distributions followed the theoretically derived pore height distribution of Dodson for the z-direction. The pore chord distribution for any spatial direction appeared to follow a log-normal distribution, when including all pore chord sizes to allow a 'continuous' distribution. The mean and standard deviation were proven to be proportional, as earlier observed from physical pore size measurements and theoretical deductions. The width of the pore chord distributions for the different spatial directions changed with the structural anisotropy. The wider the pore height distribution, the more different are the pore chord mean and standard deviation.

Most of the information obtained for the pore geometry from assessment of pore chords can be summarized in the equivalent pore representation. The ellipsoid shape of the equivalent pore, constructed as a warped surface of the mean pore chords for all spatial directions, was confirmed from the assessments of 3D images of three different paper grades having distinctly different structural properties. The ellipsoid shape was also found for the pore chord standard deviation. Additionally, it was found that the ellipsoid constructed for the solid phase had the same shape as for the porous phase and their relative size was proportional to the solid fraction of the assessed paper structure. The equivalent pore ellipsoid thus contain all information about the pore/fibre chord distributions in all spatial directions in addition to the structural anisotropy.

The studies of the pore geometry prove that the solid fraction and the structural anisotropy are the major determinants for the pore geometry.

The results reveal that there is clear differences between the pore size distribution determined by image analysis and physical assessments like mercury porosimetry, which is affected by narrow pore necks limiting the intrusion from the surfaces.

This thesis work have applied three different applications of X-ray microtomography. The three different applications include both phase contrast and absorption mode contrasting for high resolution synchrotron source X-ray microtomography and low resolution X-ray microtomography provided by a stationary source commercial scanner.

The experiences from this work have proven that the synchrotron source X-ray microtomography can be applied successfully to obtain high quality digital representations of the 3D paper structure with sufficient contrast and resolution to detect and quantify the details of the fibre network. The current technology at the applied beam lines at the ESRF, France, allows spatial resolution down to approximately 1 µm. This resolution is sufficient for obtaining realistic structural assessments that are suited for determining how the paper structure is affected by papermaking variables and itself influences the paper properties. The high resolution also provides insight into the detailed paper characteristics from visualization of the 3D paper structure.

The resolution provided by the stationary X-ray source is not sufficient to preserve the fibre network topology. However, the signal is of sufficient quality to make comparative structural assessments possible, although the numerical results from the structural assessments are not physically reasonable.

This thesis work have considered different aspects of how the working principles, image acquisition, sample preparation, sample mounting and volume reconstruction of the three applied X-ray microtomography techniques may affect the quality of the 3D images of the paper structure with regard to the subsequent image analysis. It was found that the sample mounting for the high resolution absorption mode images was clearly affecting the digital representation of the paper structure. An alternative sample mounting, avoiding the melt glue penetrating into the paper structure, is recommended for future application of X-ray microtomography. However, it must be emphasized that restricting sample movement during the image acquisition is of outmost importance to obtain 3D images with a minimal content of noise.

The applied routines for image filtering and segmentation to obtain binary representations are presented and the quality of the resulting binary structures are evaluated. The results prove that the applied image processing preserves most of the information provided by the greyscale images. However, the applied routines are not optimised. Exploiting more of the three-dimensional connectivity in the images and applying edge preserving filtering techniques may improve the image processing for future experiments. The image processing of the phase contrast images is difficult, semi-automatic, laborious and computationally demanding due to the relatively low contrast and the contrasting technique detects only the phase borders. The image processing of the absorption mode images is considerably more straightforward. The quality of the binary absorption mode images is almost as good as the binary phase contrast images, despite the lower resolution. The absorption mode is therefore recommended for the future application of high resolution X-ray microtomography. Additional benefits of the absorption mode imaging is the ability to discern mineral particles and coating and that it has no principal problems in acquiring images of high density paper grades. A benefit only provided by the phase contrast technique is that it provides sufficient contrast between wood fibres and water to acquire 3D images of soaked paper samples.

This study has applied and looked into the details of many image analysis routines and transport simulations to determine the characteristics of the imaged paper structures. Most of these routines have already been applied to low resolution 3D images of paper or to 3D images of geological samples. The main contribution from this study regarding the analysis of the structure is thus modification of some of the image analysis routines to include the surface layers after defining the surface using the rolling ball algorithm.

The practical application of the X-ray microtomography technique showed that calendering of a newsprint-like paper grade had a dominating effect on the paper structure compared to addition of reinforcement pulp, addition of retention aid and alteration of the head box consistency. The calendering resulted in a denser sheet having smaller pores and a higher resistance against transport through the porous phase, especially for the z-directional flow. The analysis of the applied factorial design yielded indicative results for the other papermaking variables. The few significant effects revealed that the addition of reinforcement fibres yielded slightly larger average pores and the addition of retention aid resulted in a slightly more complex structure. The alteration of the head box consistency seemed to have an insignificant effect on the small paper volumes.

Additionally, the assessments showed that the standard deviation for the assessed

structural characteristics were less than ±10% of the mean value. The mean values for the determined transport properties showed a higher standard deviation. However, the size of the 3D digital paper volumes render division of the volumes into sufficiently large subvolumes to maintain representative scales possible. Assessment of the transport properties of a number of subvolumes enabled a determination of the transport property:porosity relationship instead of a single mean value. In this way more information was extracted from the volume and the results were less affected by normal variation.

The results from the practical study of X-ray microtomography confirm the hypothesis that the density/solid fraction of the paper structure is a major determinant of the paper properties.

An important part of this study has been to consider which is the right technique of the 2D and 3D methods for various structural characterization applications.

There is a clear differentiation between the practical applications of the techniques. The SEM technique is the preferred technique for more repetitive and routine type assessments, for characterizations where the 3D extension of the objects are not of crucial interest or for assessments where the nature of fines and fibrils are of high importance. The X-ray microtomography is a natural choice for more complex structural assessments where the extension of the fibres and pores are of high interest, as for *e.g.* assessment of transport properties. The 3D extension of the structure may also be needed to obtain a better knowledge of how the paper structure influences the bulk paper performance properties than provided by the cross-sectional approach. X-ray microtomography is thus a powerful research tool that can provide information which is difficult or impossible to access applying other methods. However, the technique has its clear limitations when it comes to availability, representativity and resolution. It is also important keep in mind that the technique will not in the near future be an everyday technique that many scientists will have access to.

This study have helped establishing the SEM-BEI and X-ray microtomography microscopy combined with image analysis for paper structure characterisation. The tools provide many possible applications for the paper researchers that see the available possibilities. However, the results from application of the techniques for determining relationships between papermaking variables and paper structure characteristics, and possible relationships between structural characteristics and paper properties, are never better than the applied experimental scheme. Future application of the techniques for structural characterisation will hopefully add to the knowledge of the detailed properties of the paper material and thus assist in product and process optimization.

PREFACE

This thesis is submitted in partial fulfilment of the *doktor ingeniør* degree at the Norwegian University of Science and Technology (NTNU). This work has been carried out at the Pulp and Fibre Research Institute (PFI) and Department of Chemical Engineering at the Norwegian University of Science and Technology (NTNU) from 2000 to 2004, with Professor Torbjørn Helle as supervisor from 2000 to 2002 and Professor Øyvind W. Gregersen as supervisor from 2002 to 2004.

The work in this study is a part of the PROSMAT-project 130761/213: “Studies of how the paper properties depend on the individual fibre properties and the three-dimensional structure of paper“. Funding of the doctoral study was provided by Norske Skog ASA and the Norwegian Research Council.

ACKNOWLEDGEMENTS

First of all I would like to express my most sincere thanks to my supervisor Professor Øyvind Gregersen. Without his good ideas, excellent guidance, fruitful discussions and support this thesis work would not have been possible. I would also like to thank my supervisor for the first two years of my study, Professor Torbjørn Helle, for his advice and linguistic revisions of my manuscripts and this thesis.

I am also grateful to my co-supervisor Professor Shri Ramaswamy (University of Minnesota) for his help, guidance and encouragement. The months I had in Minnesota were a boost to my thesis work and will never be forgotten.

The guidance and assistance from Gary Chinga and Per Olav Johnsen (PFI) for application of SEM for assessments of paper structure characteristics is highly appreciated.

The work with X-ray microtomography 3D imaging and application of the acquired images for structural assessments required a multi-disciplinary approach, and had such complexity that co-operation was an absolute necessity to achieve the results provided in this thesis.
In this process the project team and steering committee of the 3D structure project at PFI have been a valuable support.
The contributions from the computer science students doing project and master thesis work related to the 3D project are acknowledged. The assistance from Heidi Brunborg, Torbjørn Smørgrav and especially Aslak Pedersen in helping me write the codes for 3D structural assessments when including the surface layers was invaluable.
Professor Jacques Silvy is acknowledged for introducing me to his equivalent pore concept for structural characterization.
Timm Weitkamp and Xavier Thibault's guidance to the practical application of synchrotron source X-ray microtomography imaging are highly appreciated.
The international co-operation with the groups working with X-ray microtomography and structural assessment has been invaluable. The international partners include groups at Department of Bio-based Products at the University of Minnesota (UMN), Department of Physics at the University of Jyväskylä (UJ) and Applied Mathematics, Research School of Physical Sciences and Engineering at the Australian National University (ANU). Among all the people I have had the privilege to be working with, I would like to give special thanks to Professor Shri Ramaswamy and Amit Goel (UMN), Professor Markku Kataja and Urpo Aaltosalmi (UJ) and Mark Knackstedt, Amit Goel (again), Christoph Arns and Tim Senden (ANU).

I would also like to thank all my fellow graduate students, the staff at the pulp and paper group at NTNU and people at PFI for pleasant company, interesting discussions and co-operation during these years.

Norske Skog ASA and the Norwegian Research Counsil are acknowledged for their financial support that made this work possible.

Finally my warmest thanks go to my dearest Jenny for her encouragement in ups and especially downs, for having the patience to bear with me in work-intensive periods and for just being the wonderful person she is.

LIST OF PAPERS

This thesis includes the following papers as journal articles referred to as Paper I-IV in the text:

I. Holmstad, R., Kure, K.-A., Chinga, G. and Gregersen, Ø.W., "Effect of temperature gradient multi-nip calendering on the structure of SC-paper", Accepted for publication in Nordic Pulp and Paper Research Journal

II. Holmstad, R., Antoine, C., Nygård, P. and Helle, T., "Quantification of the three-dimensional paper structure: Methods and potential", Pulp & Paper Canada, 104(7):47-50 (2003)

III. Holmstad, R., Goel, A., Ramaswamy, S. and Gregersen, Ø.W., "Visualization and characterization of high resolution 3D images of paper", Submitted for publication in APPITA Journal

IV. Holmstad, R., Aaltosalmi, U., Ramaswamy, S., Kataja, M., Koponen, A., Goel, A. and Gregersen, Ø.W., "Comparison of 3D structural characteristics of high and low resolution X-ray microtomographic images of paper", Submitted for publication in Nordic Pulp and Paper Research Journal

TABLE OF CONTENTS

ABBREVIATIONS AND DEFINITIONS

ABBREVATIONS

2D	Two-dimensional
3D	Three-dimensional
μ	Mean value
σ	Standard deviation
BEI	Backscattered electron imaging
BSKP	Bleached softwood kraft pulp
CCD	Charge coupled device
CD	Cross direction(al)
CLSM	Confocal laser scanning microscope
CT	Computed tomography
DT	Distance transform
ESRF	European synchrotron radiation facility
FEM	Finite element method
FIB	Focused ion beam
LB	Lattice-Boltzmann
LM	Light microscope
LWC	Light weight coated
MD	Machine direction(al)
MIP	Mercury intrusion porosimetry
NTNU	Norwegian University of Science and Technology
PFI	Paper and Fibre Research Institute
RBA	Relative bonded area
SC	Supercalendered
SEM	Scanning electron microscope
SSA	Specific surface area
TMP	Thermo mechanical pulp
VPSEM	Variable pressure scanning electron microscope
X-μCT	X-ray micro- (computed) tomography
ZD	Z-direction(al), perpendicular to the paper plane

DEFINITIONS

3D reconstruction:	Reconstruction of the 3D structure based on 2D images
Binarising:	The pixels/voxels in a greyscale image are set to either black or white
Digitizing/discretizing:	The transfer (in microscopy) from continuous medium to pixelated/voxelated representation
Distance transform:	Method for creating a distance map of the imaged structure
Erosion:	Binary morphological operation that uniformly reduces the size of objects in relation to the background
Filtering:	Reduction of noise in the image
Pixel:	Picture elements of a 2D digital array (image)
Radon transformation:	Method for determining the 3D structure from a high number of projection images taken during a 180° rotation of the imaged sample
Segmentation:	The first step of image analysis. Objects of interest are extracted from the background
Skeletonization:	Binary morphological operation (erosion) that reduces an object to a skeleton representation
Sobel operator:	Spatial edge enhancement filter
Smoothing:	Reduction of the local greyscale variation in the image
Surface rendering:	Transformation of a pixelated/voxelated object to a surface representation
Threshold:	Manually or automatically selected value used to segment an image into a foreground (object of interest) and background
Voxel:	Picture elements of a 3D digital array (image)

CHAPTER 1

INTRODUCTION

1.1 Background

Today still relatively little is known of how the details of the paper structure influence the paper properties. The commercial papermaking is thus mostly governed by experience of how different adjustments of raw material properties, fibre furnish, paper machine settings and post processing affects the bulk properties of the manufactured paper. The complex structure of the paper material render it difficult to derive precise comprehension models for the physical mechanisms of the papermaking adjustments to the paper web. Most existing models of the physical mechanisms governing the performance properties of paper are therefore empirical by nature.

To possibly better understand the relationship between the papermaking variables and the paper properties, it is necessary to obtain knowledge of the detailed structure of the paper. Access to the detailed paper structure allows observation of how various papermaking variables alter the paper structure, and can thus give a better insight into how the paper properties are affected. However, for most scientific and practical applications, an observation is not sufficient. It is therefore a need for a structural assessment that yields quantitative results.

Acquisition of cross-sectional images of paper, applying the backscatter mode of a Scanning Electron Microscope, yields images of the paper structure of sufficient quality for structural assessments from image analysis.

To fully understand how the paper structure is affected by the papermaking and how the structure governs the performance properties of the paper, the two-dimensional (2D) information that can be extracted from cross-sectional images is often not sufficient. Optical and transport properties depend on the three-dimensional details and extension of the fibre network and the interconnected pores. The paper mechanical properties also partly depend on the 3D extension of the fibre network. It is therefore a need for a three-dimensional (3D) microscopy technique that allows imaging of the 3D extension of the paper structure with sufficient resolution to see the details affecting the transport, optical and paper mechanical properties.

The X-ray microtomography technique allows 3D imaging of most paper grades at a spatial resolution down to approximately 1 µm. This resolution is sufficient for observing most features of the fibre network and to yield physically reasonable structural assessments. Although the resolution is not sufficient to detect all fines, fibrils and mineral particles, the 3D images and detailed structural assessments may yield at least indicative values, even for optical properties.

The relatively new possibilities provided by microscopy techniques, which yield access to the 2D and 3D features of the detailed paper structure, can be applied to obtain better knowledge of how various papermaking variables affects the paper properties through alteration of the paper structure. Improvement of the knowledge of the structural mechanisms governing the paper properties may help to a more knowledge based operation of the paper machines and be applied for process and product optimization.

1.2 Objectives of the study

This study evaluates the techniques that are considered the best present available technologies for acquisition of the detailed 2D and 3D paper structure at sufficient resolution and contrast for subsequent image analysis. It is the intention to show the working principles of the chosen SEM-BEI technique (2D) and X-ray microtomography (3D) and discuss different aspects of sample preparation, sample mounting and image acquisition procedures that may affect the image quality.
The consideration of image quality include a presentation of the applied image segmentation procedures and how the choice of filtering and thresholding criteria may affect the details of the digital representation of the paper structure. As the results from the image analyses are strongly depending on as correct digital representation of the structure as possible, the discussion of the image quality of the obtained images of the detailed paper structure are considered an important part of this study.

It is important to utilize the images of the detailed paper structure for quantitative assessments. This is best done by appropriate image analysis techniques. Improvement of old image analysis procedures and development of new routines are one of the objectives of this study, both for the cross-sectional and 3D images.

Practical application of the microscopy techniques combined with image analysis for studying the relation between papermaking variables and paper structure characteristics and the correlation between paper structure characteristics and bulk paper properties will be accomplished. The practical applications are considered to be important contributions, as no technique has proven useful before a practical application have yielded improved knowledge not accessible by other techniques.

The 2D technique of SEM-BEI and the 3D technique of X-ray microtomography will have different pros and cons for structural assessments. It is the intention of this study to clarify which is the preferred technique according to what is going to be measured and the nature of the conducted experiment.

1.3 Outline of the thesis

This thesis is basically divided in two major parts. The first major part is about the application of image analysis of cross-sectional images of paper for assessment of detailed structural characteristics. The second major part is dealing with application of X-ray mircrotomography for obtaining high quality 3D images of paper and methods for assessing features of the acquired digital paper structures. The main body of the thesis also include a chapter about assessment of pore geometry between the 2D and 3D chapters, as the performed analysis of the porous phase include assessments of both cross sections and 3D images.

The attached papers (**Paper I-IV**) are more focused on the practical application of the presented techniques for detailed assessment of the paper structure. To avoid repetition, it is therefore often referred to the attached papers for the results from practical application of the presented structural assessment techniques.

Chapter 2 is treating various aspects of the application of Scanning Electron Microscope (SEM) in backscatter mode (BEI) for acquiring high quality cross-sectional images of paper for assessment of detailed structural properties. Improved and new routines for analysis of the paper cross sections are presented. A practical study applying the analysis of SEM-BEI cross sections for assessing the effect of temperature gradient calendering to SC-paper is presented (**Paper I**).

Chapter 3 shows how the pore geometry can be characterized applying image analysis of paper cross sections and digital representations of the 3D paper structure. The findings from the characterization of the porous structures are presented and compared to earlier findings and methods. The results also show how the 3D technique may complement the 2D technique for assessing the volume extension of pores.

Chapter 4 gives a detailed explanation of the application of the X-ray microtomography technique for obtaining high quality 3D images of paper showing the detailed paper structure. Consideration of how the technique can be applied to find explanations of how papermaking variables affect the paper properties through alteration of the detailed paper structure are presented (partly in the attached **Paper II**). Methods for image processing, image analysis and simulation of transport properties performed directly on the digital representations are presented. The visualization and assessment of the synchrotron source phase contrast 3D images are summarized in the attached **Paper III**. Various aspects that may affect the image quality and the structural assessments are considered. The study include an evaluation of the application of synchrotron source compared to stationary source X-ray radiation (**Paper IV**) for image acquisition and absorption mode compared to phase contrast mode for contrasting the structural constituents.

Chapter 5 is a practical experiment showing an example of how the X-ray microtomography technique and 3D image analysis can be applied to analyse the relationship between papermaking variables, 3D structure and paper properties. The paper was produced on a pilot paper machine producing newsprint-like paper. The applied papermaking variables were: Addition of reinforcement pulp, addition of retention aid, alteration of the head box consistency and calendering.

Chapter 6 gives an overall discussion of common problems of analysing the images of the paper structure applying the SEM technique and X-ray microtomography. The chapter also include a discussion of what is the most suited technique for different practical applications.

Chapter 7 presents the overall conclusions of this work and suggestions for further work.

CHAPTER 2

CROSS-SECTIONAL (2D) ANALYSIS OF PAPER STRUCTURE CHARACTERISTICS

2.1 Introduction

The paper is often perceived as a uniform, planar material. However most of its material properties are depending on the spatial arrangement of small solid particles and pores, the detailed paper structure. To study the characteristics of the paper structure, it is necessary to obtain cross-sectional images to look inside the paper. Microscopy and image analysis of cross-directional cut surfaces through the local paper structure is the most intuitive and readily available method for characterization of the detailed paper structure.

Other methods for assessing special features of the paper structure include surface characterization, sheet splitting and β-ray based basis weight distribution. The paper surface is an important feature for most paper grades, therefore there exist a number of methods allowing a detailed characterization of the paper surface using surface microscopy or topology techniques combined with image analysis. It is also possible to split the sheet into a number of layers using adhesive tapes and obtaining images of the different layers. The method yields results of the layered paper structure and how fibre orientation change in the thickness direction. Although these methods are of great interest for the pulp and paper industry, they are considered outside the scope of this work.

Development of microscopy techniques and computer hardware now allows access to the three-dimensional (3D) paper structure. The techniques for obtaining 3D characteristics of the paper structure are treated in Chapter 4.

Microscopy is a widely used tool in pulp and paper research. The light microscope was applied for examining the structure of wood cells as early as 1665 [1]. Studies of cell wall and fibre characteristics applying microscopy were already in use in the second half of the nineteenth century [2]. However, the use of microscopy for inspection of paper cross-sections are of considerably newer date. The development of computer technology and software has during the last few decades have made it possible to assess the detailed paper structure applying image analysis. The scope of this study is to examine the possibilities and possible limitations of cross-sectional analysis of the paper structure and to explore new routines for assessment of structural properties.

The microscopy and image analysis of cross-sectional images for characterization of the paper structure may roughly be divided into three categories;

- Observation of paper structure features and quality problem detection by visual inspection
- Image analysis for bench marking and product development
- Image analysis for explanation of physical behaviour

The following sub chapters will deal with the different categories in more detail.

2.1.1 Application of microscopy for visual inspection

The most straightforward application of microscopy and analysis of cross sections is observation of structural features and detection of various structural problems. As this is the most readily available use, the most commonly use up to now has been of this form.

The plain application of microscopy observation have gained knowledge not accessible by other methods. Examples of important knowledge obtained from observation of cross-sectional images include observation of the layered structure of paper and the distribution of fines and fillers throughout the structure. Cross-sectional images can tell whether the small particles aggregate and whether they have a tendency to fill the open pores in the structure or rather locate between fibres [3]. Microscopy have been widely applied to observe the collapsing and decollapsing behaviour of pulp fibres before and after different process effects on pulp or the sampled paper material [4,5,6].

Another much used application of microscopy is for trouble shooting, detecting problem elements and structural defects. Typical problems and defects that can be observed by microscopy of cross sections include delamination, compression breaks and the occurrence of dirt, precipitations or micro-organisms in the paper structure. The microscopy may also visualize small shives that cannot be seen by direct observation of the paper sample. It is possible to observe quality problems related to poor impregnation of surface glue, ink or coating by appropriate sample preparation and choice of microscope. More specialized problems detectable by microscopy of cross sections include observation of sheet compression after crêping, quality evaluation of the gluing between fluting and liner and the regularity and quality of the undulating fluting. Microscopy is also well suited for accessing information of the applied coating formula and filler types in competitive paper products.

2.1.2 Application of image analysis for benchmarking and product development

To assess differences between different paper products, by an objective differentiation, one has to quantify structural properties. It is thus necessary to develop and apply image analysis routines that allows a quantification of useful structural properties. The microscopy and image analysis can help explain differences in end use properties that can not be explained by traditional bulk measurements.

By development of standardised image analysis routines research institutions may establish the quantification of detailed structural properties as a routine test for *e.g.* benchmarking.

2.1.3 Application of image analysis for explanation of physical behaviour

Microscopy combined with image analysis provides the paper scientists with a powerful research tool for quantification of how different modifications of raw material and paper processing affect the detailed paper structure. The development and application of image analysis routines is necessary, as the quantification allows an objective measure of detailed paper characteristics not available by other techniques.

Application of microscopy and image analysis, as a tool for finding explanation for the physical behaviour of paper, must be combined with an experimental scheme with a systematic change of the variables considered to have an effect on the paper structure. The experimental scheme is important, as it establishes the relationship between input variables and measured characteristics. Usually there is also a need to combine the image analyses with standard bulk measurements (according to ISO-standards) to understand the paper structure to bulk paper properties relationship. Obviously, it is also necessary to sample a sufficient number of the relatively small cross sections, relative to the scale of formation/flocs, to determine a bulk representative property.

The application of microscopy combined with image analysis is a tool already reported being used in the paper research. Allem [7] and Allem and Uesaka [8] reported measurement of the coating layer thickness distribution and its correlation to print quality and micro roughness of the base paper. Chinga and Helle [9,10] studied the effect of different coating techniques and formulas on the detailed coating characteristics and the print gloss. The density distribution in the z-direction under different calendering conditions were studied by Rättö et al. [11]. These studies are good examples of paper properties research based on microscopy and image analysis.

It is the intention of this work to develop new routines and improve already existing ones for improved characterization of the detailed features of the paper structure. Another important issue is to show the potential for image analyses for gaining fundamental knowledge of paper characteristics not accessible by other methods. The study thus has a main focus on the application of microscopy and image analysis to explain the physical behaviour and properties of paper. Such routines may even be applied for product development and the detection of structural problems.

2.1.4 The objective of the 2D study

The main objective of the 2D study is the same as the overall objective of this study, to contribute to a better and more detailed characterization of the paper structure to improve the comprehension of how the paper structure are interrelated to the paper properties. To achieve this, it is considered important to survey the current status of paper cross section characterization, to improve already existing routines and possibly develop new image analyses. It is considered important to show the complete cycle from image acquisition to the measured characteristics to make the technique applicable for new users. In this context it is also important to show all factors influencing the final result to reveal the pitfalls of the technique and where there will be room for improvements. Practical examples of the application of image analysis routines as a research tool is considered to be crucial, as the routines are not proven useful before they are applied to gain new knowledge not accessible by other methods.

The characterization in itself yields quantitative measurements of the paper structure and thus improved knowledge of the paper structures relationship to input variables and paper properties. This may provide new possibilities for manufacturing paper with improved properties or producing paper having the same properties, but manufactured at lower production costs. The crucial element with regards to product improvement will be to have a quantitative measure of the detailed structure characteristics. Without quantitative measures there are no means for process control or objective assessment of the process improvements.

2.2 Materials and methods

2.2.1 Choice of microscopy technique

There are a number of different techniques for obtaining cross-sectional images of paper. Among these are light microscopy (LM), transmission electron microscope (TEM), confocal laser scanning microscope (CLSM) and scanning electron microscope (SEM) the most widely used. Backscatter electron imaging (BEI) is based on detection of local average atomic number, which on a high vacuum SEM yields high contrast between fibres, pores and fillers in the cross sectional images. The high contrast combined with the potential for high magnification and a well established, straightforward sample preparation technique, known to distort the structure minimally, made the SEM-BEI technique the preferred choice for obtaining cross-sectional images for assessment of the paper structure. This study thus focus on methods based on SEM-BEI imaged cross sections. Most of the image processing and analyses are however general and should be transferable to cross-sectional images obtained by other microscopy techniques.

2.2.2 Scanning electron microscope (SEM)

Working principles

Until the invention of the electron microscope and introduction of SEM as a research tool for papermaking industry from 1959 and onwards [2], the resolution for microscopy of fibre and paper structure was limited by the wavelength of visible light. Through application of a scanning beam of accelerated electrons, the sample can be imaged with a considerably shorter wavelength than that of visible light, thus enabling a much higher magnification. In the SEM, the electron beam is focused into a sub-micrometer sized spot on the specimen and traverses over each point of the specimen surface in turn, one scan line at a time, to form a raster. The electrons reflected from each point on the specimen are collected by a detector, which transfers the electron signal into colour intensity according to the strength of the detected signal. For imaging of the paper structure through the application of SEM on cross sections, it is usually the local material composition that is of interest. Therefore the imaging is based on detecting the elastically reflected incoming electrons, the backscattered electrons. The reflected electrons fraction vary depending of the local average atomic number. The higher the average atomic number, the more backscattered electrons. However, the backscatter signal is not dependent solely on material composition. Uneven surface topography will reflect the incoming electrons in different spatial directions, meaning that non-planar surfaces will give more reflections outside the detecting region of the backscatter detector. Hence, to avoid effects from topography affecting the contrast in the images, the surface must be totally planar.

An important feature of the SEM, affecting the image quality, is the penetration of the incoming electron beam into the structure, resulting in a backscattered signal which is affected by material lying below the specimen surface. The penetration of the electron beam will be deeper the lighter the atomic density, hence the exitation volume is relatively large in paper samples. The excitation volume is also depending of the applied acceleration voltage, the higher the voltage, the deeper the penetration. The electron distribution in the specimen according to acceleration voltage and local atomic density is shown to the left in Figure 2.1 [12]. The signal volume is shaped like a light bulb for low atomic density areas, as is the case for paper. The extension in the width result in a lower spatial resolution than the focused electron spot. The backscattered electrons are reflected from the upper half of the electron distribution bulb [12], as shown to the right in Figure 2.1. The penetration depth and spatial resolution will influence the quality of the cross-sectional image.

Sample preparation

The sample preparation stage is crucial for the image quality, as it is essential that the preparation minimizes all factors that may disturb the detailed paper structure. It is thus important that the most suitable sample preparation for the specific study is chosen and is carefully performed, preferably by a skilled technician.

Sample preparation of planar surfaces for geologic and metallurgic samples for SEM have for decades been performed by grinding and polishing. The technique is transferable to paper by embedding the paper samples in epoxy resin under vacuum. The sample preparation in this study is done according to the principles proposed by Gibbon et al. [13], applying the modifications applied in Williams and Drummond [14], except the final removal of a thin layer of resin on the specimen surface. Instead an alternative epoxy resin used for embedding, which combined with backscatter imaging at high vacuum yields good contrast between fibres and epoxy without removing the resin in the surface [15]. Applying the principles for sample preparation mentioned above, the samples are embedded in epoxy, giving rigid support for the paper structure, which

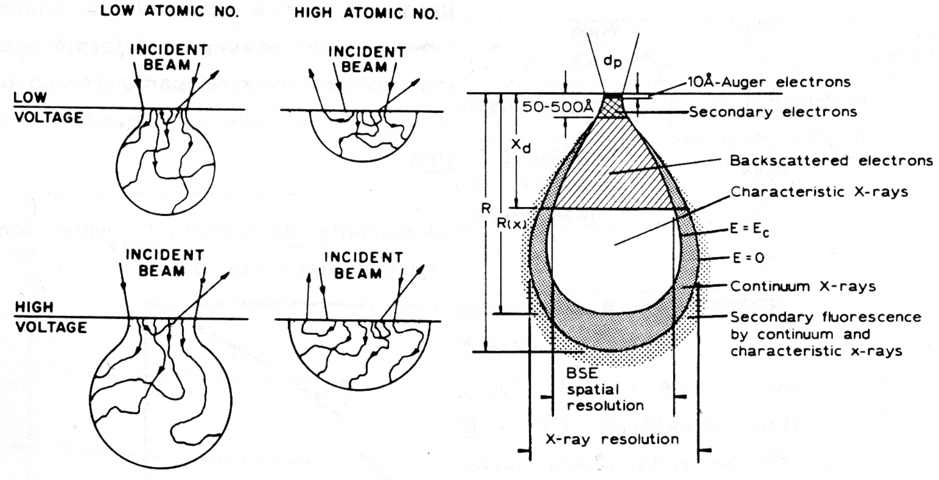

Figure 2.1 **Left**: The shape of the electron distribution in the specimen as a function of average atomic number in the local spot and the acceleration voltage. **Right**: The penetration depth (vertical) and spatial resolution (maximum horizontal width) for the different electron signals in SEM.

allows grinding and polishing of the specimen surface onto a planar surface while minimizing distortions to the structure. An epoxy block may contain up to 10 cross-sectional paper samples of 15-20 mm width. Ethanol is applied as a lubricant in grinding and polishing and as a cleaning agent in between the different steps. The ethanol solves and washes out ink and surface glue in addition to the ground off material and abrasive particles, thus disabling studies of the interaction between paper and ethanol solvable agents. An example of a prepared epoxy block, before application of the carbon coating to make the surface electrically conductive, is depicted in Figure 2.2.

An alternative to grinding and polishing the epoxy embedded specimen surface is to apply a microtome to produce a thin slice or a smooth specimen surface [2]. However, the microtome slicing will inevitably introduce more artefacts to the paper structure than will grinding and polishing, both for the thin slice and the stub. The microtoming tends to introduce distortions from knife chatter and ripped out pigments [16,17]. However, the microtoming has one advantage, as there is no need of ethanol, or other lubricants or cleaning agents, in the preparation stage, study of interaction between paper and ink, surface glue or resins is thus well suited for microtoming techniques

Other alternatives introduced to produce clean, planar surfaces for SEM are focused ion beam (FIB) [18] or micromilling [19]. Although the methods are promising, they have their main advantages in making consecutive images to produce 3D data sets. The advantages over grinding and polishing of epoxy embedded paper samples are not well documented and considered relatively marginal for the studied paper samples. The application of these techniques are therefore omitted in this study.

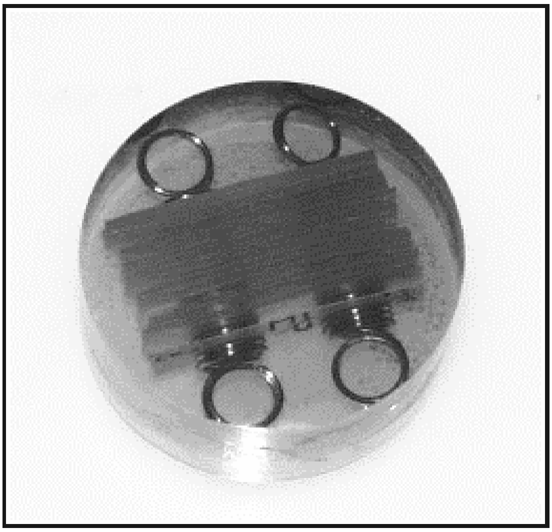

Figure 2.2 An example of a prepared epoxy block with several aligned cross-sectional paper samples embedded in the epoxy. The sample is ground and polished into a smooth surface.

Image acquisition

The preferred imaging mode for paper cross sections in SEM is the detection of backscattered electrons, SEM-BEI. As the paper material only consists of organic compounds, except for fillers and coatings, the penetration of the incoming electron beam may be relatively deep. It is thus preferable to apply a relatively low acceleration voltage to avoid blurred edges in the images. Additionally, the electron current can be controlled to adjust the number of incoming electrons, enabling an extra variable for adjusting the signal to noise ratio in the images.

In this study the cross sectional images were acquired using a Hitachi S-3000 VPSEM instrument. The BSE images were generated using 5 kV accelerating voltage with a working distance of 8-10 mm. The chosen working distance is close to the optimum trade-off between covering as much as possible of the angular distributed reflected backscattered electrons and getting the highest possible depth of field. The generated images have 256 grey tone levels.

The standard magnification applied in this study was 250X. When optical properties were of interest a spatial resolution of 2560x1920 pixels was applied, but when the interest was only for the material distribution in the z-direction the spatial resolution of 1280x960 pixels was sufficient. Lower spatial resolution will reduce the time needed for processing and analysis. The resulting pixel resolution for 250X magnification and the spatial resolutions of 1280x960 and 2560x1920, were 0.37 and 0.19 μm/pixel respectively.

The physical length of the imaged paper sample area with the chosen imaging settings were just below 0.5 mm. The imaged areas were thus relatively small compared to the size of flocs and formation effects in paper [20]. It was therefore essential to image a number of replicates to assess a reliable average of the different paper structure characteristics. The replicate images should preferably be independent to increase the representativity and reduce the normal variation. The standard number of replicates in this study were 15, where three and three images are obtained from areas on the same cross-sectional paper sample with a distance sufficient to achieve spatial independence.

2.2.3 Image processing and analysis

The image processing and analysis in this study are performed applying the public domain program *ImageJ*, available at **http://rsb.info.nih.gov/ij**. The image processing is based on built-in features, whereas the image analysis routines are developed in-house at PFI (Paper and Fibre research Institute).

It is important to remind that the results from image analyses are never better than the quality of the cross-sectional images, although image processing can improve the image quality.

Background

It is required to have a binary cross-sectional image for performing image analysis of the detailed paper structure characteristics. The microscopy image must therefore be separated into two phases. The segmentation of the structure based on the greyscale histogram is called thresholding. Normally the two phases are solid material and voids, but it is also possible to separate the fillers and/or coating into separate phases when these are present. Through staining techniques, yielding different colours or grey shades in the images, it is also possible to divide the fibrous material into separate phases, as *e.g.* mechanical and chemical pulp fibres and fines and fibres [2].

Even though the user has been careful to avoid introduction of noise or artefacts in the image, the images will never be of perfect quality. It is therefore necessary to perform one or several steps of filtering to reduce the noise. Filtering techniques will normally never have a perfect separation between noise and physically present elements. Thus, filtering techniques must be applied with precaution to find an optimum trade-off between removal of disturbing noise and preservation of solid elements. The best trade-off will usually be seen from a visual comparison between the filtered and the original non-filtered image. The filtered image where the structure topology seems best preserved is normally the most optimally filtered. Filtering can be performed both prior and after thresholding.

Filtering of greyscale images

The cross-sectional images from high vacuum SEM-BEI usually have high contrast and a low level of small scale random noise, so called salt and pepper effect. However, when random noise is present, this can be reduced by median filtering [21] on the greyscale micrographs prior to thresholding. The median filtering consists of a mask of 3x3 pixels replacing the centre pixel with the median value.

When acquiring the cross-sectional images, the aim is to spread the material content as well as possible over the available 256 grey tones to get the best possible contrast between the phases.

Segmentation/thresholding

The images are originally depicted in greyscale. The micrograph in this study has 256 different grey levels. The frequency of the different shades can be plotted in a histogram distribution. An image with good contrast shows a clear difference between the phases in the colour histogram, as shown in row 2 of Figure 2.3. Note that even the best quality images will still have some overlap between the phases. Thus, there is usually a need for filtering after the thresholding. The segmentation of the fibre phase is always the most difficult one when there are three phases present, as in the histogram of Figure 2.3, as it has an overlap to both the void and filler phase regions.

The threshold value applied in this study is always automatic when there are only two phases present. The automation allows an objective segmentation. The automation is preferable according to several studies, as the thresholding is shown to vary between operators, and even for the same person over a period of time [22].
The automatic thresholding based on the greyscale histogram is done according to Ridler and Calvard [23]. In paper samples that have more than two phases (fibres and pores), the automatic thresholding cannot be applied for more than the first step. Separation of the remaining coupled phases must be done manually. Choosing the threshold value interactively, enabled by a direct visualisation of the effect of threshold value to the classification of the pixels, will usually result in good separation. The manual threshold will often be almost as good as the automatic one, as the interactivity combined with human perception usually clearly show an optimum between the preservation of phase topology and the introduction of noise. Manual thresholding without the interactivity will result in larger subjectivity and variation. An example of a SEM cross section of good quality before and after thresholding of the different phases is shown in Figure 2.3.

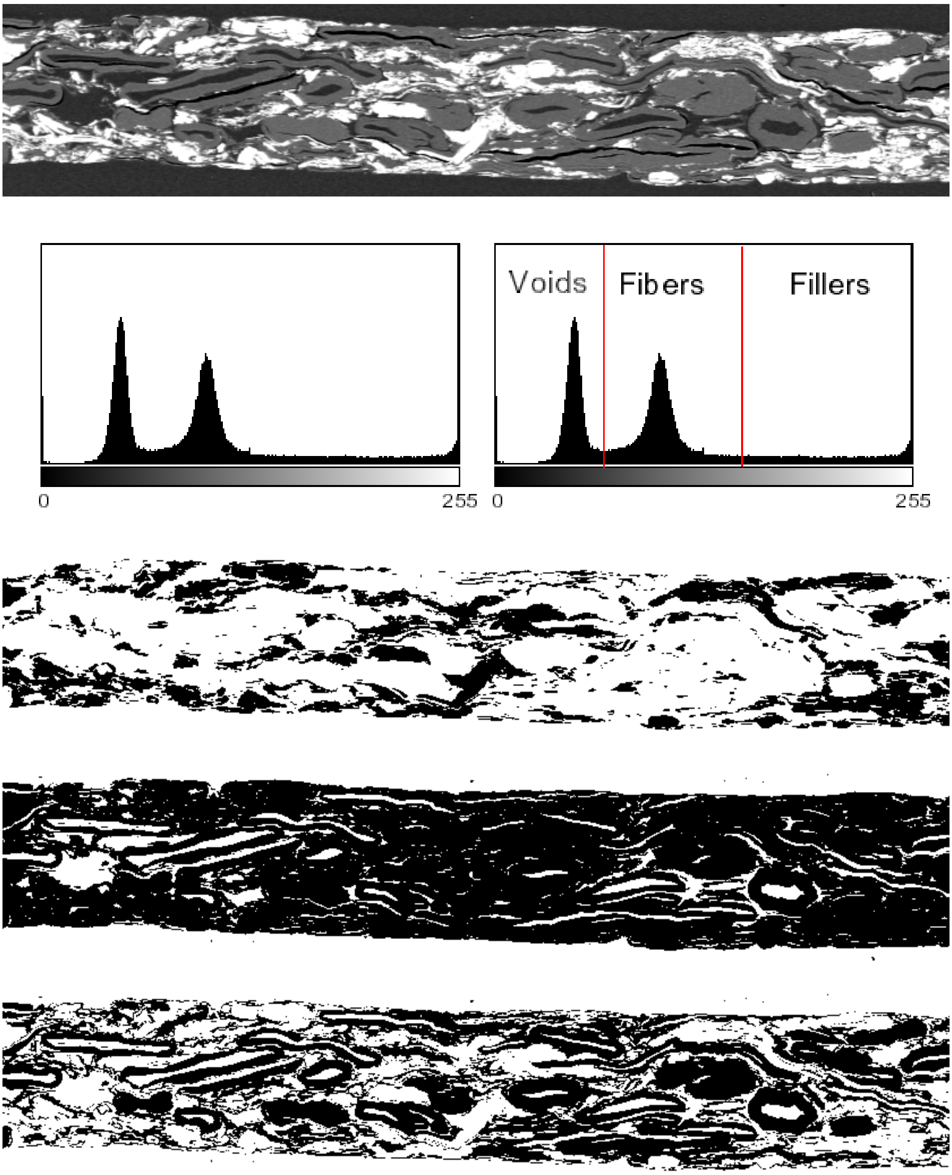

Figure 2.3 An illustration of the process of thresholding for the three phases of an SC-paper. **First row:** Original greyscale image. **Second row, left:** Greyscale histogram of the cross section. **Second row, right:** The histogram separated into the three phases. **Third row:** The resulting filler phase from automatic thresholding. **Fourth row:** The resulting solid phase from manual thresholding. **Fifth row:** The resulting fibre phase when the filler phase is subtracted from the solid phase.

The resulting binary images after thresholding in this study are by preference black foreground pixels for the solid elements and white background pixels for the pores and surroundings.

Binary filtering

After median filtering and thresholding some pixels will be misclassified due to the overlap of grey tones between the phases and some noise and artefacts might still be present. It is thus necessary to improve the binary images applying filtering techniques to the thresholded images.

Application of morphological operators is one possible approach for filtering of binary images. Such operators are well suited for handling the noise in the cross-sectional images of paper. The morphological operators are based on inspection of the neighbourhood of all individual pixels in the image. All pixels, except the ones on the edges, have 8 neighbours, as illustrated by the single black pixel surrounded by eight white pixels in the left image in Figure 2.4. According to a set threshold of neighbours, foreground pixels will either be removed or added.
The morphological operators consist of the single step operations *erode* and *dilate* and the two-step operations *open* and *close*, which both are combinations of *erode* and *dilate*, but in a different sequence.

The *erode* operator will remove pixels from the edge of solid objects, if the number of white/background pixels are higher or equal to the given neighbour threshold. The operator will thus result in smaller fibre cross-sectional areas and disconnect objects that are only slightly touching.
The *dilate* operation adds foreground pixels to the edge of the solid objects if the number of surrounding foreground pixels are equal to or higher than the set threshold. The *dilate* operation thus result in larger fibre cross-sectional areas and joins objects that are only disconnected by one or two pixels.
The *open* routine performs an *erode* step before the dilate step. The *open* operator is thus most suitable for removing small objects and disconnect slightly touching objects while keeping the fibre cross-sectional area close to constant. It will also fill small holes in the fibre walls, which are surrounded by foreground neighbours in a fashion that disables increased area by the *erode* step. However, caution should be taken when applying this routine, as it will remove much fine material if the threshold is set too low.
The *close* operation performs a *dilate* step before the *erode* step. The *close* operator is thus suitable for filling holes in the fibre walls and connecting objects without increasing the fibre cross-sectional areas significantly. It will also remove small objects, which are surrounded by background neighbours in a fashion that disables increased area by the *dilate* step.
The application of the morphological operators to a single fibre cross section, when choosing a threshold of four neighbours is shown to the right in Figure 2.4.

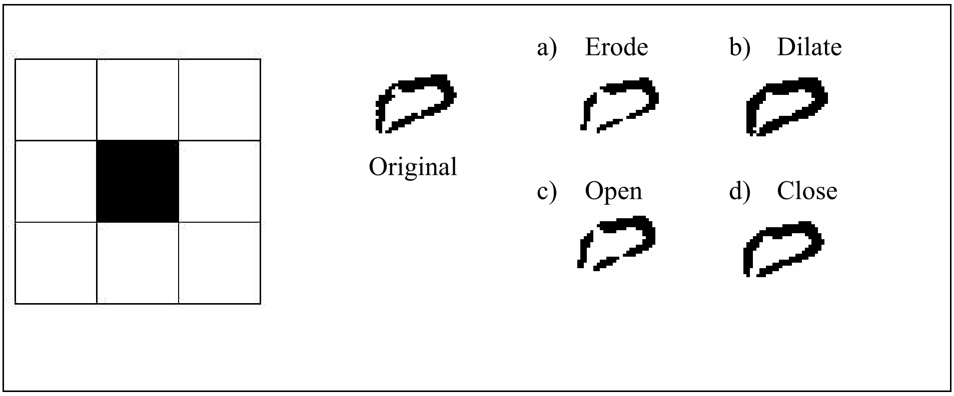

Figure 2.4 Left: The surrounding eight neighbours (*i*) to a given pixel in the binary image. **Right:** The filtering operations influence the original fibre cross section in different ways, here with a set limit of four neighbouring pixels ($i = 4$):

a) *erode* [i^{*}] Removes pixels from the edges of objects in a binary image, where continuous black areas in the image are considered objects, and the background is assumed to be white. A pixel is removed (set to white) if *i* or more of its eight neighbours are white. Erosion separates objects that are touching and removes isolated pixels
b) *dilate[i]* Adds pixels to the edges of objects in binary images. A pixel is added (set to black) if *i* or more of its eight neighbours are black. Dilation connects discontinuous objects and fills in holes.
c) *open[i]* is two following operations, first *erode* then *dilate* with the same limit *i*
d) *close[i],* as the *open* operation, but the operations are done in the opposite order
*) *i* can be chosen between 1 and 8 (as shown in the left figure)

The structure in paper usually consists of many connected, thin objects, which preferably should be preserved after filtering. Simultaneously, the cross-sectional area should be kept close to constant. The preferred morphological operator for paper cross sections is therefore usually the *close* routine with a high threshold to allow removal of small solid elements in the *erode* step.
The choice of threshold value is obviously crucial for the effect of the filtering. As the paper structure consists of many thin connected objects, it is necessary to apply very gentle threshold values. In this study the filtering by morphological operators are thus performed applying a threshold of 6 or 7 neighbours dependent of the level of noise relative to fines and fibrillar material. The application of gentle morphological operators can be performed in several subsequent iterations to remove more noise, while still preserving the network topology. The result from application of the *close* operation with a threshold of 7 and two subsequent iterations, to a binary image after thresholding, is shown to the right in row 2 in Figure 2.5.

The morphological operators usually emphasize all neighbouring pixels equally. However, in images with solid objects having a definite width to height ratio, as *e.g.* machine directionally cut cross sections, the neighbours can be differently emphasized by applying 3x3 masks. The masks are then chosen in a way that better preserves the horizontally connected pixels than the vertically connected. However, all cross sections analysed in this study are cut in the cross directional direction, thus application of masks are omitted here for the morphological operations.

The gentle filtering by median filtering before thresholding and application of morphological operators on the resulting binary image will retain a number of relatively small noisy unconnected objects. These can be removed by segmenting the cross-sectional image according to size. This filtration step is successful in removing almost solely noise, as most solid elements in the paper structure are interconnected. The result of removal of objects smaller than 1 μm^2 to a binary image after thresholding and application of gentle morphological operators are shown to the left in row 3 in Figure 2.5.

As a final step in the filtering there might be need for manual editing. When comparing the original greyscale image to the binary image after automatic filtering routines, there might still be some solid areas in the background that obviously are noise or artefacts, or topography or dust on the imaged sample surface. These must be manually removed. As manual editing is both time consuming and user dependent, it is preferable to remove as much noise as possible by automatic routines prior to the manual editing. For subsequent delimitation between structure and background, it is of utmost importance to remove all objects outside the surface, as any remaining object outside the structure will cause considerable malfunction in the definition of the surface.
A binary image after full filtering, including manual editing, is shown to the right in row 3 in Figure 2.5.

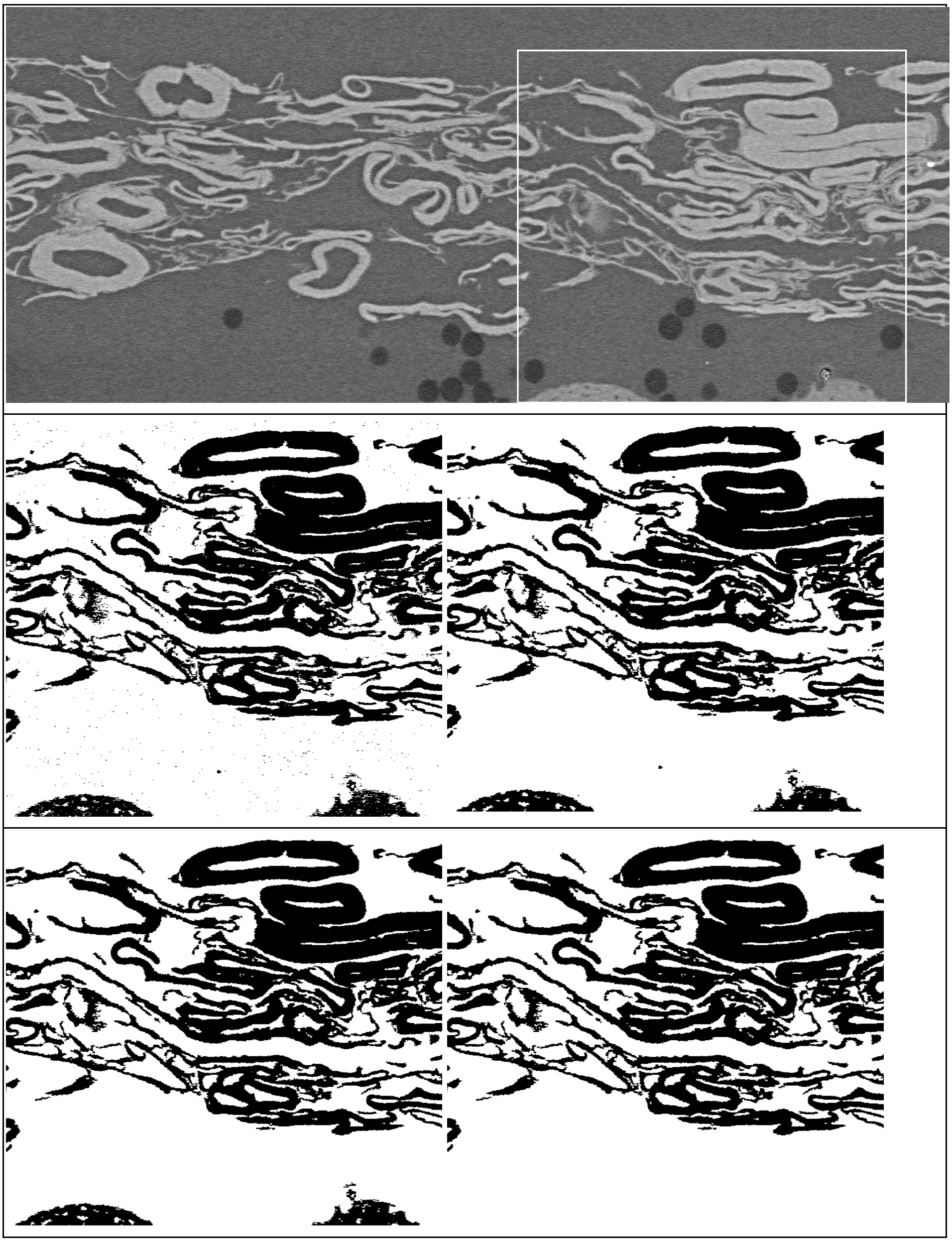

Figure 2.5 Illustration of the filtering steps on a cross section of a newsprint sample. **First row:** The original cross-section. The white square marks the area of interest. **Second row, left:** The focused area in the thresholded image. **Right:** The area after two iterations of the morphological operation *close* with a threshold of seven neighbours. **Third row, left:** The area after unconnected objects smaller than 1 μm are removed. **Right:** The area after manual editing.

2.2.4 Image analysis routines for paper cross sections

Background

To extract more information from the images than what is apparent from visual inspection, it is necessary to perform image analyses on the cross-sectional images. There exist a number of published image analysis routines in the pulp and paper research literature. (Additionally there are routines that are in-house techniques, kept from public access). Many of the published image analysis routines are based on interactive and thus relatively subjective selection of features as *e.g.* fibre cross sections, which result in user dependent results and time consuming analyses. Development of automated routines will help the analyses become more objective and much faster.

The first step of extracting information from cross-sectional images is always a segmentation, as a binary image is a requirement for all automated image analyses. Segmentation of cross sections of LWC paper grades into its constituents of coating layers and fillers have been published by Allem [7]. After removing the fillers based on size, area and shape, the resulting binary images were well suited for image analysis. The local coating layer thickness in the images was measured in 1 pixel wide (0.32 µm) vertical lines, separated by about 11.0 µm, for both sides simultaneously. From the resulting coating layer distributions, based on 30 vertical measurements in 80 replicates per paper grade, different statistical parameters were derived, including percentage of uncoated areas. The determined statistical parameters were applied for determining measures of the coating uniformity as a result of base stock micro roughness. The mean coating thickness, coefficient of variation and percentage of uncoated areas were found to correlate with print quality as determined by subjective ranking.
Based on the same micrographs as in [7], Allem and Ueaska [8] presented additional image analysis routines for assessing coated papers. The methods include segmentation of the base paper. In addition to measuring the coating thickness, the base paper segmentation allowed measurement of caliper (whole structure) and base sheet thickness. The vertical lines applied here had an inter-distance of 5 µm. The measurement based on the vertical lines include the void (porosity) and mass fractions for the base sheet. The surface roughness values of the base sheet were also determined by measuring the distance from the image edge to the first fibre pixel in each of the measuring vertical lines. The roughness was then evaluated as the arithmetic mean deviation (R_a) of the measured lines for both surfaces.

The roughness can be quantified by a number of roughness parameters when the vertical distances from a reference line to points on the paper surface are known [8]. However, if the surface roughness is not measured for determining its correlation to other properties in the cross section, the surface roughness should instead preferably be measured by surface topography methods, as the surface topography images cover a much higher surface area than detected in cross sections.

A comprehensive set of image analysis routines for assessment of coating layer characteristics have been published by Chinga et al. [9,10,24]. LWC paper is segmented into coating layer, base sheet and fillers, as in Allem and Uesaka [8]. The routines include measurement of thickness along all adjacent vertical lines. The minimal step size between the vertical lines is supported by higher utilization of information in images, as the high capacity of modern computers allows this detailed measurement within reasonable time scales.

In addition to the segmentation by thresholding, the outer surface of the coating layer was defined by application of the rolling ball principle [9,25,26], which is an objective method for division of paper and background. The surface definition enabled the determination of the pore area fraction distribution in locally uniformly thick layers throughout the thickness of the coating layer. The surface definition allowed inclusion of surface pores in the characterization of individual pores. The assessed individual pores were limited by pigments, latex, image edge and the surface definition. The individual pores were estimated by the best fitting ellipse, from which the diameter (minor axis), aspect ratio (major divided by minor axis) and orientation relative to the surface could be determined [9]. Through application of sobel operators to identify phase borders, the particle orientations were found by an alternative method to the best fitting ellipses. The two methods for orientations showed a good correlation. The measured coating layer characteristics were found to distinguish well different LWC coatings and showed good correlation to measured bulk properties for *e.g.* gloss, clay fraction in coating and pore radius measured by mercury porosimetry.

Nesbakk and Helle [27] applied a determination of surface area in cross-sectional images of paper by a direct count of phase borders in binarised cross sections of calendered paper having different fibre furnishes. The assessed surface area showed a good correlation to the light scattering coefficient of the paper samples. However, the measurement was a direct count of phase borders and not indexed to cross-sectional area or amount of solid material present in the images.

Image analysis combined with controlled grinding/microtoming, or imaging with different focus planes applying CLSM, allows determination of fibre orientation in a paper sheet. The technique also allows quantification of the change of fibre aspect ratio and fibre cross sectional area along the length of single fibres in a sheet. The method is based on interactively choosing the matching pairs of fibre cross sections in two images at two different depths according to He et al.[28]. The method is most applicable for CLSM, as the distance between the cross-sections is known in-situ and the technique has the possibility of avoiding measurement in the specimen surface if structural defects from sample preparation are suspected.

Application of user defined fibre boundaries in cross-sections also enables an estimate of bonded and free surface area [29]. This allows an estimate of RBA based on image analysis, but the method is subjective and extremely laborious.

Several assessments have been made on degree of fibre collapse and fibre wall cracking on selected fibre cross sections in the paper structure under different conditions [4,30]. Through manual selection of single fibres in the cross sections, the change of fibre wall area, fibre/lumen aspect ratio and lumen area may be determined.

The distribution of fillers and density in the z-direction have been investigated in several studies [11,13,31,32]. They have however all one problem in common, as an objective definition of the surface with a reasonable surface porosity is problematic. Thus, a reliable measurement of the filler fraction and density in the outer layer(s) is normally not applicable.

Determination of the paper surface

A determination of the paper surface in cross-sectional images allows a delimitation between the paper material and background. The delimitation is required for including the surface area when determining the porosity and dividing the structure into a number of layers. However, the definition of the surface in a micrograph is always difficult, as the surface is often relatively rough on the micrometer scale.

The most straightforward approaches for surface definition yields the extremities for the solid fraction of the outermost layers of the paper structure. Approximating the surface as a straight line results in maximum surface porosity and a decreasing solid fraction for the outermost layers of the structure. Defining the surface as the outermost solid pixel in all horizontal positions in the cross sectional images yields a minimum surface porosity and an increasing solid fraction for the outermost layers of the structure.

The problem of defining a surface on relatively high magnification micrographs is illustrated in Figure 2.6. As can be seen, the local surface is far from planar.

Figure 2.6 The surface of a typical cross sectional image of a newsprint sample. On micrometer scale the surface is rough and discontinuous.

Application of a successful method for an objective surface definition for cross-sectional images of the coating layer of LWC paper is given by Chinga and Helle [9]. The routine is based on the principle given by Sternberg for biomedical image processing [25]. The method applies a digital rolling ball, with a user defined radius, to determine the surface of the coating layer of LWC paper.

The rolling ball method is transferable to uncoated paper grades, although the rolling ball radius must be increased to yield a reasonable surface porosity. Normally a rolling ball radius of 15 µm is applied for the surface rendering. However, this radius can be adjusted according to the surface roughness and average fiber diameter. The radius may also be adapted to imitate topography measurements or simulate interaction with a printing roll, though not allowing compression of the paper.

The principles of the rolling ball routine for determining the surface of a newsprint paper sample is shown in Figure 2.7. The applied circle radius is 15 µm.

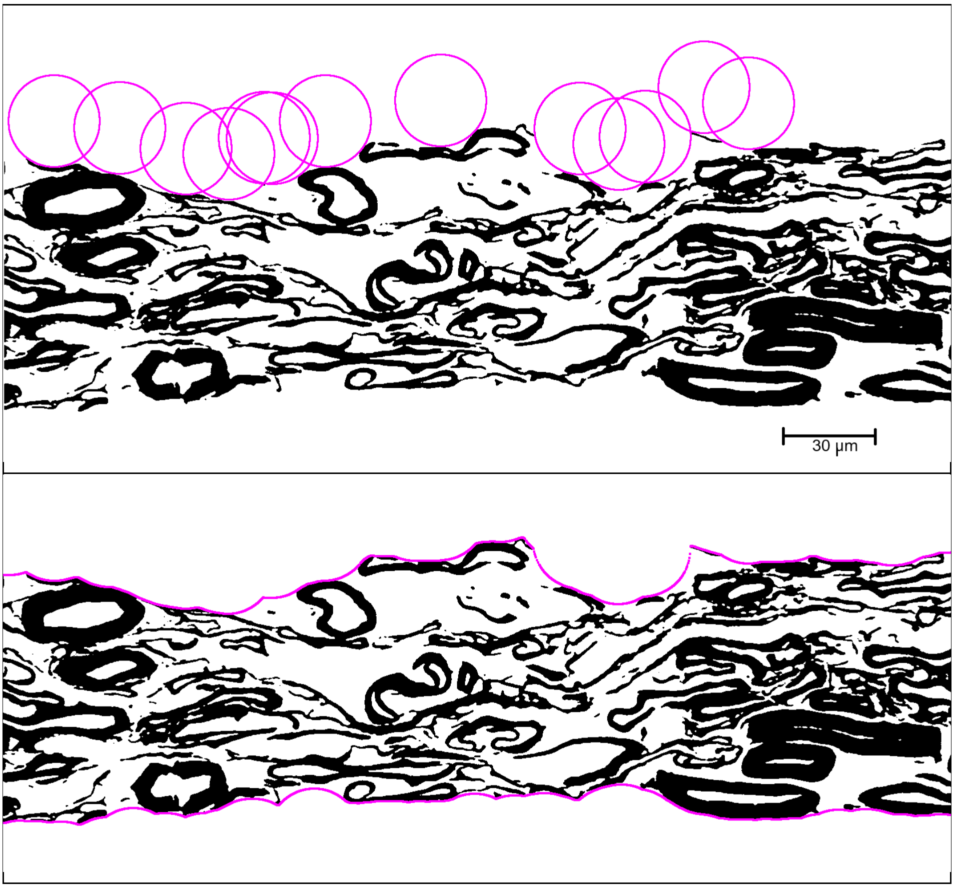

Figure 2.7 **Top**: Some selected positions of the rolling ball when rolling over the rough side of a newsprint cross section. **Bottom**: The resulting surfaces of the newsprint sample (both upper and wire side) when applying a rolling ball radius of 15 µm.

Material distribution in z-direction

An objective surface definition of the paper cross section enables a division of the paper into several layers in the z-direction. Different properties may be measured in the resulting layers for determination of the distribution in z-direction. However, it is the material distribution that usually are the most interesting for the paper maker.

Rättö et al. [11] made a good attempt of dividing the structure into layers. The applied MATLAB routine for determining the paper surface follows the surface profile in a fashion similar to the rolling ball. However, the principles for the routine is not well documented and the large number of layers combined with a too strong dependency of the profile to the outer fiber pixel, made measurements in the outermost layers more dependent of surface definition than structural properties. Nevertheless, the method presented in Rättö et al. [11], combined with the methods presented by Chinga and Helle [9] for a coating layer, are the basis for the derived method for material distribution in the z-direction presented here. The layer division is the same for this study and the two methods mentioned above.

The material distribution can be determined for porosity, solid fraction, density, fillers and fines material. Although the principles are somewhat different for the different material distributions, the same surface definition and layer division must be performed.

Having defined the surface applying the rolling ball algorithm, it is possible to divide the structure into layers that are locally uniformly thick, and still get surface layers that include a reasonable surface porosity. To achieve this layer partition, the method measures the local thickness between the two defined surfaces, as shown in Figure 2.9, and divides the vertical line into uniformly long segments that are assigned to each layer, according to the wanted number of layers. After performing this for all vertical lines in the cross-sectional images, the paper structure have been divided into layers that are locally uniformly thick, as shown in Figure 2.8.

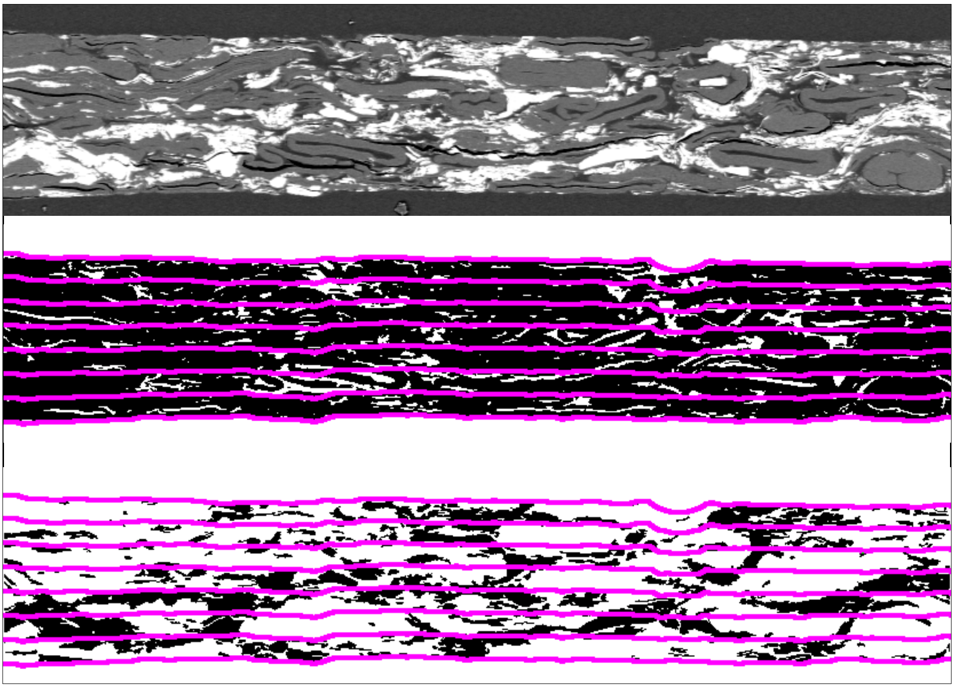

Figure 2.8 **Top**: An original micrograph of a highly calendered SC paper grade. **Middle**: The binarised structure, containing both fibres and fillers, are divided into seven layers based on the surface definition by the rolling ball algorithm. The resulting layers are locally uniformly thick and proportional to the local thickness. **Bottom**: The same layer division applied on the filler phase after appropriate segmentation

The porosity, here meaning void fraction, and the solid fraction of each layer may be determined by counting the number of voxels of each phase and calculating the fraction according to Eq. 2.1

$$\phi_n(\text{layer}) = \frac{\#\text{ of pixels of phase } n \text{ in layer}}{\text{total number of pixels in layer}} \qquad (2.1)$$

When there are only two phases present, the solid fraction (ϕ_{fibre}) is simply the complement of the void fraction and vice versa. The filler distribution can also be determined by the voxel counting approach, as long as the image is segmented into pigments in one phase and fibres and voids in the other phase. The sum of all fractions must always be unity. The filler, fibre and void fractions are thus all known when two of the fractions are known. Finding the void and fibre/filler fractions will always require an analysis as shown schematically in Figure 2.8.

The determination of the density distribution is almost as straightforward as that of the porosity and solid fraction, when there are only two materials present in the structure. Multiplying the material density of the solid phase with the solid fraction in the layer yields the layer density according to Eq. 2.2.

$$\rho_{\text{layer}} = \phi_{\text{fibre}} \cdot \rho_{\text{fibre}} \qquad (2.2)$$

However, the estimation of the fibre density in a paper cross section is difficult. The density of crystalline cellulose is 1.55 g/m^3, however as the fibre material will contain pores in the nanometer range, the real apparent density will be less. Since density does not give any information that is more informative or applicable than the solid fraction, determination of density in cross-sectional images should preferably be omitted.

By segmenting the structure according to the extension of elements applying morphological processing, it is possible to extract ‘digital fines’ from the structure. The segmented ‘digital fines’ will have a definition based on high specific surface rather than the physical size. Applying the same layer division as determined for the binary image of pores and solids, it is possible to find the fines distribution in the z-direction.

Measurement of thickness, porosity, density and basis weight

Although the thickness, porosity and density have been measured in studies found in literature, the thickness measurements have previously either been based on a straight line approach [33] yielding an overestimated thickness, or based on the outermost solid material [8] yielding an underestimation of thickness relative to the apparent thickness measured by ISO standard methods of the physical paper sample.

The determination of an objective surface, delimiting the paper structure from the surrounding background, allows an improved thickness measurement by assessing the vertical distance between the two surfaces. This thickness will be dependent on the chosen rolling ball radius. Along each vertical line in the cross-sectional images, the solid fraction and the porosity can be determined according to Eq. 2.1, by counting the number of solid pixels while simultaneously measuring the local thickness in pixels. The principle for measuring the local thickness and the solid fraction after defining the surface with the rolling ball principle is illustrated in Figure 2.9.

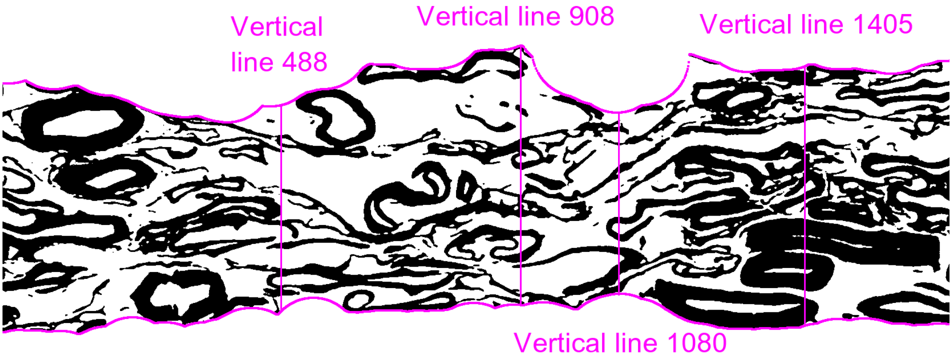

Figure 2.9 Illustration of the measurement of thickness and solid fraction in a newsprint sample based on surface definition by the rolling ball algorithm, applying a radius of 15 μm. The imaged segment of the cross section consists of 1660 vertical lines. The thickness and the solid fraction show large variations within the cross-sectional image.

After measuring the thickness and solid fraction of all pixel wide vertical lines in the cross-sectional image, the arithmetic mean for thickness, porosity and solid fraction may be found, yielding the property for the entire image. When the pixel size in the analysed images is known, the average thickness may be determined in microns. The density for each vertical line, or for the whole images based on the arithmetic mean, may be determined according to Eq. 2.2, when the solid density is known or assumed. The basis weight may also be determined for each vertical line, or for the whole image based on the arithmetic mean. The basis weight is calculated according to Eq. 2.3.

$$\beta\ [\mathrm{g/m^2}] = T\ [\mathrm{m}] \cdot \rho_{\mathrm{solid}}\ [\mathrm{kg/m^3}] \cdot 1000 \qquad (2.3)$$

When the thickness, porosity, density and/or basis weight are determined for each vertical line in the cross sectional image, it will be possible to calculate different properties from the distributions, as *e.g.* standard deviation, coefficient of variation, median, minimum and maximum. The standard deviation of basis weight is of special interest, as this gives the micro scale formation. However, the micro formation, in the size order of the pixels in the cross-sectional images, has not been much applied. As for other properties, the distribution based on the 15 replicates are of more interest than the local measurements, as these measures describe the representativity of the determined properties.

Pore heights

The principles applied for measuring the thickness may be modified to assess the vertical pore heights, as shown for finding the void fraction in Allem and Uesaka [8]. The local distance from fiber to fiber surface along a vertical line in the cross-sectional image is by definition a pore height [29,35]. Traversing each vertical pixel line from surface to surface and traversing the cross-sectional image line by line, the length of all pore heights in the cross section may be measured. The pore heights measured in line 908, 1080 and 1405 of Figure 2.9 are enhanced in the left image of Figure 2.10, to illustrate the measurement of vertical pore heights. (Note that the lines in the image are 3 pixels wide for illustrational purposes). In the same image, there are some pore heights limited by the surface definition, so called surface pore heights, these are excluded from the determination of the average pore height to avoid ambiguity. Although the surface definition does not affect the measured pore heights, it prevents unnecessary scanning through the background. The surface definition thus makes the image analysis routine more computationally effective.

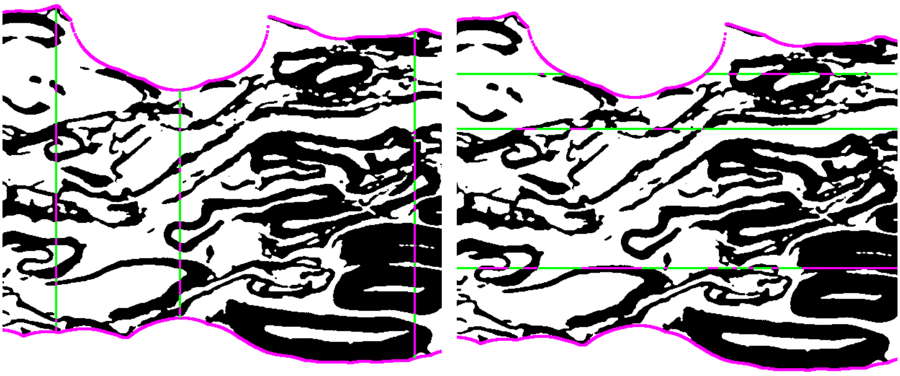

Figure 2.10 Measurement of pore heights, indicated by the green line segments in the images. **Left:** Three selected vertical lines, including surface pore heights. **Right:** Three selected horizontal pore widths, including pore widths limited by the defined surface (upper horizontal line).

The principles of measuring pore dimensions in the paper structure can also be applied horizontally, as illustrated to the right in Figure 2.10. However, the surface definition introduces surface limited pore heights (as the second pore width from left along the upper line in right image, Figure 2.10). Additionally the horizontal pore heights cut by the vertical image edge have an unknown extension. To avoid ambiguity in the pore height measurement, the surface and edge limited pore heights are not included in the calculation of the mean pore height. The surface definition is still useful in this routine, as it excludes horizontal pore heights traversing through the background between fibres.

The measurement of pore heights can be applied for characterization of the pore geometry. The characterization of pore geometry is treated in Chapter 3 of this thesis.

Specific surface area

An estimation of the specific surface area can be determined through image analysis of cross sections. Although, it is a 2D measurement of a strictly 3D property. The principal measurement is a direct count of all pixel edges between solid and porous phase, both vertically and horizontally orientated. The edge count can be done while traversing the volume, both vertically and horizontally, measuring pore heights, or as a direct measurement. The method was applied by Nesbakk and Helle [27], who found a good correlation between the number of phase borders and the light scattering coefficient. However the number of phase borders in this study were not indexed to cross-sectional fibre solid phase area or amount of solid elements in the images.

When the number of phase edges and the solid phase cross-sectional area are known, the area based specific surface area (S_A) can be calculated according to Eq. 2.4. Note that as the specific area is based on a 2D measurement the unit is m/m^2.

$$S_A\,[\mathrm{m/m^2}] = \frac{\#\text{ of phase borders} \cdot [\mu\mathrm{m/pixel}]}{\#\text{ of solid phase pixels } \cdot [\mu\mathrm{m/pixel}]^2} \cdot 10^6 \qquad (2.4)$$

When the solid phase density is known, or given a reasonable value, the weight based specific area (S_w) can be calculated according to Eq. 2.5.

$$S_W\,[\mathrm{m^2/g}] = \frac{S_A\,[\mathrm{m/m^2}]}{\rho_{\mathrm{solid}}\,[\mathrm{kg/m^3}] \cdot 1000} \qquad (2.5)$$

2.3 Results

The results of this study can be divided in three categories:

- Development of new, and improvement of existing image analysis routines for characterization of paper cross sections.
- The results and findings from application of image analysis routines for characterizing the paper structure and explanation of the physical behaviour of paper.
- The discussion of features influencing the measurement of structural properties by image analysis of paper cross sections obtained by SEM-BEI.

The developed image analysis routines are presented in the materials and methods paragraphs. The discussion of features affecting the results obtained with the chosen methods is presented in the discussion paragraphs. This section will thus focus on the results from application of the image analysis routines.

2.3.1 Effect of temperature calendering on the paper structure of SC paper

The image analysis routines were applied to cross sections of temperature gradient calendered papers to investigate the effect of line load and hot roll temperature on the paper structure. The details of the experiment and the results are presented in Paper I of this thesis.

The study were successful in applying an objective surface definition to the SC paper, yielding a reasonable surface porosity in the outer layer, applying the rolling ball method. The surface definition enabled a division of the thin and compact SC paper structure into

7 locally uniformly thick layers, where the z-directional material distributions could be determined. The solid fraction distribution in z-direction showed a gradient as expected for the temperature calendered paper. However, this gradient was not significantly altered by increased line load or hot roll surface temperature. Further investigations showed that the solid fraction gradient was caused by the z-distribution of filler from the forming section, not the calendering. The thickness of the layers of the SC-paper were 6.3-6.7 µm, depending of the calendering level.

Although the solid fraction of the outer layers showed a weak correlation to surface properties, this correlation was not statistically significant. Further studies of the surface through analysis of surface topography images showed that the temperature gradient effect was concentrated to the outermost microns of the paper structure. The combination of image analysis of cross sections and surface topography images could thus explain the physical behaviour of SC-paper when calendered by elevated hot roll temperatures and line loads in a modern multi-nip calender.

2.3.2 Measurement of pore geometry

The pore height image analysis routines were applied for the study of the pore geometry. The details of the experiments and the obtained results are presented in Chapter 3 of this thesis.

The pore height measurements enabled a direct comparison between the theoretically developed pore heights distribution [35] and the physical pore heights in real paper structures. The overall correlation between theoretical and measured pore heights was good for simple paper structures. The experimental scheme enabled an evaluation of the effect of fibre anisotropy, fibre furnish, basis weight and formation to the pore height distribution.

The principles of pore height measurement were applied for determining the parameters for the equivalent pore [36] by measuring the pore heights of 3D data sets by traversing through the volume, cross section by cross section, in the three principal directions. Through rotation of the cross sections, and measuring the pore heights in the resulting cross sectional images, the pore chords for several spatial angles (θ,φ) could be determined. The approach confirmed that the ellipsoidal shaped equivalent pore is a general feature in the porous paper material.

2.3.3 Application of 2D image analysis principles for assessment of 3D paper volumes

The developed routines were also applied for image analyses of the obtained 3D volumes by working through the volume, cross section by cross section. The results from this study are presented in Chapter 3 and 4 of this thesis.

The thickness, density and basis weight were measured as a test for correct detection of solid material for the x-ray microtomography technique. The porosity, specific surface area and rolling ball defined surface were determined in the 3D volumes based on 2D principles, but slightly modified to meet the 3D approach.

2.4 Discussion

2.4.1 Microscopy and image acquisition

The applied SEM-BEI imaging technique yields cross-sectional images of paper with high contrast between fibre material, epoxy and pigments, although careful sample preparation is crucial for the image quality. It is essential that the ground and polished specimen surface is planar, as topography will influence the contrast in the images. To control that the specimen surface is smooth enough to avoid surface topography effects, the surface of the prepared epoxy blocks are controlled in a light microscope using incident light differential interference contrast (DIC), prior to carbon coating and image acquisition. If the specimen surface is not sufficiently smooth, it is polished and controlled successively onto accepted smoothness. This control step limits topography effects.

At the applied magnification (250X), there are practically no features with the non-fibrous appearance expected for random topography effects, except a few occasional local crevices and dust particles. Usually the sampled cross sectional area are chosen in areas of the embedded paper cross section with little or no creviced or dust particles. The frequency and size of small crevices and dust particels are considered to yield small influence to the overall measured structural properties. However, cracks occur regularly for certain fibre types and high density paper grades. The defects introduced from sample preparation are discussed in the next subchapter.

The penetration of the electrons may be relatively deep into the epoxy embedded paper specimen. The penetration depth is reduced by application of a relatively low acceleration voltage of 5 kV. The applied acceleration is slightly above the limit where the current of the reflected beam from the areas with the lowest average atomic number is sufficiently high for activation of the backscatter detector. Lower acceleration voltage would thus have resulted in lower contrast in the cross-sectional images. However, the signal will still be influenced by material under the surface with the applied acceleration voltage, as shown in top left situation in Figure 2.1.

The penetration of the electrons into the structure will yield somewhat blurred phase borders. The blurring results in a larger overlap between the different phases, affecting the efficiency of thresholding for segmentation as the greyscale overlap between the phases becomes larger. The greyscale transition zone between the fibres and epoxy is more extended the larger the orientation of the fibres relative to the incident electron beam. The blurring effect is most pronounced for fillers, as the fillers can have a short extension relative to resolution and penetration depth. The fillers will thus more likely affect the detected local average atomic number in a focused spot. The blurring effect is most pronounced for the pigment to epoxy phase borders, as the change in atomic density is the largest here. An extended phase border between filler and epoxy will have a transition over the greyscale region of fibre material. The effect can be seen when studying the details of the fibre phase in Figure 2.3.

This blurring effect is reduced by the relatively low acceleration voltage of 5 kV. However, the edges between phases will never be infinitely deep. The problems with blurred edges is reduced to a minimum by optimized thresholding and consecutive filtering of the images. Comparison to the original greyscale image and knowledge of the unlikely event of a thin layer of fibre material surrounding the circumference of pigments helps guiding the filtering to a physically reasonable binary cross sectional image.

A different blurring effect is the result of the discretization of the continuous material when acquiring digital images. A higher resolution yields a lower area fraction with mixed phase information. The effect can best be comprehended from the illustration in Figure 2.11.

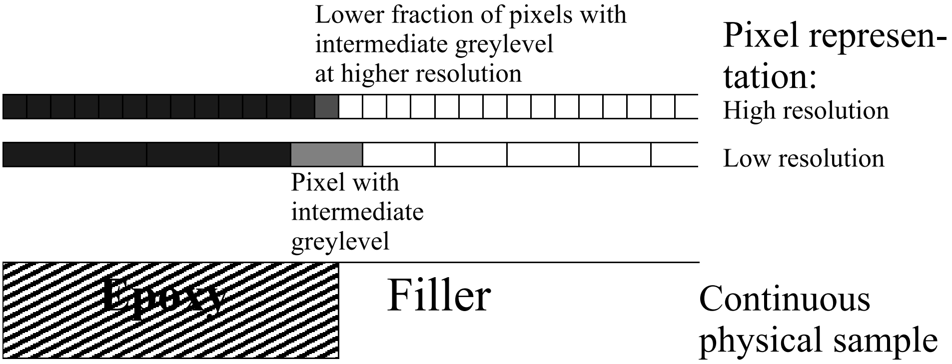

Figure 2.11 A schematic drawing of the blurring effect due to discretization of the continuous nature into finite pixels. Low resolution images will yield a larger area with mixed phase information. The physical sample is a bit simplified for illustrational purposes, the epoxy to filler transition is never as sharp as in this schematic drawing.

The choice of magnification and spatial resolution will affect the pixel resolution. The pixel resolution will put a limit to the size of detectable features in the paper cross sections, which will influence the measured structural properties. The pixel resolution should be sufficient to detect all optically active elements (> 0.2 μm) when the specific surface area is measured to allow a good correlation to the scattering coefficient. The assessment of other structural characteristics are less dependent on the resolution. Even a lower resolution may be preferable, as a lower resolution involves a larger imaged area or reduced processing time.

Regardless of application, it is always important to inform of the applied resolution in reports from image analyses, for the reproducibility and interpretation of the results.

2.4.2 Sample preparation

The proper choice of epoxy resin enables a firm support for the solid elements during grinding and polishing. Several publications have reported a cross-sectional structure that is minimally affected by the grinding and polishing technique [13,14,15]. It is also reported that the epoxy resin allows a support of the pigments in the structure, preventing them from being ripped out of the structure, as often happens in microtoming [24]. The applied technique enables a joint embedding of up to 10 samples of a width up to 20 mm length. Thus, a single epoxy block may prepare up to 200 mm of cross sections that can be imaged [14]. The large sections and introduction of few sample preparation defects makes the grinding and polishing preferable compared to microtoming the specimen. However, the cross sections are never perfect and some paper structure features are more difficult to prepare than others without introducing artefacts. A disadvantage of the grinding and polishing technique is the application of ethanol as a lubricant and washing agent, which excludes the study of interaction between paper and ethanol solvable agents as *e.g*. some inks. For such studies the microtoming technique is preferable.

When preparing epoxy blocks with embedded cross sections of paper material, fibres pulped by different processes will behave differently. The grinding and polishing is not problematic for mechanical pulp fibres. Application of confocal microscopy, allowing measurement of the fibre cross section underneath the specimen surface, have shown that bleached chemical pulp fibres may be slightly smeared out by the processing, resulting in too large fibre cross-sectional areas [69]. It is thus likely that high lignin content makes the fibres more resistant to grinding and polishing artefacts. The smearing effect of bleached chemical pulp fibres can be minimized by careful sample preparation, allowing shorter periods of grinding and polishing and longer curing intervals of the epoxy resin between grinding. More careful sample preparation allows the epoxy to give a better support to the non-rigid chemical pulp fibres.

It can also be observed that fibres oriented parallel to the specimen surface are more prone to develop defects than fibres orientated perpendicular to the surface. The problem is reasonable as there naturally will be less forces holding the fibrils, comprising the fibres, together when the fibres are orientated parallel to the surface. Cutting of the paper samples perpendicular to the fibre orientation in anisotropic paper grades will reduce the problem.

The grinding and polishing may introduce microcracks in the specimen surface. An example of such cracks can be seen in the first row of Figure 2.3 and as a peak at the left edge of the histogram in row 2. The microcracks are the thin black lines in the image. The lines are black, as there is no material in the microcracks. The microcracks are most pronounced in highly calendered grades and concentrated to the fibre wall of chemical pulp fibres or the phase boundaries between the fibre walls and the epoxy, but may extend into the void regions. The microcracks are probably a result of the softening of epoxy in ethanol, which allows the chemical pulp fibres to expand and stressed fibres to relax, which in turn introduces the microcracks when the epoxy shrinks as the swelling ethanol evaporates. The microcracks may be reduced by shorter grinding and polishing steps, minimizing contact with ethanol in the washing step and leaving longer intervals for curing between the grindings. However, the best sample preparation will probably still contain some microcracks for the most highly calendered paper samples.

When evaluating the effect of swelling and shrinking effects of the epoxy in the surface, it must be remembered that the alternative of applying water as lubricant and washing agent will be far worse. The water swell the fibres in the surface far more than the ethanol swells the epoxy and will thus introduce more sample preparation defects. The ethanol thus gives a better trade-off between being an effective lubricant and washing agent and avoiding structural defects. Other lubricants and washing agents have been considered, but none have shown a better trade-off than ethanol.

The microcracks may be reduced by filtering and image calculations, but it is not obvious to which phase the cracks should be assigned, so the operation is difficult and can never fully compensate the effect of the microcracks. In automated segmentation routines the microcracks are assigned to the void phase. The microcracks thus result in a slightly too

large void fraction. The expansion of the structure cannot be compensated for, so the problem can only be avoided or reduced in the sample preparation. Although the problem is clearly visible in cross sectional images, the problem will rarely influence the measured structural properties appreciably, as the effects are small compared to the size of the cross sections. The cracks are usually evenly distributed introducing more or less a systematic error, given the same fibre furnish and not too large differences in calendering level. The problem will have the largest effect on specific surface area and pore height measurements, as the cracks in fibre walls will introduce false pore heights and phase borders.
An alternative to avoid the microcracks is the application of a focused ion beam for sample preparation. Reports have been made showing that the ion beam is successful in preparing a smooth specimen surface without microcracks [18].

The time used in optimum sample preparation and image acquisition is well spent, as no image processing can fully compensate for a cross section of low quality. The image analysis is never better than the quality of the prepared specimen and cross-sectional image.

2.4.3 Segmentation routines

Obviously the filtering and thresholding will influence the structural properties measured by image analysis of the binary cross sections. The effects of the different steps of filtering and thresholding on the cross-sectional images of a testliner board quality have been investigated in Holmstad and Gregersen [37]. Although the choice of filtering and threshold values will clearly influence the results, the effects are relatively small within the region of applicable parameters and settings. It is also important to emphasize that there is no general reference for the image processing, as the optimum image processing will differ for different paper grades, and for different settings on the SEM. The best reference for the filtering and thresholding is by visual comparison to the original greyscale image to see whether the chosen parameters have a good trade-off between removing noise and preserving the physically reasonable paper structure.

The most important issue in filtering and thresholding is consistency. As long as the settings on the SEM and the applied filtering and thresholding is consistent within a study, the applied parameters will introduce mostly systematic errors, which will not affect the comparison between the different paper grades.

2.4.4 Image analysis routines

The described image analysis routines have some variables that are adjustable according to paper structure, furnish and image quality. The settings of these variables will influence the measured parameters.

The defined surface is important for the assessment of all the detailed structural properties described here, except the results from the pore height measurement. The choice of a larger radius for the rolling ball will result in a larger and thicker cross-sectional area with a higher porosity. The choice of the radius will influence the outer layers the most when dividing the structure into layers for determination of z-directional material distributions. The choice of rolling ball radius is not standardized, but is chosen according to fibre dimensions and the surface roughness.

The density of the solid phases are an important variable for density and basis weight measures and the weight based specific surface area (S_W). The applied density in this study is 1550 kg/m^3 for all fibre types, as no consistent values are found in literature. The applied fibre density results in generally too high densities and too low S_W.

The density measure involves a more fundamental problem than just finding the correct fibre density for different fibre types. The fibre density measures that can be found in literature are based on weight to volume approach. In images the determination of density is in fact a conversion from area, where the areas have a finite resolution when it comes to internal porosity. The internal porosity of solid phases will also be dependent of signal penetration depth and image processing. The image processing is often performed to produce as complete fibre walls and filler agglomerates as possible, as it is difficult to separate noise from true internal voids. It is thus a clear difference between the natural and digital solid elements.

To determine a correct density, it is thus necessary to perform a calibration of the area to density conversion. If there are several solid phases (n) present, it is necessary to perform calibration for pure sheets of (1-n) of the solid phases to calibrate all phases. To make it even more difficult, the area to density conversion is dependent on the pulping process the fibres have undergone and paper processing unit operations performed on the sheets. These differences in treatment can yield different solid densities in themselves. The image acquisition and image processing will also have different effect on the varying paper structures. A calibration of the area to density conversion is thus not universal for a fibre or filler type, but has to be calibrated for each experiment and paper grade to find a correct density.

Assuming that the density could be determined correctly from cross-sectional images, it is still important to consider whether the density yields any important additional information not given by the solid and filler fractions. The solid fraction yields a structural property that enables a rational comparison between all paper and board products. The absolute values of density is more of a material property. This render it difficult to do any rational comparison between different paper products and paper grades made from different raw materials, although the relative densities inbetween paper grades made from the same raw materials will yield information of the structural differences. The solid fraction to density conversion is thus not considered to yield any information that is more informative or applicable than the solid fraction.

There are thus many good reasons for not determining the density from cross-sectional images. The solid fraction will normally give the desired structural information that is sought by performing the image analysis. When there are fillers present in the structure, it is possible to divide the solid fraction into a filler and fibre fraction. The filler fraction will thus yield the additional structural information not given by the solid fraction. The solid fraction and filler distributions may thus yield the necessary information needed for evaluating two-sidedness and “density”-gradients for all paper grades and enable a rational comparison.

2.4.5 Representativity

The physical length of the imaged cross sections in this study are just below 0.5 mm, the thickness is obviously varying. The images are thus relatively small compared to the size of flocs and the normal variation in paper. It is therefore essential to obtain images of several replicates of the same paper sample. The number of replicates in this study is 15, chosen from three independent areas of five embedded paper cross sections. The chosen number of replicates have a reasonable trade-off between time consumption for sample preparation and image acquisition and a reasonably low standard deviation for the mean value of the measured structural properties. Obviously the number of replicates should be increased when handling paper grades with a poor formation or when a lower standard deviation is desirable. Storing of prepared epoxy blocks enables quick acquisition of more replicates if needed to obtain trustworthy results.

A measure of the representativity should always be given for measures determined by image analyses to enable reproducibility and credibility to the results.

2.4.6 Application of image analysis for increased knowledge of the physical behaviour of the paper material

The application of the technique for investigating the effects of calendering to the paper structure was successful in obtaining knowledge not accessible by other methods, such as solid fraction and filler distribution in the z-direction. However, the study also revealed some limitations of the technique. The cross-sectional approach is not well suited for study of the surface properties. The roughness values determined from cross sections are inferior to roughness values obtained from surface topography images. The topography images give a more representative measure as they cover a much larger area and depict facets (area) instead of lines. The technique was not successful in detecting the effects of the elevated hot roll temperatures to the surface area. However this could not be expected, as the temperature effect was concentrated to the surface, which is only a small fraction of the paper cross section. Further division of the structure into more and thinner layers was not feasible, as it will emphasize the effect of the surface definition to the density of the outer layer and produce layers with too little material for statistically significant measures. The study thus showed that the technique often preferably should be combined with other techniques to give the full picture.

The assessment of pore heights for characterization of the pore geometry is by itself useful. However, it does not extract information of the extension of the individual pores. The concept of individual pores is in itself a controversial issue, as the pores in most paper grades are interconnected and there does not yet to date exist any general agreed definition for where a pore starts and ends. Through measurement of pore heights the controversy is omitted, but the information of extension, shape, orientation and geometry of the pores are lost.

There are studies delimiting the pores by finding the pore throats [38,39], but the concept of pore throats are based on a volumetric approach and is not transferable to cross sections. The division of the porous phase into individual pores in cross sections is thus omitted in this work.

The work by Chinga [24] show a practical example of analysis of the extension, area, shape and orientation of individual pores in a coating layer, where the approach makes more sense, as the structure is much denser and the pores are less interconnected. The usefulness of assessing the properties of individual pores in the coating layer show that the approach may be useful for high density paper grades where the dense structure limits the interconnectivity between pores, which makes the delimitation less questionable.

2.4.7 Limitations of the 2D paper structure characterization technique

The cross-sectional approach apparently have limitations for assessing some of the features of the paper structure. It is not possible to determine whether the structure is layered or felted from a cross section, neither to determine the extension, shape and spatial orientation of complete pores and fibres. It is also impossible to determine transport and mechanical properties from cross sections, although the relative bonded area, assumed to be related to strength properties have been determined by manual evaluation of cross sections. Optical properties can be evaluated from cross sections by estimation of the specific surface area. The specific surface is shown to be correlated to the light scattering coefficient applying a resolution of 0.2 μm/pixel. However the technique does not distinguish between the different solid constituents and cannot take into account other factors affecting the light scattering. Other optical properties cannot be determined from cross sections.

Some of the three-dimensional features of the porous and solid phase can be determined from cross sections when combined with stereology principles, but these measures do not give any information of the individual pores and fibres. The principles for obtaining 3D information from cross sections are described in Chapter 3.
The fibre orientation and change of area and aspect ratio of a few selected fibres can be determined when the fibre cross section are identified in two cross sections with known distance [28]. Measures of pores from successive cross sections are of little use, as they have much more irregular shape than the cylindrical shape of uncollapsed pulp fibres.

Although it is possible to extract some 3D information from cross sections about fibre orientation and cross-sectional features, the three-dimensionality is necessary for tracking longer fibre segments through the fibre network to obtain information of how they take shape according to the surrounding fibres, as well as pulping, paper manufacturing and calendering.
However, when the individual fibre properties are not of any interest, or when evaluating how the preferred fibre orientation changes through the thickness direction of the sheet, sheet splitting, including image analysis of the split layers, is the preferred technique. The sheet splitting does not need to segment individual fibres and thus measures orientation of the full distribution of fibrous material.

2.5 Conclusion

The studies performed on assessing the effect of temperature gradient calendering to the paper structure and the characterization of the pore geometry through measurement of pore heights are good practical examples of how microscopy and image analysis can be applied for obtaining new knowledge of the paper material not accessible by other methods. Only through practical examples of application, such as this and other published work, can the usefulness of the technique be proven.

The findings for the effect of temperature gradient calendering of SC-paper on a modern multi-nip calender, have hopefully produced knowledge that can be a guidance for improved calendering. The improved knowledge could either assist in finding a better trade-off between improved surface properties and preservation of bulk in the paper or faciliate calendering at on-line speeds for high performance paper, such as SC-A/A+ grades.

The application of microscopy and image analyses of the cross-directional paper structure is in an early stage. New studies enabling application of image analysis routines to new paper grades and pulp and paper processing unit operations will help establishing the routine as a more standard research tool for gaining knowledge of how the paper structure influences the paper properties. New applications of the technique will generate further development of routines, possibly new routines and hopefully standardize the methods, reducing the subjectivity involved in the procedures.

Although the image analysis has shown its usefulness, the application of microscopy for direct observation of the cross-sectional paper structure, detecting special features and structural defects, will still be important and the application put most into practice. The image analysis is as such a supplement to the microscopy.

The study put focus to features of the technique that will influence the measured structural properties. The thorough investigation of possible pit falls for the technique will hopefully be a guide for further application and improvement of the technique.

The application of SEM-BEI and image analysis of the cross-sectional images provides a powerful tool for assessing the detailed features of the paper structure and gaining knowledge of how the paper structure is affected by forming and processing of the paper. However, the technique can not access structural features such as spatial extension of pores, degree of layering in the paper structure and determination of optical, transport and mechanical properties.

CHAPTER
3

PORE GEOMETRY

3.1 Background

Although paper is a complex material on the micrometer scale, it is not a completely random structure. The fibre network configuration is normally layered and for commercially manufactured paper grades the fibres have a preferred orientation. Most of the fibre material have a high length to width ratio and the fibres have a tubular shape when not collapsed, thereby giving them some regularity. The geometric properties of fibres can thus be given by distributions of *e.g.* fibre length, fibre wall thickness, coarseness and aspect ratio. However, these measures are normally obtained from unbonded fibres in wet condition and not in a sheet. The fibre geometry of single unbonded fibres can be obtained by appropriate sample preparation and light microscopy. It is also possible to extract single fibres from a bonded structure by application of 3D microscopy and fibre tracking [17], but it is difficult to extract a sufficiently large number of representative fibres yielding statistically significant measures. In general, fibres and fibrillar material in paper are fixed objects. Finding methods for assessment of fibre geometry is therefore only a practical problem without any need for definition of the fibres boundaries. The fibre geometry thus clearly deviates from the pore geometry, as the pores consist of a continuous void phase.

The paper grades considered here consist of only fibre material and pores. Thus, the structure is defined by the fibre network. The local porous structure of a fibre network is, by definition, the complement of its local solid structure. As such, we expect the spatial distribution of fibre material within the sheet to determine the distribution of porosity and the pore size distribution in the sheet.

The fillers present in many paper grades will introduce yet another element contributing to the randomness of the structure. The presence of fillers will make it more difficult to see the connections between the porous and fibrous phase. As it is the intention of this work to quantify some of the systematic properties of the paper structure, including the connection between the properties of the porous and solid phases, the fillers are omitted. However, there is no principal difference in characterizing a structure containing fillers.

The pores are the space between the resulting fibre network after paper manufacturing and processing. Except for high density paper grades, most of the pores in paper are interconnected. It is thus necessary to limit the pores by some criteria to obtain individual pores. The normal criteria for limiting interconnected pores are to find the pore throats, the narrowest part of the channels connecting the pores. However, the criteria is difficult to apply in practise for most porous materials, as pore throat definitions are derived based on model systems. There are several difficulties with the pore throat definition:

- There is no clear distinction between pore bodies and channels in a real porous material.
- What is narrow enough to define a pore throat is not well defined, and probably varying dependent of the material.
- Even if useful definitions can be found, the determination of the pore throats are computationally demanding.
- The concept of the pore necks is derived for determining flow resistance, which assumes a 3D structure and is therefore not applicable in 2D.

In practise, it has therefore not been performed any analysis of the features of individual pores in paper. However, paper properties dependent of the features of the porous phase is not governed by the detailed geometry of the individual pores, but rather the sum of the local characteristics of the continuous void phase. The pore structure is crucial for the papers interaction with light, air and fluids, but it is not well known how the details in the paper structure influence the bulk performance properties of the paper. To possibly evaluate the paper structure effects, there is a need for assessing features of the pore structure to quantify characteristics of the pore geometry that can be correlated to bulk properties.

The most applied measure of the pore phase is the pore size distribution, which is normally measured by mercury intrusion porosimetry or alternatively by gas drive methods [40,41]. The obtained pore size distributions are generally expressed in terms of pore radius or pore diameter, specifying only an experimentally determined value (assuming a cylindrical shape of the pore channels) and not a geometrically defined value [40]. It is also well known that the pressure curves determined by mercury porosimetry do not have a 1:1 correspondence to the physical pore size distribution, as the mercury intrusion is influenced by the effect that large pores can be shielded behind narrow pore necks. The mercury will thus cover some larger pores at a higher mercury pressure than the pressure assumed to correspond to the physical size of the large misclassified pores. Climpson and Taylor [42] have shown this behaviour for clay structures and Dullien and Dhawan [43] for sandstone. It is the intention of this work to consider alternative measures of pore size distribution for characterization of the void phase of paper and investigate the deviation from distributions obtained by mercury intrusion porosimetry.

An alternative method for assessing the pore geometry is by image analysis of cross sections, or digital 3D volumes of paper when available, applying quantitative stereology principles. The method allows a direct measurement of the structure, without the ambiguity involved in defining individual pores, provided that the imaged structure is a physical true representation, not significantly affected by sample preparation, image acquisition or image processing. The method allows measurement of the different size orders of the pore structure without varying external pressure to the paper structure, contrary to the mercury intrusion porosimetry.

Paper has been a model for statistical simulations and model building with the intention to gain new knowledge of how the paper structure is built up. W.W. Sampson gave an extensive review of such models at the Fundamental Research Symposium in 2001 [41].

It is the intention of this work to link some of the findings from statistical approaches to detailed structural measures obtained by image analysis of cross-sectional images and 3D volumes of paper. However, many of the statistical approaches are based on 2D networks, not having any extension in the thickness direction. 2D fibre network models are thus not readily relevant to measures from cross sections nor 3D images of paper, and are therefore not considered here.

3.1.1 Pore chords

A pore chord is the local distance between two solid elements in a paper structure. The measurement of pore chords is an important basis for deriving 3D information from cross-sectional images. As such, pore chords are a measurement according to quantitative stereology. The measurement of the local distances between the solid objects in the paper structure have been measured in cross-sectional images of paper [36,37] and in modelled 3D paper structures [34,29] and been derived in analytical statistical models [35]. The concept of pore chords have been applied in other porous materials, see *e.g.* Dullien and Dhawan [43], who performed an assessment of the void phase in sandstone. Although the pore chords have been assessed in geological samples in several studies, the pore chords have shown to be mostly applicable for determining the structural anisotropy of the structures and as input for transport problems involving “discrete free paths” like Knudsen diffusion and radiative transport [44,45]. Attempts to relate the assessed pore chord geometries for predicting material properties have been at best moderately successful [46].

The local distances between solid objects in the paper structure have been given several different names, including pore heights, chords, secants, radii and diameters. To avoid confusion when applying these concepts, it is necessary to make clear what the different concepts applied in this thesis involve.
The pore heights are the local distances perpendicular to the paper’s plane between fibres in a three-dimensional fibre network, which can be determined from cross-sectional images. The pore widths are the local corresponding horizontal distances. The pore chords are the distances between the solid elements in any spatial direction (θ, ϕ). The pore radius and pore diameter are applied for physical measurements, often assuming a spherical or cylindrical shape of the pores with a radius or diameter corresponding to the measured volumes or applied external pressures.

The details for measuring pore heights by image analysis of cross sectional images are given under image analysis routines in the materials and methods section of Chapter 2. The principles for determining the pore chords for several spatial directions are treated in the materials and methods later in this chapter.

KCL-PAKKA is a software program for simulating 3D fibre networks. A digital layered 3D fibre network is built up by deposition of flexible parallelepipeds with random orientation and length. The applied fibre lengths are according to length distributions for physical pulps. It is possible to measure the pore heights in these artificial structures by the same methods as for 3D images of paper volumes. By measurement of vertical distances in such artificial, thick fibre networks with constant fibre width and thickness, Hellén et al. [34] found the pore heights to be frequency distributed according to a negative exponential distribution behaviour, of which the largest deviations from the exponential behaviour was found for the smallest pore heights. The fixed rectangular shape of the applied parallelepipeds will yield a distinct difference for the smallest pore heights compared to pore heights encountered in fiber networks of physical fibres with an arbitrary and more continuous shape.

C.T.J. Dodson derived expressions for the analytical probability distribution for both internal and surface pore heights in idealized, random 3D paper structures [35]. The work was motivated by the findings from measurements in the simulated fibre networks derived by KCL-PAKKA. The theoretical probability distributions for pore heights (r) are dependent of solid fraction p and the number of Poisson layers n (each with a solid fraction of p), which for physical structures is best approximated as the thickness of the sheet expressed in terms of fibre thicknesses. The expression of the probability function (Eq. 3.1) is somewhat cumbersome, as it is obtained from the binomial distribution applying the probability of finding successive pores in the vertical direction to the Poisson layers. The derived pore height distribution show a close to negative exponential distribution behaviour, as observed for assessments of pore heights in KCL-PAKKA structures.

$$P_{Int}(r, p, n) = \frac{(1-p)^{1+r} p^2 (n-r-2)}{-1 + (1-p)^n + p(n+p-np)} \qquad (3.1)$$

The study also derived expressions for the mean and standard deviation of the pore heights and showed the standard deviation of pore heights to be approximately proportional to the mean pore height.

The theoretical surface pore height distribution have been confirmed by laser topography measurements by Lorusso et al. [47]. Measurement of pore radius distribution applying head gas drive methods have been performed for studying the effect of basis weight, formation and fibre furnish to the pore radius distribution [48,49]. The method yield a number weighted distribution, rather than a volume weighted distribution. It is thus easier to compare to pore height distributions than pore radius distributions obtained by mercury intrusion porosimetry. The measurements performed in [48,49] found the mean and standard deviation of the pore radii to be proportional, as previously observed by Dodson [35].

3.1.2 Quantitative Stereology

The stereology attempts to relate observations from a cross-sectional view to the true three-dimensional microstructure. The cross-sectional view can be a reflective image of a specimen surface (*e.g.* SEM-BEI) or a projected image of the structure (*e.g.* light microscope image of a microtome slice, but can principally be considerably thicker). Quantitative stereology attempts to characterize numerically the geometrical aspects of interesting features of the microstructure [50]. The quantitative stereology measures the structure in cross sections by measures that through theoretical derivations can be related to the three-dimensional structure properties. The basic measurements of a disordered structure, where individual elements can not be segmented, is by traversing lines and by pixel and phase border counts.

The principles for quantitative stereology is also transferable to measurements in 3D volumes by traversing the volume, cross section by cross section. Measurements in 3D volumes can be used to validate whether the derived quantitative stereology theories, relating cross-sectional features to the 3D structure, succeed in predicting the true features of the 3D structure.

Paper is a complex material also for quantitative stereology, as it is not totally random nor ordered and have a partially orientated structure. These structural properties introduces a need for many independent cross sections cut to obtain representative data. The orientated structure also enforces analyses of cross sections cut in several directions.

The equivalent pore theory is a practical application of quantitative stereology to paper structure. The detailed features of quantitative stereology measurements and theory relating the 2D measurements to the 3D structure is thus treated in the equivalent pore theory.

3.1.3 Equivalent pore theory

Based on the theories for quantitative stereology and actual measurements of cross-sectional images of paper, J. Silvy derived the equivalent pore theory for characterization and quantification of paper structure features [36]. Unfortunately most of the publications of the method [51,52], including the PhD thesis [53], are in French. Additionally, deriving the equivalent pore parameters have until recently been extremely laborious. The theory have therefore not been widely used in paper research, except in France [36,54] and University da Beira Interior (UBI) in Portugal [55].

The equivalent pore theory is originally a concept for obtaining 3D characteristics of paper from cross-sectional images. Advances have later allowed determination of the 3D characteristics from spatial dispersion of the light of a laser beam impinging on stacks of paper sheets [36]. The theory also includes determination of 3D characteristics of the surface properties when a high resolution topography image is available [36,53]. The application of stereology principles enables derivation of a macroscopic model based on the homogenised microscopic measurements of the geometry of the interphases between the solid and void phase in the paper structure.

The main feature of the concept is the representation of the homogenized three-dimensional porous structure by a 3D continuous closed surface, having an ellipsoidal shape.

This surface gives a conformal representation of orientation and density of the homogenized pore-fibre interfaces. The ratio between the main axes of the ellipsoid represents the structural anisotropy. The size of the true equivalent pore is scaled so that the area of the ellipsoid is equivalent to the specific surface area (S_V).

For measurements of linear intercepts in direction (θ,φ) of a three-dimensional texture according to quantitative stereology methods, the following relations applies for a porous structure. The equivalence

$$L_L(\theta, \varphi) = V_V = \varepsilon \tag{3.2}$$

where $L_L(\theta,\varphi)$ is the mean linear fraction of the secants in the pore phase for traversing, pixel wide lines in a given direction (θ,φ), V_V is the volume fraction of the pores in the texture and ε is the porosity.
The mean pore chord ($<g>_p(\theta,\varphi)$) is an important parameter for measurement of linear intercepts. The mean pore chord is determined by the relationship:

$$<g>_p(\theta, \varphi) = \frac{\sum_{i = n_p} (L_p)_i}{n_p} \tag{3.3}$$

where L_p is a single pore chord and n_p is the number of pore chords in the volume for the direction (θ,φ). The mean fibre chord ($<g>_f(\theta,\varphi)$) can be determined in a similar fashion, provided the fiber chords are measured.

When counting the number of linear intercepts per length of the traversing scan line through the paper structure, an additional texture property can be measured, that follow the relation

$$\frac{P_L(\theta, \varphi)}{2} \langle g\rangle(\theta, \varphi) = \varepsilon \tag{3.4}$$

where the texture property $P_L(\theta,\varphi)$ is the mean value of numbers of intercepts between a straight line of direction (θ,φ) and the interfaces between the porous and the solid phases in the texture.

The lineal fraction is equal to the porosity, according to Eq. 3.2. In a randomly chosen volume within a porous material, the number of pore chords (n_p) and fiber chords (n_f) must be identical. The ratio between the pore chords are then the porosity, according to relationships given in Eq. 3.5.

$$\frac{\langle g\rangle_p}{\langle g\rangle_p + \langle g\rangle_f} = \frac{\dfrac{\sum_i (L_p)_i}{n_p}}{\dfrac{\sum_i (L_p)_i}{n_p} + \dfrac{\sum_i (L_f)_i}{n_f}} \underset{n_p = n_f}{=} L_L = \varepsilon \qquad (3.5)$$

The mean fibre chord in a given direction (θ,ϕ) is thus a complement of the mean pore chord. This is in accordance to the two-phase structural definition given in the background. However, for the planar structure of paper, the surface area is of great importance for the paper properties, and should thus be included in the analyzed texture. To fulfill the relationships given in the equivalent pore model, it is thus necessary to define the boundaries of the paper structure in a fashion that yields the same number of fibre and pore chords. This is in practise difficult to accomplish, but for most commercial paper grades the number of fibre layers is sufficiently large for the difference in number of chords to be relatively small.

The equivalent pore model applies the geometrical shape, which is bounded by the warped surface constructed from a centre O ((0,0,0) in polar coordinates) by diameters plotted according to the mean values of the pore chords <g>(θ,φ) measured in different spatial directions in the three-dimensional paper structure [36,51]. The warped surface, measured in the exact angle (θ,ϕ) relative to the principal directions in the structure and with no structural or measurement defects, is an ellipsoid. To obtain a smooth and representative ellipsoid it is necessary to perform sufficient measures to determine the pore chords that are the exact average for the structure. However, in practise the ellipsoid shape must be determined by the least squares method, as the pore chord measurements are never ideal. The warped surface delimits an equivalent pore which is representative for the texture, see Figure 3.1 and Figure 3.7 and 3.8. An ellipsoid surface fits most of the particle textures encountered in practice, which makes it easy to recognise the equivalent pore and anisotropy characterised by the ellipticity: a/b, c/b, c/a. (See Figure 3.1)

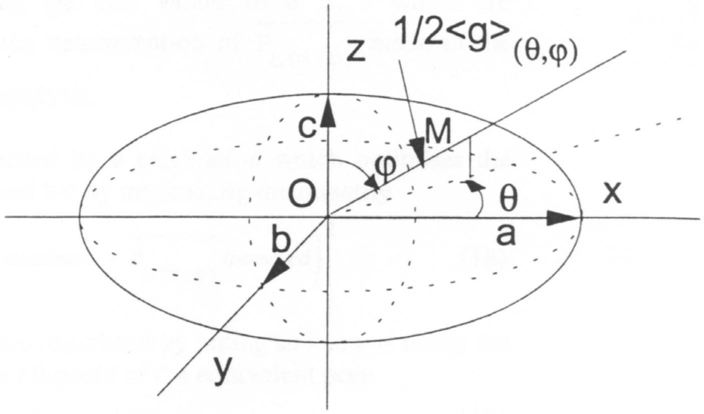

Figure 3.1 The warped surface constructed based on the directional mean chords in the pores <g>(θ,φ) is an ellipsoid representing the equivalent pore shape. The main axes correspond to the principal directions in the paper sheet. The pore chords in the ellipsoid in any direction (θ,φ) is the length from the ellipsoid surface through Origo and to the opposite surface.

By performing analyses along all three directions of the main axes of the texture we obtain:

$$\frac{a}{b} = \frac{\langle g\rangle_{0X}}{\langle g\rangle_{0Y}} = \frac{P_{L0Y}}{P_{L0X}}\ ;\ \frac{c}{b} = \frac{\langle g\rangle_{0Z}}{\langle g\rangle_{0Y}} = \frac{P_{L0Y}}{P_{L0Z}}\ ;\ \frac{c}{a} = \frac{\langle g\rangle_{0Z}}{\langle g\rangle_{0X}} = \frac{P_{L0X}}{P_{L0Z}} \qquad (3.6)$$

The ellipticities are equivalent to the structural anisotropy and define the shape of the ellipsoid. It is thus possible to determine the ellipsoid shape through measurements in only the three principal directions, if $<g>_{0X}$, $<g>_{0Y}$ and $<g>_{0Z}$ can be determined by sufficient accuracy.

The area of the elliposid constructed from the warped surface of <g>(θ,φ) values is smaller than the specific surface area (S_V), and is thus smaller than the true equivalent pore. As it is the shape of the equivalent pore that is of most interest, and not the surface area, the simplified equivalent pore, based on the mean pore chords is the one applied in practise in this study.

In addition to applying the equivalent pore concept for characterization of the paper structure, it is the intention of this work to show that the ellipsoidal shape truly can be found in the 3D structure of paper. The presence of the ellipsoid in the interphase texture of paper can be shown through measurements of pore chords in different spatial directions in digital 3D images of paper. The determination of lineal intercepts *will also show* whether the rolling ball definition of the surface yields approximately the same number of pore chords for the two phases ($n_p = n_f$). Fulfilment of Eq. 3.5 will imply this.

3.1.4 3D extension and characteristics of pores

Little is known of the 3D shape of the pores in paper, though the pore sizes are regularly measured indirectly through mercury porosimetry and gas drive based methods. These measurements do not give information of the pore shape and their extension nor any measure of connectivity. The quantitative stereology can yield measures of the structural anisotropy, average length and distribution of pore chords and phase borders per line length, but will give information of neither the 3D shape nor extension of single pores. However, the availability of a digital 3D representation of the paper structure provides the possibility for extracting information of the 3D extension and characteristics of the pores. It is the intention of this work to investigate the possibilities for extracting such information from the available 3D representations and consider their applicability and relation to other pore geometry measures and paper performance properties.

One possible approach for obtaining information of the 3D extension, connectivity and other characteristics of the individual pores is to divide the porous phase into individual pores by determining the pore necks, but the operation is difficult and computationally demanding. It is also controversial to define the pore necks, as there are no general agreement of the definition of a pore necks in a real porous material. The features of a divided pore phase is thus dependent of the applied pore neck definition. However, despite of the problems of defining the pore necks, this is the only way to acquire information of the 3D extension and characteristics of individual pores in the interconnected pore phase of paper. The details for the approaches for determining the pore necks are treated under the introduction of Chapter 4.

A different technique for measuring the pore size information is based on classical mathematical morphology [56]. The method provides a pore volume distribution omitting ambiguous delimitation, but do not yield information of the individual pores. The porous phase is covered by spheres of decreasing size, onto all pore voxels in the structure is covered. Assigning each pore voxel according to the largest sphere covering it, a pore volume distribution can be derived. The details of this method is described under materials and methods under Chapter 4.

Accessibility to digital 3D images of the paper structure enables the possibility to extract selected small subvolumes of the structure, but can not provide individual pores delimited by any criteria more than the size of the selected volume. Selecting such small subvolumes containing pores will visualize the complexity of the 3D pore extension.

3.2 Materials and methods

3.2.1 The investigated paper grades

There are three different experimental schemes with belonging paper grades for which different pore geometry characterizations have been made:

- Handsheets made from long fiber fractions of different pulps (referred to as long fibre handsheet samples)
- Selection of paper grades with distinctly different structural features (referred to as News, BSKP handsheet and Filter paper)
- Newsprint-like paper grade made on a pilot paper machine (referred to as XPM samples)

The two last experimental schemes (selection of paper grades and XPM samples) are referred to in the material and methods section of Chapter 4, as their paper structures are extensively analysed applying 3D characterization methods.

Handsheets made from long fiber fractions

To test whether the analytical expressions for pore height distributions of random layered networks, derived by C.T.J. Dodson [35], has a physical existence, handsheets with physical fibre networks as similar as possible to the theoretical network were made. The analytical pore height distribution assumes long, collapsed and rigid fibres. The theoretical fibre network does not include fines material. It was therefore decided to produce handsheets from the long fibre fraction of a bleached softwood chemical pulp, beaten 2000 rev. in a PFI mill. The choice will assure long and collapsed fibres, but the fibres will be relatively flexible. The long fibre fraction was isolated by a standard Bauer-McNett fractionator according to SCAN-M6:69 [57] standard procedures. Only the longest fibre fraction (R28/Wire sieve cloth no. 30) was later applied for the handsheets

In addition to proving the existence of the analytical pore height distribution in a physical fibre network, it was considered to be of interest to test how different features, differing from the idealized random network, influence the pore height distributions. The manufactured sheets were therefore made with different levels of formation, basis weights and anisotropy. The isotropic paper sheets were made on a standard handsheet former with manual stirring, allowing varying fibre suspension volumes and settling times. The isotropic sheets were pressed and dried according to the ISO 5269-1:1998 procedure [58]. The normal basis weight target applied here is 66 g/m^2. Additionally handsheets with the lower basis weight target of 44 g/m^2 were made to analyse the effect of basis weight. The same basis weights were targets for the anisotropic sheets formed on the dynamic sheet former[1]. The anisotropic sheets were pressed and dried by methods resembling the machine-directional strain and treatment of commercial papermaking. The applied settings were a centrifugal speed of 1400 revolutions/minute, 75 and 65 seconds dewatering time for the normal and low basis weight respectively and a pump

---

[1] The dynamic sheet former was a Formette Dynamique, rebuilt by Fibertech, Sweden. The principle is based on a pressurized pulp jet impinging on a rotating cylindrical wire.

pressure of 3 bars. The sheets were wet pressed at a line load of 6.3 kN/m and a speed of 2.1 m/min. The sheets were dried under strain on a drum with supplied heat of 52 °C for 15 minutes to yield a dryness level approaching that of commercial paper. Shortage of long fibre fraction pulp made it difficult to reach exactly the same basis weights as for the isotropic handsheets, as the amount of fibre suspension to form the large dynamic handsheets were only sufficient for one sheet for each basis weight. Based on former experience and estimating calculations, the resulting basis weights for normal and low basis weight levels were in reasonable correspondence to the basis weights obtained on the standard sheet former, see Table 3.2.

The formation is a difficult characteristic to control in sheet forming, but can be indirectly assessed by the crowding number [59]. Standard handsheets usually have a uniform formation with random fibre orientation. The good formation handsheets were formed with conditions and pulp properties yielding a crowding number of 3.5 (assuming perfect mix in the sheet former chamber), which is well below the threshold for flocculation. The standard settling time of 10 seconds after stirring should yield conditions close to perfect mix before initiating the sheet forming. The poor formation sheets were made by halving the fibre suspension volume in the sheet former, thereby doubling the crowding number, and increasing the settling time to 90 seconds, to initiate flocculation.

It is not possible to apply exactly the same formation settings in the dynamic sheet former as for the standard handsheet former, as the sheet is formed under turbulent conditions and with constant addition of dilution water. However, the conditions and resulting formation will presumably be more equal to the good formation than the poor formation on the standard handsheet former.

The experimental design is summarized in Table 3.1.

Table 3.1: The experimental design for test of the analytical internal pore height distribution.

Sample	**Formation**	**Basis weight**	**Fibre orientation**
111	Good	Normal	Isotropic
011	Poor	Normal	Isotropic
101	Good	Low	Isotropic
001	Poor	Low	Isotropic
110	Good	Normal	Anisotropic
100	Good	Low	Anisotropic

The resulting basis weights, formation and the TSO ratio for the paper grades manufactured according to the experimental design summarized in Table 3.1, is given in Table 3.2. The formation is given as the coefficient of variation (%) of the basis weight measured within an area of 7 x 7 cm^2 with an Ambertec beta formation tester The coefficient of variation is applied as the measurement of formation for easier interpretation between the paper grades having varying basis weights.

Table 3.2: The measured basis weight, formation/coefficient of variation and TSI anisotropy of the manufactured handsheets

Sample	**Basis weight [g/m^2]**	**Formation/ Coefficient of variation [%]**	**TSI anisotropy**
111	62.7	5.9	presumably 1
011	63.4	11.6	presumably 1
101	42.5	6.8	presumably 1
001	42.3	12.9	presumably 1
110	71.0	5.1	3.3±0.1
100	40.2	6.2	3.3±0.1

The formation was measured using the same square of which the basis weight was previously determined. The approach yields a calibration of the amplitudes from the beta-formation tester, thus there is no standard deviation available for the measured basis weight for the different paper grades. Both the basis weight and formation are averages of measurements of three isotropic handsheets or separate areas of the anisotropic handsheets.

3.2.2 Image acquisition, processing and analysis

General procedures for 2D images

The cross sectional images of the long fibre handsheet samples were acquired, filtered and segmented according to the principles given in the materials and methods of Chapter 2. The largest image size (2560x1920) was applied to improve accuracy of the pore height measurements.

The methods for measuring pore heights and other necessary characterization of the cross-sectional paper structure needed in this study are described in the image analysis routines in the materials and methods section of Chapter 2. However, the methods do not describe methods for determining the average fibre thickness necessary for determining pore heights and sheet thicknesses in terms of fibre thicknesses and number of layers respectively. These image analysis routines are therefore presented in this chapter.

General procedures for 3D images

The 3D images for the initial 3D paper structure volumes (news, BSKP handsheet and filter paper) and the 3D images of the newsprint-like paper grades produced on a pilot paper machine were acquired, filtered and segmented according to the materials and methods section of Chapter 4.

The method for determining pore heights, presented in Chapter 2, does not describe how pore chords at any spatial angle can be determined. The procedure is therefore described here.

The detailed description of skeletonization of the 3D porous structure and applying this for subsequent determination of pore throats and individual pores are described in the material and methods section in Chapter 4. The details of producing pore volume distributions from covering the pore phase by spheres of decreasing sizes in a digital 3D paper structure is also described in the materials and methods section in Chapter 4.

Measurements for determining parameters in analytic pore height distribution
The parameters applied in the expressions for the pore height probability distribution are; the pore height in terms of fibre thicknesses, the thickness in terms of number of layers based on the fibre thickness and the solid fraction, where the former is dependent on the surface definition. It is thus necessary to determine the fibre thickness before the pore heights and number of layer variables can be determined in correct terms. The fibre thickness must be determined from image analysis, as the fibre diameter measured from the FibreMaster and similar apparatuses are measured in wet condition. It is possible to measure the wanted fibre thickness from cross-sectional images of isolated fibres, prepared according to the principles given by Johnsen et al. [60] and Reme et al. [61]. However, the method is best suited for mechanical pulp fibres and will only measure the fibres being fairly similar in shape to a “typical” fibre. Another problem with the method is that all analysed fibres have a perpendicular orientation to the cross-sectional plane, whereas the cross-section in a handsheet will cut fibres in a random orientation and contain fibres of more varying shape. It was therefore decided to determine a measure of the fibre thicknesses in the cross-sectional images.
The applied method is based on skeletonizing the fibre network. An example of a skeletonized cross-sectional image is given in Figure 3.2.

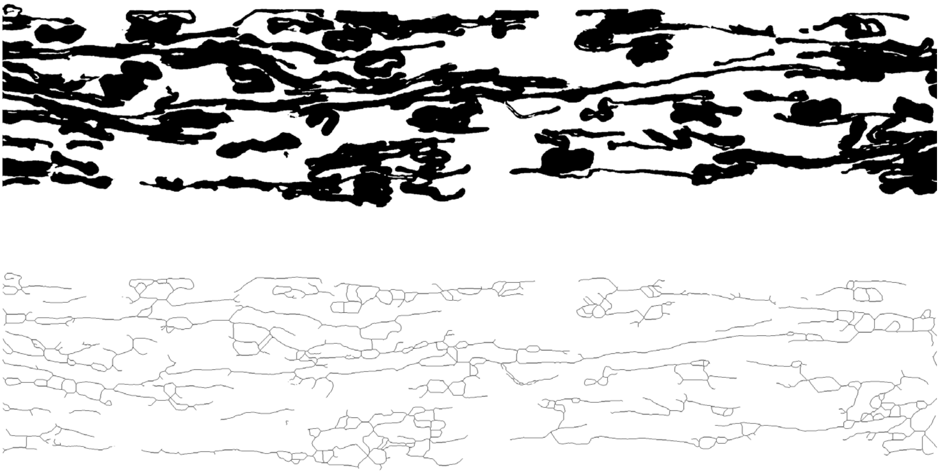

Figure 3.2 Top: A binary cross-sectional image of isotropic handsheet with good formation and normal basis weight. **Bottom**: The resulting skeleton after skeletonization of the above cross-sectional image.

An isolated collapsed chemical pulp fibre will in theory become a line when it is skeletonized. The ratio between the area of the fibre network and the theoretical perfect skeleton will thus give the fibre thickness. In practise the skeletonization does not yield straight lines for all fibres, as it focuses on preserving even the smallest features of the network topology resulting in small unevenness in fibre shape introducing additional branches in the skeleton. The cross-sectional images may thus need filtering by morphological operators for smoothing of the phase borders, to reduce the number of such additional branches while preserving the fibre network topology as well as possible. The chemical fibres have little or no surface roughness. The filtering is thus sufficient when applying the normal settings for removal of noise from the structure. The effect from fibre roughness can be seen, as the small, straight branches in the skeleton in Figure 3.2. There are relatively few branches in the network resulting from fibre roughness when comparing the detailed structures before and after skeletonization. The additional branches from the detail preservation will lead the ratio between the network and skeleton areas to be smaller than the average fibre thickness.

The chemical pulp fibres are in contact, resulting in the assumed fibre line segments in the skeleton to be the feature of more than single fibres. The fibre contacts lead the ratio between the areas to be a bit larger than the fibre thickness. It is assumed that the two effects in the relatively thin and open structures analysed here, each contributes in different direction to the determined fibre thickness. Thus the effects more or less will neutralize each other, resulting in a reasonable measure of the fibre thickness. The measured fibre thickness slightly above 4 µm confirms this.

It is also necessary to measure the thickness and the solid fraction from image analysis, as there can be large deviations from the values determined by standard bulk measurement methods. However, the measured thickness and solid fraction in image analysis will depend on the surface definition. The surface in the cross sections on this study should preferably be so defined that the surface pore heights will be similar to the ones defined in the analytical surface pore height probability distribution. However, the idealized network assumes uniform, fibre thick horizontal layers, each with the same solid fraction. The idealized surface is thus horizontal and with easily defined surface pore heights. The local surface of the fibre networks in the cross-sectional images will be relatively rough with the applied spatial resolution, as discussed in the material and methods section of Chapter 2. It is therefore necessary with a totally different approach for surface definition, ideally defining a surface following the surface features yielding pore heights similar to the ones assumed in the analytical expression. The definition of such a surface is difficult in practise. It was therefore decided to focus on the internal pore heights and define the surface as the outermost fibre pixel in each pixel wide column in the cross sectional images. The applied surface definition yields a low estimate for sheet thickness and a high estimate for solid fraction. The routine for determining the surface by the rolling ball algorithm, which was developed at a later stage, would have resulted in better estimates of the thickness and solid fraction. However, the surface definition would depend on the applied ball radius and it would require extensive trial and error to find the definition that results in a surface pore height similar to the one in the analytical expression.

Measurement of pore chords in different spatial directions

A description of the method for measuring pore heights and pore widths in cross-sectional images are given under image analysis routines in Chapter 2. The same principles may be applied for measurements in 3D volumes by analysing the volume successively, cross section by cross section. It is also possible to determine the mean number of intercepts per length of traversing line through the structure according to quantitative stereology principles.

The measurement of pore heights and pore widths in cross sectional images can only determine the mean pore chords in the three principal directions based on a limited number of sampled areas. Having access to a digital representation of the three-dimensional texture allows numerous measurements in each spatial direction (θ,ϕ) and no restrictions for the choice of the direction of the linear intercepts (θ,ϕ). The equivalent pore may thus be determined with higher accuracy compared to the thin slices of paper obtained by isotropic sampling as a larger number of pore heights and directions can be measured. However, it should be reminded that a single 3D volume is small compared to the typical sizes of flocs, and the measured structural features may thus not be representative of the paper grade. The higher accuracy for measurement of stereological features in the 3D images of paper may confirm the ellipsoidal shape of the warped surface constructed from the measured $<g>(\theta,\phi)$ values. To gain the improved accuracy, it is necessary to perform the stereological measurements in several spatial directions (θ,ϕ).

The measurements of pore chords in spatial directions outside the principal directions in a 3D representation of paper may either be done by measuring in traversing lines with an angle relative to the axes in the volume, or by rotating the volume relative to the vertical and horizontal traversing lines. The length of a line of discrete nature, diverging in direction from column or rows in the voxelized volume, is computational demanding, and often dubious, to determine with accuracy. The spatial directions were thus altered by rotating the volume. In practise, the rotation is performed by rotating the cross sections building up the volume. It is possible to reslice the volume in any spatial direction, but the rotation of cross sections are much faster and less computationally demanding. The principles for measuring pore chords in an arbitrary spatial angle (θ,ϕ) is shown in Figure 3.3.

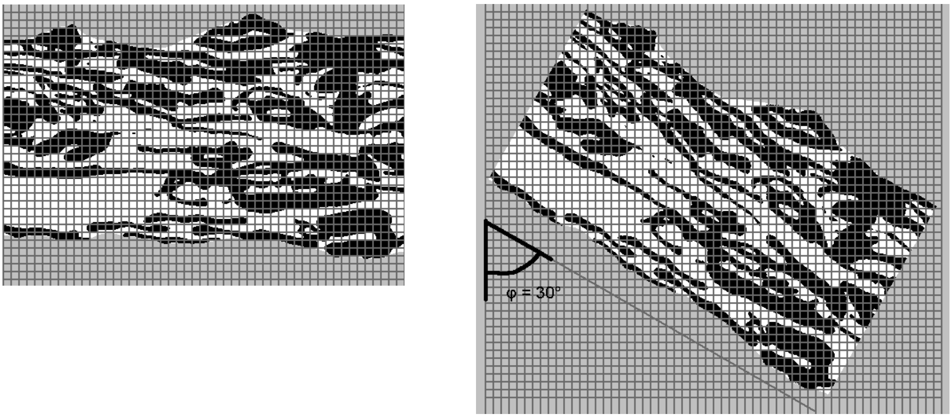

Figure 3.3 The principle for measuring pore chords in spatial angles in other than the principal directions. **Left**: The cross sectional image as assessed for the unrotated angle. **Right**: The cross sectional image is rotated the desired 30° relative to the vertical direction before the pore chords are measured by the usual vertical and horizontal traversing lines.

When rotating a binary image, the rotation will result in an original voxel partly covering several voxels in the new grid. To avoid introduction of intermediate greyscale values, the voxel is assigned to the phase with highest area fraction in the new voxel. This will introduce a so called staircasing effect, where previously smooth surfaces will be digitally roughened from the voxel discretization of the rotation. The rotated images are therefore filtered by morphological operators to reduce the staircasing effect. To assure systematic treatment of all spatial directions the *erode* operator, with a set neighbour threshold of 4, is applied to both unrotated and rotated cross sections.

The rotations in the experiment include the rotation from 0° - 90° degrees for the cross sections, in steps of 15° for all three principal planes. As the pore chords are measured both vertically and horizontally in all cross sections, the angles 90° - 180° are also covered. It is not necessary to perform the measurement for 90° rotation, as these chords are already measured at the orientation of 0°. However, measurement in images with this rotational angle can be performed as a control measurement, estimating the effect of rotation and filtering to the detailed digital paper structure.

3.3 Results

3.3.1 Pore height distribution

The cross-sectional images of the handsheets manufactured specifically for verification of Dodsons analytical pore height distribution [35] were first assessed to determine structural properties necessary as input to the analytical pore height distribution and for converting pore heights and sheet thickness into terms used in the probability distribution. The measured properties were determined as described in the materials and methods section of this chapter. The determined properties for the different sheets are given in Table 3.3. Note that the properties were determined for both MD and CD cut cross sections of the anisotropic handsheets, as the sample preparation is more problematic for MD cut cross sections. The structural parameters for all paper grades are determined based on 15 replicates of cross-sectional images of handsheets. The given deviations is the standard deviation of the determined mean values.

Table 3.3: Measured structural parameters needed for studying the validation of analytic pore height distribution model.

Sample	Fibre thickness (μm)	Solid fraction (*p*)	# of layers (*n*)
111	4.14±0.06	0.52±0.01	18.2±0.4
011	4.13±0.06	0.51±0.01	20.0±0.9
101	4.49±0.06	0.58±0.01	12.5±0.6
001	4.35±0.09	0.56±0.02	11.6±0.7
110-CD	3.84±0.03	0.46±0.01	24.3±0.6
110-MD	3.76±0.04	0.46±0.02	26.4±0.8
100-CD	3.99±0.05	0.57±0.01	10.6±0.5
100-MD	4.02±0.10	0.50±0.02	14.0±0.6

The average fibre thickness of 4.09 μm was applied as the fibre thickness for all paper samples, although the fibre thicknesses determined by the skeletonization approach is clearly influenced by differences in structural properties and sample preparation. The average fibre thickness is applied, as it is assumed that the different paper samples contain an average selection of fibres from the same pulp. The use of the average fibre thickness will thus level out some of the effects from sample preparation and normal variation between samples.

The measured internal pore height distributions for the handsheets made according to the 6 different combinations of basis weight, formation and anisotropy are presented in Figure 3.4 and Figure 3.5. The left histogram distributions in both figures are for the normal basis weight, whereas the right images are for the low basis weight sheets. Note that although the distribution for the isotropic sheet is plotted together with the distributions for anisotropic sheets and their corresponding analytical model in Figure 3.5, the isotropic sheet distribution is not expected to have any correspondence to the model line.

The distributions are each based on 15 cross sections to achieve smooth and representative pore height distributions. Repeating the procedure for obtaining estimates of the uncertainty of the intervals in the distribution would be an extensive task. However, the difference determined between MD and CD cut samples give a good estimate of the maximum deviation. The MD and CD cut samples are cross sections from the same structure, thus the pore height distribution should theoretically be identical. However, differences in "selection of structural properties" in the cross-sectional view and larger chance of sample preparation defects for the MD cut samples will introduce differences. The deviation between the replicates within the different samples are most likely considerably smaller than the differences observed between MD and CD cut samples, as all samples are cut systematically CD and thus have smaller variation in structural selection and specimen quality for image acquisition. A good estimate of variation within the different histogram intervals is thus assumed to be half of the difference between MD and CD cut samples in the same pore height interval for handsheets with the same basis weight.

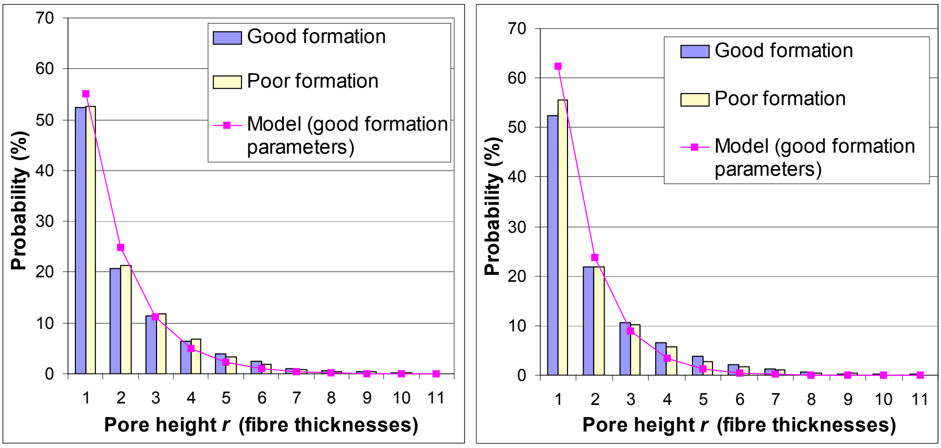

Figure 3.4 Left: The probability distribution for internal pore heights for handsheets with normal basis weight compared to the analytical pore height probability distribution (line) derived using number of layers and solid fraction of the good formation sheet. **Right**: The same plot as to the left, but for handsheets with low basis weight.

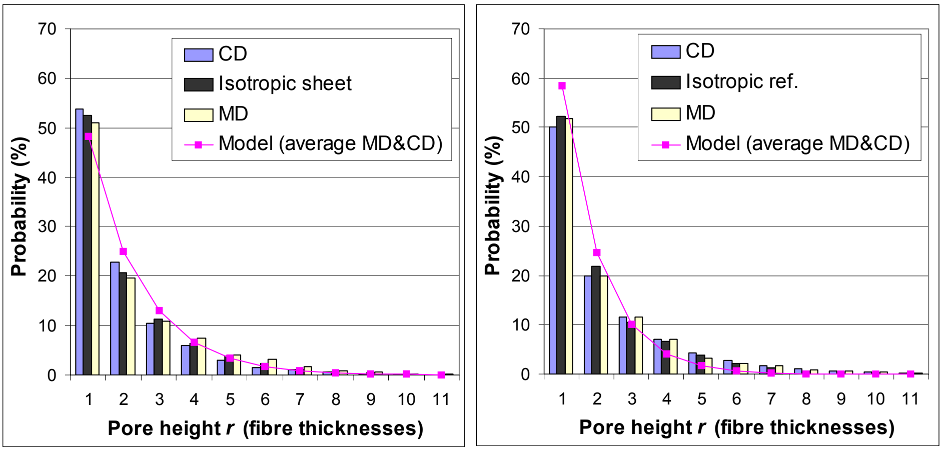

Figure 3.5 **Left**: The probability distribution for internal pore heights in anisotropic handsheets with normal basis weight compared to isotropic handsheets with approximately same basis weight (middle bars) and the analytical probability distribution for pore heights derived from the average number of layers and solid fraction found in both MD and CD cut cross sections. **Right**: The same plot as to the left, but for handsheets with low basis weight.

The results show a good correspondence between the analytical and the measured pore height distributions for all handsheets with normal basis weight. The fit is as expected best for the handsheets that are most similar to idealized fibre network, the normal basis weight sheet with good formation and random fibre orientation (sample 111).

The effect of lowering the basis weight is a larger deviation from the analytic model and a more pronounced effect of formation. The model seems to apparently overestimate the effect of decreasing the basis weight below 60 g/m^2. However, the worsening of the correlation is partly caused by the high estimate of solid fraction when determining the surface as the outermost fibre pixel in the structure. The effect is stronger for the low basis weight sheets, as the surface area is a larger fraction of the cross sectional area than for the high basis weight sheets. An improvement of the surface definition would thus probably yield smaller effects of basis weight.

The formation seems to have a small effect on the pore height distribution. At least as long as the basis weight is sufficiently high to be within a regime where the number of layers is so large that %-wise deviation between high and low basis weight areas, in average, remain relatively low. According to Table 3.2, the formation is approximately the same for normal compared to low basis weight sheets. It is thus clear that the variation is more detrimental to the low basis weight structure. The worsening of formation yields systematically a higher fraction of small pore heights, which is reasonable considering that high basis weight areas normally are more densely bonded and contain more pore heights than medium and low basis weight areas.

The effect of introducing anisotropy to the fibre network is not as clear, as for the other effects, because basis weight the basis weight and anisotropy changes are partly coupled in the experimental design. However, results indicate that the anisotropy yields more of the smallest pore heights than predicted by the analytical distribution. The effect is most clear in the normal basis weight sheets, where the change from isotropic to anisotropic fibre orientation resulted in a change from deficiency of small pore heights compared to the model to an excess of pore heights in the anisotropic sheets. The abundance of small pore heights for the anisotropic fibre networks compared to the model is reasonable considering the physical fact that aligned beams can be more densely packed than disordered beams and that the model assumes random fibre distribution. It was expected that the closer packing of the fibres should have been evident when comparing the pore height distribution of isotropic and anisotropic handsheets. However, the measured pore height distributions do not show this behaviour. The strong measured anisotropy indicates that the effect must be covered by some effects of the change of basis weight, formation, normal variation and differences in image quality.

The relatively low divergence from the model, even for paper with as strong anisotropy as over 3:1 (TSI ratio), indicates that the model is a close approximation to the physical features of the pore phase also for anisotropic fibre structures.

The analytical probability distribution for internal pore heights thus seems to be a good approximation of the pore heights in real fibre networks as long as the basis weight is not too low. The effect of formation and anisotropy is not detrimental to the correspondence between analytic and determined pore height distributions within this experiment. Whether the model is applicable for other pulps and when fines and/or fillers are introduced should be further investigated.

The study performed by Dodson also included derivation of expressions for the pore height mean and standard deviation. It was found from the analytic approach that the standard deviation was proportional to the mean. The numerical mean and the standard deviation of pore heights were therefore measured in all the manufactured handsheets. The results are shown in Figure 3.6, together with the analytic mean determined applying number of layers and solid fraction according to measures found for the individual sheets.

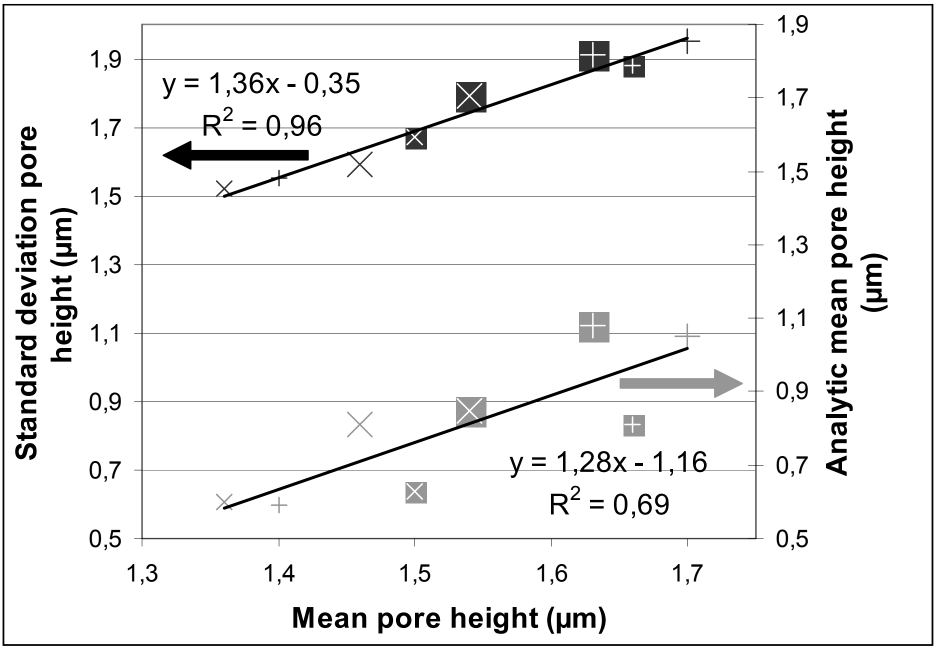

Figure 3.6 The relationship between mean pore heights (all pore height measurements) and standard deviation and analytical mean as determined according to the theoretical pore height expressions.
The 'X' crosses represent isotropic handsheets, whereas the '+' crosses represent anisotropic handsheets. The small crosses represent low basis weight sheets, whereas the large crosses represent high basis weight sheets. The plain crosses (no background) represent good formation for the isotropic handsheets and CD orientation of the cross sections for the anisotropic handsheets, whereas the crosses with solid squares as background represents poor formation for the isotropic handsheets and MD orientation of the cross sections for the anisotropic handsheets.

The results show a large deviation between the analytic and the measured mean pore heights. The reason for the difference is the totally different approach for determination of the mean pore height. The analytic expression for the mean is determined from the sum of r multiplied by the probability of r (range 0-1) for all possible pore heights ($r <= n-2$), where the applied r in the summation is the lower limit of each pore height interval of a fibre thickness. The mean for the real paper structures is determined from the mean of all pore heights measured with the accuracy of the pixel size (0.18 µm), thus approaching the integrated area under the curve for the pore height distribution. Obviously, there is thus a large deviation between the mean pore heights determined by the two methods. The integration approach is applied for the real paper structure as it involves a standard mathematical operation for both determination of mean and standard deviation, which makes the results more readily available for comparison to other measurements. If applying the medium pore height (r + 0.5 µm) for each interval as the r in the summation of the frequency of the pore heights in each interval when determining the theoretical mean, the theoretical mean pore height will be exactly 0.5 µm larger. The correspondence to the pore heights determined by image analysis would be better applying this approach, but would still be systematically lower.

Irrespective of the applied method, the standard deviation is proportional to the mean for all analysed paper grades, as proposed by the analytic findings. The standard deviation is systematically slightly larger than the mean. Despite the differences between the analytic and the measured mean pore heights, the assumption that the mean is proportional to the standard deviation is correct within the investigated basis weights, formations and anisotropy levels.

3.3.2 Equivalent pore parameters

The equivalent pore can be determined from digital volumes of paper samples obtained by *e.g.* X-ray microtomography. The three-dimensionality allows determination of pore chords in any spatial direction (θ,ϕ) and yields enough measurements of pore heights to yield accurate measures of the mean pore chords within the sampled volume. The theoretical ellipsoidal shape of the warped surface constructed from the average pore chords can thus be validated.

The mean pore chords were determined for 23 different spatial directions for digital volumes of the paper structure of a commercial newsprint (TMP) and a handsheet (BSKP) sample. The resulting warped surfaces and their fit to the proposed ellipsoidal shape are given in Figure 3.7 and Figure 3.8. The ellipsoid was determined from calculation of the best fitting ellipsoid to the measured pore chords applying a least squares method. The R^2 value is based on the difference between the measured pore chord and the distance from Origo to the ellipsoid surface for all the 23 measured spatial directions.

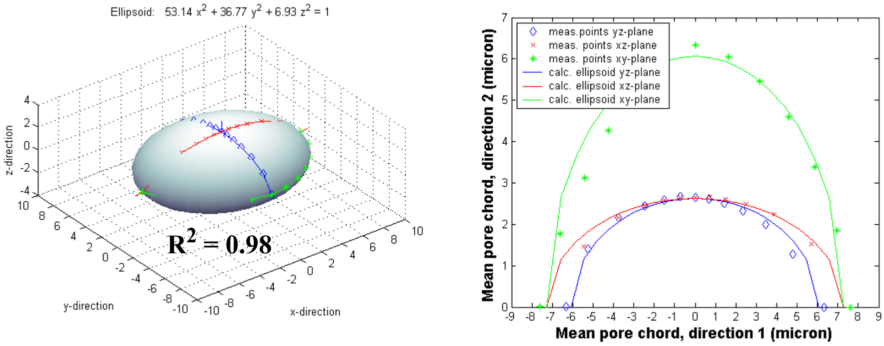

Figure 3.7 The determined warped surface constructed from measurement of pore chords in a digital 3D image of a handsheet sample. **Left**: The fitted ellipsoid with the measured pore chords plotted according to the legend in the right graph. **Right**: The half fitted ellipses for the different principal planes with the measured pore chords plotted as points according to legend.

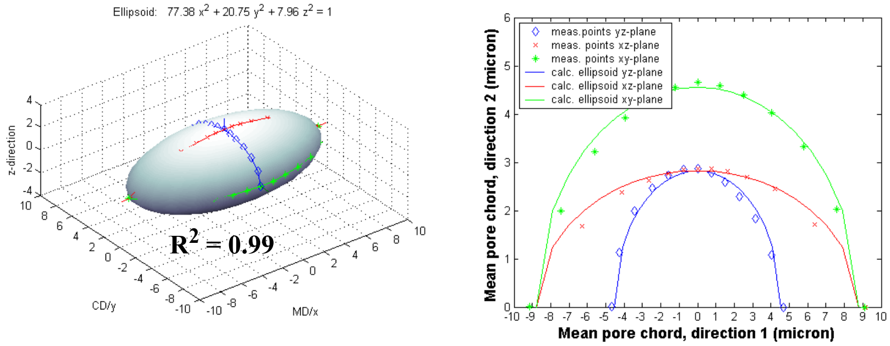

Figure 3.8 The determined warped surface constructed from measurement of pore chords in a digital 3D image of a newsprint sample. **Left**: The fitted ellipsoid with the measured pore chords plotted according to the legend in the right graph. **Right**: The half fitted ellipses for the different principal planes with the measured pore chords plotted as points according to legend.

The determined ellipsoidal shaped warped surfaces show a good fit to the determined mean pore chords. The theoretical ellipsoid shape, assumed to fit most of the particle textures encountered in practice, including paper, could thus be confirmed.

The confirmation of the ellipsoidal shape allows determination of the warped surface based on only the pore chords measured in the three principal directions, as long as a statistically significant mean pore chord can be determined. It is thus not necessary to perform the laborious task of rotating the 3D images to determine the warped surfaces. The rotations were only performed in this study for validation of the equivalent pore.

Although the true equivalent pore has a larger size than the warped surface of the determined mean pore chords, the warped surface mean derived from the mean pore chords is sufficient for most applications, as it is the shape and not the absolute size of the ellipsoid that is of interest. The specific surface area can be determined by other means in a digital paper volume.

The equivalent pore shape and relative size can be used for observation and measurement of structural changes from paper processing or other physical changes of the paper structure. A practical example is a study of what happens to the porous structure of a filter paper when it is soaked in water. The warped surfaces from the measured mean pore chords in the principal directions of the filter paper before and after soaking is shown in Figure 3.9.

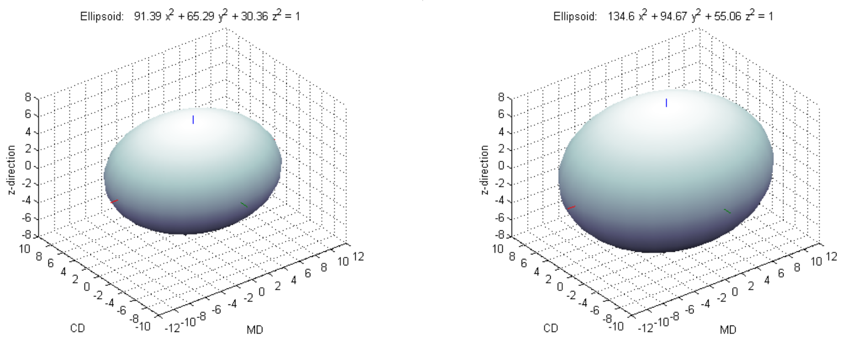

Figure 3.9 **Left**: The equivalent pore ellipsoid of the filter paper before soaking. **Right**: The equivalent pore ellipsoid after soaking the filter paper containing wet strength additives (steady-state).,

The shape of the ellipsoids show that the expansion of the structure, when soaking the samples, is similar in all directions, resulting in a larger ellipsoid with the same shape. The expansion is slightly larger in the thickness direction, compared to the in-plane directions, resulting in a rounder shape. The preserved shape after soaking show that the expansion is mainly an increase in porosity.

It is also possible to measure the chords in the fibre phase. According to Eq. 3.5, the relation between the pore and fibre chord in any spatial direction is the porosity. To test the applicability of this relation in our 3D structures and observing what happens to the fibre phase when soaking the filter paper, the warped surfaces of determined mean fibre chords for the two conditions of the filter paper structure are given in Figure 3.10.

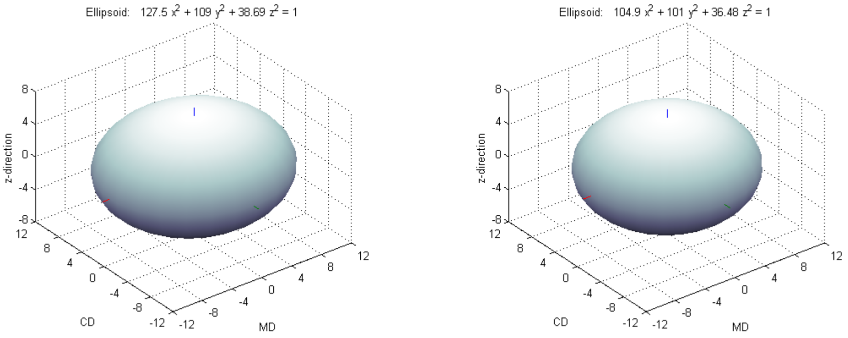

Figure 3.10 **Left**: The warped surface constructed from mean fibre chords in the principal directions of the filter paper before soaking. **Right**: The warped surface constructed from mean fibre chords in the principal direction of the filter paper after soaking the filter paper.

The ellipsoids of the fibre phase is almost identical before and after soaking the sample. The ellipsoid becomes slightly smaller and more isotropic in the sheet plane when it is soaked. The decrease in size is probably from less fibre-fibre contacts, whereas the reduced sheet plane anisotropy is most likely from normal variation in cutting direction in the almost isotropic paper grade or normal variation in selection of structural features included in the relatively small paper volumes.

The relation between the mean chords in the two phases in the three measured principal directions for both structure conditions shows a fair agreement to the porosity determined from voxel counts. The standard variation between the three directions are 2-3 units and the porosities determined from the chords are slightly smaller than the voxel count based one. However, there are no clear indications of the relations given in Eq. 3.5 not being valid, which means that the number of fibre and pore chords are close to being identical. It is thus assumed that the shape of the warped surface of the fibre phase is identical to the shape of the pore phase for all paper grades with the applied surface definition. This assumption is in agreement with the definition of the fibre network, indicating that the porous structure of the fibre network can be considered as the complement of the solid structure.

A different practical example is a study of the effect of calendering on the porous phase of two of the newsprint samples manufactured on a pilot paper machine according to a factorial design, where one of the variables were calendering. The two compared volumes have identical settings of the variables except the calendering. The warped surfaces before and after calendering are shown in Figure 3.11.

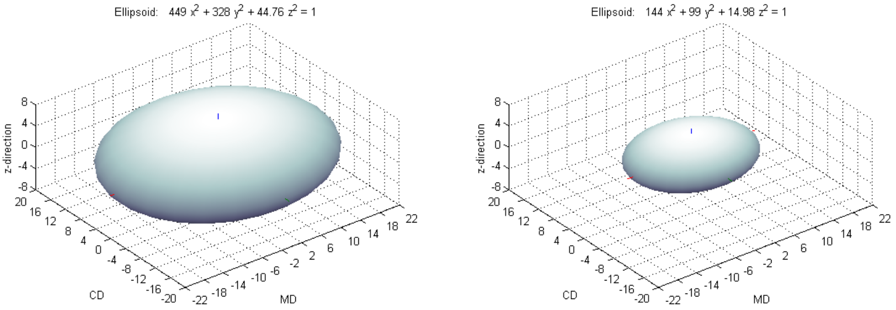

Figure 3.11 **Left**: The equivalent pore ellipsoid of the pilot paper machine manufactured paper before calendering. **Right**: The equivalent pore ellipsoid after calendering the pilot paper machine manufactured paper.

The almost conformal shape of the ellipsoids before and after calendering show that the compression of the void phase of the newsprint is equally large in all three principal directions. The results indicate a slight increase in sheet plane anisotropy, but this change is not statistically significant when analysing the factorial design including eight different paper samples. The preserved shape after calendering shows that the compression is a process mainly reducing the general porosity of the paper structure.

3.3.3 Pore chord distributions in all spatial directions

Pore chords were measured for digital paper volumes of three distinctly different paper grades; handsheet of bleached softwood kraft pulp, newsprint and filter paper of cotton linters. The pore chord measurements included measurement of both pore heights and pore widths. The constructed warped surfaces for the paper grades, as shown in Figure 3.7-3.9, show a clear difference between the determined mean chords in the vertical and the horizontal directions. The probability distribution for the vertical direction, compared to the horizontal direction seems to be of similar kind of distribution, but having different mean and standard deviation. The determined pore chord distributions for the vertical and one horizontal directions in the BSKP handsheet sample are shown in Figure 3.12. Both the frequency and length fraction pore chord distributions are shown.

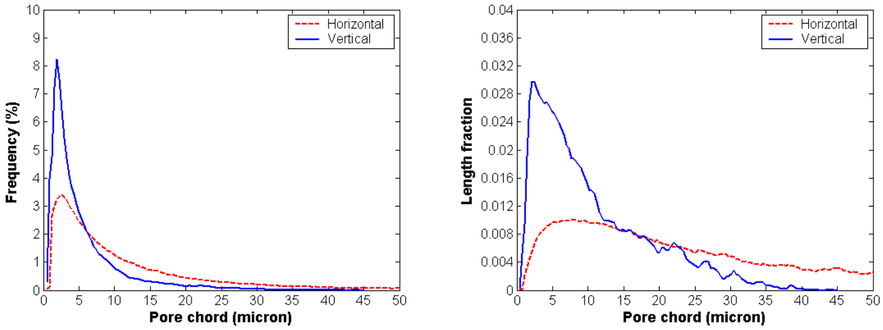

Figure 3.12 Left: Number frequency distribution of pore chords in both vertical and horizontal directions in the digitized volume of the handsheet sample. **Right:** Length weighted distribution of pore heights and pore widths in the digitized volume of the handsheet sample

It is clear that the two directions follow a log-normal distribution, although their skewness differ. The horizontal distribution is shifted towards a higher frequency of longer pore chords and considerably lower probability of short pore chords. Except for the increasing probability for the smallest pore chords, the observed frequency distributions for both directions are in agreement with the shape of the analytic pore height distributions for handsheets made from long fibre fractions. The increasing probability for the smallest pore chords is for pore chords smaller than the average fibre thickness and thus not accounted for in the analytical expression.

The determined ellipsoid for the newsprint volume (Figure 3.8) clearly shows that the sample is anisotropic, having different mean pore chords in machine and cross direction. The corresponding pore chord distributions (frequency and length fraction) are shown in Figure 3.13.

The pore chord distributions for the two directions deviate in shape as expected according to the anisotropy. The features of the frequency pore chord distributions seem to follow a log-normal distribution, similar to that for the handsheet sample.

The pore chord distribution for the vertical and horizontal directions have been found to follow the features of a log-normal distribution for all analysed paper volumes in this study. The log-normal distribution of pore chord length frequency is therefore assumed to be a general feature of the paper material.

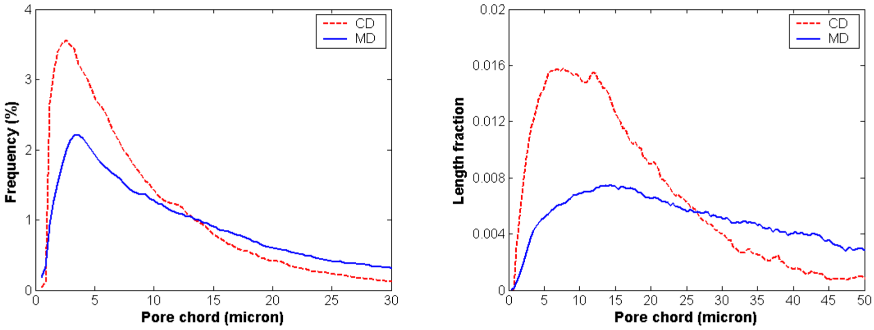

Figure 3.13 **Left:** Number frequency distributions of pore chords in both machine- and cross direction in the digitized volume of the newsprint sample. **Right:** Length weighted distribution of pore chords in both machine and cross directions in the digitized volume of the newsprint sample

The pore chord distribution must necessarily change gradually from vertical to horizontal direction and from cross direction to machine direction as their means do so according to the shape of the equivalent pore and all the pore chord distributions seem to follow the log-normal distribution. The behaviour of this gradual change is most evident in contour plots, where colours represent different length fractions. The behaviour can also be visualized in 3D plots, where the height and the colours of the surface represent the length fraction. The 3D plot and contour plot representing all pore chord distributions in the sheet plane of the newsprint sample is shown in Figure 3.14. All length fraction distributions (both top and bottom) are plotted in polar coordinates with origin in (0,0), the angle θ [-90°, 90°] relative to cross direction and the distance *r* according to the pore chord length. The distribution thus extends the longest for -45° and 45° in the contour plot.

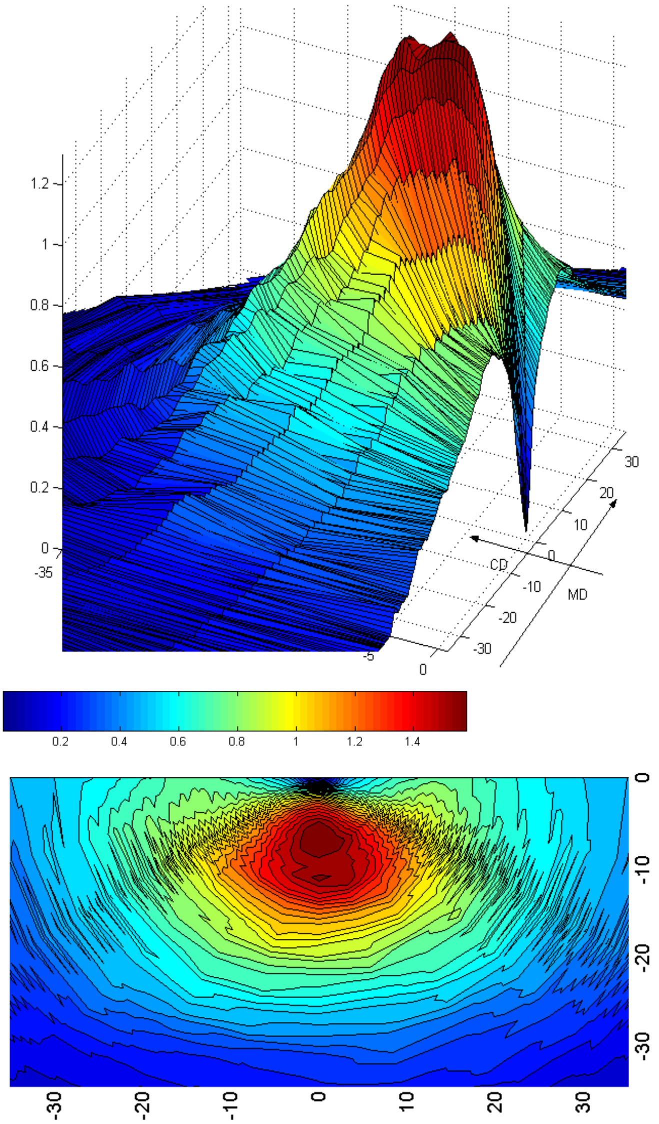

Figure 3.14 **Top**: 3D surface plot of the length fraction distribution of pore chords in all directions -90° to 90° relative to the cross direction in the sheet plane for the digitized volume of the newsprint sample. The step sizes between the measured distributions are 15°, seen as the long lines on the constructed surface. The height and colour in the plot are according to the length fraction for each interval in the discretized distribution **Middle**: Colourbar for the length fraction in both surface and contour plot. **Bottom:** Contour plot, the same plot as shown in the top figure, but from a vertical perspective. Abscissa and ordinate axis are pore chord length in machine and cross direction in respective order. The negative values are only needed for successful plotting.

.

Similar 3D plots as constructed for the sheet plane in the newsprint volume in Figure 3.14 can be constructed for any plane in any digital representation of the detailed paper structure. The features of all such plots will be the same, whereas the difference between the pore chord distributions in the principal planes will be larger the larger the structural anisotropy. The plot for the sheet plane of an isotropic structure would thus look similar to a volcano with the same slope in all directions, only with minor deviations caused by normal variation.

It is also possible to extract other characteristics from the distributions than the mean values applied for constructing warped surfaces representing the homogenised structural features of the porous phase. Useful parameters include *e.g.* the standard deviation, median, minimum and maximum. The median compared to the mean can give an indication of how stretched the distribution is without plotting the distribution. The minimum pore chord is the voxel size. The maximum pore chord can tell whether the measurements are influenced by the limited volume size. If the maximum value approaches the length dimension of the volume in the given direction, it is likely that a fraction of the longest pore chords is not included in the distribution. Measurements show that this happen for paper structures with high porosity and small physical volume.

In the analytical expression for pore heights, Dodson found the mean and standard deviations to be proportional [35]. The proportionality have also been confirmed by assessment of physical structures [48,49]. The practical measurements performed in this current study found the proportionality to be correct for the analysed handsheets irrespective of basis weight, formation and fibre anisotropy. As the pore chord distributions in any direction for all analysed paper grades have been shown to follow the same general features, it is interesting to see whether the relationship between mean and standard deviations is true even in other spatial directions.

In all analysed paper samples, the pore chord distributions become more elongated in the direction with the highest mean value. The elongation of the pore chord distribution will increase the standard deviation faster than the (number) mean. This is shown in Figure 3.15, showing the warped surface for the BSKP handsheet constructed from the determined standard deviations of the pore chords in 23 spatial directions. Comparing the ellipsoid shape of the standard deviation to the mean pore chord ellipsoid (Figure 3.7), we observe an increase in anisotropy, as the shape of the ellipsoid is more elongated. The shape confirms that the standard deviation increases faster than the mean when moving away from the vertical direction. It should also be noted that the warped surface constructed from measured standard deviations fits well with the ellipsoid shape.

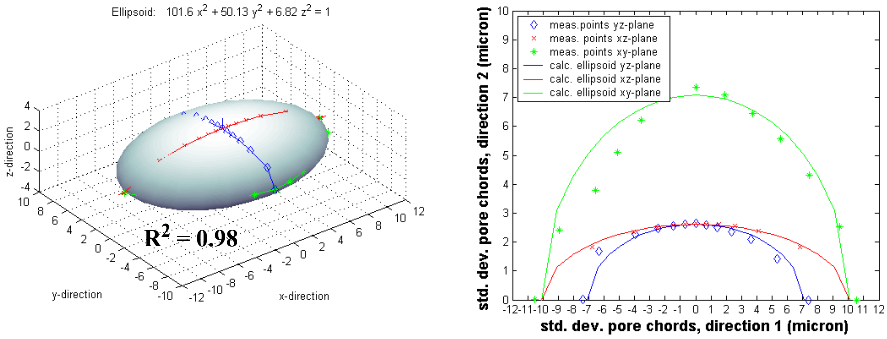

Figure 3.15 **Left:** The warped surface of the standard deviation of pore chords shows good agreement to the ellipsoid shape known for the mean values. However, the shape is more elongated than for the ellipsoid for the mean pore chords for the BSKP handsheet shown in Figure 3.7. **Right:** The fit of the assessed pore chord standard deviations in different spatial directions to the ellipse shape for each principal plane in the BSKP handsheet.

Assuming that the phases in the paper structure are complements of each other, then their chord distribution will necessarily have the same features. The lowest fraction phase must thus have the distribution with the smallest mean and the steepest curve. At a porosity of 0.5 the chord distribution must be identical. However there can be some small detailed differences due to minor structural variations in the relatively small volumes. Varying success of surface definition relative to the ideal giving exactly the same number of pore and fibre chords may also affect the similarity. The shift from the steepest curve being that of the pore phase to the fibre chord distribution being the steepest one after exceeding porosities of 0.5 is shown in Figure 3.16.

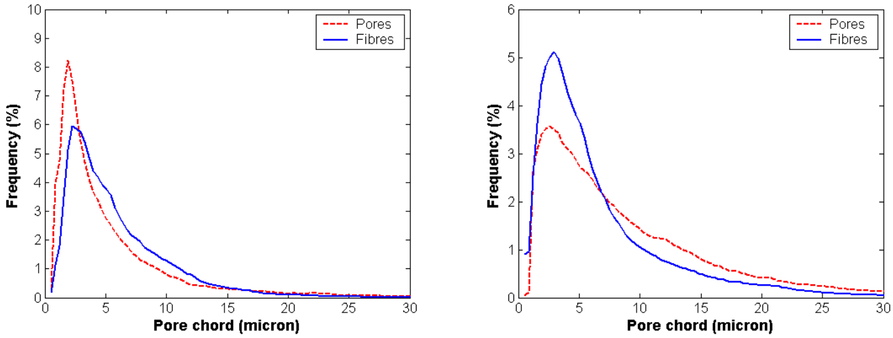

Figure 3.16 **Left**: Frequency distribution for pore and fibre chords in the vertical direction in handsheet volume, porosity = 0.464. **Right**: Frequency distribution for pore and fibre chords in the CD direction of the newsprint volume, porosity = 0.577

The distributions of both pore and fibre phases seem to follow a log-normal distribution and show the expected shift of which phase having the narrowest distribution when exceeding the porosity of 0.5. The shift according to which phase have the largest volume fraction supports the definition stating that the phases are complementary to each other.

3.3.4 Pore volume distribution

Maximal sphere method

The pore chord measures do not describe the pore volume distribution nor do they give information of individual pores, only a measure of the local extension in a given direction for the porous phase. One method of obtaining information about the volume extension is by covering the 3D pore structure with spheres of decreasing sizes until all pore voxels are covered by spheres. The method yields a pore volume distribution without having to define the pore necks.

The pore volume distributions, determined by the sphere method, for the s1 and s2 sample from the pilot paper machine experiment, described in Chapter 5, before and after calendering is shown in Figure 3.17. Assuming that the head box consistency had insignificant effect on the small imaged paper volumes, the settings are close to identical for the two samples except the calendering line load.

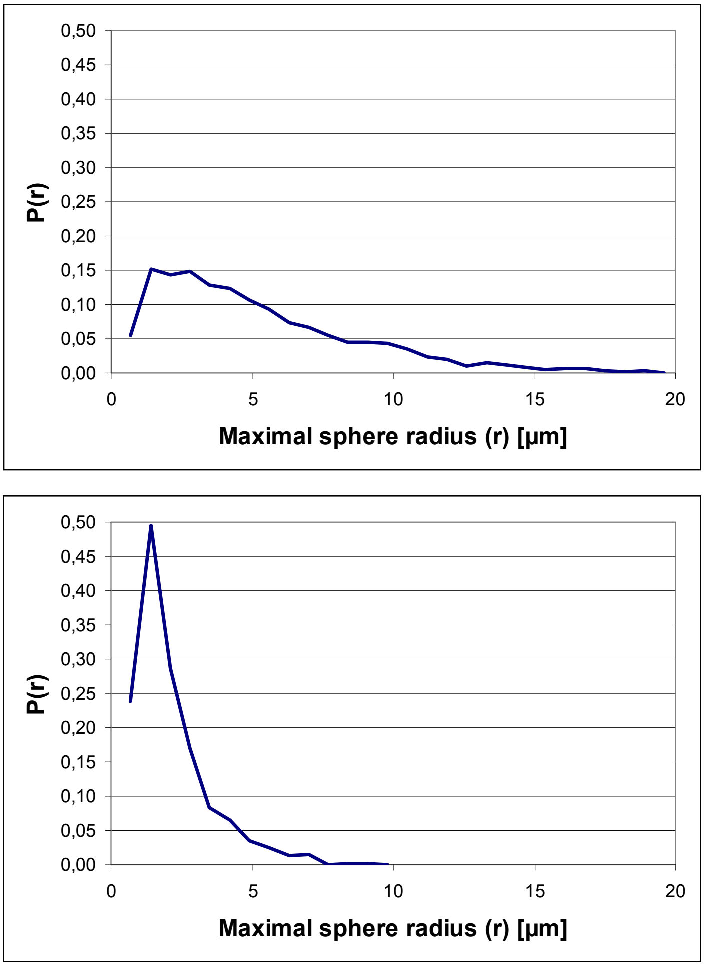

Figure 3.17 **Top**: The pore volume distribution before calendering (sample s1, density = 365 kg/m3). **Bottom:** The pore volume distribution after calendering (sample s2, density = 564 kg/m3). The abscissa reports the radius of the maximal sphere.

The pore volume distributions show the same behaviour as the determined pore chord distributions, the distributions becomes considerably narrower after calendering. The pore volume distribution is a true 3D measure, whereas the pore chord distribution is basically a 1D measure. However, the pore chord distribution can yield 3D information by measuring the pore chords for all three principal directions. The pore chord measurement thus give information about the differences of the structure when approached from different directions. The corresponding pore chord distributions for the same paper samples as the pore volumes distribution curves in Figure 3.17 were determined for, are given in Figure 3.18 for comparison. The voxel size for all the analysed digital paper volumes are 0.7 µm.

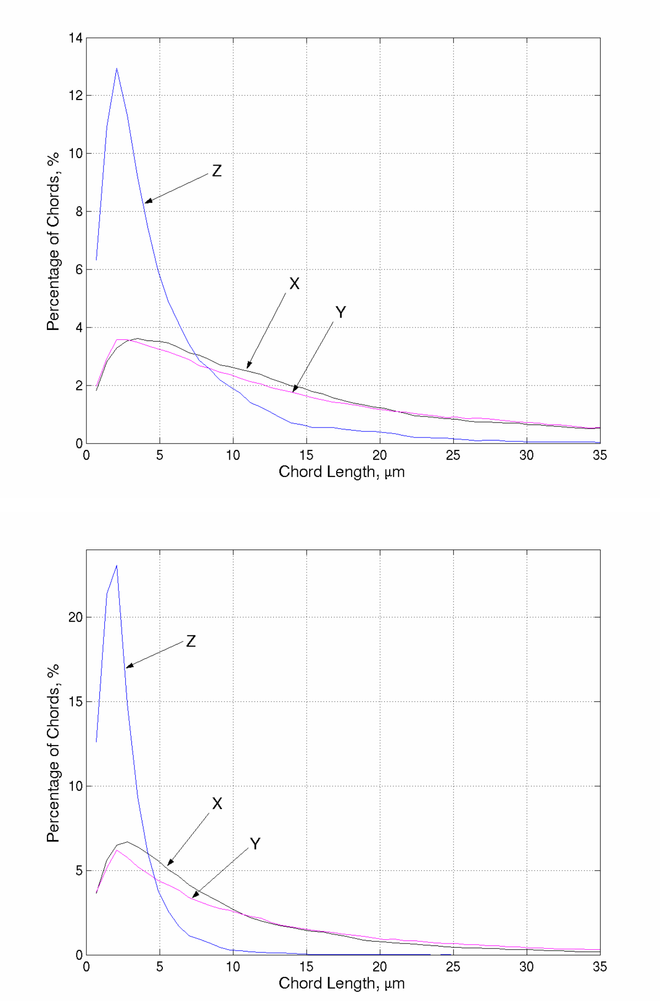

Figure 3.18 **Top**: The pore chord distribution in the three principal directions before calendering. **Bottom:** The pore chord distribution in the three principal directions after calendering. (s1 and s2)

Simulation of mercury intrusion porosimetry

The pore volume curves in Figure 3.17 are by nature similar to the curves that can be determined from mercury intrusion porosimetry. However, the assumed pore shapes are different. The mercury porosimetry assumes the porous phase to be channels of cylinders with varying radius, whereas the maximal sphere approach covers the porous phase by spheres of different sizes. An important additional difference is that the maximal sphere method will access all pores freely, whereas the mercury porosimetry must access the pores from the surfaces. The surface limitation results in the shielding of some large pores behind narrow pore necks, thereby influencing the determined pore size distribution. Additionally, the mercury intrusion porosimetry will be influenced by that the physical measurement in the initial phase (at small applied pressures) mostly will be a saturation of the surface porosity. The effect can be seen in Figure 3.19, which shows the mercury intrusion porosimetry curves for the pilot paper machine manufactured paper grades. However, assuming that the applied pressure corresponding to pores larger than 17 µm are mostly surface effects, the curves are similar to those seen for the maximal sphere method, except that the mercury porosimetry detects smaller pores for applied mercury pressures. To exclude the surface effects, the mercury intrusion porosimetry curves can be recalculated setting the volume fraction of pores larger than 17 µm to zero.

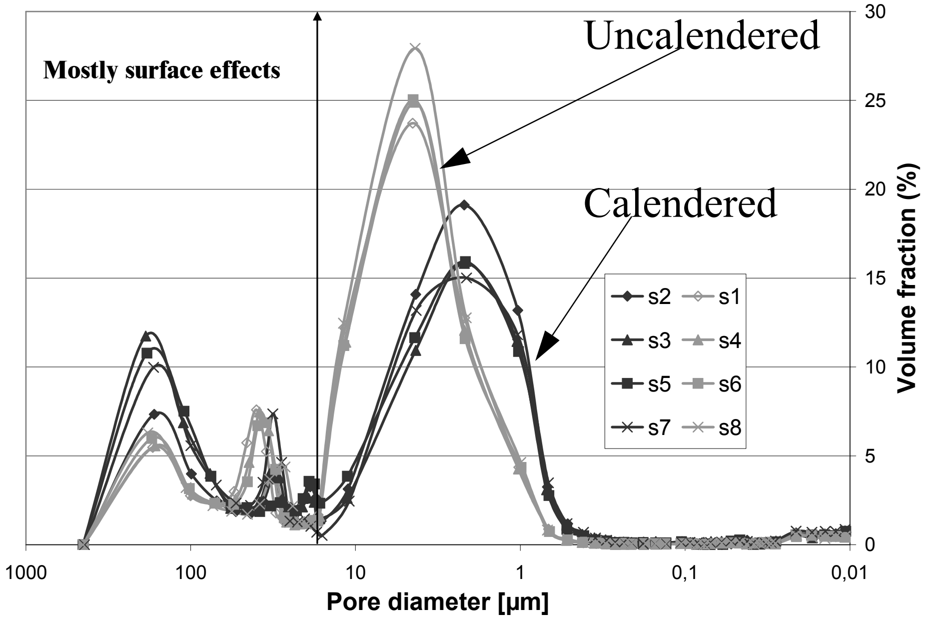

Figure 3.19 The determined mercury intrusion porosimetry (MIP) redistributed to a volume fraction distribution. The plot clearly shows the surface effects from the initial increase in the applied pressure to the mercury-paper sample system. The pressure corresponding to pores larger than a diameter of 17 µm are considered surface effects and are therefore discarded when comparing the MIP distribution to the results from the maximal sphere assessments.

The expected shielding effect of pore throats for the mercury intrusion from the surfaces and into the interior structure can be investigated by comparing mercury porosimetry to the maximal sphere method. The maximal sphere method has been used in two modes. One where the spheres only are allowed to enter the structure from the surfaces and one where the spheres are placed directly in the structure.

The difference in accumulated pore volume distribution is shown for one of the calendered samples (s5) and one of the uncalendered samples (s6) in Figure 3.20. The figure include curves for free access and surface limited access pore size distributions determined by the maximal sphere approach in addition to the accumulated pore volume distribution from physical MIP measurements.

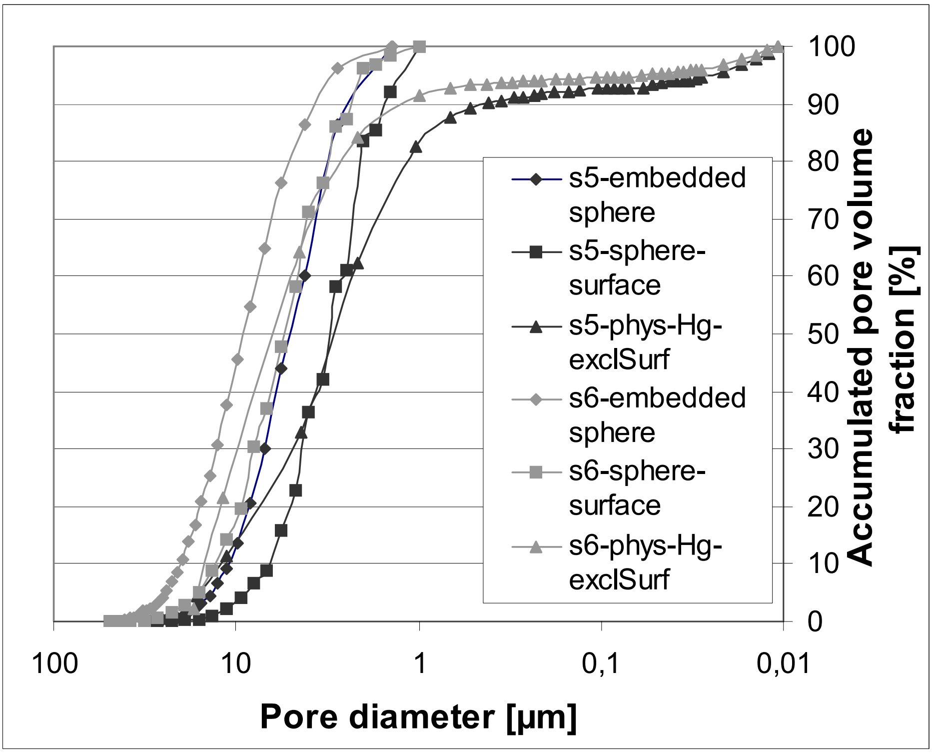

Figure 3.20 The accumulated pore size distribution determined by three different approaches. The black lines represent an calendered sample (s5) and the grey lines represent an uncalendered sample (s6). The curve for the physical mercury (Hg) intrusion porosimetry is derived when discarding pore diameters corresponding to clear effects of saturating the surface of the paper samples.

The curves in Figure 3.20 show clear differences between the methods (physical and digital) that are limited to intrusion from the surfaces and the normal maximal sphere pore volume distribution that can access all pores freely. The pore size distribution is shifted towards larger pores when all pores are freely accessed (no shielding). Thus, the approach only allowing the spheres to cover the porous phase moving in from the surfaces clearly shows the expected surface intrusion effect of larger pore volumes being shielded behind narrow pore necks.

The results also show a relatively good correlation between the physical and digital approach to mercury intrusion porosimetry. The correlation is best for the uncalendered sample. However, the relatively few measurement points of the physical mercury intrusion porosimetry at the pore diameter range of interest makes the comparison somewhat limited. There are also obvious physical differences in that the digital approach is not affected by surface saturation effects and is limited in resolution to the voxel size of 0.7 µm.

The obtained results are considered very promising and encourage a more extensive experiment allowing a detailed evaluation of the detailed paper structure's influence on the obtained curves from mercury intrusion porosimetry.

Pore volume distribution of pore throat limited pore bodies

Pore volume distributions derived from the pore space delimited into individual pores by definition of the pore necks could yield additional measurements and knowledge of the pore size distribution. However, the derived distribution would be dependent of how the pore necks were defined and determined. The preferred method for such pore volume distributions would be from reduction of the porous phase into a skeleton and determining the pore necks from the narrowest cross sectional area on each line segment. As no general agreement existed on the criteria for determination of a true node in the skeleton and a physical reasonable pore neck, no pore volume distributions were derived by this method in this thesis work.

3.3.5 Extracted subvolumes showing detailed pore extension

Although it is not possible to extract individual pores from the 3D structure without performing a delimitation of the porous phase, information of the detailed extension of pores can be accessed from selected sub volumes of appropriate size. Figure 3.21 shows some examples of details of the detailed pore structure for different voxel size resolutions and paper structure properties.

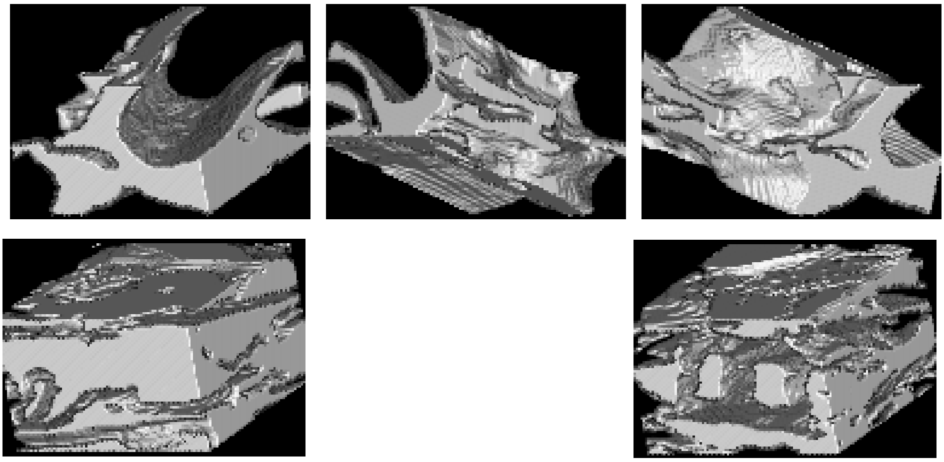

Figure 3.21 3D visualization of the detailed pore geometry in different newsprint-(like) digital volumes. **First row**: Detail of a pore as extending between three fibres and smaller solid elements in the newsprint sample obtained by phase contrast with a voxel size of 0.35 µm. The selected subvolume is 92 x 60 x 98 voxels (width x height x depth as seen in left image). **Second row, left**: A subvolume of 100x70x100 voxels (MD x ZD x CD), voxel size 0.7 µm, absorption mode, in an uncalendered paper sample of the newsprint like paper made on a pilot paper machine. **Second row, right**: A subvolume with the same dimensions and character as the left, except the volume being chosen from a calendered paper sample. The subvolume is chosen in the vicinity of two connected fibres.

3.4 Discussion

3.4.1 Analytical pore height distribution

The manufactured handsheets will have some differences to the theoretical random fibre network consisting of Poisson layers. Although these differences can be a disadvantage in the validation of the analytical pore height distribution, the differences are natural features of a fibre network. The differences between physical and natural fibre network features are therefore favourable when regarding applicability of the analytical expression.

There are two major differences between the theoretical and physical networks. In the physical fibre networke there will exist intra fibre pore heights. These pore heights are not accounted for in the theoretical approach, which applies solid, rectangular, discrete sized fibres. The second major difference is that there will be a distribution of fibre thicknesses in the physical paper structure and not a constant value as assumed for the theoretical approach to the paper structure.

The intra-fibre pore heights can be found in uncollapsed fibres, resulting in lumen pore heights and for fibres with kinks and curls, resulting in pore heights between different segments along the length of the fibre. The frequency of intra-fibre pore heights is relatively small for the analysed handsheets (Figure 3.2). The intra fibre pore heights will accordingly probably results in small deviations from the theoretical assumptions.

The distribution of fibre thicknesses are shifted towards longer and more uniform fibre thicknesses, as only the long fibre fraction is applied for sheet forming of the beaten pulp. The distribution of fibre thicknesses is in itself a characteristic of the paper material that the analytic expression should handle to be applicable to real paper structures. The results show that the analytic expression seems to handle the difference between a constant fibre thickness and varying fibre thicknesses being normal distributed around the applied mean value for the model.

The effect of basis weight to the pore height distribution is somewhat different than the theoretical approximation with the number of Poisson layers. The paper does not consist of Poisson layers, where each layer have the same solid fraction. In fact there is a transition from the bulk, where the Poisson layer approximation is close to correct, to the surface layers, where the solid fraction usually is clearly increasing towards the outermost layer, and the Poisson layer approximation is definitively not correct (see Holmstad et al. [62]). The transition from the interior to surface layers depends on the surface definition delimiting the paper structure from the background. The surface definition is more difficult to determine for a real paper structure than the uniformly thick theoretical fibre network. The large differences between theoretical and physical fibre networks, when it comes to uniformity, makes it almost impossible to adjust the surface definition correctly. The difference between the ideal and the real structures will thus be larger the lower the basis weight. The larger deviation from the Poisson layer definition for low basis weight sheets can therefore explain why the analytical pore height distribution shows larger deviations from the measured distribution for low basis weight sheets, than for normal basis weight sheets. Assuming this to have a large influence on the basis weight effects seen in the study, this implicates that the analytical model will be more correct, when increasing the basis weight of the analysed paper grade.

As for other measurements of structural properties from cross sections, the sample preparation will influence the results from the image analysis, as discussed in Chapter 2. The most decisive sample preparation step for the analysed paper grades is the grinding and polishing of the epoxy embedded cross sectional paper samples, as the chemical fibres are vulnerable to smearing effects. The smearing effect may lead to increased fibre cross sectional areas and thus a systematic error yielding too small pore heights and too large fibre thicknesses compared to a structure unaffected by sample preparation defects. However, this risk was well known when the specimens were prepared. Precautions were taken in the sample preparation to reduce the smearing effect to a minimum. It is therefore assumed that sample preparation defects have a negligible influence on the determined structural parameters and pore height distributions. Despite of the clear anisotropy in the paper samples, the non-systematic difference between MD and CD orientated samples shows that other effects than the sample preparation defects have larger influence on the measured pore height distributions.

The effect of the anisotropy could not easily be distinguished from the effects of basis weight and formation, as the basis weights and formation were not identical for the isotropic and anisotropic handsheets. The observed effects of the anisotropy is therefore more an assumption than a clear result. It is thus necessary to perform further experiments to validate the assumed effect of anisotropy.

The effect of adding fines and fillers to the analysed long fibre fraction fibre networks was not investigated. Nevertheless, measurements of pore chord distributions in 3D images of commercial and pilot paper machine made newsprint samples, which contained a large fraction of fines material, did not show any large deviations from the shape of the analytical pore height distribution. However, it was not investigated whether the distributions were dependent on more parameters than the solid fraction and number of fibre layers.

The investigation performed by Roberts and Sampson [49] on the effect by laboratory beating on the pore radius distributions in paper, as measured by a porometer, shows that the proportionality between the mean and the standard deviation of pore radii holds for paper grades with varying amounts of fines. Although the measured pore radii from the porometer and pore heights are somewhat different by nature, the results from the study of laboratory beating combined with the observed pore chord distributions for 3D images of newsprint samples in this study, indicate minor deviations from the analytical pore height distribution for fibre networks containing fines material.

3.4.2 Equivalent pore parameters

The assumed ellipsoid shape of the warped surface constructed from the measured mean pore chords in a structure could be confirmed by the measurement of the two selected, distinctly different paper grades (newsprint and BSKP handsheet). The high R^2-values for both paper grades is a strong proof, although measurements in only two paper grades without replicates is in itself a bit sparse for trustworthy conclusions. However, the ellipsoid shape is found for other porous materials and validated for paper from measurement of pore chords from cross sections and from impingement of laser to stacks of paper by Silvy and co-workers [36]. The measurement in 3D digital paper structures is thus a test where a higher detail level for a small area within a paper sample is achievable. The validation of the ellipsoid shape in these small areas thus confirm the presence of the equivalent pore as a general feature of the paper material in any size order large enough for obtaining reliable measures of the mean pore chord.

The size of the maximum length of pore chords in the horizontal directions of the high resolution 3D images (voxel = 0.35 µm) approaches the length of the shortest dimension of the 3D images for the newsprint and filter paper volumes. These results indicate that some of the longest pore chords in the structure are not detected with the applied volume size and image analysis criteria. The structural anisotropy may thus be even larger than what is detected from the mean chord measurements for these paper grades. However, the pore chord distribution shows a monotonous decrease in number frequency for increasing pore chord length. The loss of some of the longest pore chords will thus probably not be large, maybe except for a combination of small assessed volume size and high porosity of the paper grade. The loss of the longest pore chords does not seem to influence the shape of the warped surface, as the ellipsoid for the newsprint volume is not butted in the machine direction. Previous measurements of the pore chords in the filter paper volume [46] did not show such effects for the more porous filter paper sample either. The loss of the longest pore chords does not affect the equivalent pore shape significantly. The reason for this is likely a combination of that the effect is relatively small and that the effect will diminish according to the angle relative to the principal direction, where the reduction follow an elliposidal curve.

The measurement of porosity, as the relation between the mean pore chords given in Eq. 3.5, shows a relatively large variation in porosity between the different spatial directions. This is not an unexpected result, as the surface pore chords (pore chord between the fibre and the defined surface) and pore chords limited by the edge of the sampled volume are disregarded when determining the mean pore chord. The exclusion of these pore chords assures that all assessed pore chords do not depend on surface and edge definitions. However, the choice will cause the assumption of an equal number of pore chords and fibre chords to be wrong, as the systematic exclusion of the surface and edge limited pores cause most traversing lines through the structure to both start and end in a fibre chord. The lower number of pore chords relative to fibre chords does not seem to affect the measured mean pore chords more in some spatial directions than others, as there are no systematic deviations from the assumed ellipsoidal shape of the warped surface constructed from the measured mean pore chords. The number of excluded pores is relatively small compared to the number of internal pore chords in the assessed paper grades. It is therefore assumed that the exclusion of the surface and edge limited pore chords results in smaller effects than including “ill” defined pore chords in the measurements. Although, the difference in the number of pore and fibre chords in the assessed paper volumes does not seem to have any significant effect on the shape of the equivalent pore, the application of the equations found in equivalent pore theory should be applied with precaution, as they assume equal number of chords. For materials where the surface area is not as crucial as for paper, this problem can be solved by disregarding the surface area.

The equivalent pore parameters yield a homogenised characterization of the paper structure on a micrometer level. These parameters may be applied for studying the influence of the paper structure on the performance properties of the paper at the bulk level.

The most readily applicable way to apply the determined parameters is through determination of the correlation to measured sheet properties that are assumed to be influenced by the equivalent pore parameters. Examples of such paper properties can be strength, stiffness and transport anisotropy, elastic-modulus and directional permeability. For paper properties where there are clear correlations between the equivalent pore parameters and bulk paper properties, it is possible to derive empirical models. Silvy has derived a few such models [51]. However, it may be difficult to find universal expressions, as most sheet properties depend on other properties than the structural features assessed by the equivalent pore concept, and these properties obviously can change in magnitude and importance between different paper grades. Holmstad et al. [46] applied some of the empirical models derived by Silvy [51] for some selected paper properties on three distinctly different paper grades. The results showed a fair agreement between modelled and measured paper properties. However, it is also obvious from the results that the models are not fully applicable to all paper grades, as the relatively large deviations between modelled and measured paper properties most likely are influenced by other factors than normal variation in the structural features accounted for by the equivalent pore concept.

The measurement of mean pore chords is a measure of the average mean free straight path lengths in the different spatial directions in the paper structure. As the pore and fibre mean chords are complements of each other, the ellipsoidal shape holds information of free path lengths in both porous and fibrous phase. The equivalent pore can thus be applied for a statistical approach for simulating light scattering in paper. The mean pore chords and pore chord distributions in the different spatial directions may be used as an input to a Monte Carlo simulation of light scattering in a statistical paper structure. The probability of free path lengths for the light beams in the statistical structure will thus be according to the determined equivalent pore parameters. Such an approach is applied by the light scattering model derived at ACREO [63]. The knowledge of the equivalent pore allows determination of the necessary input to the statistical paper structure from measurement of the pore chords just for the three principal directions.

3.4.3 Relationships between the measured pore geometry parameters

The results show a clear relationship between the measured pore geometry parameters. It is clear that the equivalent pore, holding the information of structural anisotropy, mean pore chords and possibly frequency of phase borders in all spatial directions in the paper structure, holds many important features of the detailed paper structure.

Figure 3.14 clearly shows that the pore chord distributions also change gradually between the principal directions, in a manner similar to the surface of the ellipsoid constructed from the mean pore chords. The pore chord distributions seem to follow a log-normal distribution for all spatial direction, the distributions are only changing from a broad to a narrow distribution according to the structural anisotropy. The fit of the ellipsoid to the measured standard deviation for the pore chords in different spatial direction confirms this observed correlation.

The analytical approach to the pore chords in the vertical direction shows that the distribution is determined by solid fraction and number of fibre layers. The analytical pore height distribution could be confirmed for handsheets made to approach the theoretical fibre network. It was found from the analysis of the other handsheets that the analytical model could predict the pore height distribution relatively well even for poor formation and high anisotropy. The shape of the pore chord distributions have been shown to have correspondence to the shape of the analytical pore height distribution for any spatial direction for pore heights larger than a fibre thickness. Both can be said to follow a log-normal probability density function, although the different resolution results in a different mean pore chord. It is thus likely that the pore chord distributions for most paper grades are mainly influenced by the solid fraction and the number of fibre layers in addition to the structural anisotropy.

The application of the equivalent pore concept may thus give information of many structural features based on measurement of the mean pore chord lengths just for the principal directions. However, a general expression for the pore chord distribution and its dependency on orientation relative to the principal directions must be found if the pore chord distributions in any spatial direction are to be found directly from the ellipsoid shaped warped surface.

The pore chord distributions must also have a relation to the pore volume distributions, as they are both derived from the same physical structure. From comparison between Figure 3.17 and Figure 3.18, both showing the change of pore size distribution by calendering of the same structure, it is clear that the distributions have common features. The pore volume distribution determined by the sphere method is based on the extension of the sphere in all spatial directions simultaneously, thus it is locally limited by the direction where the porous phase has its narrowest extension. This can locally be in any direction, but when averaging over a sufficiently large volume, the smallest extension will most likely be in the z-direction. The pore volume distribution will thus follow the features of the vertical pore chord distribution the closest. However, the pore volume distribution can be said to be an averaging of the features observed by the chord approach, because of its direct 3D approach, although this is a bit simplified. The sphere approach will allow the detailed continuous features in the fibre network to limit the extension. The pore volume distribution is thus based more on the extension of individual pores than on the pore chord approach. The pore chord distribution, when measured in all three principal directions can on the other hand give information of the structural anisotropy, something the sphere approach can not do.

The detailed volume extension of individual pores may be found through determination of the pore necks of the interconnected pores. A pore volume distribution derived by this approach would be the ultimate when observing the distribution of individual pore features. However, the definition of pore necks is sensitive to the chosen definition and

the chosen approach for determining line segments in the pore phase skeleton. Pore volume distributions may thus possibly be obtained by the pore neck approach, but if there exists no physical logic for the definition of pore necks, it will be difficult to relate physical properties of the paper to the derived pore volume distribution. The pore volume distribution will necessarily be a volume distribution, as the shape of the individual pores most likely are neither cylinders nor spheres, for which a corresponding radius could be found. It is thus just the shape of the distribution that can be compared to other structural measures, not the numerical values.
The determination of a pore phase skeleton may yield information of the connectivity of the porous phase, something not accessible by the other pore geometry methods.

Although the relationships between the different pore geometry measures are of importance for the fundamental knowledge of the paper structure characteristics, the relationships to the physical (performance) properties of paper is important for the application of the knowledge of the pore geometry for improvement of paper quality.
The pore chord and volume distributions can be related to pore size distributions obtained by mercury intrusion porosimetry and gas drive methods. However, these are only alternative methods for obtaining the same measures as the distribution assessed by image analysis. The relationship between pore geometry measures and transport properties are more interesting. However, the availability of a digital 3D structure allows simulation of transport properties like permeability and diffusion. The simulation of transport properties in digital 3D structures is treated in Chapter 4.
This study has provided a systematic procedure for assessing the detailed pore geometry. However, the important task of finding the relationships between the pore geometry parameters and paper properties has yet to be undertaken. The analysis of the results of the factorial design experiment in Chapter 5 provide some correlations, but these can only be regarded as preliminary results.

3.4.4 Representativity

The studies of pore geometry included both assessments from cross-sectional images obtained by SEM-BEI and from digital paper volume images obtained by x-ray microtomography. The approaches have a fundamental difference when it comes to representativity.

The cross section approach used here includes sampled areas from 15 independent areas of the assessed paper grade. The approach ensures a good representativity of the true features of the sample, which can be quantified by the standard deviation of the determined mean value for most features. However, the distributions in themselves need to be based on several replicates, so it is normally too laborious to determine the variation of the observed frequency within the intervals. However, the distributions will normally be relatively exact for 15 replicates, given that the formation is fairly good. The smoothness of the distributions will give an indication of the stability of the results.

The cross section can never tell anything about the extension in the direction normal to the observed plane. The cross sections is thus less suited for confirming a feature of the structure, such as the equivalent pore, as the extension in more than two dimension is not known for the same area within a sheet. The availability of a detailed 3D image will give a clear relation between all the spatial directions within a given small area, yielding a relatively smooth surface of the warped surface constructed from the measured mean pore chords, but the determined structural anisotropy is only known to be correct for the small assessed area. The determined ellipsoids in this study is thus dependent on the local structural properties in the assessed volume, which can yield significant differences between an ellipsoid determined from a low basis weight area compared to a high basis weight area. Ideally the mean pore chords should therefore be determined in several independent paper volume replicates. However, low availability and high cost of synchrotron radiation x-ray microtomography beam time made it difficult to obtain the desired number of replicates.

The other pore geometry features determined from 3D images of paper will have the same characteristics as the equivalent pore parameters when it comes to representativity, although some features are less dependent on formation effects than others. The effect of formation to the different measures of pore geometry determined in small detailed 3D images of paper is investigated in more detail in Chapter 5.

3.5 Conclusions

The detailed pore geometry can be assessed by image analysis of cross-sectional images and 3D images of paper. The assessments have confirmed the analytical pore height distribution derived by Dodson for internal pore heights and the existence of the ellipsoid shaped 3D continuous, closed surface as a representation of the physical porous phase in the analysed paper grades. The assessment of the pore chord distribution, in other spatial directions than the vertical, has shown that the distributions follow a log-normal distribution in all directions, where the mean and standard deviation follow the spatial direction according to the ellipsoidal shape of the equivalent pore. The equivalent pore represent both structural anisotropy and mean pore chord and is thus a characteristic of the porous phase holding a large amount of information.

The results give clear indications of the solid fraction and structural anisotropy to be the major determinants for the pore geometry. The basis weight and fibre thickness will also most likely have effects on the pore geometry. For basis weights over an unknown threshold, for which the effect of the surface layers becomes close to negligible, the two effects can be represented by the number of fibre layers.

The measurements of pore chords combined with more advanced measures of pore volume distribution and individual pores performed in this study have shown how 2D and 3D characterizational methods may complement each other. The 3D approach may also help the understanding of how the details of the paper structure influences physical assessments of the pore size distribution. The maximal sphere approach yielded clear results showing the intrusion of the mercury to be restricted of narrow pore necks when assessing the pore sizes entering from the surfaces applying mercury intrusion porosimetry.

The study has also added to the knowledge of the detailed fibre network, as the fibre phase is the complement of the fibre phase, except for minor differences related to the surface definition.

This work has shown how the pore geometry measures can be determined and how they are related. The applicability of the methods for obtaining quantitative measures of the paper structure that can be used for improvement of paper quality is not proved. There is thus still a need for further and more practical studies of how the assessed pore phase features relates to paper performance properties.

CHAPTER

4

THREE-DIMENSIONAL (3D) ANALYSIS OF PAPER STRUCTURE CHARACTERISTICS

4.1 Introduction

4.1.1 Background

Acquisition of 3D images of paper enables a better understanding of how the fibre network is built up to form a sheet. The three-dimensionality gives access to the volume extension of pores and fibres and their spatial arrangement. The volume extension is not accessible by other techniques for characterizing paper structure, such as *e.g.* analysis of cross-sectional images, sheet splitting and β-ray basis weight distribution images. The knowledge of the three-dimensional structure is necessary for the fundamental knowledge of how the features of the detailed fibre network influence paper properties like *e.g.* optical and transport properties.

Paper is a complex material for 3D imaging, as the building blocks of the paper, the fibre material, are so small that a high resolution (μm level) is needed for accessing the features governing the paper properties. At the same time, the structural variation caused by the flocculation of fibres during the sheetforming, is at a scale of millimetres. Additionally the contrast between fibre material and voids is insufficient for most microscopy techniques at the resolution level needed for useful 3D imaging. It is thus just recently that microscopy techniques acquiring 3D images of paper with sufficient contrast and resolution to acquire detailed features of the fibre network have become available. It is thus a need for testing whether the microscopy techniques succeed in depicting a realistic 3D structure with sufficient details for acquiring useful knowledge and quantitative measures of the structural features. It is the intention of this work to perform a practical study to evaluate the applicability of the most promising new 3D imaging techniques.

It is in itself useful to obtain 3D images to observe the spatial extension of pores and fibres and seeing how they are interconnected. This can be done through different visualization techniques of the volume data. However, to exploit the full potential of a

3D digital representation of the paper structure, quantitative assessments are required. The structural parameters can be quantified by image analysis of structural features and from simulation of physical phenomena in the digital structure. Quantification is a necessity for objective observations and for comparison of different structures. This study will therefore investigate the possibilities for useful assessment of the digital paper structure and assess such parameters for selected paper grades. It is also considered important to investigate the relationship between the measured features of the paper structure and bulk paper properties.

4.1.2 Previous work on acquisition and analysis of 3D images of paper

Although 3D imaging is relatively new in research of paper materials, there have been a number of studies over the last decade applying different 3D imaging methods for visualization and assessment of the characteristics of the detailed paper structure.

A 3D image of a handsheet of beaten bleached softwood kraft pulp (BSKP) was constructed from a set of consecutive cross-sectional images already in 1992 by Hasuike et al. [64]. The data set was reconstructed from ultramicrotomed slices imaged with a differential interference microscope, which yielded a well contrasted image of the microtome slices without staining. The reconstruction was based on finding the contours of individual fibres in the cross sections and manually connect adjacent fibre contours along the machine direction by triagonal surface elements, applying transparencies and pencils to mark the contours. The reconstruction was as such a fibre segmentation routine, and thus made it possible to extract data for fibre orientation, both in vertical and sheet plane direction, and fibre-to-fibre bonding. The reconstructed data set was {0.2 x 0.2 x paper thickness} mm^3, with a resolution in the machine direction corresponding to the thickness of the microtome slices. The applied method is extremely work intensive and have clear limitations from microdeformations of microtome slices and limited resolution in the machine direction.

A later improvement of reconstructing 3D images of paper from consecutive cross-sectional images of paper was made by Aronsson et el. [17,65]. The study showed that reconstruction from microtomed slices were difficult, as the microtomed slices were easily distorted during preparation and transfer to the microscope. However, application of consecutive cross-sectional SEM images of the remaining block face, after removing 5 slices of 1 µm by microtome between each cross-sectional imaging, were successful. The method succeeded in producing a binarised 3D data set of {1.80 x 0.51 x board thickness} mm^3 of a duplex board, normally applied for milk cartons. The alignment of the cross sections and reconstruction of the digital paper structure was done by image analysis software developed by Aronsson. The resolution in the cross-sectional images were approx. 0.6 µm and the distance between the slices (in machine direction) were approx. 5.0 µm. The data sets thus consists of non-cubic voxels. The resolution in the machine direction was improved applying a routine for linear shape based interpolation (morphing), according to a method presented by Raya and Udupa [66], to produce artificial slices between the ones obtained by microscopy. The relatively long distance between the slices made the automatic interpolation inaccurate, as parts may easily be incorrectly connected. The approach was therefore only applied for small segments

where the fibre displacement and deformation was at a reasonable level.
The study focused on segmenting individual fibres and performing measures of these. The method succeeded in segmenting 10-20% of the total number of fibre segments in the digital paper volume and producing useful measures of the individual fibre segment geometries. The study applied 3D distance transforms (DT) for measuring the distances in the 3D data set. This is a very efficient and helpful measure, which can be applied successfully for analysis of all digital binary 3D volumes. The DT was applied in the study for; assisting the determination of the surface of the volume, assisting the 3D tracking of fibres, performing a pore phase extension analysis and for detecting the degree of layered structure of the paper sample.

A problem for the microtoming approach is a repeated removal of the block from the microtome for image acquisition. This introduces a variation in the reported thickness between the obtained cross-sectional images. The microtoming approach can also only acquire cross-sectional images of one paper sample per epoxy block. The thickness between the slices can be better controlled and number of paper samples in the prepared epoxy block can be increased when applying the alternative method of controlled serial grinding depth, as reported by Chinga et al. [67]. The grinding and polishing of epoxy blocks, as discussed in Chapter 2, is also known to introduce less distortions to the structure. The grinding is controlled by addition of monodisperse Ugelstad beads between the paper samples, stacked in a paper-bead sandwich. The change of cross-sectional area of the close to perfectly spherical shaped beads between two consecutive slices yields the quantitative measures of distance. Small Ugelstad beads are also added for reference when aligning the consecutive cross-sectional images. The varying gaps between the cross sections are filled applying a varying number of 'artificial' cross-sectional images obtained by linear shape based interpolation, applying the same principles as in Aronsson et al. [65]. The method was successful in producing 3D images of a newsprint-like paper and a paper of SC-quality. The controlled grinding at steps of 1.5 ± 0.45 µm and the pixel size of 0.2 µm, enabled the level of detail needed for observing the details of the high density SC paper containing fillers. The method is thus promising for acquiring 3D images when a high detail level is needed. The study did not include any quantitative measures of the reconstructed digital paper volumes.

Both the microtoming and grinding approach are invasive techniques, that will at some level distort the structure. This can possibly be improved by applying alternative methods of sample preparation. Preparation techniques applying focused ion beam (FIB) [18] and micromilling [19] have been reported to introduce less distortions than the microtoming and grinding approaches. The techniques have the advantage of producing consecutive images without removing the sample between the different slices. However, no reports have been made applying the techniques for producing 3D data sets of paper. Although the methods may introduce less distortions to the paper structure, the methods are still to some extent invasive. There exist methods that produces cross-sectional images of the paper structure applying non-invasive methods like X-ray microtomography and confocal microscopy. The application of methods like FIB and micromilling may thus be redundant as these introduce techniques that is only something between already existing invasive and non-invasive methods.

Confocal laser scanning microscope (CLSM), have been successfully applied for obtaining 3D images of paper [2,68], applying fluorescence mode imaging. The technique is able to non-destructively acquire consecutive cross sections of paper with distances in µm-scale applying optical sectioning. However, the contrast between fibres and voids in fluorescence mode is relatively low and is decreasing in the depth direction, limiting the allowed thickness of a successfully imaged paper sample. The relatively low and varying contrast in the depth direction render it difficult to apply CLSM images for quantification of 3D structural properties. However, the microscope is well suited for obtaining localized measures of 3D features of single fibres, like *e.g.* fibre wall area and local fibre orientation [28,69] and for obtaining visual information of the 3D structure for small areas [2] close to the specimen surface.

The non-invasive technique X-ray microtomography have been reported to successfully depict paper samples in 3D with relatively high resolution [46,70-85]. The voxel size in the data sets are cubic and the contrast between fibres and voids are constant throughout the volume. The consecutive cross-sections in the 3D images are automatically aligned, enabling a considerably easier generation of a digital paper structure compared to microtoming and serial grinding approaches. The reported imaging of paper volumes applying X-ray microtomography include both absorption and phase contrast imaging and both synchrotron and stationary X-ray sources. The reported voxel resolution and volume sizes are varying accordingly.

The successful imaging of 3D structure of paper applying X-ray microtomography have later been applied for assessment of 3D paper structure characteristics. Goel et al. [75] reported the internal porosity and specific surface area of thick board samples. The determined structural porosity was compared to porosity determined by caliper-basis weight measurements and mercury intrusion porosimetry. The porosity measured in the digital volumes were found to be in fair agreement to the physical measurements. Progress in development of image analysis routines and 3D imaging of a set of thick handsheet samples, with different freeness levels, have shown further progress in assessment of 3D images obtained by commercial desk-top CT scanners [76,77,78,86]. The studies cover a wide range of measured structural features, which show the applicability of the microtomography technique and extensively characterize the structural properties of the handsheet samples.

Assessment of digital 3D images obtained by absorption mode X-ray microtomography from synchrotron radiation sources have been reported. The measured variables include assessment of the paper surface's topography and structural anisotropy according to the equivalent pore concept [54] and detailed measurement of many fibre network characteristics [72,73]. The measurement of the fibre network characteristics involve determination of the fibre network by a medial axis, or more commonly known as a skeleton.

X-ray microtomography have also been applied successfully for imaging and assessing the structural properties of paper-like material like non-wovens [87] and papermaking felts [88,89]. The larger size of the constituents (*i.e.* yarns) allow a lower resolution and thus larger volume sizes than what is applicable for acquiring the needed detail level for paper structures.

The application of acquisition of 3D images of paper and analysis of the digital 3D paper structures are in an initial stage. Therefore, there is a need for evaluation of the different techniques available for obtaining 3D images. The intention of this work is to apply X-ray microtomography for 3D imaging and perform subsequent image analyses of the digital structures. To evaluate the technique it is necessary to consider how the beam characteristics, resolution, volume sizes and image processing influences the measured structural characteristics. It is also necessary to evaluate the usefulness of the different characteristics that can be determined from the digital representations of the paper structure. A useful characteristic should help increase the knowledge of how the features of the paper structure influences the performance properties of paper and/or how the paper structure is influenced by raw material and paper making variables.

4.2 Materials and methods

4.2.1 Imaged paper samples

The paper samples that have been imaged by X-ray microtomogaphy techniques and analysed were of two different sets of samples.

The first set of imaged paper samples was a selection of paper grades with clear differences in structural properties. The samples were chosen for testing the abilities of synchrotron phase contrast imaging for successfully depicting the detailed paper structure for paper products with distinctly different characteristics. The samples that were successfully imaged, subsequently reconstructed and thoroughly analysed were a handsheet of bleached softwood kraft pulp (BSKP), a commercial newsprint grade from softwood thermo-mechanical pulp (TMP) and a filter paper made from cotton linters. The filter paper was also successfully imaged in a water soaked condition. The details for the properties of imaged paper grades are given in Paper III and IV.

The second set of imaged paper samples include newsprint-like paper samples manufactured on a pilot paper machine according to a factorial design. The details of the factorial design and the properties of the imaged paper samples are given in Chapter 5.

4.2.2 Choice of technique for 3D microscopy

The basic requirement of an applicable 3D microscopy technique is a phase assignment for all individual cartesian coordinates (x,y,z) within the imaged paper volume. It is necessary to image the structure from several projections to gain enough information to extract such 3D data for a structure. Although the high depth of field in SEM enables a three-dimensional view of the sample’s surface and cut edges, the image is not a truly 3D image, as it is only a single projection yielding a visual impression. Alternatively the SEM can apply two projections to build a topography image of the surface. However, the SEM cannot non-invasively access the interior of the sample.

There are a few 3D microscopy techniques that can be considered for obtaining 3D images of paper. These are: Confocal laser scanning microscopy (CLSM) [2], SEM or LM combined with serial sectioning [64,65,67], and X-ray microtomography [*e.g.* 71,75,81,85]. Magnetic resonance imaging (MRI) can also be applied for 3D microscopy of some porous materials. However, MRI may not be suitable for paper due to the hydrophilic nature of cellulose fibres and signal interference caused by cellulose protons [90].

The preferred technique for 3D imaging is x-ray microtomography, as it gives access to the paper structure non-invasively at a uniform high resolution and contrast in all spatial directions and in all parts of the imaged paper volume. None of the other applicable techniques have this combination, as they have varying contrast (CLSM) or resolution (serial sectioning SEM/LM) in the different spatial directions. The uniformity in the 3D images from x-ray microtomography simplifies the reconstruction of the digital volume and the consecutive assessment of the extension of the pores and fibres in the structure.

The disadvantage of x-ray microtomography is the low availability and high cost of necessary beam-time for acquisition of high resolution 3D images. Acquisition of low resolution X-ray microtomography images are more available, as there exist commercial desk-top scanners. However, the lower resolution clearly limits the detail level of the 3D images.

The SEM-BEI technique combined with a controlled serial sectioning is thus considered as an applicable in-house technique when a high detail level is desired [65,67]. The SEM cross-sectional images have a better contrast, and can apply a higher resolution than what is achievable by X-ray microtomography, but the sectioning can usually not be controlled in sufficiently thin and constant slices to obtain the same resolution in the depth direction. The technique is also extremely work intensive and the 3D reconstruction is considerably more difficult than X-ray microtomography [17].

4.2.3 X-ray micro (computed) tomography (X-μCT)

Working principles for 3D acquisition

Tomography is a method for 3D imaging frequently used in material technology and in medicine. 3D imaging with resolution below centimetre scale is referred to as microtomography. The need for high resolution (voxel <1 μm) for successful acquisition of the detailed features of the paper structure requires application of X-rays of high photon energies with good penetration ability, so called hard X-rays. It is also required that the X-ray beam has a uniform wavelength with a high degree of beam parallelism, preferably with high brilliance[1] for successful imaging of the detailed paper structure. All requirements can only be fulfilled by applying hard X-rays from synchrotron sources for 3D imaging.

The basic principle of any tomography technique is taking a large set of images of the beam transmitted through the sample while the sample is rotated to different positions (rotation angle θ) for each image taken. The transmitted image will change during the rotation according to the spatial movement of the constituents of the imaged sample. From the set of the projected images, the sample material can be reconstructed into a digital representation of the imaged sample. The reconstruction is known as a Radon transformation [91], which is a routine operation with any tomography installation, solving the Fourier-like integral best fitting the set of transmitted images [71]. The principle for 3D imaging by X-ray (micro)tomography is illustrated in Figure 4.1.

---

[1] Brilliance is the photon flux density normalized to energy bandwidth and angular source size

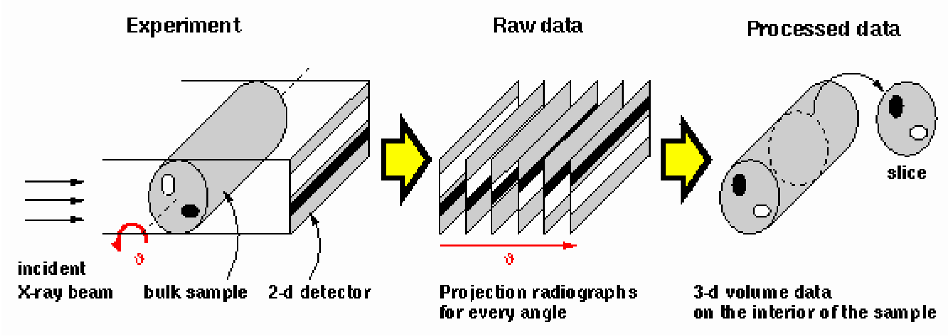

Figure 4.1 Illustration of the basic principles of X-ray (micro)tomoraphy. A projected image is formed from the X-rays transmitting the sample. The set of projection radiographs obtained during a 180 ° rotation of the sample are applied to reconstruct a digital representation of the imaged sample. Figure reproduced from: *http://www.esrf.fr/UsersAndScience/Experiments/Imaging/ID22/Applications/Imaging/TomoBasics*

The contrast in the 3D images can either be a result of different beam absorption or refractive index between the elements in the structure. The former contrast yields absorption contrast, detecting the full solid objects according to variation of local average atomic number. The latter yields phase contrast. Application of near-field coherent imaging yields phase contrast in regions of highly localized change in the refractive index of the sample, such as the borders and interfaces between the sample matrix and inclusions. The contrast is also referred to as outline mode. The near-field phase contrast appears in the form of bright and dark fringes at the position of the interface in the object. The bright fringe faces the side of lesser electron density, the dark fringe that of higher electron density [92]. The difference between the two contrasts for a single parallel X-ray beam is illustrated in Figure 4.2.

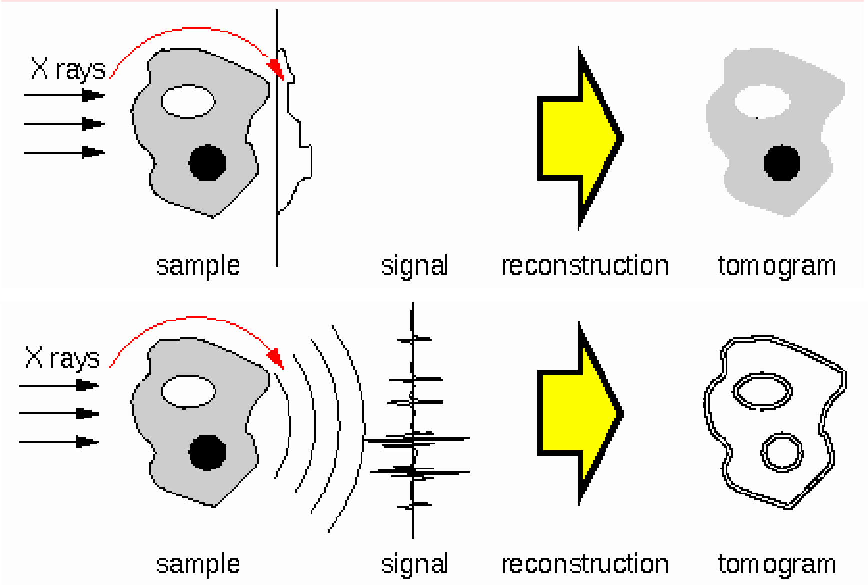

Figure 4.2 **Top**: Absorption mode imaging. The amplitude in the signal is according to the intensity of the transmitted X-ray beam. The resulting reconstructed cross section is according to the averaged attenuation coefficient of the different spatial points in the physical sample. **Bottom**: Near-field phase contrast mode imaging. The amplitude in the signal is according to constructive and destructive interference of the X-ray waves refracted at the phase borders in the sample. The resulting reconstructed cross section is according to the spatial localization of the phase borders in the physical sample. Figure reproduced from: *http://www.esrf.fr/UsersAndScience/Experiments/Imaging/ID22/Applications/Imaging/CoherentImage.*

The dominance of each contrast mode can be adjusted by the distance between the sample and the X-ray detector, for a single parallel beam (Figure 4.3). At zero distance between sample and detector ($z = 0$) there is only absorption contrast. As long as the distance between sample and detector is very small, the absorption contrast is unaltered. However, the amplitude of the phase term increases linearly with the distance z. When the distance become too large between sample and detector, the image of transmitted signals loose the resemblance to the physical sample.

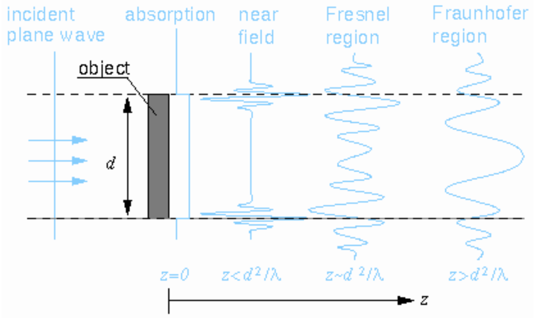

Figure 4.3 The acquired nature of the signal beams from interaction between signal and object is dependent of the distance (z) between object and detector. At zero distance there is only absorption contrast. At long distance between sample and detector transmission images lose the resemblance to the imaged object. The signal dependency of the distance between sample and detector are only valid under the condition of weak or smooth changes in projected phase. Figure reproduced from: *http://www.esrf.fr/UsersAndScience/Experiments/Imaging/ID22/Applications/Imaging/ CoherentImage.*

Not all materials have sufficient X-ray absorption contrast for acquisition of high resolution 3D images in absorption mode. The fibres in paper consist of almost purely organic components and thus have a very weak absorption contrast to the surrounding air. The phase contrast has the advantage of being more sensitive than contrast by absorption, thus enabling 3D imaging of the internal structure of organic materials. The phase contrast mode is thus more readily suitable for paper for acquisition of high resolution 3D images.

Despite the intuitive problems related to the weak absorption contrast between the cellulose fibres and the air, it has been shown to be feasible to acquire 3D images of paper in absorption mode with good contrast between the fibres and air. To achieve sufficient contrast at high resolution, it is necessary that the beam is highly coherent[1]. A long source to sample distance and small dimensions of the X-ray source enable a high coherence. Beam line ID-19 at ESRF is specifically built to achieve high coherence. The distance from source to sample is 145 m and a high-magnetic wiggler (B_{max} = 1.4 T) is used as source. The components of the beam line were designed and manufactured to avoid, as much as possible, spurious images and/or losses of coherence. [93]. The high coherence results in a projected image that is almost purely a result of superimposed amplitudes and phases, thus enabling a signal with almost purely localized phase information for the individual detector points.

The quality of the synchrotron source microtomogaphy imaging is dependent on many factors. Most of these factors will not be considered here, as the detailed physics of X-ray microtomography is outside the scope of this thesis. However, the factors having major influence on the image quality are considered in the following discussion.

---

[1] Coherence is the ability of a wavefield to show interference, requiring the amplitudes of waves to be highly correlated between different points transverse to the direction of propagation. A perfect coherence is only valid for a monochromatic point source.

As shown above, the distance from source to sample is important for the degree of spatial coherence, and the distance from sample to detector is determining whether the phase or absorption signal is dominating. The distance from source to sample is a characteristic of a beam line and cannot be altered. The detector to sample distance can be adjusted to find optimum trade-offs between contrast and resolution. However, the distances are very short, compared to the distance between source and sample. This result in a close to non-existing magnification of the transmitted signal onto the detector. The actual magnification is instead performed between a scintilator screen and the detecting CCD camera. This is a very important part of the synchrotron source X-ray microtomography, and is necessary for obtaining high resolution projection images. The basic principle of the detector is shown in Figure 4.4. The main components are; the scintilator screen that transforms the incoming X-ray intensity distribution to an identical intensity distribution in the visible wavelength range, a microscope to magnify the visible-light image and a CCD camera onto the chip of which the magnified image is projected. The physical pixel size of the CCD camera is obviously locked, thus the effective pixel size of the projected image is determined by the chosen magnifying objectives of the microscope.

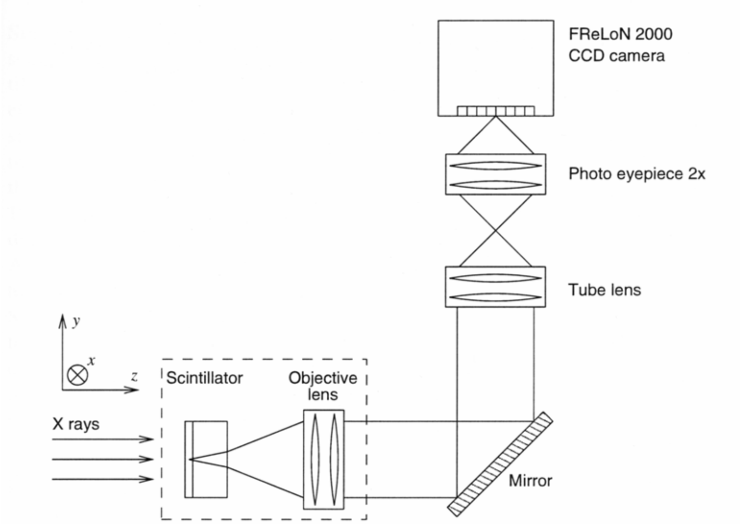

Figure 4.4 An important part of the applied X-ray microtomography set up is the detector. The scintilator transforms the X-ray into visible wavelength range, the microscope lenses and mirrors magnifies and transfers the intensity distribution to a vertically mounted high resolution CCD camera. The applied objectives in the microscope determine the voxel size resolution. Figure reproduced from Weitkamp [92].

4.2.4 Differences between synchrotron and stationary source X-μCT imaging

Although the same main principles are the basis for both synchrotron and stationary source X-μCT, there are also many differences.

The most striking difference is the proportions of the imaging equipment. Synchrotron source imaging requires a storage ring of electrons, which at the applied facility in Grenoble, France, have a circumference of 844 metres. It is the deflection of a high number of high-energy electrons, using strong magnets[1], that generates the desired X-ray radiation. The applied beam lines, ID-22 and ID-19, have a X-ray source to sample distance of respectively 65 and 145 metres. The beam line optics for producing an even, monochromatic beam with high parallelism is between the X-ray source and the experimental hutch. The experimental hutch is a large room, where the rotation stage, sample and detector is located. The hutch have lead walls of up to 30 mm thickness to avoid leak of radiation. The size scale of the synchrotron facility is almost an absurd contrast to the imaged paper volume of less than 1 mm^3. More information about the synchrotron facility and the specific beam lines can be found at http://www.esrf.fr.

The stationary source desk-top microtomography scanners are considerably smaller. As the name indicates, the instrument can be set atop a table. The X-ray source is a microfocus X-ray tube emitting polychromatic radiation. The spot size is small, approx. 5 µm, but the beam does not have the parallelism of synchrotron radiation. On the contrary, the beam has a fan/cone geometry emitted from the small spot of the X-ray tube. The small spot size and fan/cone geometry yields, when the source to sample distance is relatively large, a sufficiently high spatial coherence to enable phase contrast imaging despite the X-ray signal is polychromatic [94].

The distance from sample to detector relative to emitting spot to sample distance determine the magnification. The distance from sample to detector also determine if phase contrast or absorption signal is the predominating, as for synchrotron imaging. The enlarging fan/cone geometry limits the spatial resolution to the spot size of approx. 5 µm. The polychromaticity of the X-ray beam introduce more artificial interference patterns and more spatially distributed[2] phase border contrast in the transmitted signal than for monochromatic synchrotron radiation. The main defects are beam hardening, ring artefacts and so called star artefacts. Most of the signal artefacts are automatically corrected by included software and synchronous precision movement of object and readout area in the camera. However, the lower resolution and weaker phase borders cannot be compensated for. The removal of artefacts will usually not be perfect and will thus be a source of noise in the projected images. The technique have a much lower brilliance than for a synchrotron source, thus a longer acquisition time is needed for sufficient contrasting, although the voxel sizes are considerably larger. More information of the commercial CT scanner can be found at http://www.skyscan.be.

4.2.5 Sample preparation and mounting

A great advantage with the microtomography technique is that it generates consecutive cross-sectional images of the structure by a non-invasive method not needing any additional material for contrast or support. The non-invasive technique avoids the problems

---

[1] The magnets include bending magnets for deflection from straight path, focusing magnets to keep the electron beam small and well-defined and undulators for forcing the electrons to follow an undulating, or wavy, trajectory. The beams of radiation emitted from the different bends overlap and interfere with each other to generate a much more intense beam of radiation than that generated by the bending magnets.

[2] The polychromaticity will result in varying refraction angles for varying photon energies, thus distributing the transmitted shifted signal over a larger area on the detector than for a monochromatic signal. The higher apatial coherence, the smaller spatial distribution.

encountered with structural distortions and variation when preparing consecutive cross sectional samples for SEM or LM. However, the paper samples need to be cut in a fashion that ensures the area of interest in the paper sample do not extend considerably outside the field of view of the detector during the 180° rotation. The limitation in size of the paper samples are more of practical than technical reasons, as it has been shown that it is not required for the region of interest to be in the field of view for all projections [95].

The choice of horizontal axis of rotation put limitations to the width of the sample. The preferred width of the paper sample will depend of the beam cross-sectional profile and the accuracy of the axis of rotation and the alignment of the sample relative to the vertical middle of the beam cross-sectional profile. The alignment is normally good, as the alignment is assisted by a camera mounted exactly above the axis of rotation. The sample mounting for the near-field phase contrast images obtained in this study is shown in Figure 4.5.

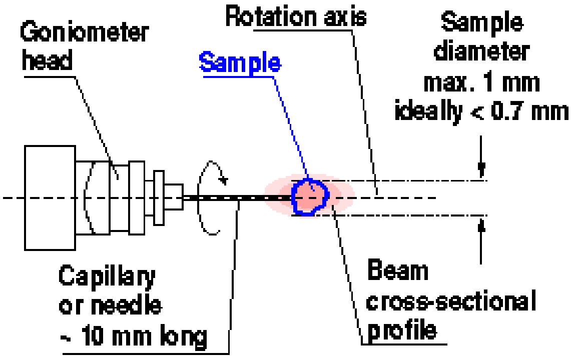

Figure 4.5 A schematic drawing showing the sample mounting for the phase contrast imaging at beam line ID-22, ESRF. The X-ray source is front of the rotation stage, the goniometer head and the detecting CCD camera is right behind the sample that is being rotated during image acquisition. Figure reproduced from: *http://www.esrf.fr/UsersAndScience/Experiments/Imaging/ID22.*

As the sample must be fixed to the rotation stage outside the filed of view, the paper is cut into a relatively long, thin strip, with a scalper or scissors, with the desired width. For the phase contrast imaging at the ID-22 beam line at the ESRF, the ideal width was approximately 0.7 mm. To support the strips of paper, having a large length to width ratio and a low bending stiffness, the samples was thread into a capillary fixed to the rotation stage to improve the alignment. The tip of the paper strip extends longer than the capillary to avoid introducing a material with a considerably higher refractive index in the X-ray beam. The imaged area was chosen in a region located a bit away from the absolute tip to maximize the size of the sampled volume and avoid including cutting defects at this volume edge. The cutting defects along the edge of the strip must necessarily be included in the imaged volume.

The principles for mounting the paper samples also render it possible to image paper strips thread into thin capillaries. As the refractive index between fibres and water is sufficiently large to yield detectable phase contrast between fibres and water [71], sealed capillaries can be applied for obtaining images of soaked paper samples. The principles for preparing capillaries with soaked paper samples are described in the materials and methods in Paper III.

The principles applied for sample preparation and mounting for the horizontal axis of rotation could in principle be applied also for the vertical axis of rotation. However, it is also possible to align the paper sample perpendicular to the vertical axis of rotation. The perpendicular alignment ensures that the paper will never extend outside the beam cross-sectional area in the vertical direction, as the thickness of most paper samples are considerably smaller. The width and length of the paper sample can thus be freely chosen, as it is of no importance for the reconstruction how far the paper sample extends outside the X-ray beam in the horizontal direction. The cutting defects can thus possibly be excluded from the imaged volume. However, it is beneficial to keep the width and length of the paper sample within reasonable scales, as it saves time for alignment of the rotational axis.

The cutting of the paper samples for the vertical mounting can be done with a scalper or with small, sharp scissors. It is also possible to perforate the sheets and obtain small circular samples of the desired diameter with appropriately small cutting tools. The 3D images obtained by absorption mode at ID-19 (ESRF) in this study was acquired from paper samples prepared by the small circular cutting tools.

The sample mounting is done by gluing the small paper sample horizontally on top of a appropriate sized capillary applying a melt glue, as shown in Figure 4.6. The capillary is then mounted vertically in a metal holder which fixes the position and alignment of the capillary. The metal holder is put in a groove with a tight fit in the centre of the rotation stage prior to image acquisition. The rotation stage, sample holder, capillary and sample, as aligned at the beam line ID-19 is shown in Figure 4.7. Application of standard sized capillaries and metal holders, and a standardized way to fix the capillaries in the metal holders, render it possible to apply a robot for the transition of the metal holders with the mounted sample to the groove in the rotation stage. The robot approach saves considerable time for sample mounting and alignment.

The commercial CT scanner has a sample holder that rotates around the vertical axis. The sample is mounted on glue atop the small, flat ‘table’ of the sample holder. The paper sample is normally attached in a manner that yields a vertical alignment of the area of interest of paper sample relative to the incoming X-ray beam. The sample holder is kept outside the field of view or is removed as a part of the image reconstruction.

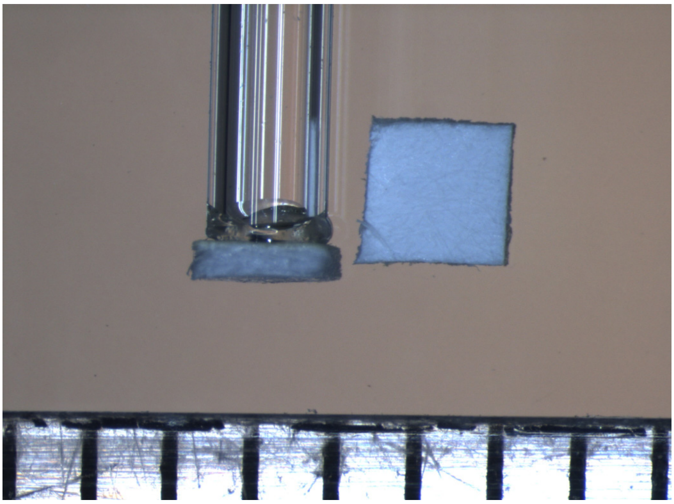

Figure 4.6 Mounting of the paper samples for the vertical rotation axis applied for absorption mode 3D images in this study. The paper sample (thick board) have been cut with small, sharp scissors, and not "perforated" as for the samples used in this thesis. The cut paper sample is glued to the top of the capillary with a special melt glue. The capillary is dipped in the hot melt glue and the wetted end is glued to the cut paper sample. The scale of the ruler in the bottom of the picture is 0.5 mm.

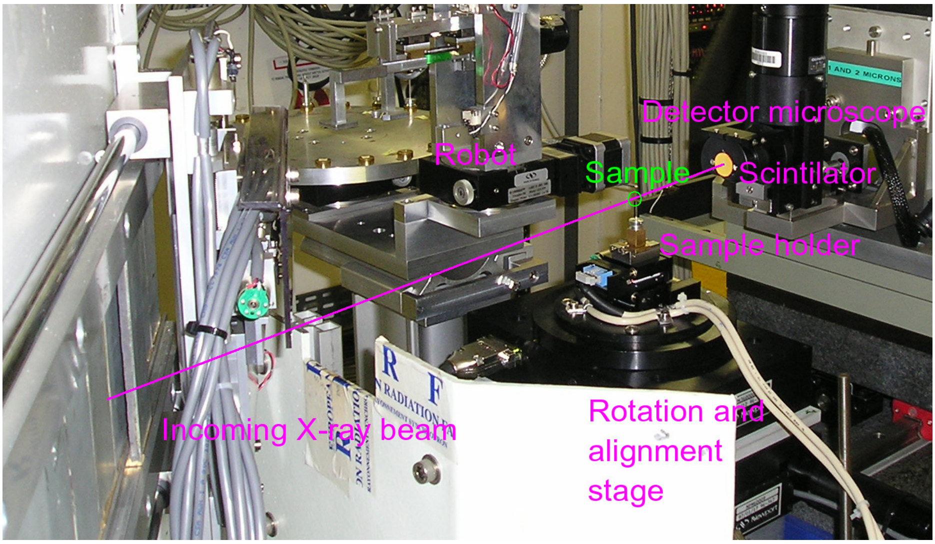

Figure 4.7 An image showing the sample mounting for the vertical axis of rotation, as done at ID-19, ESRF. The sample is aligned by movement of the rotation and alignment stage after the sample holder is placed in the groove. The path of the X-ray beam is indicated by the magenta line.

Image acquisition for synchrotron source phase contrast X-ray microtomography
The phase contrast mode images of the selected paper grades were acquired at beam line ID-22 at the European Synchrotron Radiation Facility (ESRF) in Grenoble, France. The applied photon energy was 20 keV, as this was a reasonable compromise between contrast and resolution. The image acquisition had 1251 rotation stages, with an image acquisition time of 1 second per rotation stage. The tomographic scan included also two flatfield image blocks of 10 images taken before and after the 180° rotation. Additionally were 10 dark images acquired without X-ray beam. The three 10 image blocks are needed for a successful Radon transformation of the transmitted images into cross-sectional images. The applied detector was a FReLoN CCD camera with 2048x2048 pixels. The option of binning the pixels of the CCD camera was not applied. The applied distance between sample and detector was 5.5 to 9.5 mm. The applied objective in the detector microscope resulted in reconstructed volumes with a voxel size of approximately 0.35 µm. The determined spatial resolution, limited by the X-ray scattering in the scintilator screen, is approximately 1 µm [92]. The maximum size for imaged volume is (0.7 x 0.7 x paper thickness) mm^3. However, the applicable volume size is considerably smaller, as the sample, including cutting artefacts along its edges, had to be within the field of view during the full rotation. The imaged volume sizes after discarding the distorted areas are as shown in Table 2 in Paper IV. An example of transmitted phase contrast signal image, sinogram in Fourier plane and reconstructed cross section for the imaged BSKP handsheet sample is shown in Figure 4.8.

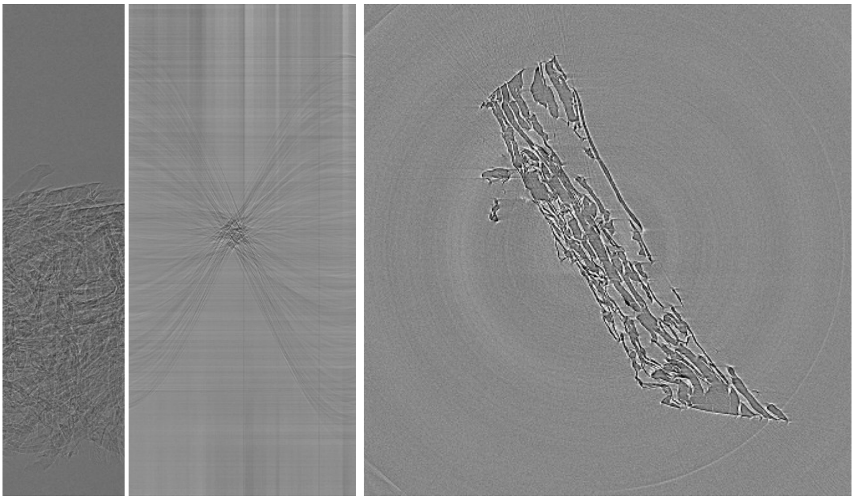

Figure 4.8 Images of BSKP handsheet from near-field phase contrast imaging. **Left**: One of the transmitted images, as obtained by the CCD camera. **Middle**: One of the flat- and black-filed corrected sinograms. **Right**: One of the reconstructed cross sectional images. The shown area of the image is 1568x1584 pixels, which is cropped from the original 2048x2048 cross section. The pixel size is 0.35 µm

Image acquisition for synchrotron source absorption mode X-ray microtomography
The absorption mode images of a newsprint-like paper grade were acquired at beam line ID-19 at the European Synchrotron Radiation Facility (ESRF) in Grenoble, France. The

applied photon energy was 18 keV. The image acquisition had 1201 projections during 180° rotation with an exposure time of 1 s per image. The procedure for image acquisition included blocks of flat and black field images according to the same procedure as for the phase contrast imaging. The detector was a CCD camera with the same properties as for the phase contrast imaging described above. The applied distance between sample and detector was 1 mm, which yields contributions of near-filed phase contrast. The chosen objective and CCD camera resulted in a voxel size of 0.7 µm. The spatial resolution is determined to approximately 2 µm. The maximum size of the imaged samples would be (π x $(1.4/2)^2$ x paper thickness) mm^3, as the resulting reconstructed volume is cylindrical due to the applied sample mounting and rotation. As working with cylindrical digital volumes poses practical problems, the true maximum size is approximately (1 x 1 x paper thickness) mm^3. The largest possible practical volume size is approximately the same, as the edges of the maximum square in the circular cross-sectional area will only touch the sample edge in the corners as long as the sampled volume is perfectly centred relative to the axis of rotation. A typical reconstructed cross-sectional image from the absorption mode 3D imaging is shown in the first row of Figure 4.9. The reconstructed digital paper volumes have a 32-bit float format. However this has to be reduced to a 8-bit integer format to enable transport of the data sets out from ESRF. The compression of the greyscale distribution is done simultaneously as a histogram equalisation, so as to not include greyscales of little value in the 256 levels available in the 8-bit data.

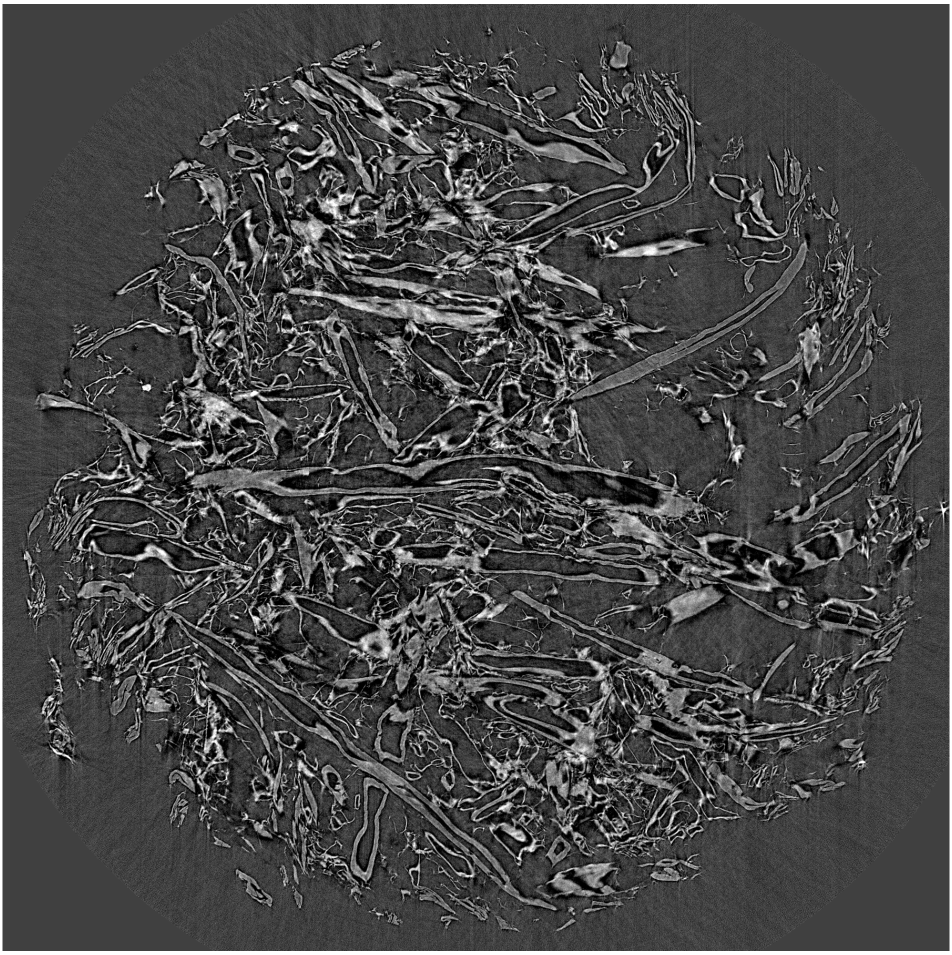

Figure 4.9 An example of a cross-sectional image as obtained by the applied absorption mode X-ray microtomography imaging. The sample is one of the uncalendered newsprint-like paper samples made on a pilot paper machine. The size of the image is 2048x2048 pixels and the pixel size is 0.7 μm.

Image acquisition for stationary source X-ray microtomography applying a commercial scanner

The low resolution 3D images of the selected paper grades were acquired applying a commercial desk-top microtomography system from SkyScan. The system has a stationary polychromatic X-ray source (microfocus sealed X-ray tube with a spot size smaller than 5 μm and beam energy that can be adjusted between 20-100 kV). The commercial scanner was of the model SkyScan-1072 [96]. The acquired images from the SkyScan scanner contain solid objects with no clear phase boundaries, which indicates that absorption mode is the predominant contrasting effect.

The voxel size is 2 μm and the spatial resolution is approximately 5 μm at the applied magnification. The detecting CCD camera have 1024x1024 pixels, at maximum covering a sample of approximately (2 x 2 x thickness of sample) mm^3 sample volume. A typical reconstructed cross-sectional image from the commercial desk-top microtomography system is shown in Figure 4.10

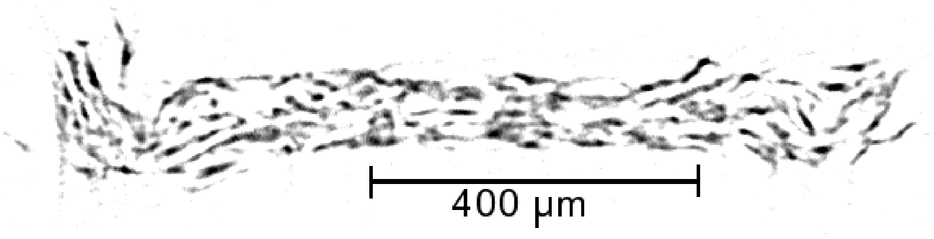

Figure 4.10 An example of a reconstructed cross-sectional image of the BSKP handsheet sample as obtained by the desk-top commercial CT scanner.

4.2.6 Image filtering and binarisation

The images obtained from microtomography are by nature similar to cross sectional images from SEM-BEI, in that they are in greyscale and do not have a perfect phase separation even for the best quality images. It is thus necessary to perform filtering to remove noise and improve phase separation. It is also necessary to binarise the images to enable image analysis of the digital structures. The images from near-field phase contrast imaging have an additional challenge for filtering and segmentation, as only the phase borders are detected. The fibre walls must therefore be assigned to the solid phase based on some other criteria than the local greytone in the images.

Phase contrast images from synchrotron radiation source

The principles for segmentation of the phase contrast images are described in detail in Antoine et al. [97]. The segmentation routine of the edge-enhanced tomographic slices consists of a series of steps involving smoothing in directions of the slowly-changing[1] structure, region growing from manual set seed points[2] and local adaptive thresholding. The different steps of the binarisation procedure and a resulting binary structures are shown in Figure 4.11.

---

[1] Slow change due to the fibres high length to width ratio.

[2] The phase is intuitively known for many regions as the dark and white side of the interference pattern coincides with the refractive index.

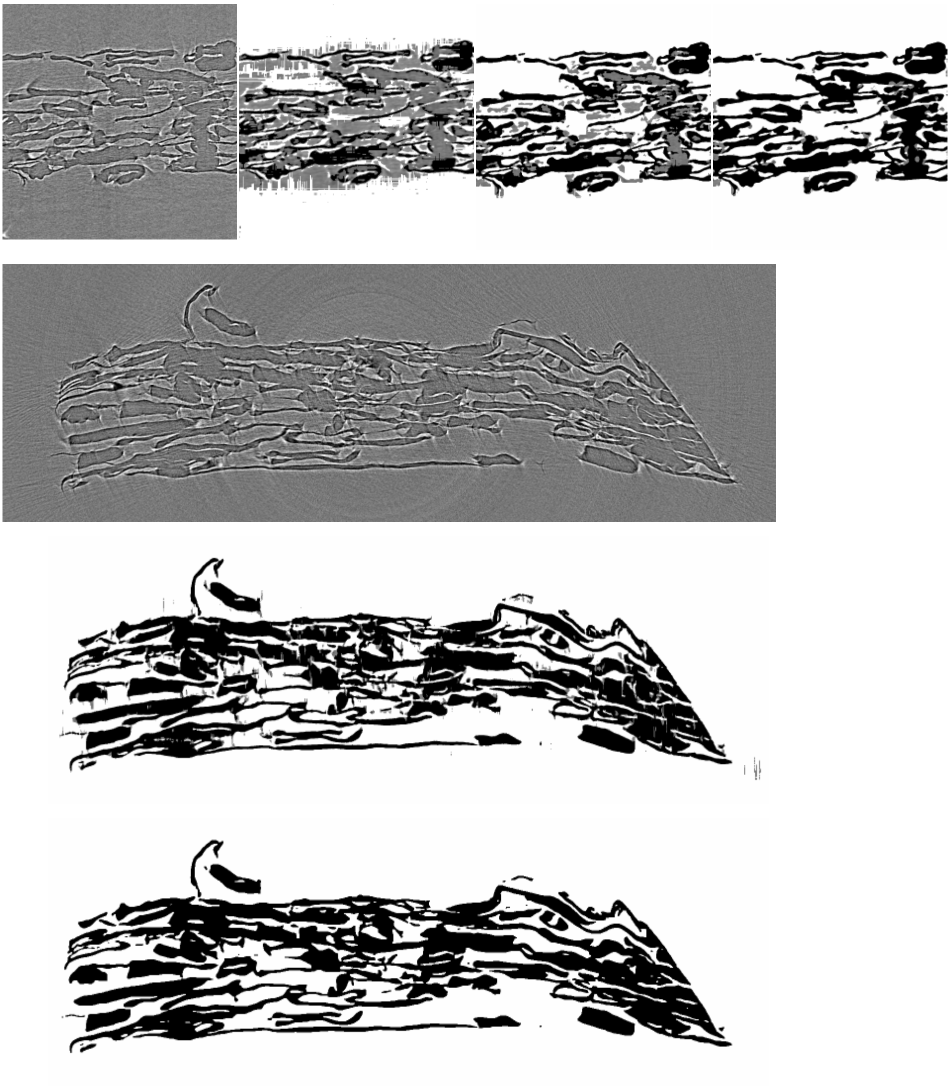

Figure 4.11 An illustration of the segmentation procedure for near-field phase contrast images. **First row**, **first column:** Original reconstructed cross-section. **Second column:** Partial binarisation after spreading from manually set seed points. Normally 15 seed point were placed in fibres and 10 in pores. **Third column**: Partial binarisation after a median filtering and local thresholding process. **Fourth column**: Binary image after utilizing the information from the phase shifts at the phase borders. **Second row**: A reconstructed cross-sectional image in the perpendicular direction relative to the images in first row. **Third row**: The cross section after reslicing the volume after as complete partial filtering in the perpendicular direction as possible. **Fourth row**: The resulting binary structure after smoothing and removal of small isolated areas and volumes. Most of the removed areas were thin lines.

Absorption mode images from synchrotron radiation source

The principles for binarisation of the absorption mode images are a sequence of prefiltering of the greyscale images, a global thresholding and finally a method for removal of the capillary and glue, attaching the paper sample firmly to the capillary during the rotation, from the cross-sectional images. The removal of glue and capillary is a necessity for obtaining a binary structure applicable for rational assessment of the structure properties. However, the separation between glue and fibres showed to be very difficult, because there was almost totally overlapping greytones for the two phases. The penetration of glue into the paper structure and subsequent removal of the glue from the reconstructed 3D images will thus affect the fibre network.

The first step of the segmentation of the absorption mode images was a detection of the preferred fibre orientation in the circular sheet plane cross sections. The cutting into a circular paper sample and subsequent gluing to the top of a circular capillary makes it impossible to keep track of the machine direction in the preparations before image acquisition. The preferred fibre orientation was found by detection of the fibre edges applying sobel operators [21]. The images were then rotated accordingly to align the fibres in the vertical direction of the cross-sectional images. Subsequently the 3D data set was cropped into the largest square fitting in the circular area. Then the cropped volume was resliced into CD orientated cross sections. A smoothing of the greyscale images were done by averaging all slices with the neighbouring slices right before and right after in sequence. The orientation of the volume in the machine direction results in small change of the structure in the small step of 0.7 µm between the consecutive cross-sectional images. The smoothing removed much of the small-scale noise, but made the greyscale transition over phase borders slightly more washed out.

The structure was then binarised by a global threshold according to the optimum between preservation of the fibre cross-sectional areas and introduction of many small solid elements, which are surely noise from the phase overlap.

The capillary and glue was removed by a watershed routine growing from the lower edge of the CD orientated cross sections. The watershed was done in several steps to remove both the capillary and glue while attempting to preserve the fibre phase as well as possible. The approach succeeded in removing the capillary completely, but the glue segmentation was moderately successful. The non-complete segmentation left small areas of glue in the structure and resulted in some fibre material being removed. The glue segmentation was worst for the calendered paper samples. Despite the encountered problems in glue segmentation, the method was considered to be the best possible approach as long as the segmentation was done on a PC, which render it difficult to exploit the three-dimensional extension of the fibres.

The different steps of the segmentation routine for the absorption mode 3D images are illustrated in Figure 4.12 and 4.13.

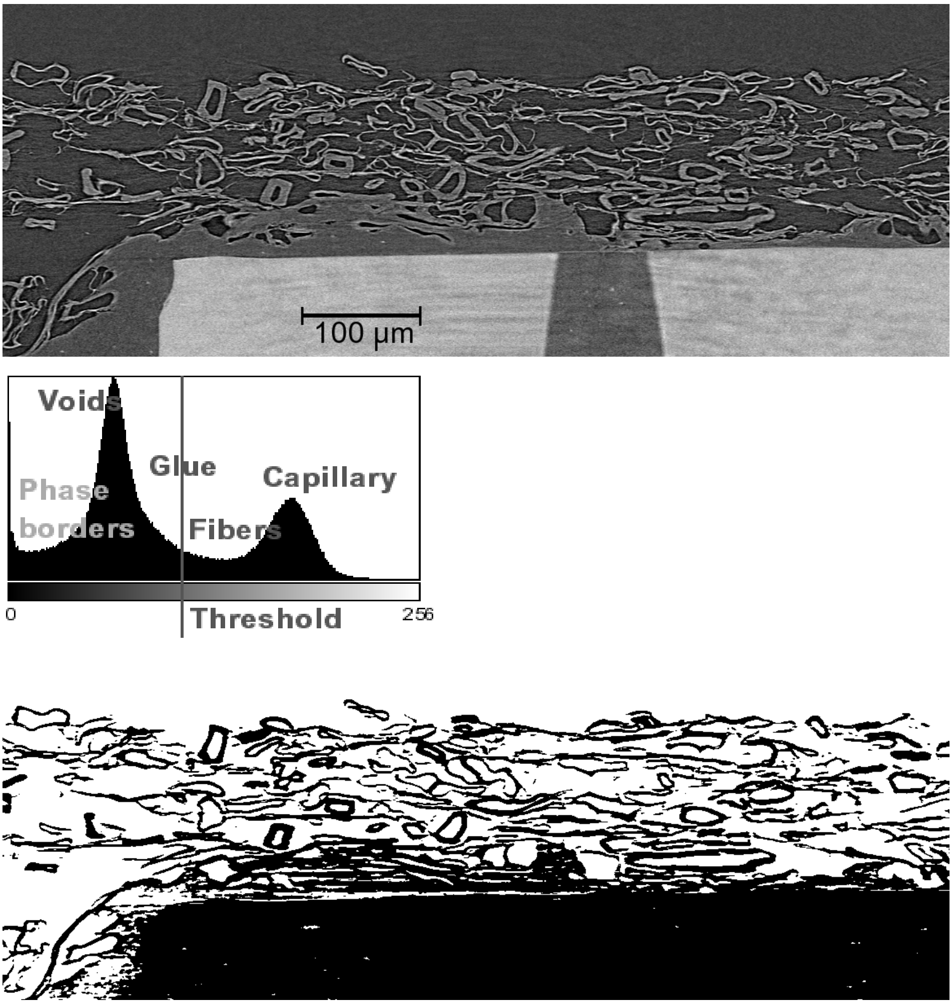

Figure 4.12 Illustration of the initial smoothing and thresholding in the segmentation of absorption mode 3D images. **Top:** A typical reconstructed cross-sectional image of a non-calendered newsprint-like paper grade (s4) after being orientated in the machine direction, cropped within the circular sample area in the sheet plane and resliced in cross direction. The continuous light gray areas are the capillary, the continuous medium gray phase between capillary and paper sample is the glue. **Middle**: The greyscale histogram for the cross section with the applied threshold for the full 3D volume marked with the vertical line. The phase classification is only indicative. The histogram do not change significantly after smoothing, but makes the local distribution of greyscales more uniform, thus reducing small-scaled noise. The indicated phase borders are the dark vicinity that is found around many fibres due to the phase contrast. **Bottom**: The resulting binary image after smoothing and global thresholding. The capillary and a fraction of the glue is included in the fibre phase.

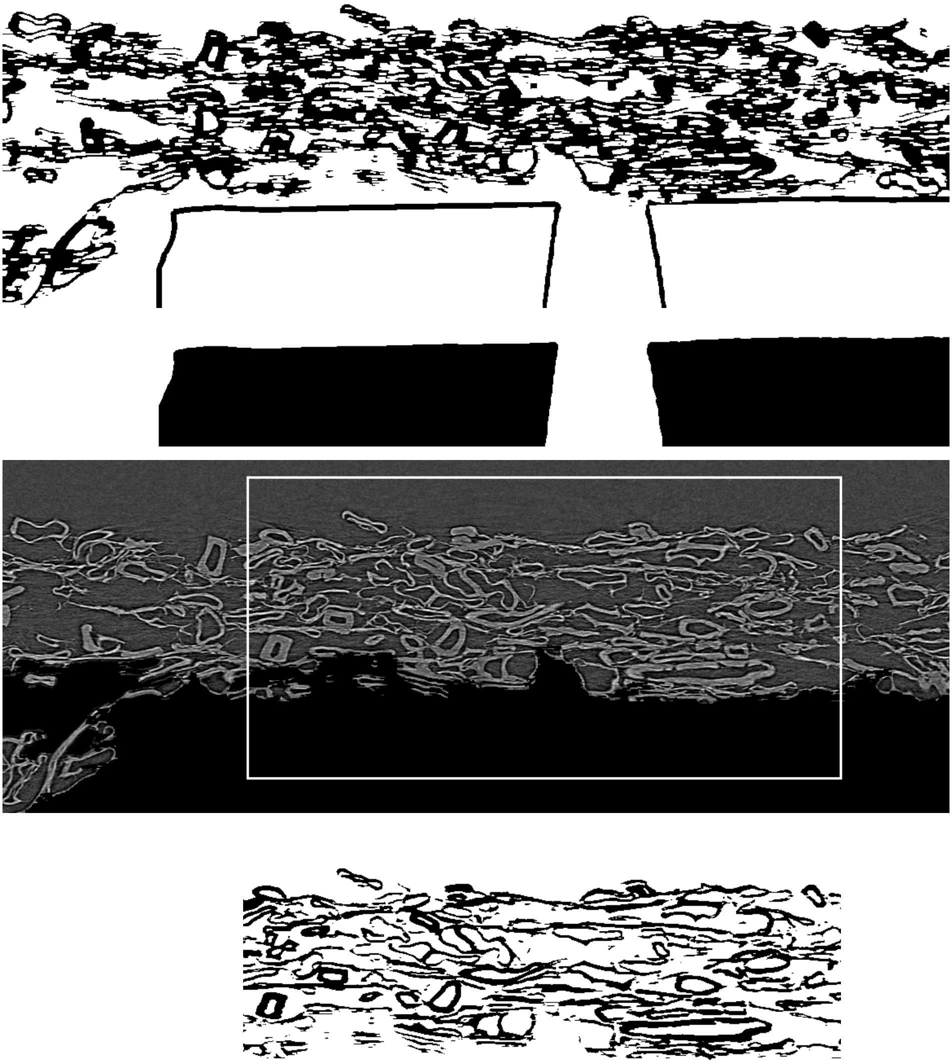

Figure 4.13 Illustration of the method for removing capillary and glue from the fibre structure. **First row**: Sobel lines, applying strong horizontal kernels, are determined for limiting the watershed of the glue region. **Second row**: Watershed of the capillary walls. The region is delimited by the localized transition from light to dark greyscales and applied distance transform. **Third row**: The region that will be removed from watershed of the glue phase region limited by the sobel lines and the watershed of the capillary regions. **Fourth row**: The resulting binary images after removal of glue and capillary and cropping a tetragonal subvolume within the sample volume that is not affected by structural defects, as *e.g.* the delamination in the left edge of the uncropped cross section.

Images from commercial table-top CT scanner (stationary source)

The segmentation of the 3D images from the table-top microtomogaphy instrument was done according to the principles presented in Huang et al. [77] and Goel [82]. The segmentation is done in a single step by a global threshold for the full volume. The approach seems to be relatively successful for the segmentation between fibres and pores. The segmentation results in many small noisy areas, especially in the vicinity of the structure, for the obtained 3D images. These areas are however removed by the subsequent 3D filtering. The quality of the binarised structures are shown in Figure 1 and 2 in the attached Paper IV. More details regarding the quality of the images and subsequent segmentation is well described in Huang et al. [77].

Filtering of binarised 3D images

Before any image analysis routines or simulations are performed on the binary 3D paper structures, noisy elements were removed. The same binary filtering was done for all 3D images obtained in this study, regardless of applied image acquisition procedure. The 3D filtering is based on an object volume criteria. A volume criteria is well suited as almost all material in the solid network are interconnected and have a relatively large size, whereas the noise is small sized and is not interconnected, but randomly distributed. A good trade-off between preservation of structural features and removal of noisy elements was found to be a noise-criterion threshold of 216 μm^3. This volume threshold was applied for all voxel resolutions, yielding the following size criteria in number of voxels:

- Synchrotron phase contrast (0.35 µm): 5038 voxels
- Synchrotron absorption (0.7 µm): 630 voxels
- Stationary source absorption (2 µm): 27 voxels

The same size criteria can be applied for the void phase. However, although it is physically impossible to find isolated solid objects ‘floating’ in void phase and thus remove such occurrences accordingly, the criteria is not physically valid for the void regions. Closed void regions can be found inside solid elements and between them. The void regions will contribute to a lower density in physical samples, but they will not contribute to transport of air and liquids in the structure. It is thus a question of application whether the small void regions should be removed. As the closed void regions will not contribute to transport, and it is uncertain whether closed void regions smaller than the applied threshold are noise or physical, the void regions smaller than 216 μm^3 were removed for all digital volumes in this study.

The implementation of the filtering technique is based on a region growing from the edges, which detects all interconnected objects. The regions that are not interconnected are removed according to the set volume threshold. Objects touching the edges are not preserved, although the chance of removing physical correct regions are larger for these regions. The applied filtering technique include an option to preserve edge objects if this is considered desirable.

The number of removed objects was relatively small for the images with sub-micrometer voxel sizes, thus not influencing the volumes significantly. The filtering was a necessity for the low-resolution images. Without filtering there would be many small noisy objects, especially in the vicinity of the paper structure.

Defining the paper surface by applying a rolling ball algorithm

To define the volume extension of the paper in the thickness direction for 3D images, is at least as difficult as determining the extension of the paper structure for cross-sectional images. Although it is problematic, it is a necessity for determining some structural properties correctly. Properties like *e.g.* porosity and hydraulic pore radius depend strongly on the surface definition.

The extension problem can be avoided by excluding the surface area from the analysed volumes. The exclusion approach has been applied for bulk, internal structure characterization in the published work from University of Minnesota [*e.g.* 76,77,82]. This can be reasonable for characterisation of the analysed thick board-like handsheets, as the surface area is only a small fraction of the structure, but for most paper qualities the approach will be unacceptable. For most paper grades the surface area is of great importance for some performance qualities.

It is possible to determine the surface as the outermost voxel in all positions in the surface seen from a vertical perspective, but as for the cross-sectional images, this will yield a low estimate for porosity. The surface definition problem is very similar to that discussed for cross-sectional images. It is thus not unexpectedly possible to solve the problem applying the same principle, only transferred into three-dimensional space. The application of the rolling ball algorithm have been successfully applied to the analysed digital paper volumes analysed by Svennson and Aronsson [26]. Although this paper volume was obtained by SEM imaging of consecutive cross sections, the principles for the applied method is directly transferable to the 3D images obtained by microtomography.

The implementation of the rolling ball algorithm was not done by application of distance transforms, as in Aronsson [17], but implemented as a development of the rolling ball algorithm for cross section into three dimensions. The cubic voxels in the microtomography volumes makes it straightforward to determine a mask with the shape of a half sphere/ball. The mask is moved along the surfaces of the paper in a similar fashion to the way a ball would roll over the details in the surface. The voids not covered by the rolling ball are assigned to be part of the paper structure. The size of the rolling ball will determine how small ‘holes’ the ball will notice in the surface structure. The approach with traversing the surface with the sphere mask will result in a few discontinuities in the surface definition for rough paper samples. The applied rolling ball radius of 15 μm results in few such discontinuities even for the paper grades having the roughest surfaces in this study. The method was therefore considered to yield a reasonable surface definition. Visual inspection of the cross-sectional images and 3D volumes confirms this. A visualization of a 3D paper structure delimited by the rolling ball procedure is shown in Figure 4.14.

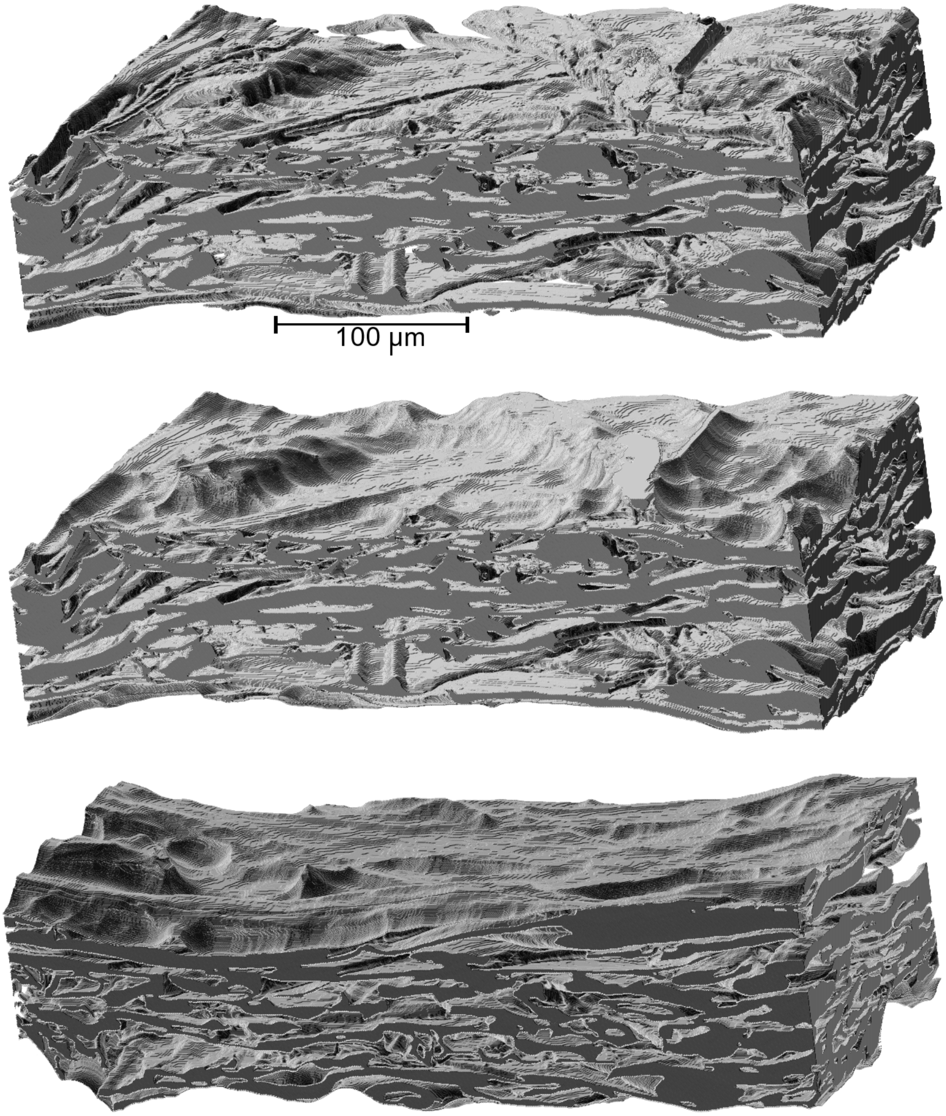

Figure 4.14 Visualization of the surfaces as determined by the rolling ball algorithm for the BSKP handsheet sample. **Top**: 3D visualization of the digital paper structure before surface definition. **Middle**: The top side surface as defined by the rolling ball algorithm applying a sphere radius of 15 μm. **Bottom**: The wire side surface defined as for the top side. The angle of view is totally opposite of that for the upper side.

4.2.7 Visualization of the digital paper volumes

An important feature of the 3D images is that it allows us to have a direct view of the three-dimensional extension of the fibre network and details of the paper structure. Browsing through the structure following the consecutive cross sections, sliced in the different principal planes, will yield some limited 3D information. However, to fully exploit the 3D information by visual comprehension, it is necessary to produce a volume rendering to get a true 3D visualization. A 3D visualization will perform a surface rendering of the objects and/or calculate the shadow effects when incident artificial light is reflected in the digital structure. There exist many software program for performing such 3D visualizations today.

In this study we have applied the public domain program *ImageJ*, using an interfaced freeware volume renderer called *VolumeJ* [98], developed by Michael Abràmoff. The volume rendering have been applied to visualize the obtained 3D structures to evaluate the quality of the binarised structures and to gain knowledge of the 3D extension of the paper structure and selected details.

The obtained 3D visualizations applying the VolumeJ plug-in is voxel based and relatively crude. By applying a surface rendering, applying the marching cube principle, the quality of the high resolution data sets are given more justice. However, the surface rendering of the large data sets is a very computationally demanding application. The high number of voxels and many detailed features made it impossible to perform the surface rendering for a full volume applying PCs. However, surface rendering of parts of the structure could be achieved. A visualization of the lower half of the BSKP handsheet volume is shown in Figure 4.15.

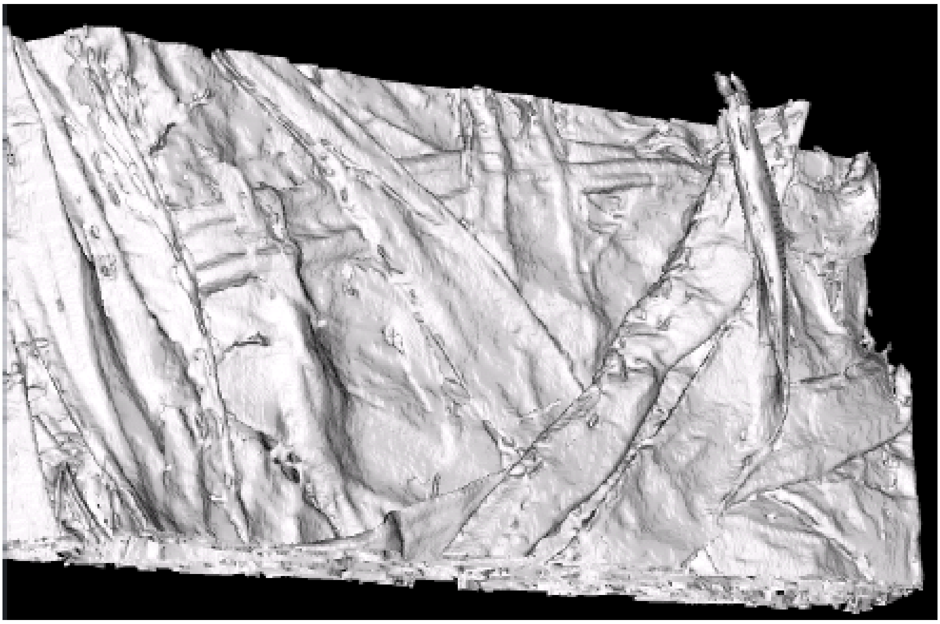

Figure 4.15 A surface rendering of the wire side surface of the BSKP handsheet volume

The surface rendering makes it possible to investigate details of the structure with a smooth surface. A detail of the top side surface of the BSKP handsheet is shown in Figure 4.16.

Figure 4.16 Detail of the top side surface of the BSKP handsheet volume showing a collapsed fibre with a pronounced kink. Other elements include a loosely bonded fibre in the back, left corner and a straight fiber in the front, left corner.

4.2.8 Image analysis and simulation routines for assessment of 3D images of paper

Background - 3D image analysis and simulation routines for porous materials

Paper is a difficult material to acquire well resolved 3D images for. The contrast between fibres and air is extremely low and the needed resolution for observing features that clearly influences the paper properties are extremely high. 3D image acquisition is easier to accomplish for porous materials where the constituents either show larger differences in material densities or a lower detail level is needed for measuring the structural details of interest. The more straightforward image acquisition and higher potential for economical benefits have been the driving force for an earlier application of 3D techniques to other materials than for the application to paper. The 3D imaging and analysis have been most extensively applied for medical imaging and investigation of the porous structure of sedimentary rocks found in oil reservoirs. Much can be learnt from practise of 3D image acquisition and analysis of other materials, where porous materials are of special interest because of the close similarities to paper properties and scientific challenges.

The application of 3D imaging in medicine is nowadays applied as a standard routine in well equipped hospitals (CAT-scan) for detecting *e.g.* cancerous tumours in human tissue. The routine have become a standard routine through prolonged focused research and development of routines for fast and automated reconstruction of the tomographic transmitted images.

Other applications of 3D imaging and structural analysis for porous materials include cement, soil, volcanic rocks, bone tissue, particle beds, cracks in metals and metallic foams. However, the main progress in assessment and simulation of 3D structures have been performed on porous rocks. The investigation of the porous structure of rocks have been extensive, as knowledge of the detailed porous structure and how this affects the transport properties can be applied for enhancing the recovery percentage of oil reservoirs. The ultimate goal of the assessment of sedimentary rocks have been development of simulation routines for multi-phase flow. Most of the image analysis routines presented in the following sections have their origins from assessment of porous rocks.

Measurements of the 3D paper structure characteristics

Paper is a material that have many distinct differences from most other porous structures. The main differences is that it is a man-made non-woven material made from relatively small, natural fibres from trees and other plants, which show large deviation in geometries. Commercial paper products usually have a very distinct anisotropy. Additionally the fibres themselves are a porous building block consisting of smaller fibrils. Most of the pores inside the fibres are usually in a size order smaller than what is detectable by microtomogaphy. For most practical assessments the fibre wall porosity may be of little or no significance, but it might be detected by methods for determination of pore size distributions in physical paper samples, as *e.g.* porosimetry.

The fibres consists of the chemical building blocks, lignin, hemicellulose and cellulose. The cellulose and hemicellulose are chains of polysaccharides with a strong affinity to water. The hydrophilic nature is a requirement for papermaking. However, the contact with water for dry paper weakens the fibre to fibre bonds, make fibres swell considerably and become straighter and can make collapsed fibres recover their cylindrical shape. The properties of paper are thus dependent of the relative humidity of the surroundings. Due to the fibres' strong affinity to water and their changing shape and properties relative to water content, will determination of the correct transport properties of liquid water and water vapour in the digital 3D paper structures be extremely difficult. The transport properties considered here are thus not correct for water transport, unless it is assumed that the fibre network do not change considerably and all transport of significance is in the porous phase.

An overview of the potential for application of 3D digital paper structures to acquire knowledge of the detailed paper structure characteristics and how they influence bulk paper properties are given in Paper II. The following image analysis routines will look further into the details of how structural features can be extracted from 3D images of paper samples.

Porosity, specific surface area and mean pore size

Porosity and specific surface area are more or less standardised structure parameters for porous materials. Porosity, or more precisely void fraction, is the relative amount of white voxels to the total amount of voxels in the structure. For paper, which have a finite, relatively short extension in the thickness direction and a relatively rough surface, the correct porosity can be a non-trivial parameter. This is due to the fundamental problem of defining the surface of the paper volume. This might be solved by applying the rolling ball algorithm for delimiting the paper structure from the background. The porosity will be dependent on the applied rolling ball radius. The larger rolling ball radius, the higher surface porosity, and thus higher porosity for the whole structure.

The specific surface area can be determined relative to the volume of the sample, the volume of solid materials or weight of solid materials. The surface area relative to the volume of the sample is in many scientific applications referred as the surface to volume ratio (S/V).

The surface area can be determined by two principles, by a direct count of the faces common to both a void and a solid voxel or applying an algorithm which decomposes the lat-

tice into vertices, and then evaluates the vertice configurations.
The vertice algorithm leads to slightly different results on the boundary, since each vertice in 3D consists of 8 voxels, however, the boundary voxels (edges, faces, corners) are carrying a lower weight in the estimation. The result of the vertice algorithm is given as Minkowski functionals. Specific surface relative to sample volume is given by 6 times the first Minkowski functional [99].

The digitising of features into cubic voxels ‘staircases’ the solid/void interface, the direct count will thus be a upper bound on the specific surface area. It is possible to compensate for the discretization for regular shapes, transferring the digital surface area to a continuum value by multiplication by a correction factor. However, the highly irregular shape of the fibres, having an alignment with the coordinate system makes such an estimation highly ambitious, as it would require hours of computing for a normal digital 3D paper structure volume. It is important to notice that the digital surface area will increase with higher resolution, as more details will be detectable.

Assuming cylindrical pores, a mean pore size can be estimated from the ratio:

$$r_{\mathrm{V/S}} = 3 \times V_p / S \qquad (4.1)$$

where V_p is the pore volume and S is the surface area of the fibres in the assessed paper volume. However, the pores in the paper are known to be far from cylindrical. The measure will as such only yield indicative results.

Thickness, density and basis weight
Thickness, density and basis weight are determined for successive cross sections as described for the methods in Chapter 2.

Pore chord measurements
A method for assessing information of the geometry of the void phase is by measurement of the pore chords in the structure. The principles for measuring the vertical pore chords, the pore heights, are described in the material and methods section of Chapter 2. The principles for measuring pore chords in other spatial direction are described in Chapter 3. From measurements of the pore chords for the three principal directions in the digital paper volumes, the structural anisotropy can be quantified. The stereology principles applied in the equivalent pore concept [36,51] have shown that a warped surface constructed form the mean pore chords for different spatial directions conforms to an ellipsoidal shape for all paper grades. More details of application of pore chords measurements for assessing pore geometries are given in Chapter 3.

Hydraulic pore radius
The pore chord measurements yield essentially information about the local 1D extension of the pores. The determination of the extension of the pores in 2D is a measure of cross-sectional pore areas. However, for all paper qualities, except high density grades, the

pores are highly interconnected in the cross sections. A delimitation of the cross-sectional pore area by determination of 2D pore necks is not desirable, as many pores delimited in 2D space might be connected in previous or subsequent cross sections. It is therefore desirable to perform a direct measure of the interconnected pore areas in the cross sections. Without performing any further delimitation of the pore space than the limited size of the volumes and the defined surface, the cross-sectional pore area is divided into individual pores only limited by solid material, image edges and the defined surface. The pore areas can contain totally enclosed fibre areas. A typical cross-section from a 3D image set is shown in Figure 4.17, where examples of individual pores within the cross-sectional area are highlighted.

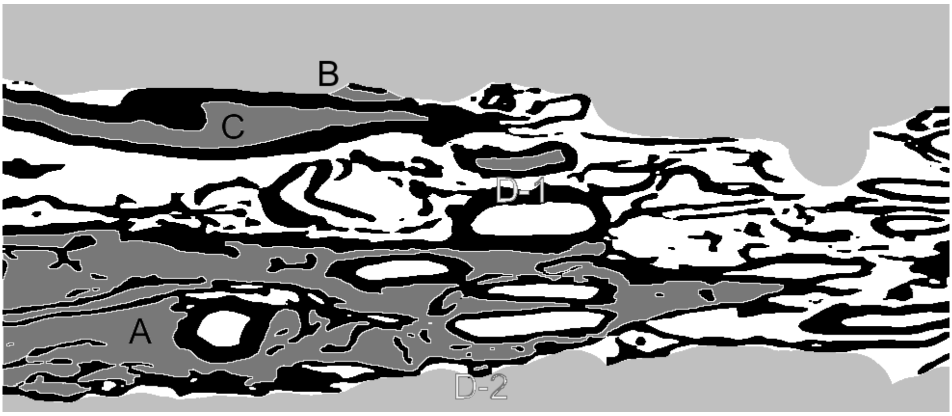

Figure 4.17 Illustration of pore areas with different characteristics in a typical cross section in the newsprint sample. Pore area A is large and branching limited by solid elements, image edge and defined sheet surface. Surface pore area B is limited by solid elements and the defined surface. Image edge pore area C is limited by solid elements and the image edge. Enclosed pore areas D-1 and D-2 is limited only by solid elements.

It is clear that a large fraction of the pore cross-sectional area is part of large, interconnected pore areas. It is thus not especially useful to determine a pore area distribution. Instead it is preferable to apply the hydraulic pore radius, yielding the equivalent radius of the pore cross-sectional area. The hydraulic radius is defined as the ratio between pore area and the perimeter of the continuous pore area (or the ratio of volume to area). The application of the hydraulic radius will yield a relatively high hydraulic radius for large areas with a simple shape. The large interconnected, branching pores will have a relatively low hydraulic radius, as their pore perimeter will be long compared to their area extension. Enclosed fibre areas will contribute additionally to a longer pore perimeter. The hydraulic radius will thus yield a sort of average radius for the constituents of the large branched and interconnected pore areas, as illustrated in Figure 4.18. The hydraulic pore radius distribution is normally given as an area weighted distribution for all consecutive cross sections in a principal direction. Information of the pore extension anisotropy can be found from measurement of hydraulic pore radius distributions for all three principal directions. More details of the method is given in Huang et al. [77].

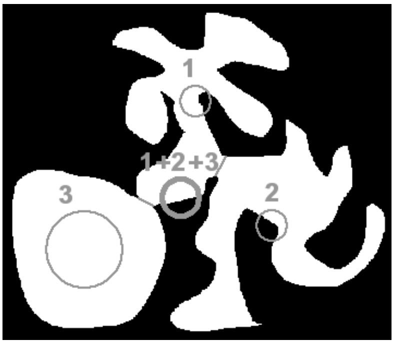

Figure 4.18 Illustration of the hydraulic pore radius concept for a large, branched pore area. The area and perimeter is determined for the continuous white area. The resulting hydraulic radius is in many ways an averaging of the hydraulic pore radii that would have been determined for the individual area marked 1, 2 and 3, delimited by the grey 'pore throats'. Note that the non-branched region 3 will have a much larger hydraulic radius than the branched regions 1 and 2, although the area of area 3 is smaller.

The measured hydraulic pore radii are dependent on the size of the cross sections and the thickness of the paper for most paper grades, as the volume edge and the defined surface will limit the pore extension. The observed anisotropy between the different principal directions is thus influenced by the width to length ratio of the digital paper volumes, as long as the volume is not cubic. The dependency of the cross-sectional area size will also render it difficult to compare different paper grades, as long as the digital volume sizes and length, width and height ratios are not kept (close to) constant. The hydraulic pore radius are therefore not applied in the assessment of pore geometry in Chapter 3, as the cross-sectional areas are varying both between the principal directions within the digital paper volumes and between the analysed paper grades.

Pore volume distribution, maximal sphere approach

The extension of pores in 3D space is often extremely complex. The pores are interconnected and difficult to delimit. A technique for measuring the pore size information, without delimiting the pore space into individual pores, is based on classical mathematical morphology [56]. More complete and generic descriptions of the basic concepts and techniques are given elsewhere [100,101]. The main element of the procedure is to define the covering radius for each point in the pore phase - this corresponds to a sizing by openings in the language of mathematical morphology. The covering radius in three-dimensional space is a sphere and in 2D a circle.

The pore volume distribution is derived from assigning all voxels of the porous phase to the largest sphere that includes the voxel. There is a largest sphere just fitting one or a few regions in the structure. This is the starting point. The remaining pore space are then sequently covered by spheres of decreasing size. The smaller the spheres, the more regions will be covered. However, the volume of the individual sphere regions is decreasing, as is the number of uncovered voxels. There is thus usually a maximum covered volume fraction for a covering radius somewhere between the maximum and smallest sphere. A pore volume distribution determined by the maximal sphere approach is shown in Figure 3.17 in Chapter 3 and Figure 4.25 in this chapter.

The critical radius is another feature that can be determined by the maximal sphere approach. When the maximal sphere size is decreased there will be a critical radius for which there will be a continuous path of maximal spheres connecting the surfaces. The critical radius is as such a minimum estimate of the drainage resistance of the structure. Figure 4.19 illustrates the concept for a two-dimensional example.

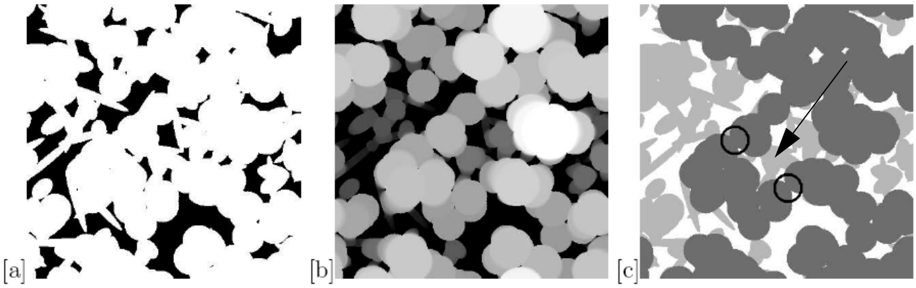

Figure 4.19 Illustration of the measurement of the local maximal radius for the pore size distribution and critical radius (λc). **Left [a]:** A model complex 2D media is shown for illustrational purposes; all simulations reported in this study are performed in 3D. **Middle [b]:** The corresponding field of covering radii $r_c(r)$ of the white phase in the left image with the greyscale proportional to maximal disk radius. **Right [c]:** The covering radii for all $R \geq \lambda c$ for connectivity in the vertical direction. The circles highlight the 'pore throats' of the critical pathway formed within the spanning cluster at breakthrough. Note that the 'pore throats' are narrower than for the possible pathway marked with the arrow.

Tortuosity - controlled random walk (rw) diffusion approach

The random, layered and often ansiostropic fibre network results in a complex complement porous network. The possible paths through the porous network for many paper grades will be relatively complex and clearly different for the movement in the z-direction compared to the in-plane directions. The complexity of the paths will be dependent of *e.g.* porosity, anisotropy, degree of layered structure. It is thus useful to find a method for quantifying the complexity of the paths through the porous structure. The tortuosity is a common measure of the complexity of such paths. The applied tortuosity definition is this study is the ratio between the length of the travelled path through the structure and the shortest linear path between the start and end point. The principle is illustrated in Figure 4.20.

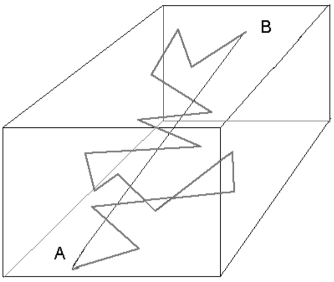

Figure 4.20 The tortuosity is defined as the ratio between the length of the travelled distance A to B and the shortest path between the start point A and the end point B.

Although molecules find their paths through the structure ‘automatically’, it is not a simple task to imitate the physical laws governing the movement on a computer. A relatively straightforward approach, for determining the paths through the digital structure, is to put a priority to the list of the 26 possible different movements from a voxel to the next, only allowing movement in the pore phase. The prioritization of movements is put to best resemble the movement of a non-wetting molecule through the sample when a pressure drop is applied across the sample, with no leak at the four other edges. The list of preferential directions will be slightly different for z-directional and in-plane paths. The list of preferential directions do not alter according to the surrounding structure. The ‘naíve’ ‘molecular walk’ will thus not necessarily pick the path of least resistance. The measured tortuosity is as such more governed by diffusive forces than least resistance paths. The tortuosity measured in this manner are therefore later referred to as diffusive tortuosity (τ_{diff}).

The initial step of the simulation is to choose a point randomly in the edge of the volume that is part of the porous phase. The simulation is continued from this point following the priority list of possible movements until a path is found through the porous structure to the opposite edge or the path and ends in a dead end. If the ‘molecule’ hits one of the four other edges, it is regarded as an illegal path, which are thus regarded as solid material. The shortest path is determined as the spatial distance between the random starting point and the end point. An easier, and more practised definition for transport, is the length of the volume in the direction of simulation. However, the paper volumes are delimited by an uneven surface in the thickness direction, which has a varying thickness. It is thus ambiguous to apply an average thickness for the z-direction. To not introduce any systematic differences between the principal directions, the shortest paths are determined to be the line between start and end point of the simulated path for all three principal directions.

Permeability and flow tortuosity

The transport properties is an important feature of the performance quality of many paper grades. Assessments of pore geometries may be performed in an attempt to quantify features of the porous structure that are expected to influence the transport properties of the paper. However, a microstructure defined by discretized digital images from X-ray microtomography lends itself immediately to numerical simulation of a number of transport properties. An alternative approach is thus to simulate the movement of liquid particles within the digital structures. The simulations will, when tuned to give a close resemblance to natural flow, yield a measurement taking into account how all detailed features within the volume affects the flow.

The lattice-Boltzman (LB) method have been applied successfully for simulation of flow phenomena for many porous structures, such as *e.g.* drainage through a bed of spheres [102] and (multi-phase) flow in porous rocks [44,45]. In this study the numerical lattice-Boltzmann method was applied to compute the flow permeability and the tortuosity of flow paths for fluid flow through the samples.

The lattice-Boltzmann method is a mesoscopic approach to computational fluid dynamics [103,104]. It is based on solving a discretized Boltzmann equation for a particle distribution function on a regular lattice. During one lattice time unit, particles propagate to their adjacent lattice points and redistribute their momenta in the subsequent collisions, whereby the distribution function is relaxed towards its equilibrium value. Each time step also involves implementation of external force acting on the fluid and of the boundary conditions at solid-fluid interfaces. The macroscopic flow quantities such as fluid density and velocity are given as appropriate moments of the distribution function (in analogy with obtaining hydrodynamic limit in the kinetic theory of gases). The flow dynamics thus obtained can be shown to obey the Navier-Stokes equation.

Permeability to fluid flow in a specified direction at low Reynolds numbers is given by Darcy's law;

$$Q = -\frac{k}{\nu}\frac{\Delta P}{L} \qquad (4.2)$$

where ΔP is the applied pressure difference across a porous sample of length L, Q is the macroscopic volumetric flux of the fluid per unit area and ν is the fluid viscosity. Eq. 4.2 is analogous to Ohm's law for the flow of electric current and *k* is the analog of the effective conductivity. *k* has the dimensions of area and may be thought of as representing the cross-sectional area of an effective channel for fluid flow through the pore space. Accordingly, any estimate of k must involve an estimate of the length scale relevant to flow. The permeability (*k*) depends on the structural characteristics of the material such as porosity, pore surface area and tortuosity of the flow paths.

The flow tortuosity is defined as the ratio of the mean length of flow paths to the thickness of the sample (in the direction of mean flow). As shown in Koponen et al. [105], a numerical estimate of flow tortuosity can be conveniently calculated using the formula

$$\tau_F = \langle|\vec{v}|\rangle / \langle v_z\rangle \qquad (4.3)$$

where $|\vec{v}|$ is the absolute value of local flow velocity, v_z is the component of velocity in the direction of mean flow (perpendicular to the plane of the original paper sample), and $\langle\ \rangle$ denotes the spatial average over the pore space. The determined flow tortuosity and permeability will emphasize the paths of least resistance, as most of the flow through the structure will be in these pores at steady-state.

Two slightly different approaches have been applied to the lattice-Boltzmann simulations in this study. The results presented in Paper III and IV have been obtained using a specific 19-link LBGK (lattice-Bhatnagar-Gross-Krook) lattice-Boltzmann model [103], where the collision operator is based on a single-time relaxation approximation [103]. The fluid flow was generated by a uniform external body force in the negative z direction [106,107]. The body force density equals the pressure gradient. The applied force was weak enough to result in a flow well in the Stokes regime everywhere in the pore space of the samples. A no-slip boundary condition at solid-fluid interfaces was implemented by a common 'bounce-back' rule [107] whereby the momenta of the particles that meet a solid wall are simply reversed. A free fluid layer with a thickness of about 10% of the sample was added on top of the sample and periodic boundary conditions were implemented in all outer boundaries of the rectangular computation volume. The simulations were continued until a macroscopically steady state was reached. The number of time steps required for that varied between 2000 and 10000.

The permeability calculation presented in the results paragraph of this chapter and Chapter 5 is based on a lattice-Boltzmann method (LB) using D3Q19 (3 Dimensional lattice with 19 possible momenta components) [108]. The implementation of the algorithm is similar to that detailed by [109]. The physical boundary condition at solid-fluid interfaces is the no-flow condition which in the LB methods is most simply realised by the bounce-back rule [110]. The pressure gradient acting on the fluid is simulated by a body force [106]. Mirror image boundary conditions [109] are applied in the plane perpendicular to the flow direction and all simulations were performed on a system with dimensions L x L x 2L. Permeability is measured in the central (L^3) subset. In all cases, the LB relaxation parameter $\tau_{LB} = 1.0$ is used.

All values of *k* are reported in μm^2.

The lattice-Boltzman simulation can be applied to simulate other important transport phenomena in paper such as coating of paper and possibly penetration of ink into the structure, although the wetting of fibres and evaporation of solvents will make this difficult.

Conductivity simulation

The permeability is a measure of the effective resistance against the flow caused by the structure. The resistance can be estimated alternatively by an approach more similar to the resistance for electric current through simulation of the conductivity. The conductivity calculation is based on a solution of the Laplace equation with charge conservation boundary conditions. The three-dimensional voxel microstructure is first converted into a network of resistors by connecting each pair of adjacent pixels by a resistor. A potential gradient is applied in each coordinate direction, and the system relaxed using a conjugate gradient technique to evaluate the field. We assign to the matrix phase of the paper a conductivity $\sigma_{paper} = 0$ and to the pore phase a normalized conductivity $\sigma_{pore} = 1$.

The result of the conductivity simulation is given as the ratio σ_{eff}/σ_f, where σ_{eff} is the effective conductivity and σ_f is the conductivity of the fluid that saturates the structure. It can be shown that the conductivity is proportional to diffusivity, employing the Einstein relation [111]:

$$\frac{D_{\text{eff}}}{D_0} = \frac{1}{\phi}\frac{\sigma_{\text{eff}}}{\sigma_f} \tag{4.4}$$

where D_0 is the free diffusion coefficient and D_{eff} is the diffusion within the porous system and ϕ is the porosity. The resulting diffusion ratio is assuming that the diffusion coefficient in the pores are D_0 and the diffusion within the fibre is zero. The assumption is in accordance to the measures of the diffusion coefficients for fibre and pore phase obtained by Massoquete et al. [112], where pore diffusion is 4-5 orders of magnitude larger than fibre diffusion.

The tortuosity of the conductive flow channels or of the diffusion process can be defined in the pore space according to Eq. 4.5.

$$\tau(\phi) = \frac{D_0}{D_{\text{eff}}} = \phi\frac{\sigma_f}{\sigma_{\text{eff}}} \tag{4.5}$$

Simulation of mercury intrusion porosimetry (MIP)

The mercury intrusion porosimetry is a method for assessing the pore size distribution directly on physical paper samples. It is known that the observed intrusion of the mercury from the surfaces of paper and into the structure will deviate from the true pore size distribution. The main differences are that the increased pressure applied for enabling intrusion into the smaller pore regions will compress the structure and large pore regions may be shielded behind narrow pore necks. However, it is not known in detail how large these effects are. A simulation of the MIP on the digital paper structures can yield a quantification of the effect of the compression and pore neck shielding for different paper grades, but only for pores larger than the resolution of the 3D images.

MIP can be found by applying the maximal sphere method, the main modification is to restrict the covering to spheres that can move into the pore channels from the surfaces of the paper. The intrusion will thus be limited by the pore necks of the structure, in the same fashion as the penetrating mercury. The applied radii in the maximal spheres will correspond to different applied pressures in the MIP. The varying radii of the maximal spheres can be correlated to varying pressures applied to the mercury. It is thus possible to generate pore size distribution in a similar manner to the progress to the curves obtained when increasing the pressure in mercury porosimetry. Comparison between the digitally simulated MIP and physically measured MIP can show the effects of the compression of the paper structure.

The difference between the pore volume distribution determined by the maximal sphere method, allowing covering of all pores independent of position, and the simulated and physically determined MIP can yield an estimate of the pore neck shielding effect.

Simulation of diffusivity

The water vapour permeation through paper is known to be, at least partly, a diffusion-type transport. The diffusivity is an important parameter for barrier coated and film laminated papers. The vapour transport through the paper under drying is a diffusive transport. It is thus useful to simulate the diffusivity of paper structures to obtain knowledge of the effect of the details of the paper structure on diffusivity.

The diffusivity can be found from a Monte Carlo simulation approach applying a form of random walk of the molecules from the centre of cubic structures and out to the volume edges applying a technique suggested by Reyes et al. [113]. The applied random walk approach is a departure from the explicit step-by-step procedure, as the molecules moves rapidly through the continuum portions of the void space, but reverts to a step-by-step method in the vicinity of the fibres. Measurements of diffusivity applying the above mentioned technique have been performed successfully on low-resolution 3D images of thick handsheets resembling paperboard by Goel [82].

Detection of pore throats, partitioning of pore space and assessment of porous structure parameters from skeletonization

The simulation of permeability, conductivity and diffusivity have been performed on porous rocks for gaining knowledge on the effect of solid matrix details on transport properties. However, it is not an easy task to locate where in the spatial structure there are much resistance against the fluid flow. To get such *a priori* knowledge, it is necessary to detect the pore throats in the structure and find the individual pores. The detection of pore throats and separating the pore space into individual pores have been under extensive research, but no general methods or definitions have yet been found.

A common approach for most attempts for determining pore throats and separating the pore space into individual pores is the determination of the medial axis of the porous phase [114-117]. It has also been attempted to detect the pore necks by multi-orientation scanning [118], but the approach is computationally demanding and is not accurate. The medial axis is a skeleton, which is the minimum representation of the porous phase preserving its topology. The medial axis transform was first proposed by Blum [119] for extracting the skeleton of a shape. The medial axis transform of a shape is the locus of the centres of all maximal discs contained in the shape. A maximal disc contained in the shape is any circle with its interior that is contained in the shape (*i.e.*, has empty intersection with the exterior of the shape) such that the circle touches the boundary of the shape at two or more points [119]. In 3D, the medial axis is not determined by the maximal circle, but the maximal sphere. The definition of the maximal sphere is also that the sphere touches the boundary of the shape, or more correctly the pore, at two or more points. However, the complexity of determining the maximum sphere is much higher due to the higher dimensionality.

The medial axis in practise may be determined by at least three principally different methods:

- a thinning algorithm performing an erosion or ‘burning’ of the porous structure until no more voxels can be removed without disconnecting the voxel skeleton [114]
- A determination of a Voronoi representation of the shape and reducing this down to the elements constituting the medial axis [120]
- A determination of the distance transform (DT) of the porous structure and from this finding paths through the structure following the maximum distances in the structure [26].

The properties of the resulting skeleton will be influenced by the applied method, as the different approaches will be differently affected by the details of the porous network. The methods will as such produce first pass skeletons with different features.

The result after applying the above mentioned methods will normally result in a skeleton with more voxels than what is needed to make the skeleton consisting of the minimum number of voxels needed for preserving the important features of the porous network. The skeleton determination is sensitive to the details of the pores, as all features of the porous phase should be preserved in the intention of representing the shape of the object with the skeleton. This can be seen in for an image in two dimensions in Figure 3.2 in Chapter 3. In 3D there are obviously more details that can result in such dead-end branches of the skeleton. Different approaches and criteria can be applied for removal of such unnecessary details.

The first pass skeleton will normally contain more voxels than what is needed for the minimum skeleton just preserving the connectivity. The necessary removal of adjacent voxels having the same maximal sphere can be done according to varying criteria and approaches, where one of the most important criteria is how connectivity of the skeleton is defined. The definition of connectivity in 3D space is complex as each voxel have 26 adjacent voxels. Different definitions of 3D connectivity, as defined by Liang and Ionnadis [117], is shown in Figure 4.21

There are thus many free variables in the determination of the medial axis representing the minimum skeleton needed to hold the information of the substantially important features of the porous phase. No method have yet proven to be superior to others, so there are no standard methods for the determination of the medial axis and most groups working on determining 3D medial axes thus have their own special procedure. The most refined and automated generation of a medial axis have been reported by a group at SUNY-SB, lead by B. Lindquist [114,115,121].

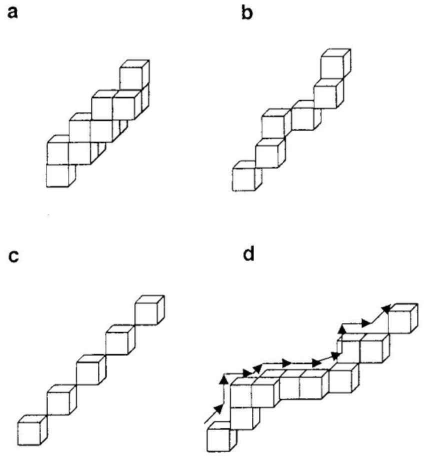

Figure 4.21 Illustration of (a) 6-adjacent, (b) diagonally adjacent, (c) diametrically adjacent, and (d) λ-adjacent paths in discrete 3D space

Once the medial axis is determined, information and many structural parameters can be determined directly from the medial axis and from visualization showing the complexity of the interconnected pores in a more comprehensive representation than the binary structure. From the erosion/burn and the DT a distribution of the 3D extension of the porous phase can be derived [114]. The skeleton, when it is a true minimum of the shape of the pore phase, will consist of only line segments connected in joint voxels. The line segments are so called branches and the joint voxels are so called nodes. The number of branches connected to the individual node will yield information of the connectivity of the structure when a distribution of the connectivity for all the nodes in the analysed volume is determined [115]. However, the chosen approach for determining the medial axis will influence the determined connectivity. It should also be noted that the determination of the skeleton normally will contain mostly nodes with three branches. This involves a high probability of several nodes within a pore body, as shown in the 2D case in Figure 4.22. It is thus necessary to perform a procedure for reducing the number of nodes with a connectivity of three, to obtain a skeleton having a closer resemblance to the ideal skeleton, where each node correspond to a single pore body. Alternatively, nodes that are close likely belonging to the same pore body can be identified and grouped together to obtain the correct numerical results without modifying the skeleton.

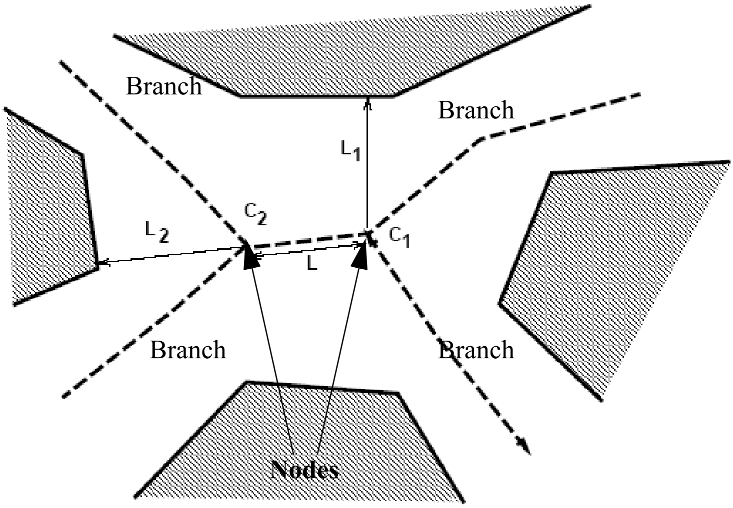

Figure 4.22 Illustration of the medial axis resulting from a coordination number 4 pore body. The problem is to identify such close nodes as a single node.

The main advantage of the medial axis is that it is a good basis for determining the pore necks. If an ideal skeleton have been derived, where each node correspond to a pore body, there will be a pore throat on each branch limiting the flow to the adjacent pore body. The detection of pore throats once the medial axis is known thus breaks down to finding the point on each branch where the maximum sphere is the smallest and finding the minimum surface normal to the local spatial orientation of the branch. This is not a trivial task, but far easier when there is a guidance such as the medial axis. Once unambiguous pore necks have been determined for all branches, then the continuous pore phase is divided into individual pores. An example of a medial axis (red) with the determined pore necks (green) for each branch for a sandstone sample is shown in Figure 4.23. The representation clearly shows the complexity of the porous structure, where the possible paths through the structure are localized (red paths) and which paths show the least and most resistance to flow (small green surfaces indicate narrow pathways.

The separation of the pore phase into individual pores delimited by pore necks enable determination of many parameters for pore volume, pore necks, position in the volume, correlation between pore and pore throat features and many other parameters. It is also possible to extract individual pores as delimited by the pore necks and study the details of its 3D extension, as exemplified for a sandstone sample in Figure 4.24. The medial axis can also be applied for guidance for simulation of transport properties.

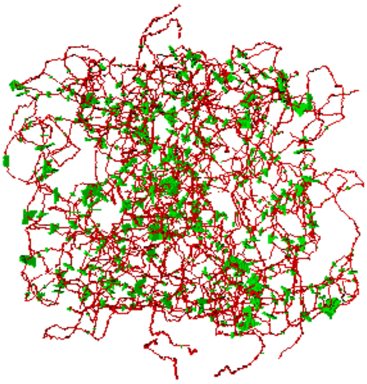

Figure 4.23 The medial axis as determined for a sandstone sample applying the 3DMA code of SUNY-SB [121]. The red lines is the medial axis and the green surfaces are the determined pore necks for each branch of the skeleton. Figure reproduced from: http://www.ams.sunysb.edu/~lindquis/3dma/3dma.html#examples

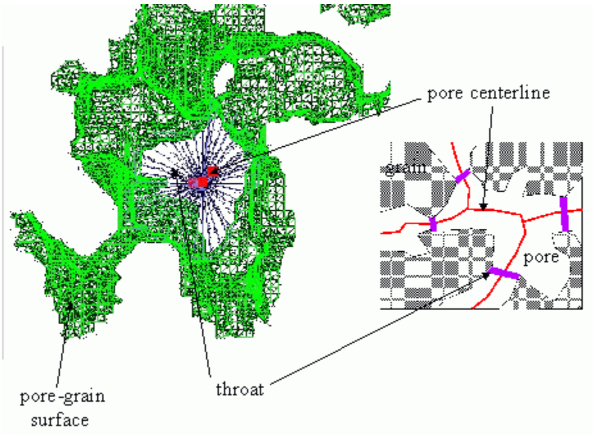

Figure 4.24 An example of the 3D extension of a pore in a sandstone sample. The pore is delimited by pore throats as determined from the medial axis. Figure reproduced from: http://www.ams.sunysb.edu/~lindquis/3dma/3dma

It should be emphasized that although the medial axis can be applied for determining many interesting structural parameters and gain more knowledge of the detailed pore extension the method is very dependent on the chosen approach. The determination of the medial axis is a difficult and computationally expensive procedure. There exist no standard approach for determining the medial axis and no reference for controlling whether the nodes in the resulting skeleton have a close to ideal correspondence to pore bodies. If the medial axis is determined, it is therefore necessary to give a detailed description of the applied procedure. However, assuming further development and refining will standardise the method to yield an unambiguous representation, with 1:1

correspondence to the original digital pore space, the method can yield many interesting measures for assessment of pore geometry, connectivity and how detailed features influence transport properties.

Measures of the fibre phase

This study focuses on the characterization of the pore phase. It is nevertheless just as important to gain knowledge and measurements of the solid phase. However, as the solid phase is the complement of the void phase, many of the measures of the pore geometries will be valid for the solid phase as well. The measurement of pore and fibre chords is a good example of this.

As the fibres have a finite spatial extension, the assessment of the individual fibres is in principle easier than assessment of individual pore characteristics. However, although the fibre constituents can be easily comprehended from observation of the cross sections, the segmentation of individual fibres from the fibre network has shown to be a complicated task for computer programming.

Yang [72,73] applied a method where the medial axis of the solid phase was determined. The method succeeded in extracting many useful characteristics of the fibre phase, fibre bonding and fibre segments. Aronsson [17,26,65] succeeded in extracting individual fibres from the fibre network and assessing features of the fibre geometries. Both Yangs and Aronssons methods are promising for assessing detailed measures of the fibre phase, where the ultimate goal would be to segment the fibre network into its individual constituents with a 1 to 1 correspondence to the physical network. A perfect segmentation would allow measurement of the free surface area and the bonded area, thus yielding a direct measure of the relative bonded area. A perfectly segmented fibre network can also be applied for FEM simulation of the fibre network mechanical properties, as voxels inside the fibre matrix and in fibre-to-fibre contact areas can be assigned different properties. However, it is an open question whether the research progress and computer development will make this possible.

Measurement of surface properties

It is possible to measure surface properties like *e.g.* roughness from the surface topography of the 3D paper structures. However, there exist instruments specially designed for measurement of the surface properties. The dimensions, length scales and planar alignment of the measured surface are better suited for characterization of properties related to the bulk performance properties of paper. The characterization of surface properties from 3D images might however be useful to relate surface properties to the interior characteristics. It is when the interior properties are of importance the 3D information has unique capabilities.

Simulation of optical properties

The digital representation of the paper structure allow simulation of transport of fluids. The simulation of the interaction between fibres and light is in principle possible to determine by related methods. A prerequisite for optical simulation is however a digital structure with a smooth surface, as light by nature can be reflected in all spatial directions. It is thus necessary to process the ‘staircased’ voxel representation into a smooth representation. This can be accomplished by a marching cube algorithm [122]. For successful simulation of optical properties a model for the lights interaction with the solid objects must be found. The model must be detailed enough to yield a realistic result, but not so complex that it becomes too computationally demanding. Brunborg et al. [123] have derived the basis for a model that can be applied for simulation of optical properties of paper. However, the model needs tuning by measurement of many material and structural properties needed as input for the interaction between structure and light. A simulation using complex paper structure has not been performed.

The ultimate goal for determining optical properties is successful simulation of a relatively large digital paper structure with a resolution of 0.2 µm, where the phase borders are smoothed and a correctly tuned model for the interaction between light and solid elements.

Simulation of network behaviour under physical influence

It is plausible that the development of computer resources and knowledge of the physical properties of paper, fibres, fibre bonding and pigments will enable a simulation of the network behaviour under physical influence. The methods applied to date assume the fibre network to be unaffected by the surroundings. The key issue is to quantify the effects of humidity and external forces to the fibre network, which will require 3D imaging of the same paper structure under different physical conditions. This is a problem yet to be resolved.

4.3 Results

Like the study of cross-sectional paper structure by SEM-BEI, the results of this study can be divided in three categories, all evaluating different aspects of the applicability of recently available methods for acquiring high resolution 3D images revealing the detailed spatial distribution of the fibre network.

- Consider and implement image analysis routines and simulation procedures useful for characterization of detailed 3D images of paper structure.
- The results and findings from application of image analysis routines and simulation procedures for characterizing the paper structure and explanation of the physical behaviour of paper.
- The discussion of factors influencing the assessed structural properties determined by image analysis and simulation procedures performed on 3D images of paper obtained by X-ray microtomography.

The image analysis routines and simulation procedures that have been considered and found useful for assessment of the structural properties of paper are presented in the materials and methods paragraphs. The discussion of features affecting the results obtained with the chosen methods is presented in the discussion paragraphs and the attached Papers III and IV. This section will thus focus on the results from application of the image analysis routines and simulation procedures.

The implemented image analysis routines and simulation procedures have been applied to assess the detailed structural characteristics of two different sets of paper samples, of which the results are presented in the next subchapters.

4.3.1 Results from analysis of high resolution phase contrast images

The initial assessment of the high resolution 3D images obtained by synchrotron source phase contrast microtomography were done on a PC. The initial assessments include mostly 3D image analyses performed on consecutive cross-sectional images, the only exception is the restricted random walk yielding a diffusive like tortuosity. These initial assessments are presented in the attached Paper III. The results include visualizations and assessment of a filter paper in both dry and soaked condition. Most of the applied image analysis routines are based on procedures originally developed at University of Minnesota and previously applied for lower resolution 3D images [76,77,82] of thick handsheets. The main exception for the routines applied in this thesis work is that the surface area is included in the analyses, enabled by the surface definition determined by the rolling ball algorithm.

In addition to the initial assessments of the phase contrast data sets performed on PCs presented in the attached Paper III, more assessments were performed exploiting the three-dimensional data sets by applying true 3D analyses and transport simulations. Such demanding analyses and transport simulations had to be performed applying parallel computing or supercomputers. The additional assessments included pore size distribution based on the maximal sphere method, determination of the critical radius, conductivity, yielding estimates of diffusivity and diffusive tortuosity, and permeability. The permeability was determined by two different approaches. Permeabilities were determined initially on the complete volumes including the surface layers, applying a specific 19-link LBKG (lattice-Bhatnagar-Gross-Krook) lattice-Boltzmann model [103]. These simulations were performed at the Department of Physics at University of Jyväskylä in Finland. Results from these simulations are presented in the attached Papers III and IV. At a later stage the permeability was simulated dividing the volumes into a set of uniformly sized subvolumes and excluding the surface layers.

The division of the large 3D data sets into subvolumes enables reasonable computational times and several measurements for each volume that gives one the ability to generate a transport property:porosity relationship across a range of porosities rather than a single data point. However, it is important that the transport properties are measured at representative scales, *i.e.* where the size of the system compared to some statistical scale (*e.g.* correlation length, mean pore size) is large. As the pore size of paper is the order of 2-8 microns, simulations performed on samples of {100 x 100 x paper thickness} μm^3 should give realistic results. Simulations at this scale (max. 200 - 300^3 voxels) are feasible on modern workstations, contrary to the full volume size.

The lattice-Boltzmann method applied for the later stage permeability simulations were based on a D3Q19 (three-dimensional lattice with 19 possible momenta components) approach [108]. The simulations were performed at Applied Mathematics, Research School of Physical Sciences and Engineering, Australian National University (RSPhysSE, ANU). The results from the later stage permeability simulations are presented in this chapter.

In addition to the subvolume based permeability simulations, all the additional 3D structural and transport analyses presented in this chapter are given for the phase contrast 3D images of paper and have been performed at RSPhysSE, ANU.

The porosity, mean pore size (Eq. 4.1) and mean pore radius determined by the maximal sphere method are all determined for the volumes when excluding the surface layers. The results are presented in Table 4.1 and include assessments performed on both high- and low-resolution 3D images.

Table 4.1: Porosity and mean pore sizes measured on high- and low-resolution images of the three investigated paper samples. The $r_{Vp/S}$ values are determined from the surface to volume ratio according to Eq. 4.1. The r_{psd} is the mean radius for the pore size distribution determined by the maximal sphere method.

Paper grade	Porosity (%)	$r_{V_p/S}$ [µm]	r_{psd} [µm]
Handsheet (High)	48.9	4.98	4.62
Handsheet (Low)	45.6	9.30	5.80
Filter (High)	66.5	9.20	7.11
Filter (Low)	61.2	12.6	8.38
Newsprint (High)	59.6	4.83	3.81
Newsprint (Low)	60.3	11.0	7.95

The pore size distributions determined by a volume approach applying the maximal sphere method are given in Figure 4.25. The pore size distributions are given as volume frequency distributions (voxel count). The assessments include both high- and low-resolution 3D images of the paper structure. The small-scaled variation seen for the high resolution images are a result of the plotting in MATLAB in discrete intervals and are not actual structural features of the samples.

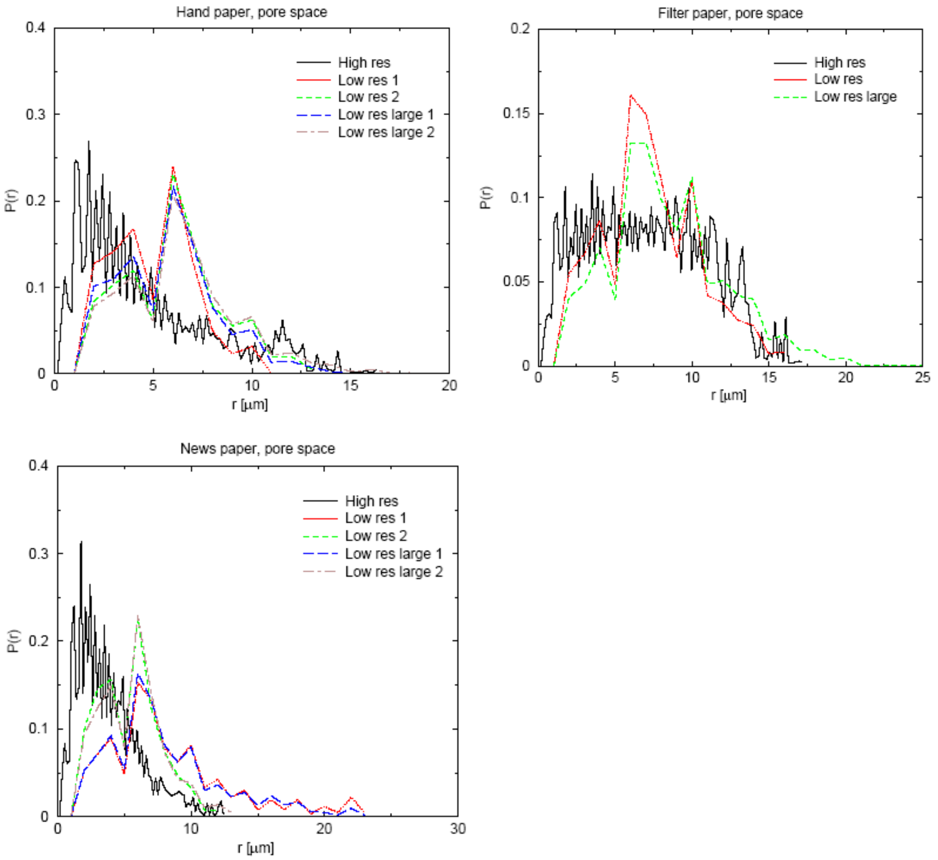

Figure 4.25 Pore size probability distribution as determined by the maximal sphere method for both high- and low-resolution images. **Top, left:** Handsheet distributions. **Top, right:** Filter paper distributions. **Bottom:** Newsprint distributions.

A number of important differences can be seen in all three measured distributions. The analysis of the low resolution images shows a consistent pore size distribution, peaked at $r \approx 7\ \mu\text{m}$ and exhibiting a gaussian-like distribution in pore size for the three different paper types. In contrast, the high resolution images of the three papers show very different morphological signatures. The handsheet and newsprint exhibit peaks in the distribution at $r \cong 2\ \mu\text{m}$; the filter paper exhibits a broad and flat pore size distribution from $1\ \mu\text{m} < r < 12\ \mu\text{m}$. Mean values of the pore radius defined by the distributions are given in Table 4.1.
The difference in the distributions between the high and low-resolution data is believed to be due to insufficient resolution of the low-resolution CT scanner.

Figure 4.26 shows the plots of the assessed normalized conductivity (σ_{eff}/σ_f)of the three different papers based on the high and low resolution data for the three orthogonal directions. The conductivity is mostly of interest for determining well-known paper properties like diffusivity and diffusive tortuosity. However, the conductivity is plotted directly here, as it is directly structurally derived. The diffusivity and tortuosity are calculated from the diffusivity and the porosity (Eq. 4.4 and Eq. 4.5), which is also the ordinate of the plots.

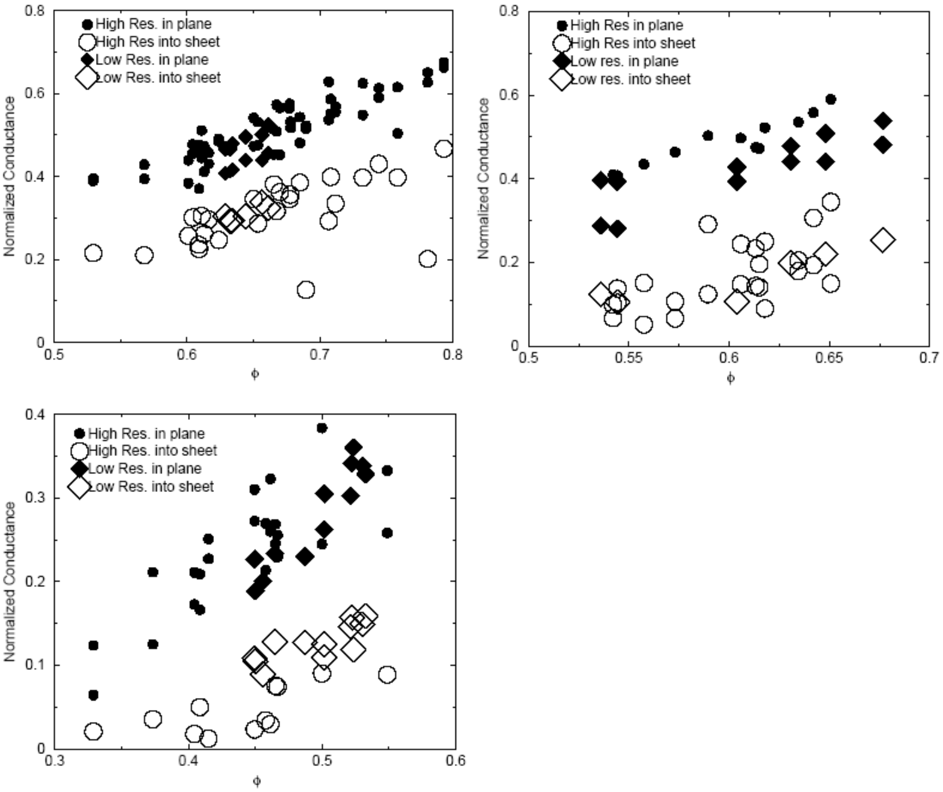

Figure 4.26 Measurement of conductivity of; **Top, left:** Filter paper, **Top, right:** Newsprint and **Bottom:** Handsheet

The plots clearly show that the high- and low resolution 3D images yield similar results for conductivity. There are clear differences between z-directional and in-plane conductivity for all the three paper grades, where the in-plane conductivity is consistently larger than transversally through the sheet.

The obtained results for computed continuum permeability *k* of the three different paper grades based on the high and low resolution data are given in Figure 4.27.

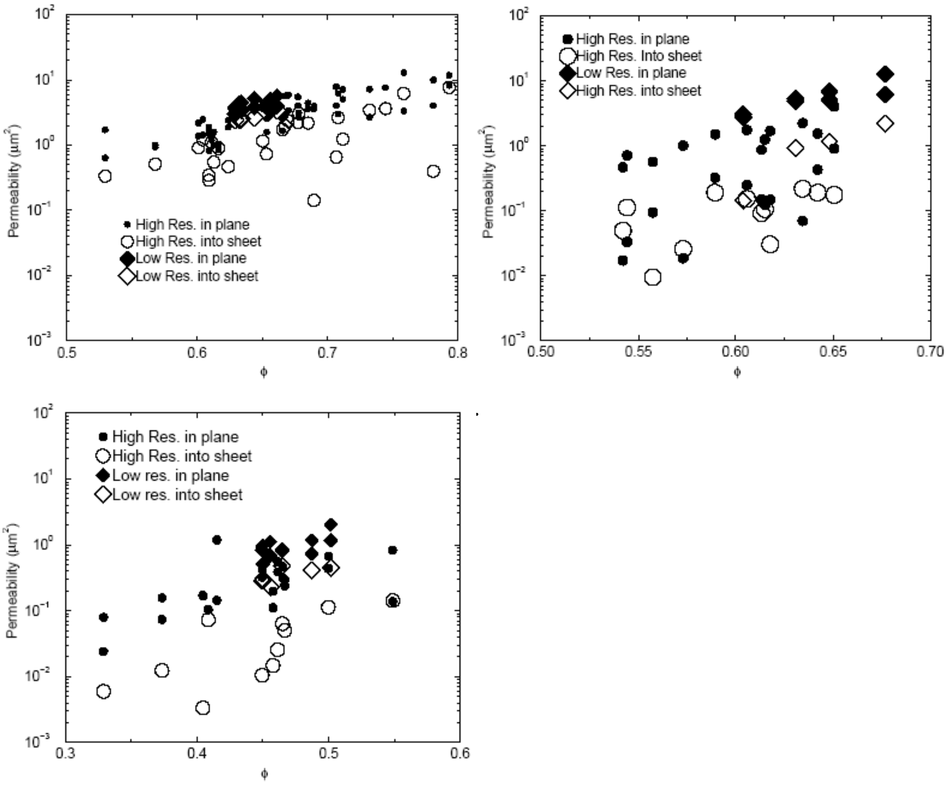

Figure 4.27 Measurement of permeability on; **Top, left:** Filter paper, **Top, right:** Newsprint and **Bottom:** Handsheet.

The permeability from the low resolution images is consistently somewhat larger than the prediction from the high resolution images; this is expected as the measured pore sizes in the low-resolution images are larger. In the case of handsheet and newsprint, the differences are approximately one order of magnitude. The difference for the more open structure of the filter paper is less pronounced. In all cases the permeability in the plane of the sheet is greater than through the sheet.

The size orders seen between the paper grades and the principal directions are as expected and follow the same trends as seen in the attached Paper III.

Comparison of permeability results to common permeability trends

As the high resolution data is of a better standard, the permeabilities of the three different paper grades are compared based on the simulation of high resolution images. In Figure 4.28 the high resolution permeabilities both through the sheet (left) and along the machine direction (right) for all three paper types are plotted. The permeability of the three papers can be described as an exponential of the porosity ϕ. The three papers do not show the same permeability:porosity trends. A fit of the permeability to the form

$$k = ae^{(b\phi)} \tag{4.6}$$

for the three different papers is shown in Figure 4.28 (left). Values of the fitting parameters a and b are given in the legend. The observed trend in permeability from highest to lowest (filter > handsheet > newsprint) is consistent with the mean pore size measured for the three paper types (Table 4.1). In contrast the permeability in the plane of the sheet for the three different paper types is very similar, and follows Eq. 4.6 with a = .0077; b = 9.02.

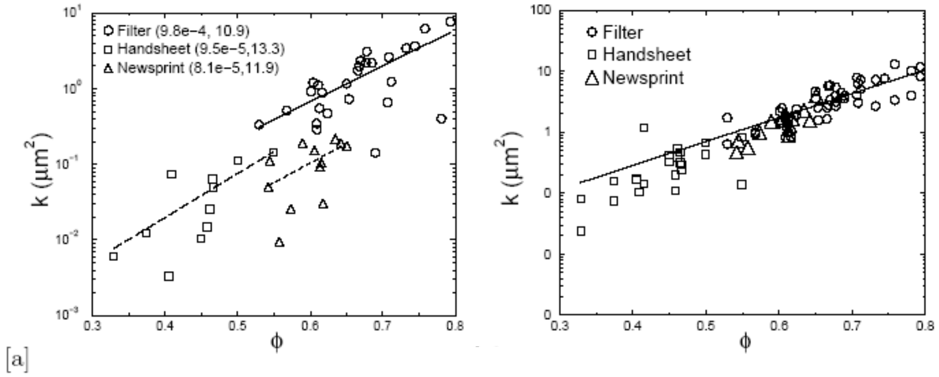

Figure 4.28 Left: Permeability simulated on the high resolution images in the z-direction. Values of the empirical fit to Eq. 4.6 are given in brackets. **Right:** Permeability simulated on the high resolution images in the machine direction.

One of the most basic techniques for estimating permeability is the Kozeny-Carman formula, which for a cylindrical tube is given by:

$$k = \frac{\phi^3}{c\tau S} \tag{4.7}$$

where S is the specific surface area of the web and τ is the tortuosity of the medium. In many empirical methods τ is embedded into the coefficient c. A common empirical fit for fibrous materials which have been shown to give a good match to model paper structure [124] is given by Eq. 4.8.

$$c\tau = 3.5\frac{\phi^3[1 + 57(1-\phi)^3]}{[1-\phi]^{1/2}} \tag{4.8}$$

In the left graph of Figure 4.29 the match to the prediction (Eq. 4.7 using Eq. 4.8 as the $c\tau$ constant) is shown. It is found that the filter paper gives an excellent match to the correlation. In contrast the newsprint gives permeability 2-5 times smaller than predicted by Eqs. 4.7+4.8 and handsheet exhibit permeabilities 4-20 times smaller than that predicted by the empirical correlation. This result indicates that the correlation is most appropriate for filter paper and may indicate that the process-based model structure [124] mimics most closely the structure of a filter paper.

τ, which defines the diffusive tortuosity of the flow channels, can be related to the effective resistance to electrical current flow across a fluid saturated pore space, according to Eq. 4.5. Applying this relation, and assuming the flow channels are shaped like cylindrical tubes, leads to the permeability prediction [130]:

$$k = \frac{\phi(V_p/S)^2}{2\tau} \qquad (4.9)$$

The values simulated for conductivity yield a measure of τ for each subset and which are applied in Eq. 4.9 to predict the permeability. The results from applying these permeability predictions are compared directly to the numerical data for flow through the sheet in Figure 4.29 (right). The prediction of the empirical equation is good for all three data sets, and exhibits a similar scatter to that observed in the direct calculation of permeability.

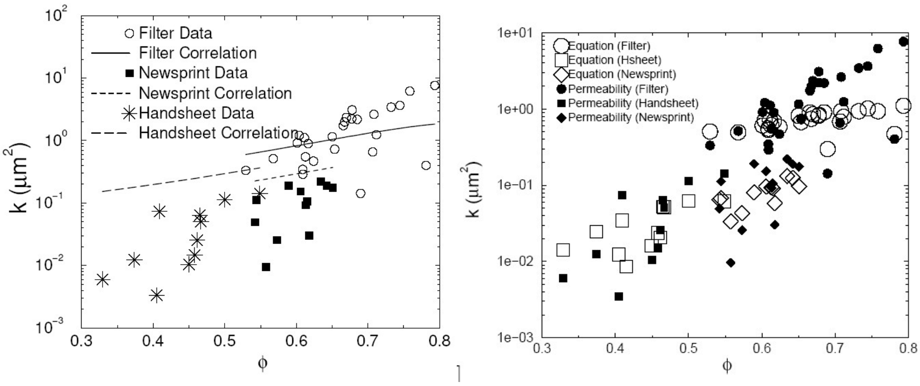

Figure 4.29 **Left**: Comparison of the fit of Eq. 4.7 (using Eq. 4.8 as the empirical $c\tau$ constant) to the permeability data. **Right:** Comparison of the fit of the empirical equation Eq. 4.9 to the permeability data. The fit of Eq. 4.9 is good for all 3 papers, while Eqs. 4.7+4.8 only matches the filter paper data.

4.3.2 Results from analysis of high resolution absorption mode images

The results from analysis of high resolution 3D images of paper acquired in absorption mode are presented in Chapter 5. The applied resolution was 0.7 μm. The experimental scheme applied for the newsprint-like paper grade allowed simultaneous assessment of the effect of four papermaking variables to the detailed paper structure. The experiment thus gives a supplement to the study performed on the phase contrast 3D images, as it shows how the X-ray microtomography technique and image analysis can be applied to find structural explanation of the paper's physical behaviour.

The experiment also included a method for estimating the effect of basis weight variation. However, the results from the basis weight variation assessment are also partly included in the subchapter discussing the effect of formation in this chapter.

4.4 Discussion

4.4.1 Correspondence between physical and digital structure

Image acquisition and reconstruction

Several factors in image acquisition procedures and the applied reconstruction algorithms may affect the quality of the obtained 3D images of the paper structures. The quality of the images, as for most microscopy techniques, is a trade-off between contrast, resolution and signal-to-noise ratio. Additionally, undesired disturbances to the signal should be avoided or suppressed as much as possible.

The signal-to-noise ratio is normally high for synchrotron source microtomography due to the high monochromatic X-ray flux. The applied acquisition time of 1 second yields a low level of small scaled noise, even for the smallest applied effective voxel size of 0.35 µm. The much lower X-ray flux from the stationary source applied in the commercial CT scanners requires a longer acquisition time per rotational stage even for the considerably larger effective voxel size. To avoid extremely long acquisition time for a full 3D image, a trade-off must be done between quality and time. There are thus a lower signal-to-noise ratio in stationary source imaging. Fewer rotational stages during the 180 ° scan will also contribute to a higher amount of noise.

The signal-to-noise ratio is a limiting factor for the choice of photon energies, at least for absorption mode imaging. A higher contrast between the constituents can be obtained for lower photon energies, but the lower the photon energy, the fewer X-rays will reach the detector. There is thus a lower practical limit for choice of photon energy depending on the material density and sample dimensions.

The photon energy and the distance between sample to detector is crucial for the edge enhancing inline phase contrast signal. The limiting factor is the finite width of the edge enhancing fringes, which are governed by the Fresnel diffraction:

$$\Delta_{\text{fringe}} = \sqrt{\lambda \times z} \tag{4.10}$$

where λ is the wavelength[1] of the X-rays and z is the distance between sample and detector. It is a necessity that the width of the fringes are larger than the effective voxel size to enable detection of the resulting interference pattern. The applied photon energy of 20 keV and the sample to detector distance of 5.5 and 9.5 mm yields respectively a fringe width of 0.58 and 0.77 µm. The Fresnel diffraction also sets a lower limit to the spatial resolution, which is considerably lower than the theoretical spatial resolution for the highly coherent synchrotron source signal. It should also be considered that the phase contrast scales proportionally with the distance between sample and detector. It is therefore a clear tradeoff between spatial resolution and contrast when choosing the distance. The applied sample to detector distances and photon energies are considered to present a reasonable compromise between contrast and resolution.

The applied photon energy and distance between sample and detector for the acquired absorption mode images yields narrower fringe widths than the voxel size. The phase

---

[1] The X-ray wavelength is dependent of the photon energy. The wavelength λ in Ångströms are given by 12.4 divided by the photon energy (E) in keV ($\lambda = 12.4/E$).

contrast effects will thus not be visible in the transmitted images. However, the dark areas in the vicinity of many fibres indicate that the relatively rough fiber surfaces have locally in many instances refracted the X-ray signals, resulting in a low exposure to X-rays for these locations on the detecting CCD screen. The spatial resolution of the absorption mode images are limited by the chosen detector optics and ultimately by the X-ray scattering in the scintilator, transferring the X-ray signal to visible light. The same scintilator is also applied for the phase contrast imaging, thus putting an additional physical limit to the achievable spatial resolution also for the phase contrast image acquisition. The applied photon energy in absorption mode imaging is considered to yield a reasonable trade-off between signal-to-noise ratio and contrast.

In addition to enable phase contrast imaging, the difference between spatial resolution and voxel size in practice involves that all voxels contain information from spatially adjacent submicrometer subvolumes in the physical sample. The effect lead to uncertainties in whether small objects are physically reasonable objects and thus set a practical limit to which size of objects that with certainty can be distinguished from noise. The degree of spatial overlap of information, as long as it is at a reasonable level, will for larger objects in phase contrast imaging have little practical influence on contrast, as the Fresnel fringes are concentrated to the phase borders. The absence of detectable refraction fringes in the absorption mode images result in a gradual intensity distribution from solid to void fraction. The increased overlap of the greyscales of the phases will render it more difficult to perform a perfect segmentation of the phases. However, the dark vicinity seen around many of the fiber borders probably limits the reduced edge contrast effect.

Beam-profile fluctuations might lead to strong ring or quasi-ring artefacts [97,125]. The complete ring artefacts can be removed almost entirely applying intermediate flatfield images as correction [92] or by filtering of the ring objects in the power spectrum [97]. The present quasi-ring artefacts in the obtained phase contrast images in this study have shown more difficult to remove. Example of strong quasi-ring artefacts are shown in Figure 4.30.

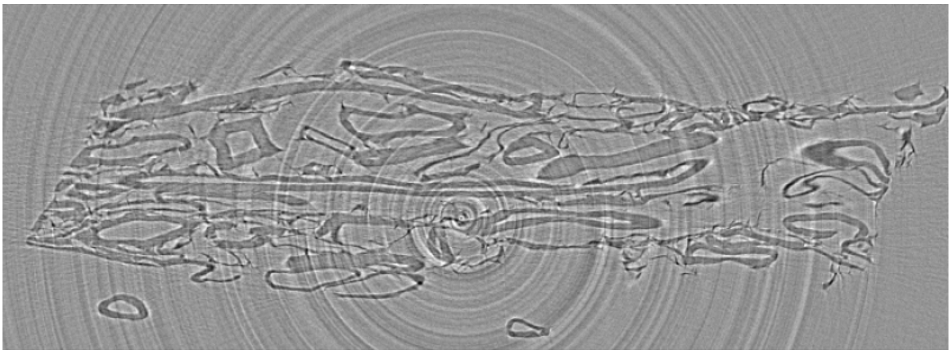

Figure 4.30 Example of strong quasi-ring artefacts in the in-plane direction parallel to the transmitted phase contrast signal. The cross-sectional image is from the uncalendered newsprint sample in the area that is most severely influenced by the quasi-ring artefacts.

The ring and quasi-ring artefacts are most detrimental to the centre of the sample, as the density of the rings is the highest in the close vicinity of the axis of rotation. Performing most of the filtering and binarisation procedures in the in-plane direction perpendicular to the plane aligned with the transmitted images, have shown to yield 3D structures minimally influenced by the ring artefacts. The applied procedure for image processing, as described in Antoine et al. [97], succeeded in suppressing the effect of the quasi-ring artefacts, except for the exact centre of the rotation. The damaged region in the centre of the sample was at worst representing maximally two percent of the volume. The effect is thus not considered to be detrimental to the measured structural characteristics, not even for the most influenced sample, the uncalendered newsprint volume. The quasi-ring artefacts will have most influence on detailed assessments such as *e.g.* specific surface area and mean pore chord lengths.

The development at the synchrotron facility in France have been towards more stable beam profiles. The problem with ring and quasi-ring artefacts are thus currently a smaller quality problem than at the time the phase contrast 3D images of this study were acquired. The progress can be observed as less artefacts in the absorption mode images, which were acquired three years later than the phase contrast images. The effect of ring and quasi-ring artefacts in the absorption mode images are almost non-existent.

Ring artefacts will also be the result of the polychromaticity of the stationary X-ray source applied in the commercial scanner. This effect is known as beam hardening. The rings are not evident in the 3D images, as the phenomenon are taken care of by image acquisition procedures and software applications in the scanner set up. However, the beam hardening effect will most likely be a source for noise in the acquired images.

Involuntary sample movement during image acquisition may introduce so called star artefacts. These are clearly present in the synchrotron source phase contrast images. An example of these artefacts are shown in Figure 4.31. Runout of the rotation axis in the sample stage can cause such effects. The runout of the sample stage applied for synchrotron source phase contrast imaging was in the order of ± 0.5 μm [126]. Internal degrees of freedom of the sample itself may also affect the quality of the tomograms. A particular case in this category is the tendency of the horizontally suspended sample to hang down. The essential consequence of this is a vertical displacement of each projection image of the sample. The displacement varies smoothly with angular position, causing artefacts that make point-like features appear as three-spiked stars [92].

The low bending stiffness of the imaged paper qualities make the horizontally mounted samples in phase contrast images more exposed to this type of artefacts. The gluing of the small paper samples to the capillary, applied for absorption mode imaging, will eliminate the problem of involuntary sample movement almost completely. However, involuntary sample movement may also be caused by change of paper structure with varying humidity. It is therefore of utmost importance for high image quality of paper that the sample is well acclimatized to the humidity level in the experimental hutch. It is also a requirement that the climate of the experimental hutch is close to constant, which is fulfilled for the experimental hutches at the ESRF.

The presence of star artefacts and missing interface between fibre and pores are treated in the procedure for segmentation of the phase contrast images as presented in Antoine et al. [97]. The star artefacts could not be distinguished from fibrils, sticking out of the main body of the fibre much in the same fashion as the sample movement artefacts. The star artifacts are therefore removed at the expense of fibrillar material. The uncalendered newsprint sample may thus have a lower fraction of fibrils than it would have had without the presence of star artefacts.

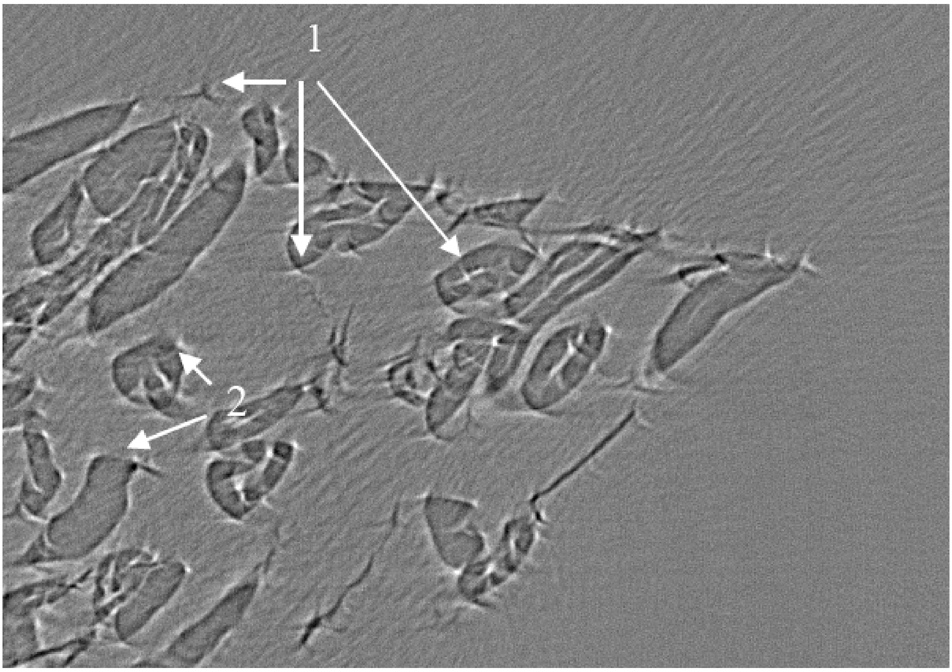

Figure 4.31 Part of a reconstructed image of filter paper showing noise due to movement of the sample during its scan (1) and missing interface between fibre and pores (2).

The digitization will affect the 3D images much in the same sense as for cross-sectional images obtained by SEM-BEI, as discussed in Chapter 2. However, the reconstruction procedure from transmitted images to sinograms in backprojections and final reconstructed cross-sectional images yields an additional step of interpolation. The digitization will as such lead to voxels with intermediate greytones in the transition zone between the phases. The effect can result in less sharp phase borders, as indicated by the regions numbered ‘2’ in Figure 4.31.

It should be emphasized that the phase transition is necessarily not very sharp for paper, as the fibres in themselves are a porous material. A prerequisite for edge-enhancing phase contrast is a sudden phase shift. Fibres may have varying fibrillation and surface roughness in an order of the voxel size due to differences in pulping and papermaking. It is thus not unexpected that the phase border between fibres and voids locally can be difficult to detect by near-field phase contrast. The missing interface between fibres and voids, as exemplified in Figure 4.31, may therefore also be physically reasonable.

It is clear that the 3D images are not always of perfect quality for all areas of the sample and that the quality can vary between different volumes due to reasons the user do not have any possibility to influence. Nevertheless, it is considered that the effects from image acquisition settings and image reconstruction procedures have minor influence of the results from the entire volume. However, the voxel/spatial resolution will be determinant to the detection level and will as such have a major influence on the assessed structural properties This effect is therefore discussed more thoroughly in the following, especially in the attached Paper IV.

Effect of sample preparation/mounting

Although the X-ray microtomography technique is in principle non-invasive, the sample must be cut to the size order of the projecting X-ray beam. The width of the imaged area of the paper samples are 0.7-2 mm depending on the voxel size (0.35 - 2 µm) and the number of pixels on CCD screen (2048x2048 or 1024x1024) detecting the signal after it is transferred to visible light frequencies and magnified. For all the three applied imaging modes, the sample edges are within the field of view. It is the intention to assess paper structure characteristics, and not defect characteristics. This involves that the cutting defects at the edges will in practise limit the size of the imaged volume, as the parts that have clear defects are discarded from the analysed volume.

The synchrotron source phase contrast 3D images have relatively large edge defects from cutting the paper into thin strips with a scalper. The resulting unaffected paper volumes are therefore considerably smaller than the maximum width of 0.7 mm. All four reconstructed volumes were approximately equally affected, as shown in Table 1 in Paper III. The length is restricted to 512 x 0.35 µm, as the image acquisition was limited to 512 cross sections to keep the data size of the volume to a reasonable level for consecutive storing, image processing and analysis at the time the images were acquired (in 2000). The paper samples had minor defects in the thickness direction. Except for the edge defects, only a few occasional fibres are deviating from normal features at the paper surface. The part of the fibres sticking abnormally out from the surface were removed in the digital paper volumes to avoid peculiar surface definition and ill-defined surface porosity.

The paper samples imaged by the commercial CT scanner was with intention kept narrower than the maximum of 2.1 mm, as it was the intention to compare the imaged volumes to the relatively small synchrotron source phase contrast digital paper volumes. The cut width was therefore slightly larger than 1 mm. Some of the imaged paper volumes at low resolution showed to be clearly deformed from the sample cutting and subsequent mounting. The width was therefore smaller than the maximum of >1 mm for some of the imaged paper volumes when aiming to extract as large volumes as possible from the data sets. The uncalendered newsprint volumes had the most severe defects, limiting the width to approx. 0.4 mm, as shown for 'Large' samples in Table 2 in Paper IV. The lengths of the imaged paper samples were normally approaching the maximum length, as the samples were not cut in this direction within the field of view. One of the dry filter paper volumes had a severe surface artefact, as a large fraction of the fibres in the surface was sticking up from the surfaces. This made it impossible to apply this volume for consecutive image analysis, as the surface definition with the rolling ball would result in a peculiar surface from the digital balls movement on top of the raised fibres. The structural assessment of the filter paper at low resolution thus only included one volume, contrary to the two assessed volumes of uncalendered newsprint and BSKP handsheet. The reason for the surface artefact is not known.

The synchrotron source absorption mode images were prepared by a totally different approach than the other applied modes. The samples were not cut by a scalper but punched out in circular shape. The punching appear to not crease the paper as much as for the cutting by scalper, but the fibres are picked out from the sample along the full circular edge. However, the edge defects do not affect the volume size considerably, as the maximum rectangle within the circular sample is only influenced at the corners touching the circular edge. After punching out the circular samples, the small paper areas are glued to a thin capillary. The combination of the cutting, subsequent handling of the small samples and then gluing them to the capillary, have for many of the imaged volumes resulted in a delamination of the structure in the edges. The edge delamination can be seen to the images in Figure 4.12. Another defect observed for two of the high resolution absorption mode images are artefacts on the top side looking like remains of glue absorbed on the surface. The fibre picking, delamination and surface artefacts limits some of the volumes to widths/lengths down to approx. 0.5 mm, compared to the maximum size of approx. 1 mm. Gained experience at beamline ID-19 at ESRF, have subsequent to this image acquisition shown that the edge effects advantageously can protrude outside the field of view, thus enabling little or no discarding additional to the area that is outside the maximum square in the circular imaged area.

Although the imaged paper samples are affected by edge defects for all three imaging methods, the edge artefacts are considered to yield little or no influence to the assessed structural characteristics, as the affected areas are discarded from the analysed areas. However, the smaller volumes will naturally be slightly less representative than achievable, as the assessed areas cover less material. The volume size might also influence the results, as discussed in more detail in Paper IV.

The synchrotron source absorption mode imaging is different in the sense that the samples are glued. The gluing is performed partly to avoid involuntary sample movement during rotation, which is known to introduce star shaped artefacts. The gluing is successful in preventing sample movement, as can be seen by the absence of star artefacts in the reconstructed cross sections. Even though the glue solved one problem, it introduced a new one. A special polymer that is fluid when heated and cures relatively fast when removed from the heat, is applied as glue. The glue permeates into the pores of the paper at the surface that is glued to the capillary. The glue is not a problem for visual inspection of the digital 3D structure, as the continuous glue phase is by nature relatively easy to distinguish from the fibre material constituents. However, the glue have overlapping greytones with the fiber phase, and is therefore difficult to remove from the digital structure for subsequent image analysis. The applied method for filtering, binarisation and glue removal was moderately successful in separating the glue from the fibre phase. Most of the glue was removed, but at the expense of fibre material in the lower half of the paper volumes. The basis weight calibration showed that up to 8.6 g/m^2 of solid material might have been removed by the glue removal. However, a considerable part of the loss might be due to a fraction of the fines material not being detectable at the applied resolution. A method exploiting the three-dimensional extension of the glue might have had more success in separating the two phases correctly, but it would require application of computers with higher capacity than the best available PCs. Image filtering applying edge preserving procedures, like anisotropic diffusion [127] or

SUSAN filtering [128,129] might have reduced the problem compared to the applied smoothing of the cross-section by averaging over the two adjacent slices.

The edge defects and gluing problem show a general problem for 3D imaging of paper at the resolution required for acquiring the details of the paper structure. The combination of high resolution and the CCD screen and increasing data size restricts the physical extension of the imaged volume. Cutting the paper samples into the required small sizes will eventually lead to some edge defects. Supporting the structure by embedding it in resin/epoxy is not desirable, as this will be detrimental for the contrast between fibres and voids. The best solution is therefore considered to be cutting the samples by methods known to crease the sample minimally and mount them in a manner that allow the defective edges to be outside the field of view. The gluing of the samples to a capillary may show to be the best possible mounting, as long as a gluing method can be found that prevent the applied glue to permeate into the paper structure. An alternative approach is to focus the image acquisition to thick boardlike paper samples, as the affected surface layers will then only include a small fraction of the imaged volume. The surface properties are also less important for such paper qualities than the thinner paper grades. It is recommended that other cutting and gluing systems are looked into. Alternative methods that might be more successful may include ion beam cutting and application of a glue with distinctly higher X-ray absorption than paper.

Effect of image processing of reconstructed cross sections

The cross sections obtained after image acquisition and subsequent reconstruction are clearly different for the three applied microtomography methods. The differences require that the cross sectional images are processed differently to yield segmented binary structure. The influence of the chosen filtering, binarisation and phase separation are therefore treated individually for the three microtomography applications.

The filtering of the phase contrast cross sections are the most difficult, as the outline tomography yields more or less the same average greytone for fibres and voids. The applied semi-automatic procedure is adapted to filter or smooth out the quasi-ring and star shape artefacts. Meanwhile the procedure must carefully preserve the fringe pattern at the phase borders and fill the fiber phase, even where the phase border is weak or almost non-existing. The semi-automatic procedure over numerous steps have shown to be necessary to extract the structural information in the images with a low level of disturbing artefacts and noise. Automatic routines have been tested, but all yielded considerably noisier binary cross sections than obtained by the semi-automatic routine. It is therefore considered that for the difficult and unique high resolution phase contrast images, the applied semi-automatic procedure are preferable.

The main disadvantages with the applied routine is the required time to perform the filtering and segmentation. Producing a binary cross section of high quality took several days due to the interactive selection of seed points and processing on a moderately fast computer by year 2000 standards. A minor disadvantage is removal of the star shaped artefacts, which could not be distinguished from fibrils. It is therefore likely that the binary 3D image of the uncalendered newsprint sample have a too low level of fibrils in the structure. Removing the quasi-ring shaped artefacts could not be done completely, although the smoothing and filtering in the perpendicular direction succeeded in encountering/reducing the greytone frequency below a detrimental disturbance level for the outer rings. The inner zone quasi-ring artefacts was detrimental to the local observed paper structure. For the worst influenced reconstructed volume, the uncalendered newsprint, about 2% of the volume was clearly influenced by the noisy quasi-ring artefacts. The quasi-ring artefacts have been considered removed by other methods, but the best possible method, averaging with intermediate flat-field images, could not be applied as no intermediate flat-field images were obtained during the 180 ° scan. It is also a possibility to remove the rings by an alternative transform as *e.g.* an adapted Hough transform. However, the complexity of the method performed on a full 3D data set and the already achieved quality of the applied semi-automatic procedure discouraged further investigation of this possibility.

Altogether it is assumed that the applied procedure yield 3D data sets of good quality well suited for subsequent analysis. It should also be emphasized that the early stage of the technique resulted in more artefacts in the images than what is apparent in reconstructed synchrotron source 3D images after four years of progress. It has also shown to be possible to achieve 3D images of good quality with absorption contrast exploiting the high spatial coherence at beamline ID-19 at ESRF. The improved quality of the synchrotron source microtomography images and good quality images in absorption mode have therefore discouraged possible further development of image processing of near-field phase contrast 3D images.

The applied procedure for segmenting the synchrotron source absorption mode cross sections yield binary structures of decent quality. The absorption contrast is in principle much easier to process, as the greytone levels of fibres and voids are mostly covering different ranges. However, due to the sample mounting there is a third phase, the glue, distributed in the intermediate greytone range between voids and fibres. The segmentation and removal of this phase yields the main challenge in the image processing. It should also be mentioned that the applied processing do not exploit the apparent phase contrast visible at most phase borders between fibres and voids and glue and voids. An edge preserving filtering technique would as such most likely be better suited for removing the small scale greytone variation in the data set than the applied uniform smoothing. Well suited filtering techniques include anisotropic diffusion [127] and SUSAN [128,129] filtering. The smoothing probably results in a higher fraction of misclassified voxels than what would be achieved with optimally tuned edge preserving filtering. However, most of the misclassified voxels are removed in the last binary filtering step, removing small isolated volume objects.

The largest disadvantage of the absorption mode processing is its moderate success in removing the glue that have permeated into the porous phase of the structure. The best solution to the gluing problem is to avoid it from permeating into the structure. However, when the damage have happened, methods must be found to remove the glue in the 3D data sets. Independent of chosen method, the segmentation between glue and fibres will never be perfect as long as the glue phase is in the transition greytone level between fibres and voids and have no clear boundaries between fibres and glue. It is therefore considered that the possibilities of exploiting the 3D extension of the fiber elements would only yield slightly improved 3D images. Application of edge preserving filtering might have resulted in a better phase separation after filtering and global thresholding, but the absence of phase contrast between fibres and glue would limit the improvement.

The low resolution microtomographic images were obtained applying a commercial CT scanner. The acquired 3D images have a histogram distribution of greytones where the voids are only represented by a single greytone. The histogram distribution appear to be more or less constant throughout the volumes. This leaves little room for alternative image processing than the applied global threshold. The processing is thus in fact only a choice of which greytones are regarded as noise and can be included in the void phase. The nature of the acquired cross sections might be a result of the 'black box' processing of the transmitted X-ray signal performed by the software included in the SKYSCAN set-up. The applied image processing, included the subsequent binary filtering removing small isolated 3D objects, are therefore assumed to be the best possible processing of the obtained greyscale cross sections.

4.4.2 Effect of resolution and image size

The effect of voxel size/spatial resolution and volume size are important parameters influencing the assessed structural characteristics. The size order of these effects comparing high resolution phase contrast imaging obtained from synchrotron radiation to low resolution 3D imaging, applying a commercial CT scanner, have been thoroughly investigated in the attached Paper IV and by subsequent 3D analyses and simulations performed at the Australian National University (ANU) [84].

Evidently, the results will also be affected by differences in detection mode (phase contrasting or absorption), volume reconstruction and image processing, which are difficult to distinguish from the resolution and image size effects by only performing a direct comparison of images obtained at the different resolutions. The experimental scheme thus also include image cropping and resolution downscaling in order to isolate the pure resolution and image size effects. The attempt to isolate the pure resolution and image size effects were only performed for the permeability simulations (including the surface layers), as it is considered that the flow simulations in general are most sensitive to the detail level and the extension of analysed structure and will thus reveal the clearest differences. The chosen property for isolating the pure resolution and image size effects were chosen to give an alternative approach to the results obtained from the analyses performed at RSPhysSE, ANU.

To isolate the image size results one of the maximum size low resolution 3D data sets were chosen for each paper grade. The chosen maximum size, low resolution data sets were then divided into as many subvolumes as possible having the same size as the identically sized small volume for high and low resolution. The permeability were then determined for each of the small subvolumes according to normal procedures. The subvolumes are identified with the tag 'LSub'. To isolate the resolution effects the resolution of the high resolution volumes were decreased by combining voxels and assigning the larger voxels with a solid fraction lower than 50% to the void phase. The resolution was reduced down to that obtained for the low resolution images. The downscaled volumes are identified as 'red.res.'. The results from the attempt to isolate pure resolution and image size effects are summarized in Figure 4.32.

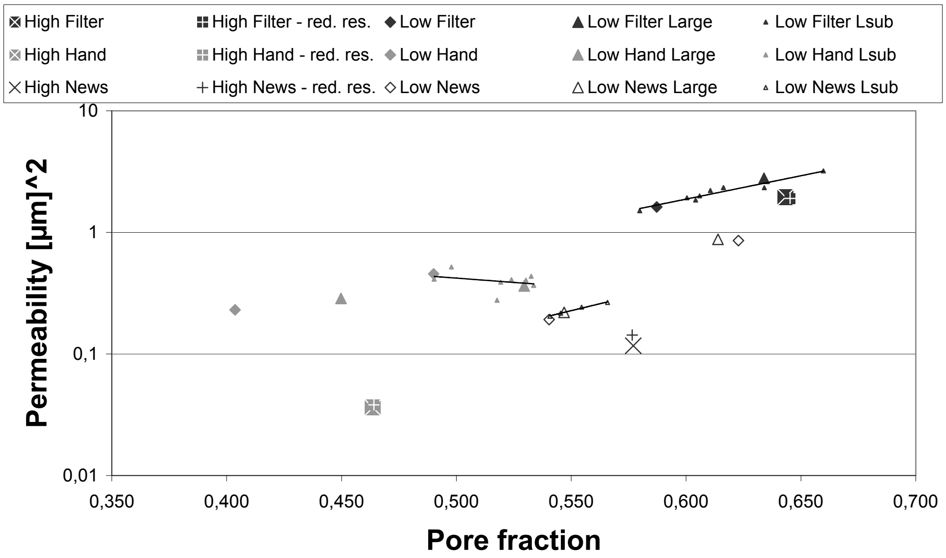

Figure 4.32 The effect of resolution and image size to the assessed permeability for the three investigated paper grades of BSKP handsheet, uncalendered newsprint and cotton linters filter paper. The 'LSub' volumes are subvolumes of one of the large low resolution volumes, where the size is identical to the Low and High volumes (see Table 2, Paper IV). The 'red. res.' volumes are the high resolution volumes, where the voxels are merged to yield a resolution reduced to 2 µm, the same as for the low resolution images. The drawn lines are the best exponential fit for the large, low resolution images and their subvolumes of the three more thoroughly investigated low-resolution volumes.

The attempt to isolate the image size and resolution effects yielded clear results. The image size effect seen from comparing the subvolumes (Lsub) to the large low resolution sample showed to have little influence on the determined permeability. However, the resolution of the two image acquisitions proves to have a clear effect on the permeability. The lower resolution of the commercial CT-scanner leads to a higher permeability as the resolution is insufficient to detect many of the small fibre network details limiting the transport through the structure. Reduction of the resolution of the high resolution images have little or no influence on the permeability, as few significant features are lost in the resolution reduction. The resolution effects are most pronounced for the dense and complex structures of BSKP handsheet and the newsprint, for which the permeability is approximately one order of magnitude larger for the low resolution images compared to the results for the high resolution images. The more open structure of the filter paper is almost unaffected by the resolution. The resolution effects on permeability are in good agreement with the findings based on lattice-Boltzmann simulations of permeability performed at RSPhysSE, ANU, shown in Figure 4.27.

The difference in the pore size data between the high and low-resolution images is believed to be mostly due to insufficient resolution on the low-resolution scanner. The effect of distortion of the high-resolution image have been considered by convoluting this image with an isotropic 3D Gaussian blurr. The effect of blurring a high resolution image of newsprint is shown in Figure 4.33, where successive distortion with a gaussian of different σ is shown. The blurred images are then phase separated to give the same pore volume. The resultant pore size distribution of the high resolution image is strongly changed by distortion moving in general to larger pore sizes. The high resolution image after distortion by a gaussian blur of standard deviation $\sigma = 3$ µm (or $\sigma = 8$ voxels) is visually similar to the higher resolution samples. The calculated pore size distribution on the high resolution images after distortion with a Gaussian of $\sigma = 3$ µm is shown in Figure 4.34. The true resolution of the images obtained on the commercial scanner is likely a few times worse than the applied σ in the plots. True resolution would be dependent on the contrast between the fibre matrix and air. Studies have been undertaken across a range of σ. The results indicate that the minimum resolution required for accurate measurement of pore structure for generic paper samples is approx. 1 µm.

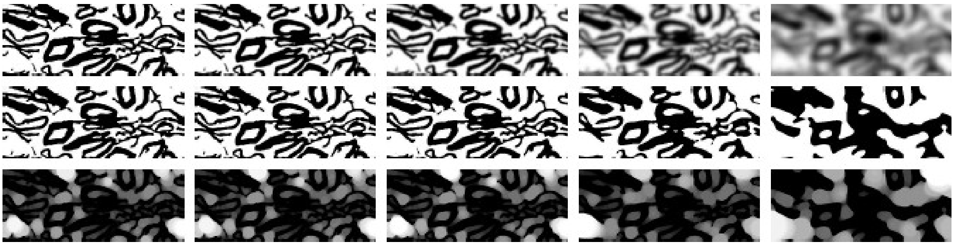

Figure 4.33 Illustration of the effect of distortion on an image of newsprint. **First row:** Left hand image is synchrotron image at 0.35 µm resolution. The images in the next four columns are after blurring with a Gaussian of $\sigma = 1, 2, 4$ and 8 voxels. **Second row:** The image after phase separation to the same pore phase fraction. **Third row:** The corresponding distribution of pore sizes in the white (pore) phase. The grey scale is proportional to the pore size.

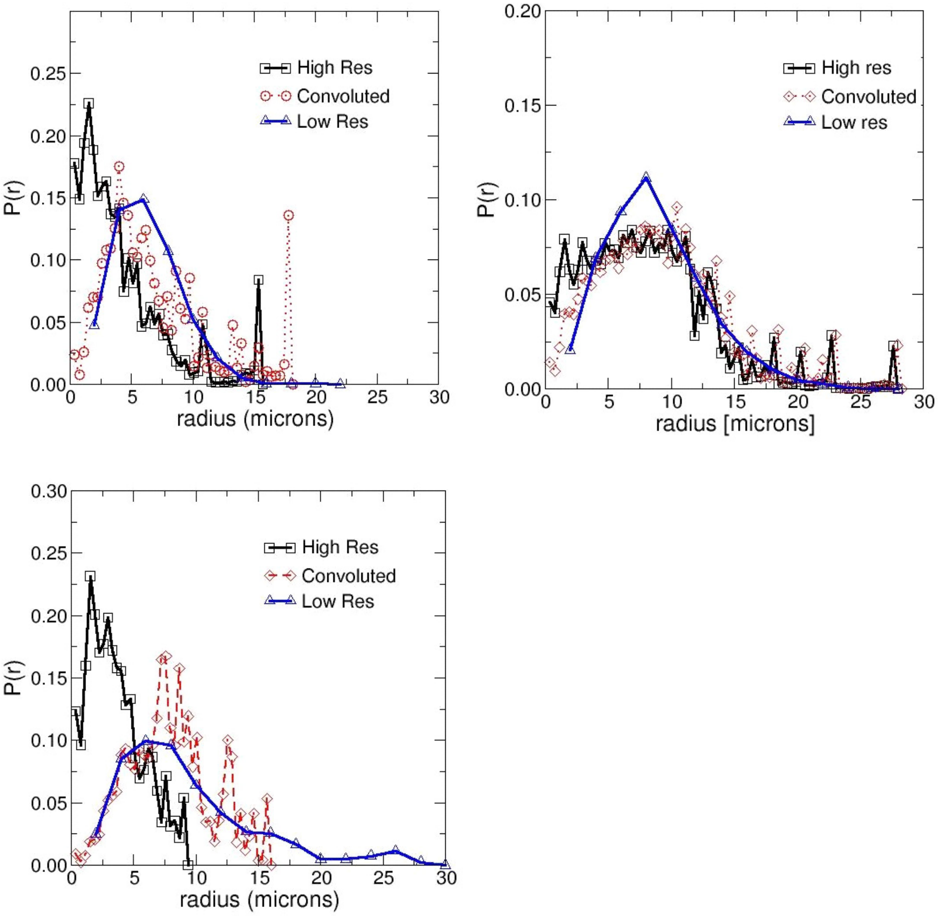

Figure 4.34 Pore size distributions of **Top, left:** the handsheet, **Top, right:** the filter paper and **Bottom:** the newsprint on both low-resolution (blue) and high-resolution (black) images. The red, dashed curve shows the high resolution data after convolution with a Gaussian filter with $\sigma = 3$ μm.

The investigation of resolution effects has shown that the increased detail level in high-resolution X-ray microtomography positively affects the measured structural characteristics determined from image analysis of the 3D images, although both synchrotron and stationary source techniques detects approximately the same amount of solid material. The higher detail level in high resolution images result in higher specific surface area, generally smaller hydraulic radius, higher tortuosity and lower permeability with clearer differences between samples and principal directions. The differences, especially for transport properties, are more pronounced for the low porosity paper grades compared to the more open structure of the filter paper. The high-resolution images are expected to yield more physically reasonable results and to be less affected by noise. The higher detail level implies more correctly measured parameters, which makes the high-resolution images more suitable for fundamental research on improving the knowledge on how the paper structure affects paper properties as *e.g.* optical and transport properties.

The disadvantage of the high-resolution images is low availability and high cost of required hard X-ray beam time. It can thus sometimes be a good alternative to apply the low-resolution technique despite the lower detail level when doing comparative studies. The availability is better and the cost much lower than for the high resolution technique, and the detail level is sufficient to give structurally dependent trends as long as the various paper grades show sufficient structural variation. However, applying low-resolution images even for comparative studies can be misleading if the range of porosity and/or complexity of the analysed structures are too wide. Particularly paper grades containing a high level of fines are poorly suited for the low resolution 3D imaging.

The lower cost of the low resolution CT scanners also makes it more realistic to image several replicates, which improves the representativity of the small imaged volumes better than increasing the size of the imaged volumes.

4.4.3 Effect of formation and representativity of assessed paper volumes

A major concern of the application of 3D image acquisition and subsequent assessment of the obtained digital paper structures is the representativity of the rather small volumes. Comparing the replicate low resolution volumes shown in Figure 4.32 and the study of basis weight variation performed in Chapter 5 for high resolution images (Voxel dimension = 0.7 μm) yields indicative results on the effect of formation and the representativity.

The results show that the standard deviation for most assessed geometric structural properties is within ±10% of the determined mean value for the high resolution absorption mode 3D images. This is a promising result regarding formation effects and representativity, as the assessed data sets most likely have a higher basis weight variation than most (commercial) paper grades due to the paper being made on a slow (20 m/min.) Fourdrinier pilot paper machine, shives occurring with a relatively high frequency in the volumes and an effect from digital removal of glue from the structure. Additionally the areas chosen for the replicate samples were chosen to get as wide selection as possible of basis weights. It is therefore likely that the small volumes acquired at a resolution of 0.7 μm are sufficient to yield indicative results of detailed paper structure characteristics, as long as caution has been taken to avoid areas of clearly high or low basis weight areas of the sheet.

The situation is somewhat different regarding transport properties. The transport simulations will always have a tendency to emphasize the areas with the highest porosity within a given volume, as the resistance against transport is the smallest in these areas. The emphasis on the high porosity areas are in accordance with the physical behaviour of fluid transport. However, the behaviour render the transport properties to be more dependent on the occurrence of low resistance areas than they are on the average structure within the volume. Transport properties thus naturally show a higher variation between replicate volumes than the geometric structural parameters, especially for the z-directional flow. The diffusivity was found to vary by ±10% in MD, ±10% in CD and

±25% in z-direction. The variation of permeability was found to be even larger than for the diffusivity, with a determined variation for the five replicates of ±30% in MD, ±40% in CD and ±85% in z-direction.

The simulated transport properties are more dependent on porosity than on the basis weight. The results presented in Figure 4.32 show that permeability is exponentially dependent on the porosity. This is particularly clear for large filter paper volume and its corresponding subvolumes. The same behaviour is taken into account when determining the transport properties of the high resolution absorption mode 3D images as a set of subvolumes rather than determining a single value for the complete volume. The approach thus provides the structures dependency to the varying porosity areas in the volume, which provides a more informative assessment and more representative result than a single value for the whole volume. The exponential behaviour of z-directional permeability to the porosity for the high resolution phase contrast mode images can be seen in Figure 4.28.

The results obtained for the five replicate volumes of the s4 sample from the factorial design show in addition to the variation between the small subvolumes also the variation between the full volumes. Figure 5.12 shows the variation for the z-directional permeability in the absorption mode volumes. Figure 5.13 include the variation of the in-plane permeability both for the machine- and cross-direction. The results show the exponential relationship between permeability and porosity for the subvolumes and that the relation also applies for the larger independent volumes. However, the deviation from a common exponential relationship are most pronounced for the z-direction. As expected the s4 volume, containing a large shive, is the sample that deviates most clearly. The higher level of variation for the z-direction is most likely due to the layered structure of paper, which yields a higher sensitivity to localized high porosity areas for the z-directional transport compared to movement in the in-plane directions.

4.5 Conclusion

The results from this study show clearly that X-ray microtomography can be applied successfully to obtain 3D images of paper of high quality preserving the essential topology of the imaged paper samples. The artefacts introduced during image acquisition, volume reconstruction, sample preparation, mounting and image processing have been determined to be of little influence to the results of the structural and transport assessments. The major exception is the sample mounting with melt glue for the synchrotron source absorption mode images. The melt glue penetrated into the structure and the subsequent removal of the glue from the digital images introduced a random and relatively large variation of basis weight and surface structure in one of the surfaces of the paper volume.

Both high resolution phase contrast and absorption mode imaging have been performed at the synchrotron source facility at the ESRF, France. The applied spatial resolutions of approximately 1.0 and 2.0 µm respectively have both shown to be sufficient to acquire reasonable assessments of structural and transport characteristics able to distinguish the performance of different paper samples. The volume reconstruction of phase contrast images was extremely difficult and required semi-automatic routines to obtain satisfactory results. The semi-automatic reconstruction routines are labour and computationally intensive. The quality and preserved detail level of the binarised

absorption mode images (voxel = 0.7 μm) are comparable to the binarised phase contrast images (voxel = 0.35 μm), despite the lower resolution of the greyscale images. As the filtering and segmentation of the absorption mode images were much easier and could be done applying automatic routines, application of absorption mode imaging are recommended for later acquisition of high resolution 3D images.
The low resolution images obtained using a commercial CT-scanner showed to be of considerably lower quality than the high resolution 3D images. The spatial resolution of approx. 5 μm is not capable of detecting the small details especially influencing the specific surface area and transport properties. The effect of resolution is most pronounced for low porosity samples. However, the low resolution images have shown to detect the larger pores relatively correctly. The low resolution technique may therefore be capable of ranking assessed paper samples correctly, although the numerical values for the measured parameters are incorrect due to the low detail level. The low resolution images are thus not well suited for fundamental research on improving the knowledge of how the paper structure affect various paper performance properties.

Although the image acquisition were successful for the paper samples assessed in this study the experiments have shown some limitations to the technique. It was not possible to obtain high quality images for high density paper grades when applying the phase contrast imaging mode. The phase contrast technique is also known to be unsuitable for acquiring images of paper grades containing pigments. The absorption mode image acquisition is not known to have such limitations. However, future studies applying absorption mode imaging should study possible limitations to the technique. A common limitation for all techniques is the resolution. The technique can thus not to date yield correct simulations of optical properties, as the required resolution is approximately 0.2 μm, half the wavelength of the highest frequency of visible light.

The main objection against the X-ray microtomography have been the small size of the assessed paper volumes compared to the known size of flocs found in paper. The study showed promising results for X-ray microtomography regarding these objections. The standard deviation of specific surface area and different pore geometrical characteristics showed to be less than ±10% of the determined mean value for five replicates showing larger basis weight and structural variation than five randomly chosen paper volumes. The transport properties show a larger variation between different replicate paper volumes, as these are strongly dependent on porosity. The problem can be omitted by determining the transport properties for a set of identically sized subvolumes, for which a transport property:porosity relationship can be found, instead of obtaining a single value for the complete volume.

The study included assessment of several structural and transport characteristics. Among the studied characteristics there were a focus on different aspects of the pore geometry (pore chords, hydraulic radius, pore size (volume) distribution) and transport properties (diffusivity and permeability). The results obtained for the applied characteristics showed expected trends between samples and the orthogonal directions within the paper volumes. The assessed structural and transport properties were able to yield useful information on how various paper making variables influences the detailed paper structure, although the experimental scheme and a large random effect from digital glue removal somewhat limited the results obtained from the analysis of the factorial design.

The findings in this study, introduction of high resolution 3D images as source for structural assessments, introduction of new structural and transport characterizations and new and improved methods for determining some of the other properties are considered to be important steps in the initial stage of the application of X-ray microtomography in fundamental research in paper. The future development of the technique and suggestions for further work included in this thesis will hopefully show improved and extended application of X-ray microtomography for paper research.

CHAPTER 5

A PRACTICAL EXAMPLE OF THE APPLICATION OF X-RAY MICROTOMOGRAPHY FOR PAPER RESEARCH

5.1 Introduction

The initial image acquisition of 3D images, as presented in Paper III and IV, was not designed to show any systematic variation in paper properties. The selected papers were chosen with regard to testing the X-ray microtomography techniques ability to successfully depict the detailed 3D structure of different paper grades. It was therefore difficult to evaluate the potential of the technique for applicable assessment of the paper structure characteristics. The lack of systematic evaluation of the imaged paper grades and unknown processing variables made it difficult to apply the measured structural properties for gaining knowledge of how the detailed paper structure change according to raw material and paper making variables, and how the paper structure influences the bulk paper performance properties.

The application of 3D imaging and analysis of paper is in an early stage. The main focus have therefore been on presenting the principles of the technique and showing that it can be applied successfully for 3D image acquisition of a variation of paper and board qualities. However a research tool have not been proven useful before it is shown that the technique can be applied for gaining knowledge of the properties of paper material not more easily accessible by other methods. To obtain more than what is achievable from visualization of the 3D volumes, quantifications of the structural properties are necessary. However, to relate the assessed structural properties to input variables and bulk properties it is a need for an experimental scheme where the paper making variables can be controlled and quantified and there is a large quantity of paper where bulk paper properties can be measured.

Only one experiment investigating a controlled paper making variable have already been performed and published for 3D image acquisition and structural analysis for paper and board. An extensive analysis have been performed on the acquired set of 3D images, where different assessed structural properties have been published in a number of publications including Ramaswamy et al. [76], Huang et al. [77], Goel [82], Gupta et al. [131] and Aaltosalmi et al. [86]. The results have shown the applicability of relatively low resolution 3D images, obtained by a commercial CT scanner, to quantify differences in the paper structure features of boardlike handsheets according to refining levels.

Although quantifications have been performed in other scientific application of 3D imaging and analysis of paper samples, there have been only one investigated volume [26,72], or there have been no systematic range of the paper structural properties of the imaged paper grades [46,79,80,81,83].

It is the intention of this study to perform a controlled experiment applying X-ray microtomography from a synchrotron source for 3D imaging and perform 3D image analysis and simulations of the resulting digital paper structures. The main goal of the experimental scheme is to show how the 3D imaging and assessment of the digital paper volumes can be applied to gain knowledge of the influence of paper making variables to paper structure and how features of the detailed paper structure may affect bulk paper performance properties. A successful experiment will support the usefulness of applying X-ray microtomography for gaining knowledge of the detailed material properties of paper.

5.2 Materials and methods

5.2.1 The analysed paper grades

The experimental scheme was performed according to a 2^{4-1} factorial design [132] to enable a preliminary study of the effect of several paper making variables simultaneously. The paper was made on a pilot paper machine to best resemble commercial paper making, while still having control over most paper making variables. Paper making on a pilot paper machine have also the benefit of producing a high quantity of paper, which can later be applied for imaging and paper testing. The control over all paper making variables enables measurement and keeping the variables that are not part of the experimental scheme close to constant. The chosen pulp was a thermo-mechanical pulp made from Norwegian spruce at a Norwegian paper mill. The pulp was retrieved after second stage refining, but before screening and latency treatment. The applied pulp thus contained a fraction of shives. The measured pulp properties before latency was 5.4 shives per gram of dry pulp. The freeness level (CSF) was 145 mL. Latency treatment (10 minutes at 80° C) was applied to the mechanical pulp fibres before papermaking to achieve realistic sheet forming.

The paper was produced on a Fourdrinier pilot paper machine built in the 1960’s. The width of the paper from the paper machine is approx. 0.55 meters after trimming. All the paper grades manufactured in this study were produced at a machine speed of 20 m/min.

Four paper making variables where chosen, which were thought to likely have a major influence of the paper properties, but through clearly different mechanisms. The variables where chosen at levels that were assumed to affect the detailed paper structure. The chosen factorial design was a reduced two level 2^{4-1} design, yielding eight different paper grades. The chosen paper making variable were:

- Pulp consistency in head box
- Addition of reinforcement pulp (BSKP)
- Addition of a fixation agent
- Calendering

The pulp consistency in the head box was chosen because this was assumed to influence fibre orientation and degree of felted structure. The special design of the head box on the pilot paper machine had no possibility for adjusting the jet to wire ratio, which was by design locked to a 1:1 ratio. The higher consistency is assumed to result in higher flocculation and thus a higher fraction of the fibres resisting against orientation in the flow direction when passing the constriction in the head box ‘lip’. The head box consistency is a difficult variable to control and adjust during paper making, as the measurement of consistency, applying the standard gravimetric method, is relatively time consuming. The variables will thus alter in a more random fashion than the desired high and low levels in the factorial design. However, as long as the consistency is known this effect can be accounted for in the analysis of the factorial experiment.

The reinforcement pulp is known to improve the strength properties of paper, but the detailed mechanism for the strength improvement is not known. It is considered likely that at least part of the mechanism is an alteration of the detailed paper structure. To assure that the reinforcement pulp had a significant effect and that a fraction of reinforcement fibres could be found in all the small imaged paper volumes, where an addition of 20% of total pulp applied. The reinforcement pulp was a commercial bleached softwood kraft pulp. The chemical pulp was beaten in an industrial refiner at an intensity of 15 kWh/ton prior to sheet forming. The pulp had a dewatering level of 23 °SR after refining.

The addition of fixation agent was assumed to increase the wire retention considerably and thus result in a higher fraction of fines material in the structure. The fixation agent, a linear low molecular weight cationic polyelectrolyte (cross-linked epiclorohydrin-dimethylamine (Epi-DMA)), was added to the stock chest, where the pulp suspension was under constant mixing. The applied dosage was calculated based on stock chest consistency and level. The addition of fixation agent was 0.08%. The dosage is approximately 50% higher than normal dosage applied for the fixation agent at a commercial paper mill. The dosage was increased to assure clear effects and to compensate for the non-ideal addition point.

The calendering was performed off-line on a pilot soft nip calender. The calendering is assumed to increase the solid fraction of the paper structure considerably. The calendering in the resilient nip will introduce an additional two-sidedness to the structure, as the calendering was only performed once in a single nip configuration.

The factorial design and chosen levels are summarized in Table 5.1.

Table 5.1: The factorial design of the experiment. The numbers in parentheses show the applied levels of the variables for the analysis of the factorial design experiment.

Sample #	Calendering level (kN/m)	Mass fraction reinforcement fibres	Head box consistency (%)	Addition of fixation agent (mg/kg fibres)
s1	0 kN/m (-1)	0.0 (-1)	0.40 (-1.04)	0.0 (-1)
s2	120 kN/m (1)	0.0 (-1)	0.54 (1.07)	0.0 (-1)
s3	120 kN/m (1)	0.20 (1)	0.41(-0.98)	0.0 (-1)
s4	0 kN/m (-1)	0.20 (1)	0.53(0.96)	0.0 (-1)
s5	120 kN/m (1)	0.20 (1)	0.51(0.56)	0.8 (1)
s6	0 kN/m (-1)	0.20 (1)	0.40 (-1.12)	0.8 (1)
s7	120 kN/m (1)	0.0 (-1)	0.42 (-0.86)	0.8 (1)
s8	0 kN/m (-1)	0.0 (-1)	0.56 (1.38)	0.8 (1)

The paper manufactured on the pilot paper machine was stored under standard climate conditions for paper (50 RH(%), 23 °C).

The manufactured paper was thoroughly tested for standard bulk paper properties. The measured paper properties were chosen for control of uniformity and to test if the factorial design had succeeded in introducing expected differences in paper properties assumed to be affected by the detailed paper structure. The measured bulk paper properties could later be applied for studying correlations between assessed structural characteristics and bulk paper properties.

5.2.2 Method for assessing effect of basis weight variation

Background

A problem that is unavoidable when acquiring 3D images of paper is that the volume of the 3D images at the needed resolution is smaller than, or in the size order of, the flocs in the paper. The flocs are assumed to be of major influence to the variation in paper structure parameters. The variation in paper caused by flocs can be quantified as the variation of basis weight at an appropriate scale level. The high cost and low availability of the desired synchrotron source X-ray microtomography imaging render it difficult to acquire the required number of replicates to obtain statistically significant measures of the structural properties for the non-uniform paper material. It is thus desirable to find a method for assessing the effect of basis weight to possibly adjust the measures of single, small volumes to more representative values.

Principle

The approach for assessing the basis weight variation is based on determining the basis weight of the same paper volume by both beta radiation formation images and 3D images obtained by X-ray microtomography. A conversion between the basis weights measured by the two methods can then be found. This requires several replicates of the same paper grade to be assessed by both methods. Replicates of 3D images of the same paper grade also enable a quantification of the effect of basis weight to the assessed structural features. When an applicable conversion between the beta radiation and X-ray microtomography basis weight have been found, it is assumed that the basis weight distribution from the beta radiation imaging and the conversion can be applied to find whether the imaged 3D paper structures are obtained from high or low basis weight areas. Structural properties that are observed to be influenced by basis weight effects can thus be adjusted to the expected value for the mean basis weight of the paper grade.

Acquisition of the basis weight of small areas applying beta radiation method

It is essential that the same areas are assessed by the two imaging methods. To achieve this there is a need for a reference in the measured paper sheets that is not affecting the local paper structure. This was accomplished by taping small parts of polyethylene transparencies with a small circular hole along the edge of the imaged paper sheet, as shown in Figure 5.1.

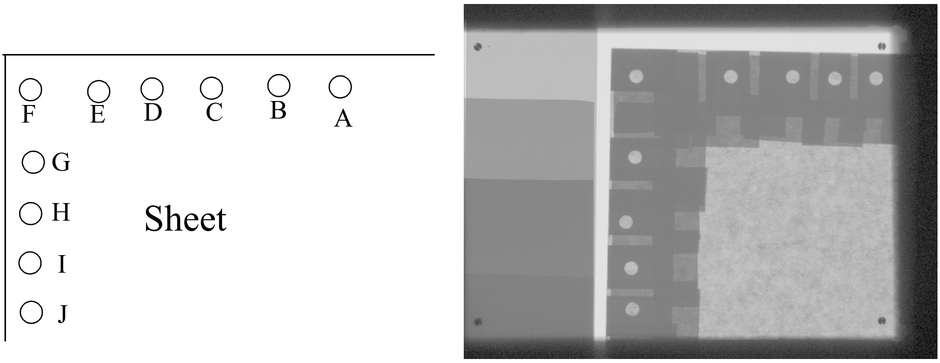

Figure 5.1 **Left**: Each circular hole in the adhered transparency pieces was assigned a letter for recognising the positions relative to one corner in the paper sheet. **Right**: The sheet with the adhered holed transparency pieces are exposed to beta radiation for 20 minutes and a formation image where the individual circular areas can be recognised and a basis weight can be determined relative to the reference in the left edge of the image. Note that an extra image was needed to cover circle A.

The beta formation images were acquired on a Fuji BAS 1800 II scanner. The height and width of the imaged area, including the reference and surroundings on three sides, had a width of 1000 pixels and a height of 750 pixels. The pixel resolution was 0.2 mm. An exposure time of 20 minutes was applied. Four constant reference areas with known basis weight were included in all beta formation images for calibration.

The application of the holed transparency pieces were successful in determining the basis weight for small areas applying beta radiation. The circular holes were subsequently marked with a pen following the contours of the holes in the transparency pieces. The attached polyethylene transparency pieces could then be removed. The marked circles were later applied as a guidance for cutting the smaller circular samples for X-ray microtomography imaging, as close to the centre as possible. For the correlation it was assumed that the X-ray microtomography images were obtained for the exact middle of the circles. The beta radiation basis weight was therefore determined for small circular areas centred inside the larger circles. The small areas was chosen to approximately the same size as the imaged surface area in X-ray microtomography imaging in absorption mode at ID-19, ESRF. The different areas are illustrated in Figure 5.2.

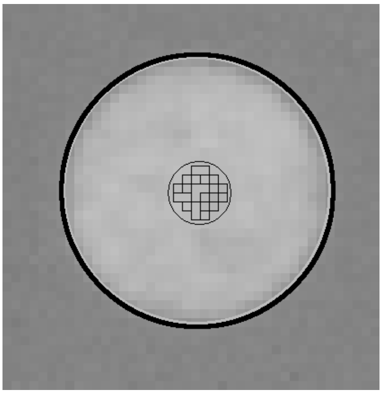

Figure 5.2 The different areas in a selected marked circular area (D) of the beta radiation image applied for finding the correlation between basis weights as determined by X-ray and beta radiation imaging. The large circle emphasize the size of the area limited by the adhered polyethylene transparency pieces. The smaller circle show the position and size of the area imaged by X-ray microtomography assuming the paper is cut in the exact centre. The squares mark the pixels which were applied for determination of the basis weight applying the beta radiation formation image. The area is the best achievable approximation to the circular X-ray imaged area for the 0.2 mm sized pixels, when restricting the extension to be inside the assumed X-ray imaged area.

After measuring the basis weight for the 10 marked areas in the beta radiation formation images according to the described method, the 4 areas which showed the widest selection of average basis weight for the 24 pixel large subaraes were chosen for subsequent X-ray microtomography imaging. The basis weight variation inside the small subareas was relatively small for all subareas.

In addition to the beta radiation formation image that was obtained for correlation between beta and X-ray radiation imaging, one beta formation image were acquired for each of the slightly different paper grades from the factorial design experiment. The beta formation images were applied for finding the average basis weight, as acquired with beta-radiography, and the distribution of basis weight. The acquired images were applied to determine measures of formation. However, the main intention was to apply the distribution for estimating the divergence from the average basis weight for the assessed volumes for the eight samples from the factorial design experiment.

5.2.3 3D image acquisition

The 3D images were obtained by synchrotron source X-ray microtomography applying absorption mode imaging as described in Chapter 4. The size of the analysed digital volumes are given in Table 5.2. The dimensions are limited by edge defects of the imaged circular area. The edge defects are fibre picking and delamination from the cutting and gluing of the sample to a capillary. Areas that show clear structural defects or artefacts like *e.g.* glue on the top surface are discarded when possible. Shives are considered to be a normal variation of the structure and not an artefact. The volume size is given as surface area, as the thickness of the assessed paper volumes are varying.

Table 5.2: The dimensions of the imaged paper volumes. The volumes given in bold are from calendered paper samples.

Sample	**Surface area - MD x CD (mm^2)**
A	0.830 x 0.630
B	0.941 x 0.770
E	1.022 x 0.770
I	0.557 x 0.819
s1	0.837 x 0.679
s2	**0.630 x 0.553**
s3	**0.806 x 0.518**
s4	0.582 x 0.602
s5	**0.704 x 0.469**
s6	0.770 x 0.511
s7	**0.665 x 0.483**
s8	0.770 x 0.518

5.2.4 Image segmentation and analysis routines

The digital paper volumes were binarised and filtered as described for high resolution 3D images in the materials and methods section of Chapter 4. The methods for the assessed characteristics of the detailed paper structure are also given in Chapter 4. The specific surface area (SSA), pore chords (<g>), structural anisotropies, hydraulic radius and restricted random walk (rw) tortuosity are all determined including the surface volume of the sample.

The surface to volume ratio (S/V), interior pore chords, mean pore radius (maximal sphere method), critical radius, diffusivity and tortuosity (based from conductivity simulation) and permeability are all determined for the largest possible interior volume excluding the surface areas.

3D visualization of the final binarised imaged digital 3D paper structures are shown in Figure 5.3 and Figure 5.4. The figures show both surfaces of an uncalendered (s6) and a calendered sample (s5).

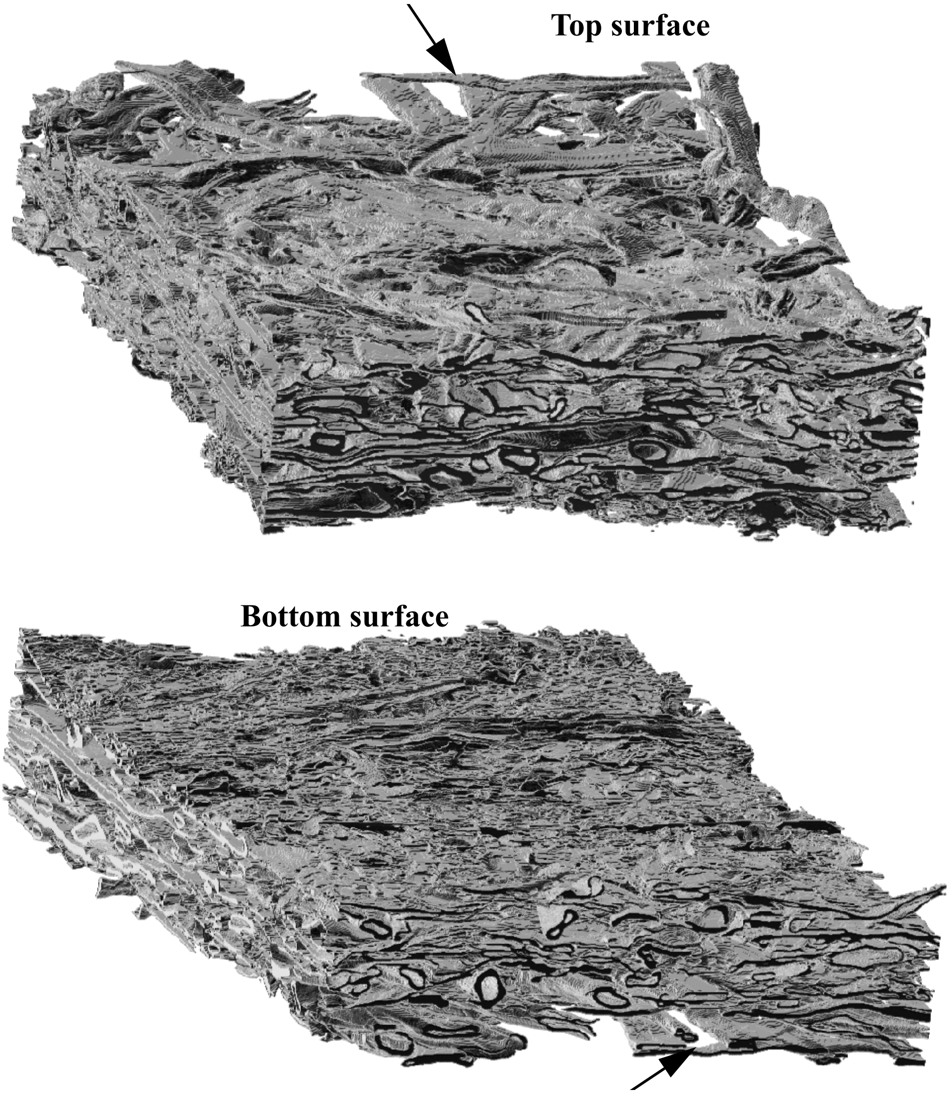

Figure 5.3 3D visualization of an uncalendered paper sample (s6). **Top:** The upper surface of the volume, the top side of the sheet. **Bottom:** The lower surface of the volume, the wire side of the sheet. (The volume is flipped 180 ° relative to the upper visualization). The digital removal of glue, that have penetrated into the structure, clearly introduce structural defects to the surface.
The arrows indicate the same fibre as seen in the two visualizations.

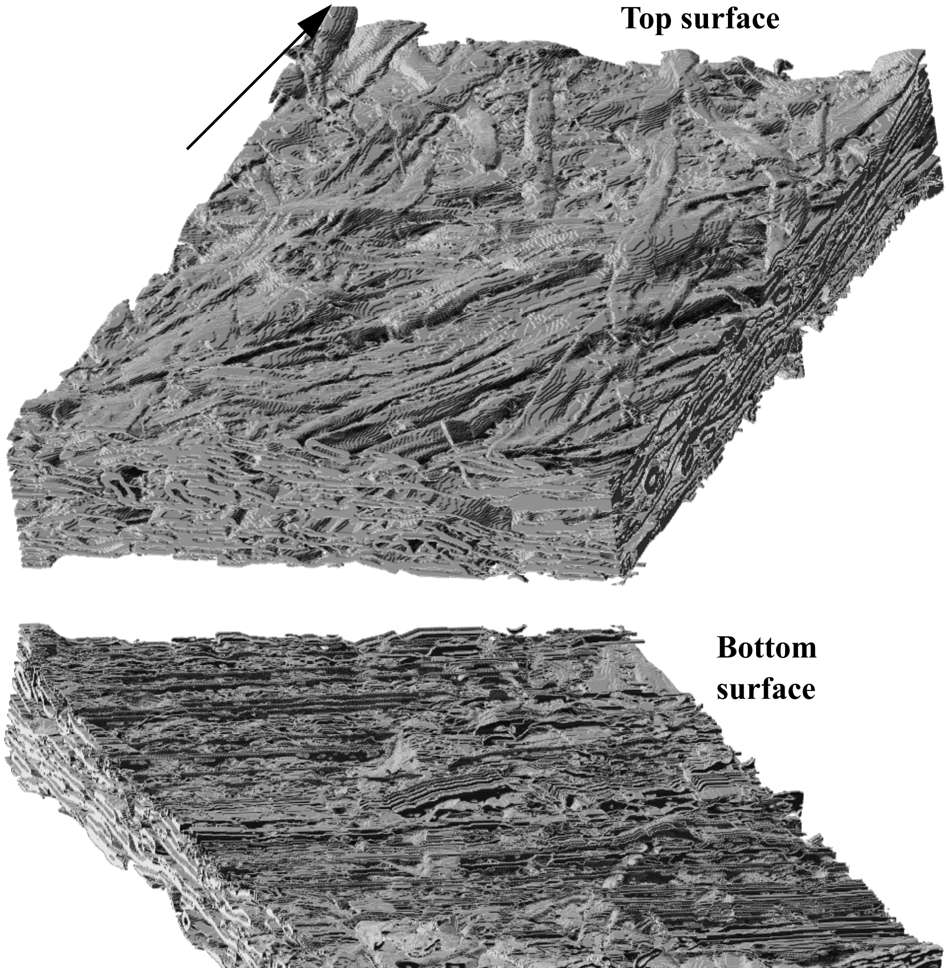

Figure 5.4 3D visualization of a calendered paper sample (s5). **Top:** The upper surface of the volume, the top side of the sheet. **Bottom:** The lower surface of the volume, the wire side of the sheet. (The volume is flipped 180 ° relative to the upper visualization).
The digital removal of glue, that have penetrated into the structure, introduce structural defects to the surface. The arrows indicate the same fibre as seen in the two visualizations.

5.3 Results and discussion

5.3.1 Correlation beta-radiography and X-ray microtomography basis weight

The basis weights as determined by image analysis of the X-ray microtomography images and beta radiography showed good correlation, as shown in Figure 5.5.

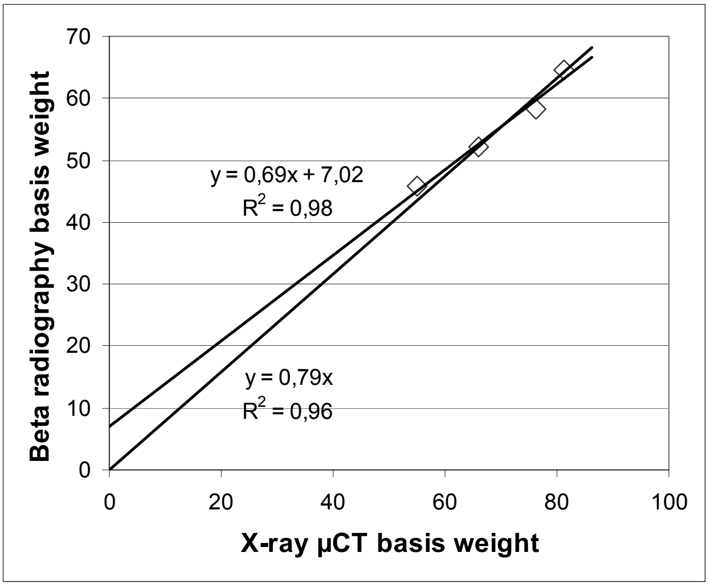

Figure 5.5 The determined correlation between basis weights measured for small areas with β-radiation and image analysis of the corresponding 3D images obtained by X-ray microtomography. The assumed fibre density is 1550 kg/m^3.

The results indicate that the applied method was successful in obtaining measures of more or less exactly the same areas of the paper sample. The good correlation also shows that there are little or no variation in signal quality for the X-ray imaging. Assuming the assessed areas are from exactly the same parts of the paper structure, it is possible to apply the correlation for interpretation of the measured basis weights determined by image analysis of the microtomographic paper volumes.

The first consideration that should be given is whether the intercept is at zero beta radiography basis weight. The sample preparation and subsequent image processing showed that the mounting by glue was detrimental to one of the surfaces of the digital structure. From manual inspection of the cross-sectional images, it is clear that the fibre-glue segmentation resulted in loss of fibre material. As there are only a few voxels of glue remaining in the digital structure after image processing, the glue removal results in an effective loss of basis weight. Thus there should be an intercept.

The spatial resolution of the X-ray images was 2 µm. There will therefore be a fraction of the fibre material that is not detectable for the X-rays. The limited spatial resolution may therefore lead to a loss of material. The systematic loss of fines material makes it reasonable that the intercept should not be zero.

It is clear that the basis weight, as determined by image analysis of the 3D images, are systematically considerably larger than for beta radiography. The applied fibre density of 1550 kg/m^3 is probably the main cause of this overestimation.
The beta radiography measures are systematically lower than the basis weight determined on samples according the ISO standards. The incorrect calibration thus increases the difference between X-ray and beta radiation basis weights. However, the difference between the beta radiography basis weight and the physical basis weight is known to be a constant. In this instance the beta radiography basis weights are approx. 86% of the physical basis weights. The too low calibration of the beta radiography images will only influence the ratio between the basis weights determined by the two different techniques, not the linear correlation.
Applying the more correct calibration of the beta radiography basis weights, the linear correlation is $y = 0.80x + 8.59$, when assuming a systematic loss of material in the X-ray images. The value of 8.59 g/m^2, seems reasonable from the observed effect of the glue and possible systematic loss of small details. The linear correlation also shows that applying the fibre density of 0.80 x 1550 kg/m^3 as the area to density conversion yields in average a reasonable numeric basis weight. The magnitude of the area to density conversion is in accordance with what is observed for cross-sectional images obtained by SEM-BEI. However, the slope of the basis weight correlation between beta- and X-ray imaging is most likely also influenced by the fines material not detected at the 0.7 µm voxel size of the X-ray microtomography. The fibre area density estimate of 1240 kg/m^3 is therefore likely a little too high. To render it possible to determine an unbiased area to density conversion, it is thus necessary to either keep the fines fraction constant, so that the ‘invisible’ fines fraction may be mostly reflected in the intercept, or obtain an alternative measure determining the fraction of small particles that cannot be detected.

The basis weight correlation may also be affected by the image processing in addition to the image acquisition. Especially the applied threshold may influence the area of solid elements significantly. The applied threshold has been chosen to preserve as many details of the physical fibre network and complete fibre cross sections as possible. Although small isolated objects are removed, the chosen threshold may yield an overestimation of the solid material in the structure. The choice of threshold and subsequent filtering will also remove most of the fibre wall porosity visible at the applied resolution (voxel = 0.7 µm). The chosen binarisation procedure do not exploit the phase contrast information in the images yielding improved contrasting of the fibre wall edges. An edge preserving filtering technique will improve the phase separation and thus result in less chance of misclassification of voxels and overestimation of solid elements.
The threshold applied for all the digital volumes in this study have been chosen on the same criteria, to preserve the topology of the structure, but at the same time give a reasonable trade-off to not introducing too much noise. The choice of threshold will be reflected in the slope of the basis weight correlation to beta radiography measurements.
The effect of threshold level and filtering criteria clearly show the need for individual calibrations for all experiments to determine a correct fibre density, as image acquisition

settings, mounting and image processing all can vary between various experiments even though the properties of the fibre furnish is the same.

The correlation between X-ray and beta radiation basis weights can be applied to determine whether the small volumes obtained by X-ray microtomography are in high, medium or low basis weight areas. The distribution of basis weights for the eight slightly different paper grades are determined by beta radiography imaging of a sheet of approx. 120 x 120 mm^2. The measure yield a good estimate of the mean basis weight for the different paper grades. Converting the beta radiography mean value to X-ray microtomography scale, applying the found correlation, yield a reference of estimated mean basis weight for the paper grade. This enable a quantification of basis weight deviation from the estimated mean. The found basis weight deviation can then subsequently be applied for correcting measured variables for basis weight effects. The principle is illustrated for the s4 sample in Figure 5.6. The determined deviation is shown in the beta-radiography scale to include the distribution.

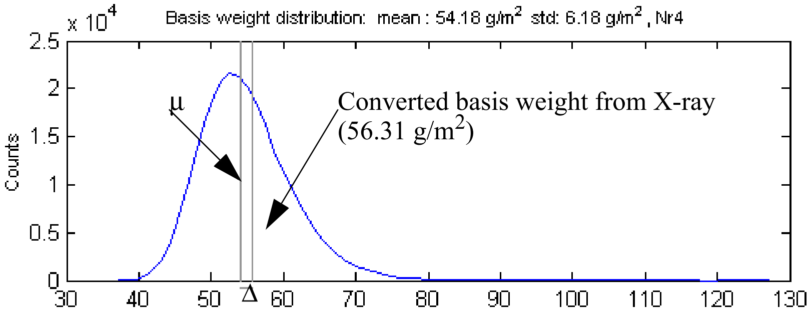

Figure 5.6 It can be determined whether the imaged volume is a high or low basis weight area, applying the found correlation between microtomography and Beta-radiation basis weights. The difference (Δ), in scale of X-ray microtomography basis weights, is applied to correct for the basis weight effect according to the found dependency of basis weight for the different measured characteristics.

The four areas that were selected and imaged for the correlation of basis weights were chosen on purpose to show as large differences as possible. The selected areas for the eight slightly different paper grades were chosen in representative areas within the sheets where the basis weight distribution had been determined previously by beta-radiography imaging. The imaged volumes are thus expected to show smaller variation than the four volumes selected for determining basis weight correlation. It is thus expected than when plotting the mean basis weights determined by X-ray microtomography, there will be a weak correlation to the mean determined for the much larger areas by beta radiography. The basis weights are plotted in Figure 5.7.

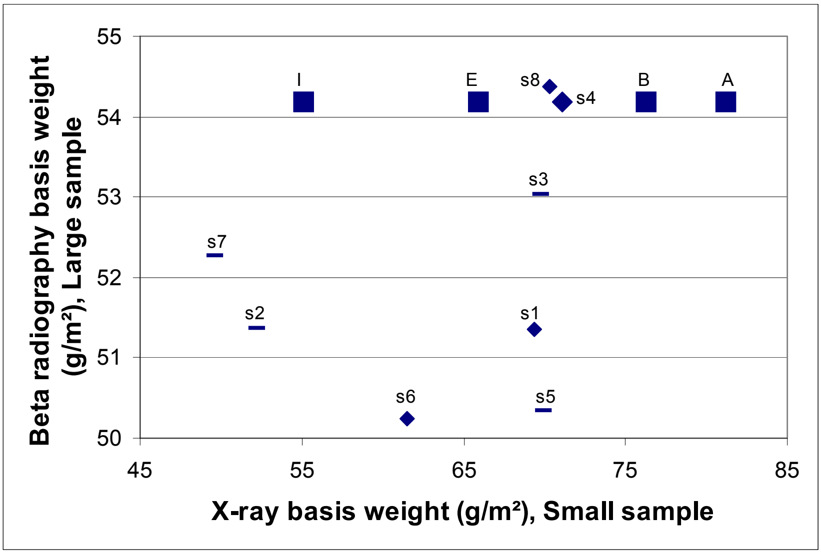

Figure 5.7 The correlation between the basis weight determined for small paper areas (<1 mm x <1mm) by X-ray microtomography and the basis weight measured for large areas (120 x 120 mm^2) determined by beta radiography imaging. The small areas are chosen within the large area for all volumes except volume A, B, E and I, which are, taken from a replicate sheet of sample s4. The line shaped points are representing calendered paper grades.

The scattering in the plot is larger than expected from normal variation. There are also samples that clearly deviate from the expected relation between the basis weights for the two different methods. The absence of high basis weight areas, as determined for sample A and B, yield additional indications of that the clearly deviating samples are affected by more than normal variation. Visual inspection of the strong deviation of volumes s2 and s7, shows that these volumes have more pronounced effects of gluing defects. The s7 sample is in addition the only sample with a clear deviation from lying planar on the capillary. The curved surface may influence the basis weight slightly. However, the reason for the curving is probably much more detrimental. The curving is caused by a severe delamination, where a part of the surface structure have departed from the main structure. The loss of this surface structure will affect the measured basis weight. However, the discarded surface structure assures that the structural characteristics are determined on a more representative paper structure.

5.3.2 Assessment of basis weight effects for structural characteristics

It is important to assess the basis weight effects for the structural characteristics. The assessment will yield an estimate of the effect of the normal variation in the paper grade, which is considered to be strongly correlated to formation effects. The assessment of the basis weight effects to the determined structural characteristics can also be applied to compensate for the selected volumes deviation from mean basis weight, applying the method mentioned above. The basis weight effects for the structural characteristics assessed in this study are shown in Table 5.3. The $R^2(4)$ value is the R-squared value to the linear fit of the four digital volumes A, B, E and I. The $R^2(5)$ is the R-squared value of the same volumes and s4 volume, which is from the same paper grade. The $\mu \pm \sigma$ is the mean and standard deviation for all the five digital paper volumes acquired from the s4 sample.

Table 5.3: The effect of basis weight on the determined structural characteristics. Porosity and thickness are not analysed as the basis weight is calculated from these values.

Structural characteristic	**$R^2(4)$**	**$R^2(5)$**	$\mu \pm \sigma$
S/V (μm^{-1})	0.60	0.27	0.20 ± 0.01
SSA (m^2/m^3)*10^3	0.16	0.09	312 ± 9
SSA (m^2/g)	**0.94**	**0.91**	**0.60 ± 0.03**
<g> - ZD	0.53	0.29	7.1 ± 0.4
<g> - CD	**0.98**	**0.60**	**19.0 ± 1.1**
<g> - MD	0.47	0.16	22.5 ± 3.0
Pore chord - ZD	0.04	0.02	6.4 ± 0.4
Pore chord - CD	0.66	0.23	19.8 ± 1.7
Pore chord - MD	0.70	0.69	26.9 ± 3.3
Structural anisotropy - MD/CD	0.00	0.00	1.19 ± 0.18
Structural anisotropy - ZD/CD	0.38	0.03	0.37 ± 0.03
Structural anisotropy - ZD/MD	0.05	0.04	0.32 ± 0.03
Hydraulic radius- ZD	**0.98**	**0.84**	**6.20 ± 0.23**
Hydraulic radius - CD	0.02	0.02	3.11 ± 0.15
Hydraulic radius -MD	**0.80**	**0.80**	**2.96 ± 0.09**
Mean radius, maximal sphere method	0.33	0.23	6.9 ± 0.7
Critical radius -ZD	0.03	0.03	10.4 ± 4.3
Critical radius- CD	0.01	0.00	4.3 ± 0.8
Critical radius-MD	**0.96**	**0.56**	**4.9 ± 1.1**
(rw) Tortuosity -ZD	**0.96**	**0.66**	**2.58 ± 0.30**
(rw) Tortuosity - CD	0.02	0.01	1.18 ± 0.05
(rw) Tortuosity -MD	0.41	0.27	1.09 ± 0.03
Diffusivity - ZD	0.39	0.19	0.16 ± 0.04
Diffusivity - CD	0.01	0.02	0.56 ± 0.05
Diffusivity - MD	0.74	0.64	0.76 ± 0.07
Permeability - ZD	0.04	0.02	0.51 ± 0.42
Permeability - CD	0.13	0.13	1.16 ± 0.45
Permeability - MD	0.36	0.36	2.88 ± 0.89

The correlation between the determined structural characteristics and basis weight are generally relatively low. There are just a few of the structural characteristics that follow linear relationship to basis weight. Assuming there is a significant linear correlation for $R^2(4) > 0.8$, there are only six characteristics that are significantly influenced by basis weight. These are marked in bold in Table 5.3.

The standard deviations are smaller than what could have been expected with the wide selection of basis weights. The low correlation to basis weight indicate that variation of other effects, both structural and technique dependent, most often have a larger effect on the standard deviation. The standard deviation is for most properties smaller than 10% of the determined mean value. Larger variation is systematically found for transport related properties in the z-direction. The systematically larger variation in the z-direction is probably caused the systematically shorter extension of the volumes in this direction, and thus larger influence of high basis weight areas. The mean pore chord for the machine direction also shows a divergently large variation. This is most likely caused by the large shive in volume s4, yielding a considerably lower mean pore chord in the machine direction for this volume.

The large deviation for the critical radius indicate that the characteristic may not be well suited for assessing significant features of the paper structure. In fact this characteristic have mostly been applied for verifying whether 3D images of porous structures have sufficient resolution for simulation of transport properties [45]. A critical radius of at least 3 x {voxel dimension} is needed for application of *e.g.* non-slip conditions at phase borders for lattice-Boltzmann simulations. The assessed critical radii for the five replicates in this study show as such that the image resolution is more than sufficient for simulation of transport properties. Further adding to the large deviation between replicate volumes, for the critical radius, are varying sizes of the volumes. Ideally all volumes should have identical size and shape for comparison between the replicates. The volumes should also preferably be cubic to enable comparison between the transport resistance for the three principal directions. Future application of critical radius should take these considerations into account for an objective consideration of whether the characteristic may yield useful structural information for paper.

The $R^2(5)$ values are generally considerably lower than the $R^2(4)$ values, especially for characteristics that showed a clear linear relationship to basis weight for the four volumes; A, B, E and I. An example of this is shown in Figure 5.9. The results clearly indicates that the structure of the s4 volume is deviating considerably from the four other volumes. This was confirmed from visual inspection of the volumes, exemplified in Figure 5.8. The cross sections reveal a large shive orientated normally to the machine direction,.

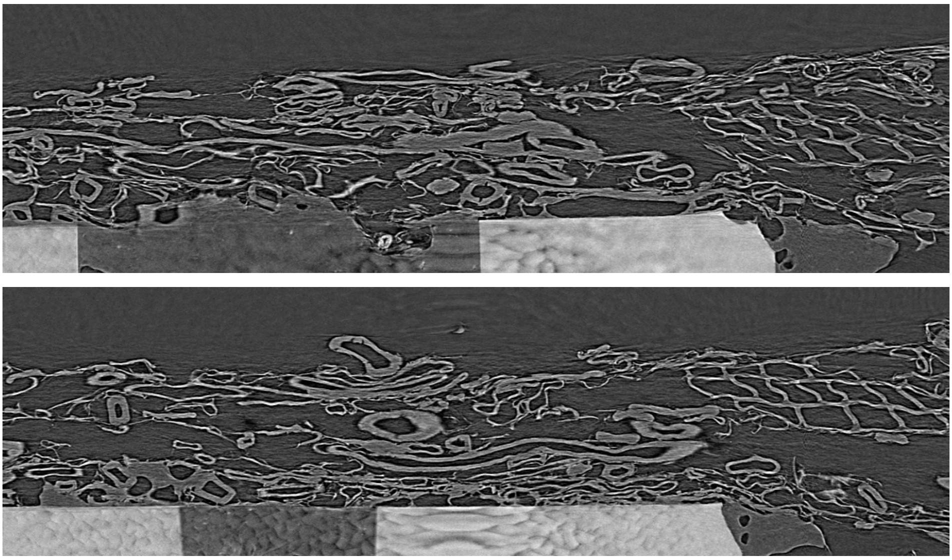

Figure 5.8 Illustration of the large shive found in the s4 volume. The shive is orientated in the cross direction. **Top:** A cross section from the left edge of the volume. **Bottom:** A cross section from the middle of the volume.

For the six characteristics that showed a significant linear correlation to basis weight were the effect of basis weight determined according to the described beta-radiography method. A practical example of the basis weight correction is shown in Figure 5.9 for the tortuosity in the z-direction for the s4 sample.

The correction of basis weight will only compensate for the deviation of basis weight as determined in the digital volumes and the average determined for the whole sheet. As shown in Figure 5.9, the correction will compensate for the higher than mean basis weight determined for volume s4. However, as the deviation from the mean basis weight is caused by other effects than ordinary formation effects, in this instance a large shive in the structure, the basis weight compensation may as likely make the compensated structural parameter less than more representative of the paper grade. Obviously the basis weight correction cannot normalize the effect of the shive. However, the availability of replicate volumes (A, B, E and I) for this paper grade enables application of the mean value of the five replicate volumes instead of the single measure from the s4 volume.

There are also other effects that may introduce variation. The imperfect glue removal might have varying effect, even though the basis weights of sample A, B E and I seem relatively unaffected. Figure 5.7 shows that the glue effect is more pronounced for sample s2 and s7 than for the other samples. This will affect the analysis of the factorial design. It is assumed that other effects from the image acquisition and subsequent image processing will have minor effects on the structure compared to the glue effect.

There might also be other structural effects than the shives and glue effect that introduces considerable unaccounted variations in the assessed structures. The magnitude of the glue effect and possibly unaccounted structural effects will introduce a relatively high variation in the assessed effects from the analysis of the factorial design.

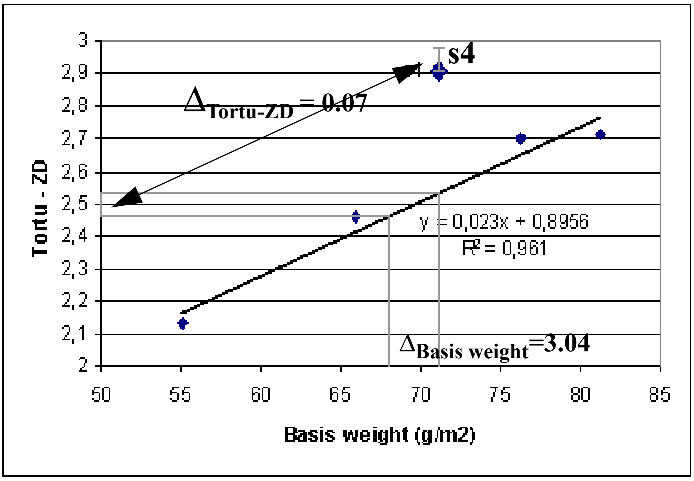

Figure 5.9 An example of linear dependency to measured basis weight for a structural characteristic - here exemplified by the z-directional tortuosity. Note that the s4 volume, containing a large shive, clearly deviate from the relationship between the four other volumes and are therefore not applied to determine the linear relationship.

The correlation between beta and X-ray radiation determined basis weight, determined mean basis weight from beta radiation imaging and the found linear relationship enable an estimation of the deviation from average basis weight and the effect of this to the assessed structural property. As the s4 sample contain a large shive the compensation will not in this instance be to any help, more on the contrary.

5.3.3 Results from analysis of the experimental design - Relationship between papermaking variables and paper structure characteristics

Analysis of the factotrial design without basis weight corrections

The results from the analysis of the factorial design without applying basis weight corrections are given in Table 5.4. The effects that are significant at a 95% confidence level are marked ++/--. Where the signs show whether the effect lead to an increase or decrease of the structural characteristic. The effects that are significant at a 90% confidence level are marked +/-. The effects that had no significant effect are marked 0. The left column under each paper making variable show whether the effects are significant or not on a 95 and 90% confidence level. The right column under each paper making variable represent the size order of the effect, which can be seen relative to the mean value given in the second column of the table.

Table 5.4: The results from the analysis of the factorial design without performing basis weight correction to characteristics that are significantly dependent of basis weight (bold properties).

Property	μ	**Calender-ing**		**Reinforce-ment pulp**		**Head box consist-ency**		**Fixation agent**	
Porosity (%)	58.0	--	-8.0	0	0.4	0	0.1	0	0.3
S/V (μm^{-1})	0.27	++	0.04	-	-0.02	0	-0.01	0	0.01
SSA (m^2/m^3)*10^3	376	++	56	0	-15	0	-3	0	9
SSA (m^2/g)	0.58	-	-0.03	0	-0.01	0	0.00	0	0.02
<g> - ZD	5.14	--	-1.57	++	0.23	0	0.08	0	-0.02
<g> - CD	15.2	--	-3.3	0	0.4	0	-0.1	0	-0.3
<g> - MD	16.5	--	-4.5	0	0.8	0	0.1	0	-1.3
Pore chord - ZD	4.39	--	-1.41	0	0.17	0	0.14	0	-0.04
Pore chord - CD	14.4	--	-3.9	0	0.6	0	0.1	-	-0.3
Pore chord - MD	17.3	--	-5.5	++	1.8	++	1.1	--	-1.4
Mean radius, maximal sphere method	3.99	--	-1.67	0	0.33	0	0.32	0	-0.18
Structural anisotropy - MD/CD	1.07	0	-0.07	0	0.03	0	0.01	0	-0.08
Structural anisotropy - ZD/CD	0.33	--	-0.03	+	0.01	++	0.01	+	0.01
Structural anisotropy - ZD/MD	0.32	0	-0.00	0	0.00	0	0.00	0	0.03
Hydraulic radius- ZD	4.78	--	-1.23	0	0.10	0	-0.03	0	-0.21
Hydraulic radius - CD	2.33	--	-0.67	++	0.08	0	-0.00	--	-0.08
Hydraulic radius -MD	2.29	--	-0.60	0	0.08	0	0.04	0	0.00
Critical radius -ZD	4.01	-	-2.10	0	1.48	0	0.64	0	-0.32
Critical radius- CD	3.31	--	-0.76	0	0.24	0	0.10	-	-0.35
Critical radius-MD	2.66	--	-0.99	0	0.01	0	0.14	0	-0.21
(rw) Tortuosity -ZD	2.78	++	0.29	0	0.04	0	-0.05	-	-0.15
(rw) Tortuosity - CD	1.16	0	0.01	0	-0.00	0	-0.01	0	-0.00
(rw) Tortuosity -MD	1.11	0	-0.01	0	0.02	0	0.01	0	-0.02
Diffusivity - ZD	0.11	--	-0.03	0	0.01	0	0.00	0	0.01
Diffusivity - CD	0.54	0	-0.03	0	-0.02	0	-0.01	0	-0.00
Diffusivity - MD	0.68	-	-0.05	0	0.03	0	0.03	0	-0.01
Permeability - ZD	0.10	--	-0.10	0	0.07	0	0.04	0	-0.04
Permeability - CD	0.51	--	-0.38	0	-0.01	0	0.13	0	-0.04
Permeability - MD	1.08	--	-0.88	0	0.19	0	0.36	0	-0.03

Calendering: The calendering had a clear effect on most of the assessed structural characteristics. The surface to volume ratio increased and the porosity decreased, showing that the compressive force yields a denser structure. The pore geometry parameters show generally smaller pores in all spatial directions, which is far from unexpected. The simulated transport properties show that the transport through the structure is hindered for all three spatial directions.

The restricted random walk tortuosity and diffusivity are however little or not affected by the calendering. The results may indicate that the glue removal, have created artificial 'channels' through the structure close to the bottom surface. This is especially true for the CD-direction, which can be confirmed by recapitulating that the digital removal of the glue phase was performed on CD-orientated cross-sectional images.

The structural anisotropy in the sheet plane is unaffected by the calendering, supporting that the calendering is strictly a compressive force acting on the structure.

The calendering increased the volume based specific surfaces, but lowered the weight based. The results thus indicated that the void volume is considerably more affected than the surface area by the calendering. The clear effect on surface to volume ratio and small effect on specific surface area per weight indicate that the calendering have not increased the number of fibre-fibre contacts extensively.

Addition of reinforcement pulp: The effect of reinforcement pulp to the structure is not as clear as for the calendering. Generally the effects are considerably smaller than for calendering and for most instances it have no significant effect. However, occasional effects can be seen for some pore extension characteristics. These may indicate that the added chemical fibres reduces the fraction of small pores. The decreased number of small pores may be a result of localized better bonding between the fibres, leaving little or no porous space between the fibres. This is a reasonable result of the added chemical fibres as they are known to be more flexible and have a higher bonding degree. The lower surface to volume ratio at a 90% confidence level support the observation. Additionally it is known that the addition of the chemical pulp fibres will reduce the fraction of fines and fibrils in the structure, which will contribute to averagely larger pores. A lower fraction of fines will also reduce the surface to volume ratio. The observed increase of the pore extensions with addition of reinforcement fibres are thus not unexpected. It is likely that the effect is caused by a combination of better bonding and a lower fraction of fines. However, as a better bonding may also reduce the number of the larger pores, it is probable that the main contribution is caused by a lower fraction of fines material and less fibrillated fibres.

The applied image analysis methods do not yield any direct measures of the fibre phase, which could have yielded clearer results for the effect of addition of the chemical fibres to the paper structure. For future research on effect of reinforcement pulp it is probably necessary to stain the mechanical pulp fibres and apply measures of the fibre phase, fibre network and single fibre properties to obtain a better understanding of how the reinforcement pulp increases the paper strength.

Increased head box consistency: The head box consistency was increased with intention to reduce the structural anisotropy in the sheet plane by hindering the alignment of fibres. It was also expected that the increased head box consistency would lead to a more felted structure and worsening of formation. However, the latter effects are difficult to assess by the determined structural characteristics. Assessment of the degree of layered structure would require tracking of a high number of individual fibres through the structure. Formation effects are usually in the order of millimetres and can thus not be measured at the scale of the small acquired 3D volumes. Nevertheless, the two significant effects (pore chord length in MD and structural anisotropy ZD/MD) indicate that the increased head box consistency leads to more extended pores in the sheet plane. The worsening of the formation would lead to such effects. However, the effect are only seen for the two characteristics for which all the four papermaking variables are determined to be significant. The head box consistency effect is the lowest for both instances. As it may be a statistical coincidence that suddenly all effects are significant for only two of many variables and the head box consistency is the lowest of the effects, the head box consistency is assumed to have no significant effect on the detailed paper structure for the small assessed volumes.

No effect was detected for the structural anisotropy in the sheet plane. The significant increase of mean free spatial length in machine direction with increased head box consistency indicate that the worsening of formation have a higher effect on the pore extensions than the potential increased fibre alignment. Future research of the effect of fibre orientational anisotropy should apply sheet manufacturing known to introduce significant effects on fibre alignment.

Addition of fixation agent: The addition of a fixation agent are expected to yield a more complex structure, where the increased amount of fine material will somewhat restrict the transport through the structure and yield reduced extension of the pores.

There are few significant effects for the addition of fixation agent, but the significant effects (pore chords in CD and MD, structural anisotropy ZD/MD, hydraulic radius in CD, critical radius in CD and tortuosity in ZD) indicate that the added amount of fines material have reduced the pore extension somewhat as expected. The reduced tortuosity in z-direction and reduced critical radius in machine direction at a 90% confidence level are the only indications of an increased restriction against transport through the structure.

General comments: The calendering have a strong effect compared to the other variables. The results thus indicate that the void fraction is crucial for the detailed structural properties. The effect of the other variables, which affects the void fraction considerably less than the calendering, are thus partially concealed by the large calendering effects. For later studies of the effects of paper machine variables the studied effects should preferably be at a more constant void fraction level. The relatively high uncertainty level in the effects render it difficult to achieve significant effects for other variables than the strong calendering. It should also be remembered that for the confidence level of 95%, still 1 of 20 effects concluded to be significant may be caused by random variation.

Analysis of the factorial design with basis weight corrections

The six structural characteristics that were determined to be linearly dependent of basis weight were adjusted according to the beta-radiography method. The adjusted structural characteristics were put in the factorial design and analysed as normal. The results applying the basis weight corrected results are given in Table 5.5.

Table 5.5: The results from the analysis of the factorial design after performing basis weight corrections to the structural characteristics that were determined to be significantly dependent of basis weight

Property	μ	**Calender-ing**	**Reinforce-ment pulp**	**Head box consist-ency**	**Fixation agent**
SSA (m^2/g)	**0.59**	0 -0.02	0 -0.03	0 -0.00	0 0.02
<g> - CD	**15.2**	**-- -3.0**	0 0.0	0 -0.1	0 -0.2
Hydraulic radius- ZD	**4.80**	-- **-1.16**	0 0.01	0 -0.04	0 -0.19
Hydraulic radius -MD	**2.28**	-- **-0.62**	0 0.11	0 0.04	0 -0.00
Critical radius-MD	**3.39**	0 -0.48	0 -0.12	0 0.04	0 -0.27
(rw) Tortuosity -ZD	**2.76**	+ **0.22**	0 0.14	0 -0.03	0 -0.17
Diffusivity - MD	**0.68**	0 -0.04	0 0.01	0 0.03	0 -0.01

The basis weight correction was intended to introduce new significant effects that were previously concealed by the basis weight variation of the small digital volumes. Similarly the correction might eliminate effects showing to be caused by random basis weight variation. The results after basis weight correction showed no clearer effects. Some effects became less or non significant. The results after basis weight correction thus indicate that some of the effects that were considered to be significant without basis weight correction were in fact only a result of coincidence of the basis weight variations.

However, it is known that there are other considerable sources of variation in this experiment than the formation effects. Figure 5.7 shows clearly that the s2 and s7 volumes are distinctly different from the other digital paper volumes, having a considerably lower basis weight. Visual inspection of the volumes showed that these volumes were the most affected by the digital glue removal. Basis weight corrections to volumes clearly influenced by other and possibly larger non-systematic variation may introduce a ‘correction’ to the worse for these volumes, as is the case for the z-directional tortuosity of the s4 sample as shown in Figure 5.7.

The considerable difference between the digital structure of the s2 and s7 sample compared to the other volumes are considered to introduce large non-systematic variation that cannot be compensated for. For most factorial designs there exist several measurements of each setting or there is a possibility to redo outliers. In this study the outliers found for the s2 and s7 sample must still be applied for the analysis of the factorial design, because the low availability or high cost of synchrotron radiation X-ray microtomography makes it impossible to depict several replicate volumes of each paper grade or redo the image acquisition. The abnormal structure of the s2 and s7 sample are therefore detrimental to the applied factorial design. Later studies should therefore try to find sample mounting methods avoiding glue penetrating into the paper structure when mounting the samples for image acquisition.

Although the basis weight correlation was not very helpful for reducing the level of variation in the experiment, the determination of the correlation yielded valuable information of the normal variation for the assessed structural properties. It is a promising result for the further progress of application of X-ray microtomography for assessment of the detailed structural properties that many of the assessed characteristics show weak correlation to the basis weight and have smaller standard deviation than expected.

Evaluation of the assessed structural characteristics

Although the application of the factorial design was moderately successful, the performed experiment include unique 3D images and structural characterization which is not done justice to by the factorial design approach.

The obtained structural measures are in themselves of great interest. The most readily accessible information not exploited by the analysis of the factorial design are the observed differences between the three principal directions. All of the characteristics show that the resistance towards transport (diffusivity, permeability and (rw) tortuosity) is the highest in the z-direction and the lowest in the machine direction. It is also observed, as for the measurements of the phase contrast 3D images, that the extension of the pores are the largest in the machine direction and the smallest in the z-direction (pore chords, hydraulic radii, critical radius).

Some of the characteristics were assessed both including and excluding the surface layers. The surface to volume ratio is approximately 40% higher when including the surface layers. This is not an unexpected result, as all the outermost fibres in the surface are unbonded on one side. However, the difference is probably in this instance to some extent exaggerated. The large increase if surface area may partly be due to the resulting surface structure of the bottom surfaces from digital removal of the glue phase that had penetrated into the structure. Comparing the results for pore chords including the surface layers (<g>) and excluding the surface layers show that the mean pore chords are shorter in the z- and cross direction and longer in the machine direction when excluding the surface layers. The results may again be influenced by the glue removal, of which the varying effect of cross and machine direction are most influenced. The interior pore chords also include the edge pore chords limited by a fibre in one end and the edge of the volume in the other. The reduction of the extension of the already thin structures in the z-direction will thus yield lower pore heights.

The determination of most of the structural characteristics includes numerous measurements in the digital volumes providing distributions, of which means and standard deviations can be found. However, the distributions contain valuable information, which is not exploited by the application of the factorial design. The experiment thus include a large amount of information, which should be exploited to do justice to the unique, detailed and valuable paper structure information contained in this experiment. One such example is the volume based pore size distribution obtained by the maximal sphere approach. Figure 5.10 shows an example of applying the obtained data to study the effect of basis weight variation, calendering and removal of reinforcement pulp when assuming the head box consistency has insignificant effect.

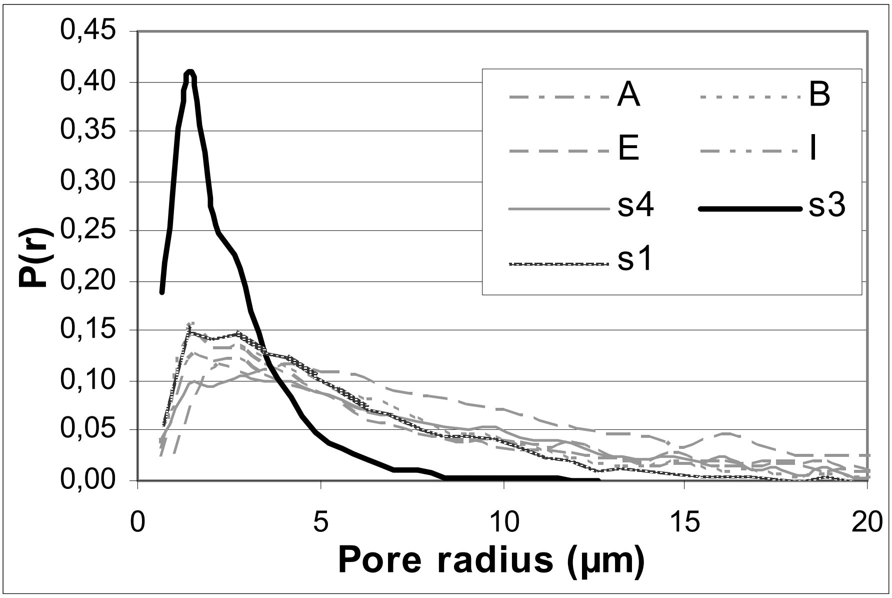

Figure 5.10 Effect of basis weight variation (A,B,E,I,s4), calendering (s3) and removal of reinforcement pulp (s1) to the pore size distribution.

The distributions in Figure 5.10 show in more detail what is observed from the mean values. The replicate samples of the s4 paper grade (A,B,E,I,s4) show a significant variation in pore size distribution. The s1 paper grade is manufactured similar to the s4, except that it does not contain reinforcement fibres. The paper structure consisting of 100% TMP shows a pore size distribution having smaller pores but not considerably different from the densest of the s4 replicate volumes. The s3 paper grade, of which the only difference for the paper making is the calendering level, show a pore size distribution shifted far towards smaller pore sizes compared to the uncalendered samples. The pore size distributions can thus both show the structural differences between the paper grades and yield explanation of reasons for the small and often insignificant effect of the non-calendering paper making variables.

A second example shows how the direct calculation on the images can allow for a quantitative comparison of the effect of papermaking variables on the transport properties of the sheet. Figure 5.11 most clearly illustrates the effect of calendering on permeability and diffusivity of the paper samples. Comparing the results at approximately the same porosity, the difference between the transport in the three principal directions are apparent. The resistance against the transport is considerably higher for the z-direction compared to the in-plane directions for both permeability and diffusivity independent of calendering level. It is also possible to see significant effects of the anisotropy for the transport in the machine and cross directions.

The determination of the transport properties include assessment of 4-12 subvolumes, which had representative scales, for each paper volume except for the s7 volume[1]. The approach yields, in addition to more reasonable computation times for the transport simulations, a transport property:porosity relationship that yields additional information compared to a single mean value. The method is as such less vulnerable to basis weight variation. Figure 5.12 shows the z-directional permeability:porosity relationship for the five replicate volumes of the s4 paper grade. Similarly Figure 5.13 show the in-plane permeability:porosity relationship for both the machine and cross direction. Although all three of the permeability:porosity relationships seem to follow an exponential behaviour common to all replicate volumes and their subvolumes, there are clear differences between the z-direction and in-plane directions.Numeric differences can be seen between the permeabilities in the z-direction compared to the in-plane directions. It is also clear that there is a larger deviation between the large volumes (marked with lines) for the z-direction than seen between the large volumes in the in-plane directions. The s4 volume show the largest deviation from the common exponential behaviour. However, this especially large deviation can be explained by the presence of the large shive in the structure (see Figure 5.8). Ignoring the s4 volume, there is still a larger deviation relative to the common trend compared to the deviation seen for the in-plane directions. The most likely structural explanation of this difference is the layered structure of the thin paper samples yielding a higher sensitivity to high porosity areas for the z-direction.
The MD and CD permeability:porosity relationships clearly show the anisotropy, where the CD permeability is consequently lower than the MD permeability.

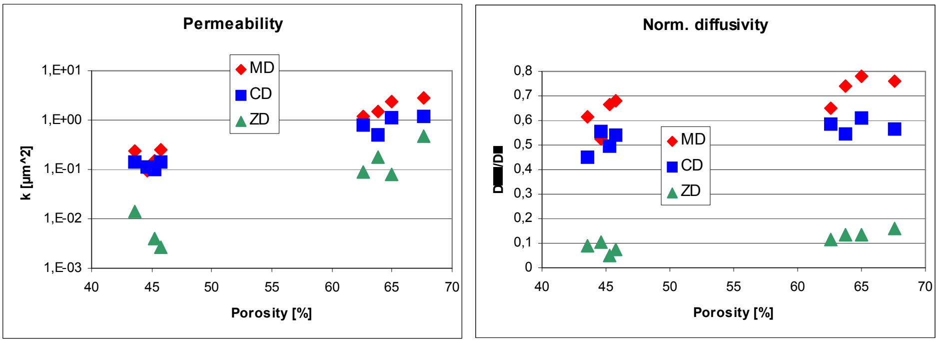

Figure 5.11 Quantification of the effect of papermaking variables on transport properties. **Left**: The effect on the permeability. **Right:** The effect on the normalized diffusivity (D/D_0)

---

1. There could only be extracted one singe volume of sufficient size from the s7 sample due to a significant tilt of the sample relative to the assumed sheet plane (normal to the capillary).

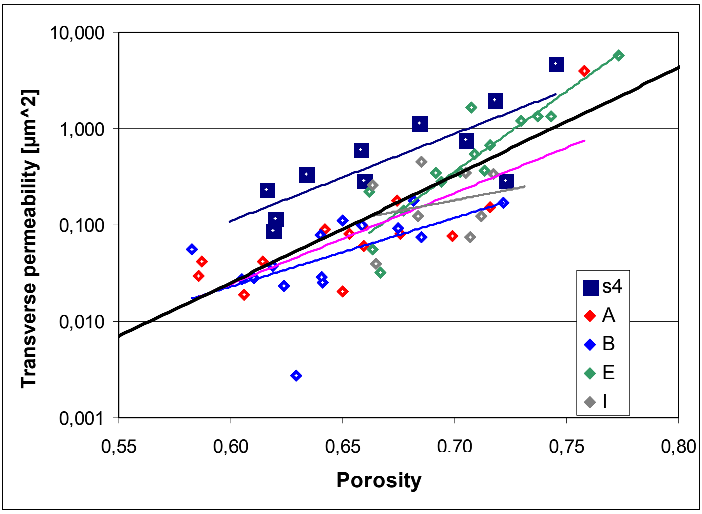

Figure 5.12 The z-directional permeability:porosity relationship for the five replicate volumes of the s4 paper grade. Each digital volume are analysed as a set of subvolumes, for which the permeability is determined.

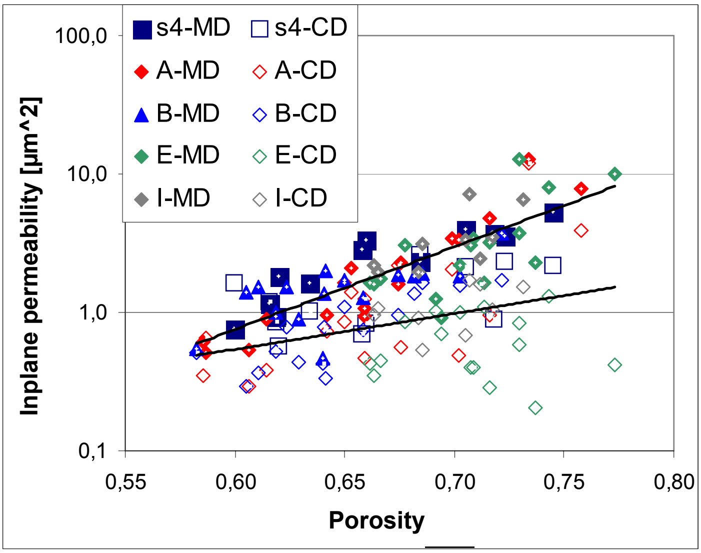

Figure 5.13 The MD and CD permeability:porosity relationship for the five replicate volumes of the s4 paper grade. Each digital volume are analysed as a set of subvolumes, for which the permeability is determined for both the machine and cross direction.

In addition to the examples given above of various distributions of structural characteristics, it is also possible to obtain similar results as determined for the suite of paper samples imaged applying phase contrast mode (presented in Chapter 3 and 4 and the attached Papers III and IV). Amongst the results not presented here for the absorption mode images are the pore chord, hydraulic radius and restricted random walk diffusive tortuosity distributions.

5.3.4 Correlation between detailed structural characteristics and bulk paper properties

The assessed structural characteristics are expected to correlate to physical measurements of the bulk paper properties. However, the analysis of the effects showed a very clear effect of calendering. Most of the structural characteristics and bulk properties are thus split in two fractions, one for calendering and the second for the uncalendered sheets. The two level behaviour is an unavoidable feature of the chosen experimental scheme, although more equal effects of the various papermaking variables may have resulted in an improved scatter of the paper properties compared to this study.
There are performed many different measurements of the physical properties of the paper samples and a high number of structural and transport characteristics (Table 5.4) of the digital paper structure have been determined. However, there are not many measured physical properties for which it is expected to find correlations to structural characteristics. The physical experiments mostly focus on strength, optical and surface properties of the paper, whereas the characteristics determined from the digital structures focus on assessing the pore geometry and transport properties. Future development of methods for characterizing the digital paper structure may succeed in determining optical and strength properties. However, at this initial stage of assessing features of the 3D structure of paper, it is the transport properties that are the most readily available.

Among the bulk paper properties considered to show a relationship to the structural characteristics is the scattering coefficient of the paper. The specific surface area per weight of solid material is ‘normalized’ in the same manner as the scattering coefficient is normalized to the basis weight of the assessed paper sample, and should as such show the best relationship to the scattering coefficient. The correlation is shown in Figure 5.14. The results show that there is no correlation between the physical and digitally determined properties when including all volumes. The correlation improves when excluding the two volumes (s2 and s7) that previously have shown to be the most affected by the digital glue removal. However, the correlation is not statistically significant. It is expected that the correlation would have been improved if the surface effects from the glue had been avoided. Better correlation have been observed for SEM images having sufficient resolution for detecting all features in the size order able to refract the incident light [27]. The resolution of the X-ray microtomography technique is as such not able to detect all such light scattering features, which will influence the correlation negatively.

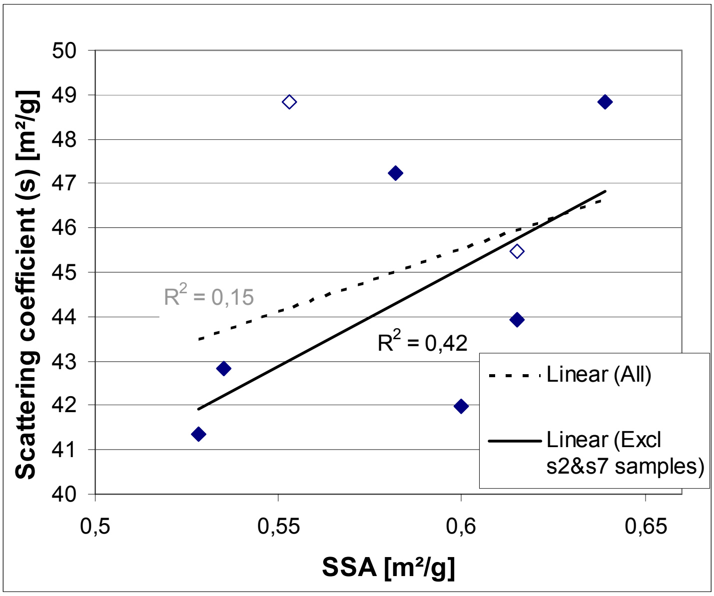

Figure 5.14 The correlation between the scattering coefficient determined from physical experiments and the specific surface area relative to weight of solid material as determined from image analysis of the digital paper volumes. The diamonds are given for the s2 and s7 volume, which were the most affected by the digital glue removal. The correlation is determined both for all volumes and when excluding the two clearly deviating volumes.

The assessment of the pore chords are also a measure of the structural anisotropy. It is possible that the in-plane structural anisotropy could be correlated to strength anisotropy as determined by various bulk measurements. However, the paper grades produced here show small variations in anisotropy. Additionally, shives can be found in some of the imaged paper volumes. The shives are often orientated normally to the machine direction, clearly influencing the pore chord measurement, and thus the structural anisotropy. The two volumes that have been determined to have a MD/CD ratio smaller than 1 are therefore not included when considering the correlation to the strength anisotropy. Figure 5.15 show the determined correlation between the in-plane structural anisotropy and the physically determined anisotropies for different mechanical properties.

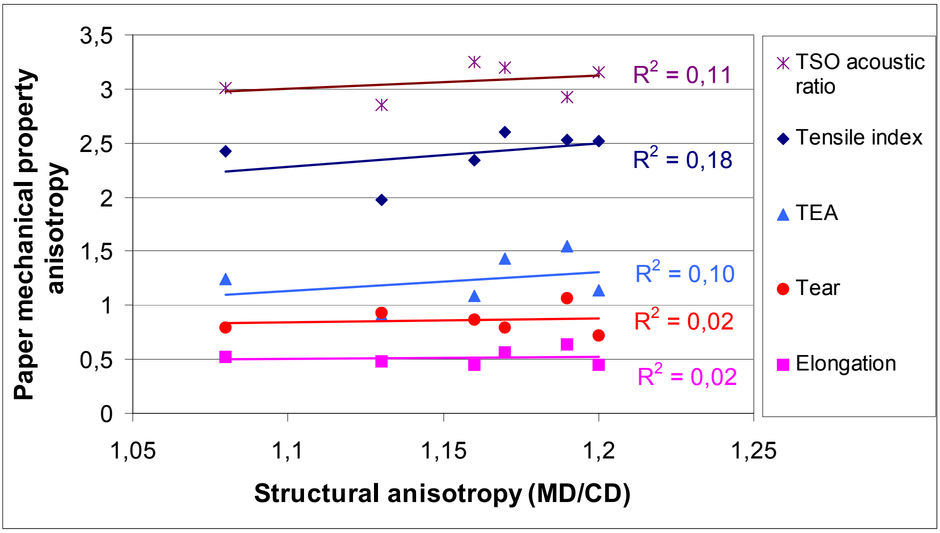

Figure 5.15 The correlation between the in-plane structural anisotropy and various paper mechanical property anisotropies.

The results show no significant correlation between the in-plane structural anisotropy and any of the paper strength anisotropies. The plot indicate that both the structural and strength anisotropies show a normal variation around a mean value and are thus not significantly influenced by the chosen paper making variables. Analysis of the effect of the head box consistency confirm this observation, as it seems that the consistency have had little or no effect on the manufactured paper, maybe with an exception for the formation. It is therefore expected that future research focusing on the effect of varying anisotropy may find correlations, although no correlations were found in this experiment.

Despite the focus on transport properties for the assessment of the digital structures there have not been performed any physical measurements especially adapted for determining permeability and diffusivity of the different paper grades. This study have put focus on establishing the microtomography technique for imaging the 3D structure and assessing various characteristics of the resulting digital paper structures, not finding structure:bulk property relationships. It is therefore only the standard Gurley permeance measurement among the determined physical measurements that can be expected to show any correlation to the determined transport properties.

The correlation between the Gurley permeance and the various measured of pore geometry parameters and transport properties of the digital structures are shown in Figure 5.16 and 5.17.

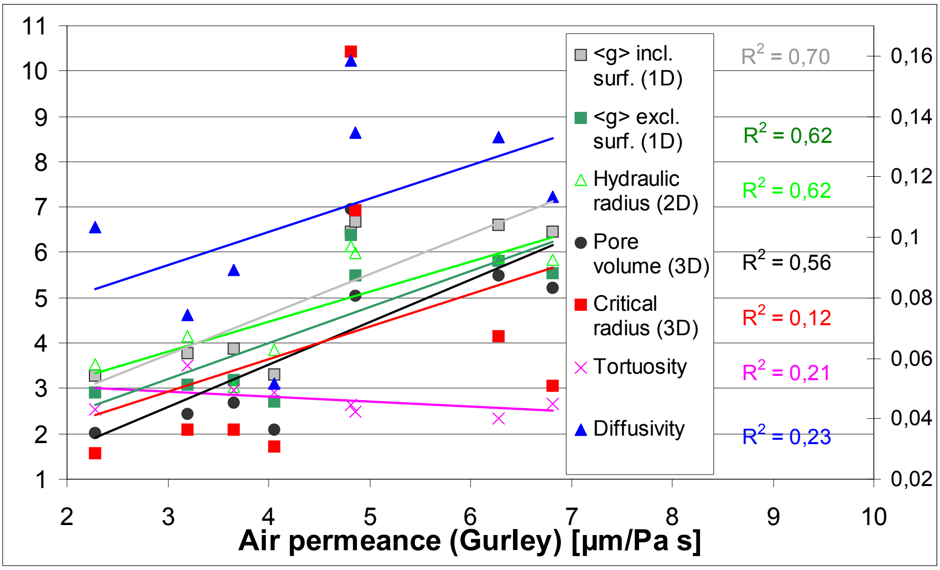

Figure 5.16 The correlation between the physically determined air permeance according to the Gurley method and various pore geometry and transport property characteristics determined from the digital structures

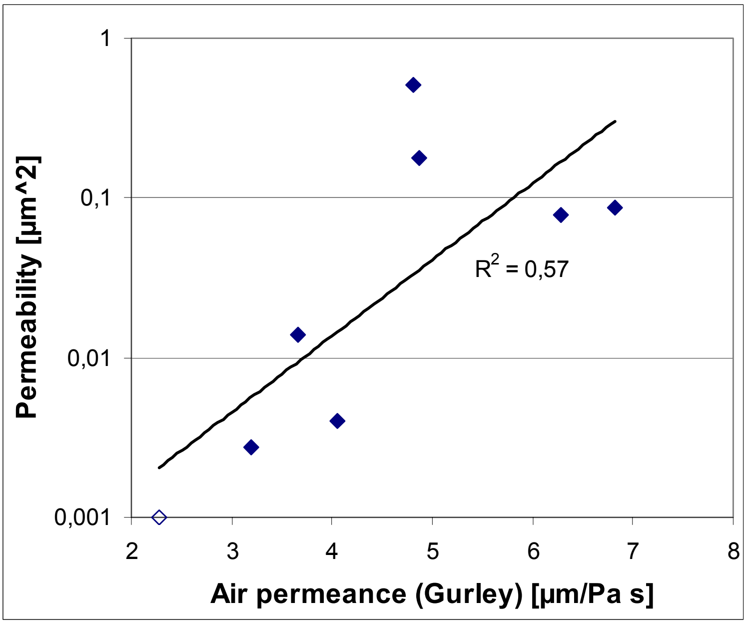

Figure 5.17 The correlation between the physically determined air permeance according to the Gurley method and the permeability determined from the digital paper structures applying lattice-Boltzmann simulations.The empty diamond is for the s7 volume of which the permeability was determined to 0.00. The value 0.001 is an estimated value allowing logarithmic scaling.

The results show a better correlation between the air permeance and the digitally determined pore geometry and permeability measurements than for any of the other possible correlations. It is somewhat unexpected that the pore geometry measurements show a better correlation than the permeability. However, this can be explained by the relatively high variation found for the determined mean values of the z-directional permeability and the applied factorial design yielding practically only two levels. The relatively good correlation found for this experiment, which is not well suited for studying the correlations between structural and bulk properties, show a high potential for further studies of the pore geometry and structural details may influence the transport properties.

Future studies applying X-ray microtomography applying the principles put forward in this thesis work can with advantage determine especially adapted physical transport measurements (*e.g.* diffusivity) to evaluate the quality of the predicted transport properties from the digital structures. For all properties for which it is expected that it is likely to be correlations between structural and bulk properties, it is also recommended to apply more than two levels when studying the effect of selected papermaking variables. Studies of the correlation between detailed structural characteristics and bulk paper properties should preferably be performed for single effects, as *e.g.* refining levels, as performed by Ramaswamy et al. [76], Huang et al. [77] and Goel [82]. It is also essential that the relatively large random errors from glue penetrating into the structure are avoided in future experiments.

5.4 Conclusion

The application of a factorial design for the experimental scheme showed to be moderately successful. The calendering had a dominating effect influencing directly on the porosity. Results also indicated that addition of BSKP tended to increase the mean extension of the pores and addition of the fixation agent lead to a more complex structure with averagely smaller pores. These results are as expected, but are for most of the assessed structural and transport characteristics statistically insignificant. The alternation of head box consistency showed to have no significant effect on the detailed paper structure in the relatively small assessed volumes.

The large effect of the calendering thus partly concealed the effect of the other paper making variables. The additional random variation caused by the glue removal effect, especially for the measures including the surface layers, introduced a higher variation affecting the needed size of the effects to be statistically significant. The attempt of determining the effect of several papermaking variables simultaneously was as such a bit ambitious for the application of a technique in its early stage. However, the experiment clearly showed that the solid fraction is of utmost importance for the characteristics of the detailed paper structure.

The results clearly show that the calendering is a compression of the paper, yielding a very distinct effect on the solid fraction, reducing the extension of the pores and increasing the resistance against transport through the structure, especially for the z-direction. The effect on solid fraction by calendering, as compared to the other studied paper making variables, was considerably larger.

It was the intention of the experimental scheme to quantify the effects of basis weight variation to the assessed structural characteristics. The chosen method, applying beta radiography images of small circular areas as a reference was successful. The observed linear relationship indicates that the applied methods for image acquisition and subsequent image processing yield a systematic loss of fibre material. The main loss of fibre material in this study is probably caused by the lost fibre voxels when removing the glue phase from the structure. Later studies will hopefully avoid this gluing problem. Assuming the gluing problem and other structural defects from sample preparation and mounting can be avoided, the applied beta-radiography correlation method can yield a qualified estimate of the effect of limited resolution to the amount of solid material detected. The method can also be applied to calibrate the area to density constant. The found estimate of 1240 kg/m^3 is as such a reasonable estimate for the softwood TMP fibres. However, this constant will also partly compensate for the fines material not detected at the resolution of 1-2 µm. It will also be affected by the threshold and filtering criteria chosen for the image processing.
The extensive analysis of basis weight effects showed that the variation caused by the varying basis weight was relatively small for many assessed structural characteristics, despite the selected wide range of basis weights. This is a promising result, as one of the largest disadvantages of the high resolution X-ray microtomography 3D imaging technique is the expense and low possibility to acquire replicate volumes of the imaged paper grades. The found standard deviation indicate that most structural characteristics yielding useful assessments of the structural properties can be determined within a certainty of ± 10%. However, it should be emphasized that the transport related characteristics, especially for the z-direction, show a consistently larger variation caused by the basis weight variation. The larger variation for transport properties can best be compensated for by determining transport property:porosity relationships instead of single mean values. Such an approach requires analysis of the digital volumes as a set of subvolumes of a sufficient size to yield representative scales of the structural characteristics.
It was found that the linear dependency to basis weight was relatively low for most structural characteristics. The correlation is probably worsened by enclosed shives and the non-systematic glue removal effect. It is thus possible that the dependency to basis weight is larger than detected in this study. However, it is clear that other variations than the basis weight are more decisive to the assessed structural characteristics than basis weight.

The experimental scheme, in essence only yielding two solid fraction levels, was not well suited for considering the applicability of the assessed structural characteristics for increasing the fundamental comprehension of how the detailed paper structure influence the bulk paper properties. For such considerations, study of a single paper making variable under a wider range of conditions is better suited.

The synchrotron source 3D images are of generally high quality. The applied structural characteristics were successful in assessing what could be interpreted from visual inspection of the digital paper volumes and what could be expected from the applied papermaking variables. The determined distributions for many of the structural and transport characteristics yield additional information to the mean values applied for the analysis of the factorial design. The distributions do the detailed measures of the paper structure more justice than the factorial design approach. The results as such show that the application of X-ray microtomography is a promising technique for gaining knowledge of the properties of the detailed paper structure and how it influences paper properties. The current stage of application of X-ray microtomography resolves the structure:bulk property relationship best for transport properties.

CHAPTER

6

SUMMARIZING DISCUSSION

6.1 Introduction

This study has covered two principally different techniques, SEM imaging and X-ray microtomography, for assessing various detailed features of the paper structure. Although there are many differences between the two techniques, there are also several common problems. It is the intention of this chapter to summarize important common concerns for both techniques.

SEM imaging and X-ray microtomography are both interesting and useful tools for paper research. However, both techniques have certain advantages and disadvantages. Which technique is the best to apply for different practical and scientific applications will wary. This chapter will discuss which choice is the best dependent on the application and requirements of the obtained results.

6.2 Surface definition

A problem recurring in this study, and for other scientists analysing cross sections and digital 3D structures, has been the determination of a limit for the extension of the paper structure, or in other words to determine a useful, objective definition of the surface. The small size of the cross sections and the 3D volumes makes a linear approach inappropriate, as it will result in an extremely large surface porosity for all paper grades except smooth/glossy grades like SC or coated paper. The totally opposite approach is to determine the local surface to be the outermost solid particle in each pixel/voxel column of the cross sections/3D images. Such an approach will result in a low thickness and a high solid fraction/density (compared to the apparent measures from physical bulk measurements) and a locally discontinuous outer layer of the structure at sharp fibre edges.

It is therefore necessary to find a method being able to determine a surface definition somewhere between the extremities, but still being objective, well working for all varieties of paper structures and being fully automated. After various attempts it was found that the rolling ball principle, as applied in this study for both cross sections and 3D structures, is well suited for solving the surface definition problem. The rolling ball principle has also been acknowledged as the best surface definition to date by other researchers working with similar problems [17,26]. The rolling ball principle is fully automated and works for all varieties of paper structures. However, the diameter of the ball may need to be adjusted according to the surface roughness of the sample, what is going to be measured from the digital structure and even according to whether it is of interest to obtain a surface approaching a physical test like *e.g.* surface definition by a stylus of a given size. In this sense the method is not fully objective. Application of a constant diameter of the ball for comparative studies using a sufficiently large common diameter will also yield the variation in surface roughness as a variation in surface layer porosity. For sufficiently large ball diameters most valleys found in the surfaces of the assessed paper samples will appear so narrow, compared to the curvature of the rolling ball, that the ball will not penetrate appreciably into the structure even for the roughest samples.

An additional benefit of the rolling ball principle is that it will result in thicknesses and solid fractions/densities in the size order of the apparent physical measures. The rolling ball principle thus fulfil all desired requirements for a good surface definition, as long as the ball diameter is reasonably chosen compared to the surface roughness of the samples.

6.3 Fibre density

A second recurring problem in this study has been to determine or find a constant for the fibre density yielding a realistic area to density conversion to determine the amount of solid material (basis weight), the density of the structure and/or specific surface area (SSA) per gram of fibres.

Although it may be of interest to relate the basis weight and density of the digital structures to physical measurements, such a comparison should be applied with caution both for cross sections and 3D images. The problem of area to density conversion should preferably be avoided except for applications when it is essential to check the correlation between the amount of material detected by the imaging technique and physical measurements. Normally the conversion from solid fraction to density does not yield any additional information. It will instead introduce an additional source of error because the applied fibre density will at best be an estimate. The SSA (m^2/g) depends on the fibre density. However, the measure will also vary with the applied pixel/voxel resolution, the image acquisition and the image processing. The determined SSA will thus not give any close resemblance to a physical assessment, even if a physically correct fibre (area) density is applied. For comparative studies it is therefore sufficient to apply a good estimate for the fibre density, especially when the samples contain the same fibre furnish. The struggle for determining a correct area to density conversion is thus normally a problem that only needs to be solved to determine the amount of solid material detected when establishing a technique, and should be no concern for routine analyses. Additionally, the results in this thesis work have shown that the evaluation of whether the X-ray microtomography 3D image acquisition has the ability to detect the correct amount of solid material rather should be done applying an area reference instead of the applied basis weight reference.

For the instances where it is considered necessary to apply a fibre density, the experiences from this study show that the applied fibre density of 1550 kg/m^3 is probably too high for all pulp types. The applied density is the same as for native cellulose, but the fibre segments/cross sections obtained by the paper structure microscopy will contain small pores not detected at the applied resolutions. Filtering of the greyscale images will normally smooth the greyscale values dependent of the vicinity and will thus possibly even remove small micropores that are not distinguishable from normal variation in greyscale intensity. The setting of threshold is different for the SEM and X-ray microtomography images. The automatic threshold of the SEM images yields an objective phase separation. The threshold set for the X-ray microtomography is based on an interactive observation of the best trade-off between preserving the fibre cross sections as complete as possible and the introduction of noise. Despite the visual reference, the method allows for some subjectivity, which will affect the fibre density of the 3D images. It is most likely that this subjectivity may tend towards a threshold that assigns too many voxels to the solid fraction. Additionally, the choice of filtering criteria for the binary images attempts to remove small void regions in the fibre walls, as most of these regions most likely are noise. However, a fraction of these regions may be cavities in the fibre wall. The resulting binary fibre segments/cross sections may thus have a significantly lower area density than the 1550 kg/m^3 for both SEM imaging and X-ray microtomography.

The limited resolution, especially for the X-ray microtomography technique, further complicates the area to density conversion, as a fraction of the solid materials, the smallest fines and fibrils, will not be detected. It is thus necessary to determine the fraction of solids not detected by the technique, before it is possible to determine a realistic area to density conversion from calibration efforts. It is also important to note that it is necessary to run new calibrations for all experiments to obtain realistic area to density conversions for all the applied microscopy techniques, as the amount of small particles and area density may vary with both pulp and paper processing, and the image acquisition and processing.

6.4 Choice of technique (2D vs. 3D) for structural characterization

The decision of which is the best choice among the structural characterization methods, either applying (SEM) cross sectional or 3D imaging of the paper structure will depend on a number of factors. The most important factor is what is going to be measured, as it for most purposes is like the Norwegian expression “to kill sparrows with cannons” to determine structural characteristics by high resolution X-ray microtomography when it just as well may be determined applying SEM cross sections. The nature of the needed assessment is another issue. A more routine type characterization will have demands totally different from a characterization done with focus on obtaining fundamental knowledge of the paper structure. Another issue is the availability of the techniques and whether it is important to obtain results with low uncertainty. The choice of technique may also be influenced by the required resolution to see the details considered important for the results. The different factors that will determine the preferred technique will be discussed in the following subchapters.

6.4.1 Accessibility

The main drawback of the high resolution X-ray microtomography technique is the requirement of a synchrotron facility. There exist very few 3rd generation synchrotrons able to generate the desired X-ray beam characteristics with beamlines applied for microtomography imaging. There are currently only three such facilities in the world [133], of which only one is situated in Europe (the ESRF). It is a “tough” competition between various biology and material science applications and between scientists from the various funding countries for the available beam-time at the ESRF. It is therefore difficult to get allocated beamtime for the 3D imaging needed for structural characterization. The high resolution X-ray microtomography will thus not be an everyday research tool in the near future. Alternatively it is possible to buy beamtime, which allows easier access, but commercial beamtime is costly. The best solution is therefore to apply the easier available cross-sectional techniques as long as they yield adequate results.

Because of the low availability and high cost of the high resolution X-ray microtomography, building 3D structures from consecutive cross-sectional slices based on serial grinding or microtoming may be an alternative. Such a technique may be an in-house technique offering superior contrast and resolution in two of the principal directions. However, it has a considerably lower depth resolution. The consecutive cross sections approach has a high demand on man-hours for building up a digital volume of reasonable size. It may thus be at least as costly as buying X-ray beamtime. The low resolution commercial tomography scanners yield a more accessible and cheaper alternative for comparative structural studies. It yields however results that can be far from the physically correct values due to the limited resolution. The technique as such is less suited for obtaining fundamental knowledge of how the detailed paper structure influences the bulk paper performance properties. However, the resolution is sufficient to detect structural differences above the scale of small pores and fibre network details. The method is thus applicable for comparative studies.

Scanning Electron Microscopy (SEM) has become more or less a standard research tool for many pulp and paper research institutions and is therefore accessible to most pulp and paper researchers. The instrument has been applied for a relatively long period, which means that there exist well proven standard routines for sample preparation and optimal image acquisition. It is also well known what factors may influence the quality of the images allowing these artefacts to be avoided or to some degree compensated for. The 2D technique is as such much more readily applicable than the 3D technique. For most applications it is thus natural to select the SEM for imaging the structure, as long as it can provide the structural information of interest.

6.4.2 Image resolution

The resolution of high resolution X-ray microtomography is somewhat limited when it comes to detecting the fines and fibrils in the fibre network. The SEM technique has the ability of acquiring good contrast images with a resolution far better than what is needed to see all details affecting the light scattering of visible light. Nevertheless, the X-ray microtomography provides the 3D extension of the fibres, the coarsest fines and the pores, which may be of great help for certain applications.

It is likely that the resolution of X-ray microtomography will further improve in a not too distant future. However, the price for better resolution, for any imaging technique, is a smaller assessed image or volume. The smaller size may be relatively easily compensated for by obtaining more replicates for SEM imaging, but increasing the number of replicates for the high X-ray microtomography will most likely prove difficult also in the future. There will therefore exist an optimum trade-off between resolution and volume size for X-ray microtomography, as long as computers are unable to handle digital volumes in the size order of Terrabytes! The current optimum is most probably around 0.7 µm, as the sizes of the volumes are theoretically 8 times larger than for a resolution of 0.35 µm. The imaging technique for the 0.7 µm resolution is more well proven for paper and the increased detail level for the highest resolution is still not sufficient to see all optically active details in the paper structure.

If the detection of fines and fibrils are considered to be essential for the structural assessment, the SEM is the obvious technique. However, for applications where the main focus is to find relations between detailed structural properties and bulk paper performance, the 3D technique may prove to be better suited despite the lower detail level. This is so as the 3D information allows simulation of transport and optical properties in digital structures. Although the 1-2 µm resolution is too low for physically reasonable simulation of light scattering, a simulation may yield information on how differences in structural composition and how the bulk compared to the surface layers affects the scattering ability.

6.4.3 Representativity

Due to the low availability or high cost of high resolution 3D images from X-ray microtomography, the number of replicates will normally be low for most experiments involving 3D characterization of the paper structure. Although it has been shown that the standard deviation of structural properties are < 10% of the mean, this variation may be too large for comparative studies where the differences between the samples are relatively small. It is not realistic to increase the number of replicates of 3D images to a number yielding considerably lower standard deviations of the mean due to the high demand on the beamlines. However the representativity may be improved by applying basis weight (or other) corrections with reference measures by other techniques as exemplified in Chapter 5. The representativity will also be less of a concern when choosing an experimental scheme with several levels of the paper making variable(s). The standard deviation for the various structural and transport characteristics will then only appear as a slightly lower correlation seen as *e.g.* lower R^2-values.

The higher availability of the SEM technique renders it more practical and realistic to acquire the number of images needed to obtain representative results. Although the extension of the detected structure is extensively smaller for the two-dimensional images compared to 3D images, the higher possibility for freely choosing as many independent cross sections as needed to obtain representative results makes the SEM technique better suited for gaining more accurate structural assessments.

6.4.4 Choice of the right tool according to problem complexity

The SEM technique is nowadays a readily available technique for pulp and paper research and is known to yield high quality cross sections of paper. The needed resolution and representativity for structural assessments of cross-sectional images of paper are easily achievable. However, there are paper structure characteristics that can not be determined from the 2D information alone. It is the intention of the following section to explore which structural assessments that are sufficiently complex to require 3D imaging.

To determine the material distributions (solid fraction, fillers, and fines) in the z-direction it is considered that applying SEM cross sections will be the best approach. The choice is based both on resolution, representativity and that the 3D information is not crucial. However, for more fundamental understanding of for instance solid fraction gradients, the 3D information accessible by X-ray microtomography may yield useful insight into surface and interior relationships, given that the technique can handle the high density paper grades.

Determining the specific surface area based on SEM cross sections will normally yield a more realistic measure than 3D images due to the higher resolution and improved representativity (assuming 15 or more independent replicates). However, specific surface area is by nature a three-dimensional parameter quantifying the surface area of volume objects. Light's interaction with the paper is also by nature three-dimensional. The results obtained from cross sections are thus somewhat limited due to the lack of structure information in the vicinity of the imaged structure. It is therefore important to keep these limitations in mind when evaluating the results from cross sections. To gain improved fundamental knowledge of the relationship between the paper structure and optical properties, the digital 3D images of the paper structure is a requirement. However, to obtain realistic measures it is desirable that the resolution of the X-ray microtomography technique is improved to around 0.2 μm, preferably allowing acquisition of volumes in the size order of at least 1x1x{paper thickness} mm^3. (This corresponds to an image size of at least 12 Gigabytes for a paper being 100 μm thick!).

The characterization of the pore geometry is best done applying 3D images of the paper structure. The assessment of cross sections allows measurement of hydraulic radii and pore chords. Measurement of pore chords from both MD and CD cut cross sections also allow determination of the structural anisotropy. However, this can be determined much faster and more convenient applying laser techniques [36,55]. The nature of pores make themselves three-dimensional. It is therefore clear that cross-sectional methods lack essential information, which can be provided applying 3D imaging. The 3D methods allow a more correctly adapted technique for assessing the extension of the pores and also the possibility of determining the connectivity of the porous network.

The three-dimensional technique is essential for the determination of transport properties. The transport pattern can never be realistically determined from cross sections, as it is a very unlikely event that the transport only will go through the imaged plane.

Although it is not considered in this thesis, the 3D images may also be exploited for determining useful information of the bonded fibres and fibre network. Such measures are obviously not accessible from cross sections. In addition to determining the extension, orientation and geometry of the fibres, the three-dimensional information can possibly be exploited for determining the connectivity/free fibre length of the fibre network. Provided that the fibre network can be segmented into its individual fibres and fines/fibrils, a direct measure of the relative bonded area can be determined. Such a segmentation is also a good starting point for FEM simulations for the strength properties of paper.

Image acquisition applying absorption mode X-ray microtomography of paper grades containing fillers will possibly allow the determination of a size distribution of filler agglomerates as they appear in the paper structure.

CHAPTER 7

CONCLUDING REMARKS

7.1 New technique, new possibilities

7.1.1 Image analysis of SEM cross sections

Although the SEM is a technique that has been applied relatively long in the pulp and paper research, the quantification of structural characteristics of the imaged cross sections is quite recent. The well-suited embedding technique (epoxy) and personal computers having fast processors and high memory capacity are both requirements for the structural characterization that have been introduced only during the last decade or so. The image analysis of paper cross sections is thus a technique still under development. The intention of this study is thus to be a step forward in the application of SEM for the assessment of structural characteristics.

This study has shown that the SEM imaging of paper cross sections at submicrometer resolution can be applied for more than visual comparison and detection of structural defects. Image analysis provides a method for quantification of the structural characteristics, a necessity for objective comparison between various paper grades and the study of the effect of different papermaking variables to the paper structure. However, the results from image analysis are dependent on the quality of the cross-sectional images. It is therefore important to understand which factors influence the quality of the cross-sectional images and how the quality is best maintained during the needed filtering and segmentation steps to obtain a binary structure suited for image analysis. This work has therefore focused relatively much on all such details influencing the quality of the binary cross-sectional images. It will hopefully provide assistance and guidelines for future applications regarding image quality. This is of outmost importance, as the results from the image analysis is reflected by the quality of the analysed images.

Routines have been reported in literature for image analysis of different features of paper cross sections. Most of the routines have had problems in defining the extension of the relatively rough surfaces of the small, high resolution cross sections. As the surface definition clearly influences most of the structural characteristics that can be extracted from cross sections, it is considered that the objective definition of the surface applying the rolling ball algorithm is an important improvement in application of cross-sectional analysis. Through different segmentation of the cross-sectional images and the surface definition for the complete structure, the material distribution of solid fractions, fillers and fines in the z-direction can be determined based on the objective surface definition. The main contribution from this work regarding image analysis routines is thus the introduction of the objective surface definition and the methods for determining the material distributions in the z-direction. The work also includes improvements of existing routines for the determination of local thickness, solid/void fraction and basis weight, measurement of pore heights/widths and specific surface area. This thesis thus provide an overview over which structural characteristics that can be determined from paper cross sections, but excludes measurements of the coating layer, fillers and surface roughness [1].

It is important to emphasize that the assessment of structural characteristics should be regarded as a tool for performing quantitative research of how various papermaking variables alter the paper structure and thereby affect the paper properties. To fully exploit the technique, it is important to see all the possibilities the technique provides. Through the application of cleverly designed experimental schemes, applying the cross-sectional technique for structural assessments, it is possible to gain new knowledge of the behaviour of the paper material for different papermaking variables. The practical example presented here in the attached Paper IV, for the effect of temperature gradient calendering on SC-paper, shows a good example of how the technique can yield detailed answers to the behaviour of paper under various conditions. The example also shows that the technique may need to be combined with other techniques to provide clear conclusions. As long as paper researchers are able to see the possibilities provided by the technique, it is considered that the SEM imaging of paper cross sections and subsequent image analysis will provide much useful information of the papers detailed physical characteristics in the future.

7.1.2 3D microscopy and structural assessment

This study is part of the initial step of applying 3D microscopy for the assessment of the detailed features of the paper structure. The focus has therefore been to test the ability of the technique to acquire high quality 3D images of the detailed paper structure and to establish the application of various structural assessments for quantifying the characteristics of the digital paper structures.

X-ray microtomography is a non-invasive microscopy technique that provides a possibility to acquire 3D images of paper. The X-ray beam characteristics of synchrotron source radiation is sufficient for good contrast between fibres and air at a spatial resolution of 1-2 µm. The acquired 3D images show that the synchrotron source radiation X-ray microtomography, having submicrometer sized voxels, yields digital paper structures with a well preserved topology revealing the detailed fibre network. The phase contrast imaging is also able to yield sufficient contrast between water and fibres, providing a possibility for image acquisition of soaked paper samples. The phase contrast technique is not suited for paper grades containing fillers and high density paper grades.

---

[1] The surface roughness is better determined by surface topography methods like e.g. laser profilometry

Paper grades containing fillers and/or having a low void fraction is better suited for absorption mode contrasting.
The commercial CT scanners have too low resolution to reveal the detailed features of the fibre network and interconnected pores. However, the acquired images from the commercial scanners can successfully be applied for comparative studies, although the quantitative results are not physically reasonable. In this context it should be reminded that the spatial resolution of the hard X-ray microtomography techniques of 1-2 μm is not sufficient to detect the smallest fines and fibrils in the structures. The quantitative results will thus deviate from physical measurements for the high resolution 3D images, but are still considerably more realistic than the low resolution techniques. However, it is always expected that results from image analysis will yield technique dependent results. The results from the image analyses are thus not expected to reproduce physical assessments, but yield structural assessments able to give additional information on how the detailed paper structure are affected by papermaking variables and itself influence the paper properties.

Because of the focus on exploring the possibilities provided by 3D microscopy of paper, the priority in this thesis work has been to find working filtering and segmentation routines yielding binary images that preserves most of the essential information in the 3D images, not to find the optimum image processing. There is thus a high potential for development of improved image processing routines, possibly exploiting the three-dimensional information better than in this thesis work.
Despite the relatively simple approach to filtering and segmentation of the 3D images, it is possible to see clear differences for the applied contrasting modes regarding image processing and quality of the resulting binary paper structures. The phase contrast images, having a relatively low contrast and only detecting the phase borders, involve a difficult, labour and computationally expensive procedure to produce binary images that preserves most of the details found in the greyscale images. The low contrast combined with the pure phase border information results in a relatively large chance of misclassifying voxels. The image processing of the absorption mode images are considerably simpler than for the phase contrast images. The contrasting technique depicts the complete fibre walls and has a relatively good contrast, improved by elements of phase contrast information in the projected signal. The procedure for obtaining binary images that preserves most of the information in the images is thus in principle much simpler than for phase contrast images. However, the penetration of melt glue having approximately the same absorption properties as the fibre phase introduces some additional problems. Except for the difficulties due to the additional glue phase, it is considered that the absorption mode images yield binary images of approximately the same quality as the phase contrast images due to the better contrast and simpler image processing. The application of absorption mode is therefore the recommended contrasting technique for future image acquisition of dry paper structures. Application of an alternative sample mounting excluding the melt glue and using edge preserving filtering procedures utilizing the three-dimensional covariation in the greyscale volumes will most likely improve the quality of the absorption mode images compared to the good quality images presented in this thesis work.

The structural characteristics determined for the digital 3D paper structures in this thesis work have been focusing mostly on pore geometry and transport properties in addition to basis measurements like porosity, specific surface area and reference measures like thickness, density and basis weight. Additionally there are many assessments that can be determined for the fibre network (Yang [72,73]) and the individual fibres (Aronsson [17,26] and Hagen et al. [134]), that can yield additional information not provided from characterization of the structural anisotropy. The future development of the assessment of the digital 3D paper structures might also see simulation of optical and paper strength properties performed directly on the digital paper structures. The applied routines in this thesis work are thus only a starting point, showing some of the possibilities for quantitative assessment of the detailed structural characteristics provided by the availability of high resolution 3D images.

It is important to remember the basis for obtaining measurements of the detailed paper structure. Although it is possible to determine various characteristics of the images, the assessments are of greatest interest if they can be applied for yielding insight into how the paper structure properties influence the bulk paper properties. In this initial phase it is important to be creative and see new possibilities to what can be quantified in the 3D images. However, practical applications, exemplified in Chapter 5 of this thesis, will show which characteristics that yield useful insight to paper property:paper structure relationships. All structural and transport characteristics assessed in this study have proved to yield insight to papermaking variables:paper structure characteristics, with a possible exception for the critical radius.

The practical applications of the X-ray microtomography technique for assessing the effect of various papermaking variables in this thesis work have given some new insights into how the detailed paper structure is affected. The results from analysis of the applied factorial design revealed a dominant effect of calendering. Calendering resulted in a paper structure having lower solid fraction, significantly reduced extension of the pores and an increased resistance against fluid flows through the porous phase of the structure. The effects were most pronounced in the z-direction.

The results gave indicative results for the other papermaking variables, of which most were not statistically significant due to the dominant effect of the calendering and a relatively large random variation due to the digital procedure for the removal of the glue applied for sample mounting. The few significant effects proved that addition of 20% BSKP reinforcement pulp resulted in slightly larger pores and the addition of the fixation agent resulted in a more complex structure with slightly smaller pores and higher resistance against flow transport. Alteration of the head box consistency had an insignificant effect on the observed small paper volumes.

The results from the experiment confirm that the solid fraction is the major determinant for most structural properties. To study effects that are expected to influence the paper structure through other mechanisms than changing the solid fraction it is therefore recommended to try to keep the solid fraction at a constant level.

The experiment also included assessment of the effect of basis weight variation. The results showed that the standard deviation was less than ± 10% of the mean value for the assessed structural characteristics. This is a promising result for the future application of high resolution X-ray microtomography, especially considering that the assessed paper volumes were chosen for as wide variety of basis weights as possible, and containing shives and a relatively large additional random variation from the digital glue removal. Assessments of commercial paper grades will thus probably show even lower standard deviations.

The transport properties show a clear relationship to the porosity of the assessed volumes. It is therefore more difficult to obtain representative mean values for the transport properties than for the structural characteristics. This is best resolved by determining the transport property:porosity relationship based on subvolumes rather than a single mean value for the complete volume.

The 3D microscopy and subsequent image analysis is a new research tool, providing many possible applications for those who see the possibilities. It is important to create experimental schemes well adapted for determining the effects of papermaking variables to the detailed paper structure and possibly also to find clear relations between structural characteristics and bulk paper performance properties. The experiences from the practical example presented in Chapter 5 show that it is recommended to apply three or more levels for the chosen papermaking variables to reduce the vulnerability to random variation for the small assessed paper volumes. To find paper property:paper structure relationships it is also important to perform physical measurements and structural assessments that are expected to have clear correlations. The future will likely yield many interesting results from the application of the 3D techniques presented here as long as paper scientist see the available possibilities.

7.2 Right technique for right application

An important part of this study has also been to consider which among of the 2D and 3D methods is the right technique for various structural characterization applications. Although there are no totally clear answers to this, some guidelines may be given.

There is a clear differentiation between the practical applications of the techniques. The SEM technique is the preferred technique for more repetitive and routine type assessments, for characterization where the 3D extensions of the objects will not be of crucial interest or for assessments where the nature of fines and fibrils are of high importance. The X-ray microtomography is a natural choice for more complex structural assessments where the extension of the fibres and pores are the key interest, as for e.g. assessment of transport properties. The 3D extension of the structure may also for many instances prove to be needed to obtain a better knowledge of how the paper structure influences the bulk paper performance properties. X-ray microtomography is thus a powerful research tool that can provide information which is difficult or impossible to access applying other methods. However, the technique has its clear limitations when it comes to accessibility, representativity and resolution. It is also important keep in mind that the technique might never be an everyday technique that many scientists will have access to.

7.3 Suggestions for further work

7.3.1 2D microscopy and analysis of cross-sectional images

Although the sample preparation of SEM cross sections applying embedding in epoxy and subsequent grinding and polishing are known to support the paper structure and thus yield minimal distortions, it is known that it may result in a smearing effect. This can be especially difficult for fibres orientated along the ground and polished surface and for chemical pulp fibres. To evaluate this smearing effect, it is desirable to measure the cross sectional area at the surface and a few micrometers under the surface applying confocal microscopy. Experiences with SEM imaging at NTNU/PFI show that the smearing effect most likely is insignificant as long as the sample preparation leaves sufficient time for curing before grinding and some time between the various grinding and polishing steps to let the ethanol evaporate and the surface structure stabilize. However, it will still be an improvement to obtain quantitative measures of the smearing effects for various pulps.

To possibly reduce the distortion of the structure to an even lower level than for the technique of grinding and polishing epoxy embedded samples, it is possible to test sample preparation by the focused ion beam (FIB) or micromilling. These are relatively expensive techniques that are not currently in-house techniques in pulp and paper research institutions. It might however be worth investing in such equipment, especially if it is desirable to build 3D volumes from consecutive cross sections. The lower level of structural distortion might yield an easier 3D reconstruction. Furthermore, the techniques of FIB and micromilling are especially designed for such applications.

The rolling ball algorithm allows an objective surface definition of the surface of the cross-sectional paper structures. However, the choice of the radius of the applied circle still leaves some subjectivity. It may therefore be desirable to determine a criteria for the choice of radius based on the surface roughness to standardize the routine.

7.3.2 Assessment of pore geometry

To obtain more detailed knowledge of the three-dimensional extension of the pores in paper it is desirable to apply a skeletonization procedure of the porous phase. Such an approach may be used to partition the continuous porous phase into individual pores based on a pore neck criteria. A partition based on a physically reasonable pore throat definition in the digital paper volumes may yield information of connectivity and pore body geometry:pore neck geometry in addition to the shape and extension of the individual pores. However, as there is still disagreement of the skeletonization and pore neck criteria for the somewhat simpler systems of porous rocks, it is recommended not to apply these procedures for the more complex structure of paper at the current stage. When the criteria are physically reasonable it is considered that the information retrieved from the skeletonization approach will yield physically dependent pore geometry features that can yield insight into how the detailed pore geometry influences the transport properties of paper.

An additional insight to the effect of the local pore geometry to transport properties can be obtained from transport simulations. As the transport property is determined from solution of how the local details influence the flow, visualization of the flow paths will yield direct insight into how the local geometry influences the transport through the structure. An example of a local flow determined from lattice-Boltzmann simulation of the flow through a complex digital porous example volume is given in Figure 7.1.

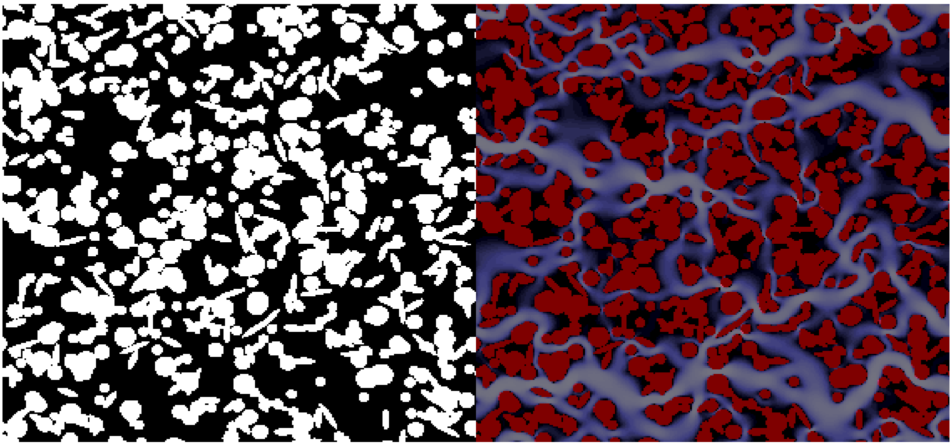

Figure 7.1 An example of how simulation of fluid flow in digital porous structures can yield information of how the local pore geometry influences the fluid flow through the structure. **Left:** A cross section of the example porous structure. Voids are black. **Right:** The resulting local flow paths from lattice-Boltzmann simulations of the flow through the digital porous volume.

The availability of digital 3D paper structures allows an evaluation of what is actually measured when applying physical measurements of the pore size distribution applying mercury intrusion porosimetry (MIP). Flow simulations may show the effect of narrow pore necks shielding large pore volumes for the mercury intruding the porous phase from the surfaces. The results from MIP simulations compared to physical measurements may also yield information of how the possible compression of the paper structure at high applied pressures in MIP influences the assessed pore size distributions. Although this thesis work presents initial results from simulation of MIP, there is large potential for determining more detailed explanations of how the pore geometry influences the mercury intrusion and thus the obtained pore size distributions derived by the physical measurement.

7.3.3 3D microscopy and assessment of structural characteristics

The X-ray microtomography is a technique that is currently only at an introductory stage for application in paper structure research. It is thus naturally that most elements of the technique will be improved and new possibilities for structural assessments may be found. The suggestions for further work is thus relatively extensive, but will hopefully give guidelines to the development and future application of the technique.

Although the currently achieved resolution for hard X-ray imaging is sufficient to see the detailed fibre network it is desirable with an even better resolution to resolve the effect of the smallest fines, fibrils and possibly fillers to the assessed structural characteristics. The development of the optics at the synchrotron facilities are currently towards the so-called nanotomography. It is thus likely that higher resolution will be available in a not too distant future. The technical development will most likely also introduce faster computers with a larger memory capacity allowing digital paper volumes of the same physical size as today, but with a higher resolution. This will require CCD-detectors with a larger number of pixels. The possible development towards higher resolutions may be especially useful for simulation of optical properties. However, it should not be forgotten that there will always be a trade-off between image resolution and the size of the imaged paper structure.

The sample preparation, especially for the absorption mode imaging at the ESRF may be significantly improved. It is recommended to either cut the paper samples with laser cutting or focused ion beam to reduce edge artefacts. Alternatively, the samples may be cut so large that the distorted sample edges are outside the field of view. However, this will increase the time needed for aligning the sample before image acquisition.

Mounting of the sample by attaching the paper sample on top of a capillary with a melt glue should be avoided, especially for thin paper grades as assessed in this study. The melt glue is harmful for the obtained detailed paper structure of the attached surface layer. It is recommended to evaluate alternative methods for sample mounting applying a glue with a higher X-ray absorption than paper or a hydrophobic glue for attachment. As the capillary approach allows the application of a faster image acquisition and thus more acquired images in an allocated beamtime at the ESRF, alternative sample mountings to the capillary approach are not recommended unless it is needed for acquisition of samples under varying physical conditions.

The application of adhering the paper sample of interest to the capillary via a piece of the glue surface of a Post-It note has shown to yield a sample mounting to a capillary with minimal penetration of the glue into the paper structure. The difference to the melt glue applied in this thesis work is shown in Figure 7.2.

An improved sample mounting avoiding the loss of solid material due to the digital removal of the glue phase from the paper structure will allow improved gains from the basis weight correlation method presented in Chapter 5 of this thesis. The application of the method is recommended to determine how much of the solid material that is retained in the binary digital representation and evaluating the fraction of fines and fibrils not seen at the applied resolution. The method will also yield a good estimate of the fibre density and may be applied to correct for basis weight effects for assessed area deviations from the mean basis weight determined by beta-radiography imaging.

A possible experimental scheme for an evaluation of how the effect of the applied resolution, image acquisition settings and subsequent images processing affects the quality of the images will be to produce paper sheets of a pulp with fibres that have a low degree of fibrillation and produce sheets of both the whole pulp and only the long fibre fraction. The sheet without fines can be applied to determine a correct estimate of fibre density, whereas the sheet containing fines may be applied to determine the amount of fibre material not detected at the applied resolution.

The image quality is dependent of the applied threshold value. Although the current threshold value is based on an observed trade-off between preserving the fibre cross sections as complete as possible and avoiding introduction of noise, there is room for improvement. It is therefore recommended to find a criteria for an automatic threshold based upon well-suited experiments. Assuming the filtering has been optimised through

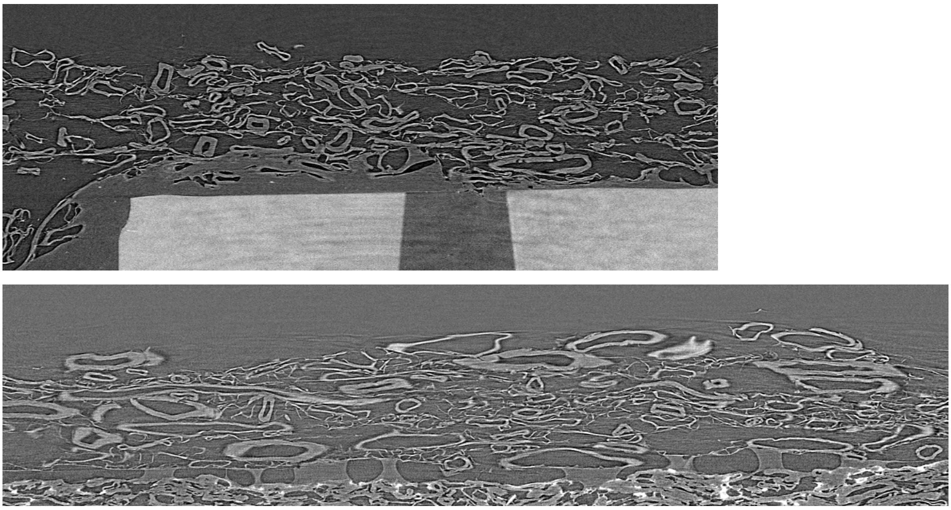

Figure 7.2 **Top:** A cross section of the imaged paper structure when applying a melt glue for attaching the paper sample to a capillary for absorption mode, synchrotron source X-ray microtomography 3D imaging. The glue penetrates into the structure and is difficult to discern from the fibres. **Bottom:** A cross section of the imaged paper structure when applying a piece of a Post-It for gluing the paper sample to the capillary. The Post-It note itself is glued to the capillary with the melt glue. The non-wetting glue of the Post-It note is only in contact with the paper structure and do not penetrate into the structure. The pigments in the surface layers of the Post-It note make it easy to discern the two different paper structures.

application of more 3D based methods that preserves the phase borders, the correct threshold can be determined from a calibration sheet made from uniform fibres, where the extension of the fibres are known. Possible examples of such fibres may be rayon, viscose or glass fibres. However, the application of fibres having the closest resemblance to pulp fibres will also yield the most reliable results.

The practical application of the X-ray microtomography technique to determine the effect of papermaking variables to the detailed paper structure will be improved by experience. The choice of experimental schemes is decisive for how much information may be gained from the 3D images and the possibility to validate hypotheses on the paper structures that influence paper properties. However, the possibilities will always be somewhat limited by the resolution and image size of the digital volumes compared to the size of the details in the paper structure and formation effects. The experiences made in this study show that it is preferable to apply experimental schemes with three or more levels of the applied papermaking variables. It is also recommended to keep the variation of the void fraction at a reasonable level, if it is desirable to evaluate the effect of papermaking variables that are considered to influence the paper structure through other mechanisms than changes of the void fraction. It must be expected that the choice of the applied levels for the chosen papermaking variables will yield too small or too large differences of the paper structure in this initial stage. However, experiences from this study and future studies applying X-ray microtomography will yield better estimations for reasonable levels for structural assessments.

There are numerous applications where it is possible that the availability of the 3D paper structure may yield useful insight that improves the knowledge of the relation between papermaking variables, paper structure characteristics and bulk paper performance properties. The experiences gained from this thesis work and other published experiments show many interesting possibilities for the technique. The possibilities are theoretically limited almost only by the imagination, but practical experience may show that it is not physically possible to make the desired image acquisitions. The following section includes many examples of ideas for useful application of the technique, that are yet to be tested. To keep the size of this somewhat 'speculative section' to a reasonable length, the possible applications are only treated briefly.

Possible new applications of the X-ray microtomography technique

It is possible to apply absorption mode imaging for paper grades with coating and/or fillers. The study of the coating layer may yield insight to the relation between the local paper structure and the coating thickness. The study of the fillers may show to which degree the fillers aggregate and whether the fillers are mostly distributed between fibres or in the cavities of the structure. The relatively high X-ray absorption of the minerals will probably result in a straightforward segmentation of the fillers and coating, but the introduction of a third phase may increase the difficulty of the fibre phase segmentation.

This thesis work has shown that it is possible to obtain 3D images of soaked paper samples applying phase contrast imaging. It is desirable to study how the 3D paper structure changes with varying humidity levels. The possibility of studying the effect of drying and wetting of the paper structure would yield useful insight into the physical behaviour of paper.

The study of the effect of relative humidity could be achieved by changing the environment of the experimental hutch or build a small, closed sample chamber of a material that will not affect the quality of the transmitted X-ray signal significantly. However, due to the strong restrictions to stability during the 180° rotation for the high resolution imaging, it may be difficult to obtain images of high quality without typical ring artefacts from sample movement. The alternation of relative humidity can be done in a manner that allows assessment of the same paper volume under various conditions, which makes the evaluation of relative humidity effects relatively straightforward if images of sufficient quality can be obtained.

The main difficulty of evaluating the effect of drying and wetting the paper structure is that it is impossible to image the same paper structure with varying dryness levels. It is possible to freeze the structure under different wetting and drying levels applying cryo-fixation techniques. Cryo-fixation with hydrophile liquids that become solid at room temperature allows the stability needed for X-ray microtomography imaging, but the method is destructive to the imaged sample. To evaluate the effect of wetting and drying the paper it is thus necessary to obtain representative quantitative results, preferably applying a paper grade with a good formation to better visualize the effects to the detailed paper structure.

The simulation of diffusivity can be done applying a random walk method as an alternative to the LaPlace/conductivity approach applied for the diffusivity assessments in this thesis work. Assessment of diffusivity applying both methods for the same

structure can yield useful information of the pros and cons of the two methods.
The diffusivity simulation in the digital structures also allow movement of the liquid molecules through the fibre phase. However, there is a need to determine criteria for when the water molecule will enter and leave a fibre/void surface to allow physically reasonable diffusivity simulation. Assuming a physically reasonable criteria for entering/exiting the fibre phase can be found, the simulation can be applied to determine estimates of the diffusivity in the fibre phase relative to the void phase. The random walk diffusivity simulations can thus yield useful insight to the diffusion mechanisms in paper.

In addition to the simulation of fluid flow to determine the permeability, tortuosity and diffusivity, simulation of transport in the digital structures may yield insight into how ink and coating covers and penetrates into the paper structure. However it is a prerequisite that realistic parameters for the physical properties of the liquid phase can be found.
The digital paper structures also allow simulation of mercury intrusion porosimetry, as described above for the assessment of the pore geometry.

High resolution 3D images may be applied to find relationships between local surface characteristics and the underlying interior structure, as the detailed structure allows assessment of surface topography and roughness measurement of exactly the same surface area for which the detailed structural characteristics are determined. However, the practical study presented in this thesis in the attached Paper I shows that this can be well determined applying a combination of SEM and laser profilometry.

The X-ray microtomography allows image acquisition under varying compressive or tension forces. However, to enable practical implementation, it is necessary to design a loading cell able to compress or stretch the small paper samples in a controlled manner. An applicable loading device must be made from materials well suited for application in the intense X-ray radiation. An alternative approach is to deform the paper well into the plastic region in several stages with increasing load levels and image the same volume between each loading step. The largest difficulty with this approach is to mount the sample in a non-destructive manner that sufficiently restricts sample movement and to image exactly the same area of the paper sample for each loading cycle since the sample must be removed for each loading cycle.

The high resolution images allow a physically reasonable simulation of the light scattering in the paper structure. A requirement for the optical simulation is a well preserved topology of the fibre network and a transfer of the volume representation from voxel based to a continuous surface based representation. It has been shown that it is possible to generate a surface based model using the marching cube principle for the high resolution phase contrast images. However, this approach generates an extremely high number of triangular surfaces, resulting in a data set that is so large that optical simulation becomes too computationally expensive for practical applications. Future development may thus need to find routines for decreasing the number of triangular surfaces without losing essential information.
It is also required to find reasonable physical inputs to the simulation model of the light scattering of the incident light beams.
The current resolution is too low to yield physically reasonable simulation results, even if

correct estimates for the scattering at the phase borders may be determined. However, simulations will allow quantification of the effect of the surface scattering relative to interior scattering. Simulations may also quantify the effect of adjusting the simulation variables that can be freely chosen. The experiences from light scattering simulation at the current resolution may supposedly be applied for 3D images with submicrometer resolution when such images are available. The simulation of light scattering, and possibly other optical properties, can then possibly yield direct information on how the detailed paper structure affects the optical properties.

This thesis work has focused on assessment of the properties of the pore phase. However, assessment of single fibre properties and the fibre network can be found in literature. Although assessments of the solid phase are not applied in this study, the assessments of the solid phase are as interesting as the assessments of the void phase for increasing the knowledge of the detailed properties of the paper structure. The future development of the X-ray microtomography technique is thus recommended to include implementation and improvement of the assessments of the properties of the solid phase.
The skeletonization of the fibre phase allows measurement of the fibre network properties and fibre orientation. However, to obtain measurements of the properties of individual fibres, as they appear in the bonded sheet, it is necessary to segment the single fibres from the continuous fibre phase. This is a difficult and complex procedure. However, the small distance between the cross sections in the high resolution X-ray microtomography images allows utilization of the high length to width ratio of the fibres for the segmentation. When aligning the volume in machine direction, the fibre cross sections of a fibre will overlap when comparing adjacent slices. Application of a watershed based routine to the MD aligned high resolution 3D paper structure show promising results [134] for fibre segmentation. The 3D image in the top of Figure 7.3 is a representation of the network of the fibres that could be segmented from a high resolution 3D digital paper structure using the watershed based routine. Below the fibre network in Figure 7.3 is also an example of a single segmented fibre shown.

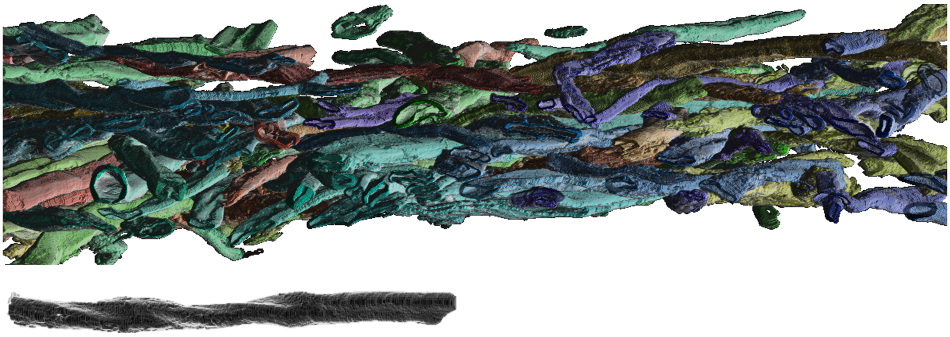

Figure 7.3 Top: A representation of all the individual fibres that could be extracted from an uncalendered newsprint-like digital paper volume obtained by absorption mode high resolution X-ray microtomography. **Bottom:** A representation of a single individual segmented fibre from the same volume as above.

In addition to yield assessments of the properties of single fibres, as they appear in the bonded structure, segmentation of individual fibres allows determination of estimates for the relative bonded area of the fraction of fibres that can be extracted from the fibre network. Future developments may succeed in segmenting all individual solid objects of the paper structure. Such a perfect segmentation may provide a direct measurement of the relative bonded area of the imaged paper grade. A fibre network segmented into its individual constituents will also be a good starting point for finite element model (FEM) simulation of the mechanical properties of the paper structure.

REFERENCES

1. Hooke, R., *Micrographia*, Dover, New York, 1665.
2. Moss, P.A. and Groom, L., "Microscopy" in *Handbook of physical testing of paper,* ed. by Borch J., Lyne M.B., Mark, R.E. and Habeger. C.C. Jr, Marcel Dekker Inc., New York, USA, Vol. 2, Chapter 5, pp 149-265 (2002), ISBN 0-8247-0499-1.
3. Bown, R., "A review of the influence of pigments on papermaking and coating", *Fundamentals of papermaking materials - 11th fundamental research symposium*, Cambridge, UK, vol. 1, pp 83-138 (1997).
4. Forseth, T.E.F. and Helle, T., "Effect of moistening on cross-sectional details of calendered paper containing mechanical pulp", *J. Pulp Pap. Sci.*, 23(3):95-100 (1997).
5. Gregersen, Ø.W. and Hestmo, R.H., "Fibre wall damage caused by calendering", *Nordic conference on paper calendering*, PFI, Trondheim, Norway (2000).
6. Kibblewhite, R.P. and Brookes, D., "Dimensions and collapse behaviour of kraft and bisulphite fibres in wet pulps and 'in situ' in handsheets". *Appita J.,* 31(2):111-118 (1977).
7. Allem, R., "Characterisation of paper coatings by scanning electron microscopy and image analysis, *J. Pulp Pap. Sci.*, 24(10):329 - 336 (1998).
8. Allem, R. and Uesaka, T., "Characterization of paper microstructure: a new tool for assessing the effects of base sheet structure on paper properties", *Microscopy as a tool in pulp and paper research and development*, Stockholm, Sweden, pp 43-52 (1999).
9. Chinga, G. and Helle, T., "Structure characterisation of pigment coating layer on paper by scanning electron microscopy and image analysis", *Nord. Pulp Pap. Res. J.*, 17(3):307-312 (2002).
10. Chinga, G., Helle, T. and Forseth, T., "Quantification of structure details of LWC paper coating layers", *Nord. Pulp Pap. Res. J.*, 17(3):313-318 (2002).
11. Rättö, P., Hornatowska, J., and Rigdahl, M., "Effect of high-temperature and soft-nip calendering on the density of paper", *Nord. Pulp Pap. Res. J.*, 16(3):172-177 (2001).
12. Goldstein, J.I., Newbury, D.E., Echlin, P., Joy, D.C., Romig, A.D., Lyman, C.E., Fiori, C., and Lifshin, E., *Scanning Electron Microscopy and X-Ray Microanalysis: A Text for Biologists, Materials Scientists, and Geologists*, Plenum Pub. Corp., New York, USA (1992), ISBN 0-3064-4175-6.
13. Gibbon, D.L., Simon, G.C. and Cornelius, R.C., "New electron and light optical techniques for examining papermaking", *Tappi J.*, 72(10):87-91 (1989).
14. Williams, G.J. and Drummond, J.G., "Preparation of large sections for the microscopical study of paper structure", *J. Pulp Pap. Sci.*, 26(5):188-193 (2000).
15. Fjerdingen, H., Forseth, T.F., Gregersen, O.W., Helle, T., Johnsen, P.O., Kure K.-A., and Reme, P.A., "Some mechanical pulp fibre characteristics, their process relationships and papermaking significance", *Fundamentals of papermaking materials - 11th fundamental research symposium*, Cambridge, UK, vol. 1, pp 547-605 (1997).

16. Walbaum, H.H. and Zak, H., “Internal structure of paper and coating in SEM cross-sections, *Tappi J.*, 59(3):102-105 (1976).
17. Aronsson, M., “On 3D fibre measurements of digitized paper - from microscopy to fibre network”, Doctoral thesis, Swedish University of Agricultural Sciences, Uppsala, Sweden (2002). (ISBN 91-576-6338-6).
18. Kim, S.T. and Dravid, V.P., “Focused ion beam sample preparation of continuous fibre-reinforced ceramic composite specimens for transmission electron microscopy”, *J. Microscopy-Oxford*, 198(5):124-133 (2000).
19. Alkemper J. and Voorhees, P.W., “Quantitative serial sectioning analysis”, *J. Microscopy-Oxford*, 201(3):388-394 (2001).
20. Kellomäki, M. and Jetsu, P., “Measurement of floc size and sharpness using second-order statistics of grammage map”, *Progress in paper physics seminar*, Syracuse, NY, USA, pp 98-101 (2002).
21. Gonzalez, R.C. and Woods, R.E., *Digital image processing*, Addison-Wesley publ. company Inc. (1993), ISBN 0-201-60078-1.
22. Russ, J.C., *The image processing handbook*, 3rd Ed., CRC Press (1999), ISBN 3-540-64747-3.
23. Ridler, T.W. and Calvard, S., “Picture thresholding using an iterative selcetion method”, *IEEE Trans. Syst. Man Cybern.*, 8(8):630-632 (1978).
24. Chinga, G., “Structural studies of LWC paper coating layers using SEM and image analysis techniques”, doctoral thesis (2002:14), Norwegian University of Science and Technology, Trondheim, Norway (2002). (ISBN 82-471-5406-4).
25. Sternberg, S.R., “Biomedical image processing”, *IEEE Computer*, 16(1):22-34 (1983).
26. Svensson, S. and Aronsson M., “Using distance transform based algorithms for extracting measures of the fiber network in volume images of paper” *IEEE Transaction on systems, man and cybernetics - B*, 33(4):562-571 (2003).
27. Nesbakk, T. and Helle, T., “The influence of the pulp fibre properties on supercalendered mechanical pulp handsheets”, *J. Pulp Pap. Sci.*, 28(12):406-409 (2002).
28. He, J., Batchelor, W.J., Markowski, R., and Johnston, R.E., “A new approach for quantitative analysis of paper structure at the fibre level”, *Appita J.*, 56(5):366-370 (2003).
29. Niskanen, K. and Rajatora, H., “Statistical geometry of paper cross sections”, *J. Pulp Pap. Sci.*, 28(7):228-233 (2002).
30. Hestmo, R.H., Gregersen, Ø.W. and Lamvik, M., “Calendering of wood containing paper: a laboratory study of temperature, moisture and pressure effects on fibre wall damage”, *Nord. Pulp Pap. Res. J.*, 17(1):9-13 (2002).
31. Szikla, Z. and Pauloporo, H., “Changes in z-direction density distribution of paper in wet pressing”, *J. Pulp Pap. Sci.*, 15(1):11-17 (1989).
32. Le, P.C., Zeilinger, H. and Weigl, J., “Verteilung der Pigment- und Binderbestandteile über den Strichquerschnitt”, *Wochenblatt für Papierfabrikation*, 121(8):284-293 (1993). (in German)
33. Dickson A.R., “Quantitative analysis of paper cross-sections”, *Appita J.*, 53(4):292-295 (2000).
34. Hellen, E.K.O., Alava, M.J. and Niskanen, K.J., “Porous structure of thick fiber webs”, *J. Appl. Phys.*, 81(9):6425-6431 (1997).

35. Dodson, C.T.J., “On the distribution of pore heights in random layered fibre networks”, *The science of papermaking - 12th Fundamental research symposium*, Oxford, UK, vol. 2, pp 1037-1042 (2001).
36. Silvy, J., Caret, C., Belamaalem, B., and Mahrous, M., “The three-dimensional structure of paper: methods of analysis and implications on his physical properties”, *International Paper Physics Conference*, Niagara on the lake, Canada, pp 1-5 (1995).
37. Holmstad, R., and Gregersen, Ø.W., “Image analysis of characteristic structure elements in paper cross sections”, Progress in paper physics - a seminar, Grenoble, France, vol. 2, pp 15-28 (2000).
38. Dullien, F.A.L., *Porous media: fluid transport and pore structure*, 2nd Ed., Academic Press, San Diego, USA (1992), ISBN 0-12-223651-3.
39. Kwiecien, M.J., MacDonald, I.F., and Dullien, F.A.L., “3-Dimensional reconstruction of porous-media from serial section data”, *J. Microscopy-Oxford*, 159(3):343-359 (1990).
40. Yamaushi, T.and Murakami, K., “Porosity and gas permeability” in *Handbook of physical testing of paper*, ed. Borch J., Lyne M.B., Mark, R.E. and Habeger. C.C. Jr, Marcel Dekker Inc., New York, USA, Vol. 1, Chapter 6, pp 267-302 (2002), ISBN 0-8247-0499-1.
41. Sampson, W.W., “The structural characterisation of fibre networks in papermaking processes: a review”, *The science of papermaking - 12th Fundamental research symposium*, Oxford, UK, vol. 2, pp 1205-1288 (2001).
42. Climpson, N.A. and Taylor, J.H., “Pore-size distributions and optical scattering coefficients of clay structures”, *Tappi J.*, 59(7):89-92 (1976).
43. Dullien, F.A.L. and Dhawan, G.K., “Characterization of pore structure by a combination of quantitative photomicrography and mercury porosimetry”, *J. Colloid Interf. Sci.*, 47(2):337-349 (1974).
44. Torquato, S., *Random heterogeneous materials: microstructure and macroscopic properties,* Interdisciplinary applied mathematics; vol. 16. Mechanics and materials, New York, Springer Verlag,, 2002. (ISBN: 0-387-95167-9).
45. Sahimi, M., “Flow phenomena in rocks - from continuum models to fractals, percolation, cellular-automata, and simulated annealing”, *Rev. Mod. Phys.*, 65(4):1393-1534 (1993).
46. Holmstad, R., Antoine, C., Silvy, J., Costa, A.-P. and Antoine, J., “Modelling the paper sheet structure according to the equivalent pore concept”, *Research techniques for tomorrow's papermaking, COST Action E 11 Characterization methods for fibres and paper, Final workshop*, Espoo, Finland, pp 15-25 (2001).
47. Lorusso, M., Dodson, C.T.J. and Sampson, W.W., “Effect of mineral content on the void structure of uncoated mechanical supercalendered (SC) papers”, *Progress in paper physics seminar*, Syracuse, NY, USA, pp 38-42 (2002).
48. Dodson, C., Handley, A., Oba, Y. and Sampson, W., “The pore radius distribution in paper. Part 1: the effect of formation and grammage”, *Appita J.*, 56(4):275-280 (2003).
49. Roberts, S. and Sampson, W.W., “The pore radius distribution in paper. Part 2: the effect of laboratory beating”, *Appita J.*, 56(4):281-283, 289 (2003).
50. Underwood, E.E., *Quantitative stereology,* Addison-Wesley series in metallurgy and materials, Addison-Wesley, Reading, Mass., USA (1970).

51. Silvy, J., “La transformation conforme du pore equivalent, methode d'homogeneisation de la texture des milieux polyphasés”, *Recents Progrés en Genie des Procedés. Diffusion Lavoisier Tech et Doc*, Paris, 3(7):484-493 (1989). (in French)
52. LeCoq, L., Silvy, J., and Lascaux, M.P., “Etude de la structure de medias fibreux filtrants à gradients de pores”, *Recents Progés en Genie des Procedés. Diffusion Lavoisier Tech et Doc*, Paris, pp 137-138 (1995). (in French)
53. Silvy, J., “Etude structurale de milieux fibreux”, Thése de Doctorat d'Etat (Ph.D. thesis), Université Scientifique et Medicale et Institut National Polytechnique de Grenoble, France (1980). (in French)
54. Bloch, J.-F., “Surface characterisation: modelling from 3D to 1D”, *International Paper Physics Conference*, Victoria BC, Canada, pp 61-63 (2003).
55. Fiadeiro, P.T., Pereira, M.J.T., Jesus, M.E.P. and Silvy, J.J. “The surface measurement of fibre orientation anisotropy and misalignment angle by laser diffraction“, *J. Pulp Pap. Sci.*, 28(10):341-346 (2002).
56. Serra, J., *Image analysis and mathematical morphology,* Academic Press, London, Great Britain (1982), ISBN 0-12-637240-3.
57. SCAN-M6:69, “Fibre Fractionation of Mechanical Pulp in the McNett Apparatus”, Scandinavian Pulp, Paper and Board Testing Committee (1969).
58. ISO 5269-1:1998, “Pulps - Preparation of laboratory sheets for physical testing - Part 1: Conventional sheet-former method”, ISO (1998).
59. Kerekes, R.J. and Schell, C.J., “Characterization of fiber flocculation regimes by a crowding factor”, *J. Pulp. Pap. Sci.*, 18(1):J32-J38 (1992).
60. Johnsen, P.O., Skinnarland, I., Helle, T. and Houen, P.J., “Distribution of lignin and other materials on particle surfaces in mechanical pulps”, *International Mechanical Pulping Conference*, Ottawa, Canada, pp 93-107 (1995).
61. Reme, P.A., Johnsen, P.O. and Helle, T. “Assessment of fibre transverse dimensions using SEM and image analysis”, *J. Pulp Pap. Sci.*, 28(4):122-128 (2002).
62. Holmstad, R., Gregersen, O. and Chinga, G., “A method for evaluation of the true density distribution in the z-direction of paper”, *Progress in paper physics seminar,* Syracuse, NY, USA, pp 43-47 (2002).
63. Beland M.-C., Hainzl, R., Mattson, L.H., Quinteros, T.B., Granberg, H.T., Berglind, R. and Bjuggren, M., “A new light scattering model for simulating the interaction between light and paper”, *International printing and graphic arts conference*, Savannah, GA, USA, pp 9-17 (2000).
64. Hasuike, M., Kawasaki, T. and Murakami, K., “Evaluation method of 3-D geometric structure of paper sheet”, *J. Pulp. Pap. Sci.*, 18(3):J114-J120 (1992).
65. Aronsson, M., Henningsson, O. and Savborg, O., “Slice-based digital volume assembly of a small paper sample”, *Nord. Pulp Pap. Res. J.*, 17(1):29-33 (2002).
66. Raya, S.P. and Udupa, J.K., “Shape-based interpolation of multidimensional objects”, *IEEE Trans. Med. Imag.*, 9 (1):32-42 (1990).
67. Chinga G., Johnsen P.O. and Diserud, O., “Controlled serial grinding for high-resolution three-dimensional reconstruction”, *J. Microscopy-Oxford*, 214(1):13-21 (2004).
68. Goel, A., Tzanakakis, E.S., Huang, S., Ramaswamy, S., Hu W.-S., Choi, D. and Ramarao, B.V., “Confocal laser scanning microscopy to visualize and characterize

the structure of paper", *Fundamentals and numerical modelling of unit operations in the forest products industries. AIChE forest products symposium*, pp 75-79 (1999).

69. Dickson, A.R., "The quantitative microscopic analysis of paper cross-sections: sample preparation effects", *Appita J.*, 53(5):362-366 (2000).
70. Shaler, S.M., Wang, H., Landis, E., Keane, D.T., Mott, L. and Holzman, L., "Microtomography of cellulosic structures", *Product and process quality conference and trade fair*, Milwaukee, WI, USA, pp 89-96 (1998).
71. Samuelsen, E.J.. Helle, T., Houen P.-J., Gregersen, Ø.W. and Raven, C., "Three-dimensional imaging of paper by use of Synchrotron X-Ray Microtomography", *J. Pulp Pap. Sci.*, 27(2):50-53 (2001).
72. Yang, H. and Lindquist, B.W. "Three dimensional image analysis of fibrous materials", *SPIE - Applications of Digital Image Processing XXIII*, pp 275-282 (2000).
73. Yang, H., "A Geometric and Statistical Analysis of Fibrous Materials from Three-Dimensional High Resolution Images", Ph.D. thesis, State University of New York - Stony Brook University, USA, (2001).
74. Gureyev, T.E., Evans, R., Stevenson, A.W., Gao, D. and Wilkins, S.W., "X-ray phase-contrast microscopy of paper", *Tappi J.*, 84(2):52 (2001).
75. Goel, A., Tzanakakis, M., Huang, S., Ramaswamy, S., Choi, D. and Ramarao, B.V., "Characterization of the three-dimensional structure of paper using x-ray microtomography", *Tappi J.*, 84(5):72 (2001).
76. Ramaswamy, S., Huang, S., Goel, A., Cooper, A., Choi, D., Bandyopadhyay, A. and Ramarao, B.V., "The 3D structure of paper and its relationship to moisture transport in liquid and vapor forms", *The science of papermaking - 12th Fundamental research symposium*, Oxford, UK, vol. 2, pp 1289-1311 (2001).
77. Huang, S., Goel, A., Ramaswamy, S., Ramarao, B.V. and Choi, D., "Transverse and in-plane pore structure characterisation of paper", *Appita J.*, 55(3):230-234 (2002).
78. Ramaswamy, S., Ramarao, B.V., Goel, A., Lee, G., Choi, D. and Lavrykov, S., "Theoretical and experimental investigation on liquid penetration in porous media", *Progress in paper physics seminar*, Syracuse, NY, USA, pp 136-140 (2002).
79. Holmstad R., Antoine C., Nygard P. and Helle, T., "Quantification of the three-dimensional paper structure: Methods and potential", *P. & P. Can.*, 104(7):47-50 (2003).
80. Bloch J-F., Reverdy, N. and Thibault, X., "Structure analysis of papers using x-ray microtomography", *Progress in paper physics seminar*, Syracuse, NY, USA, pp 32-33 (2002).
81. Holmstad, R., Ramaswamy, S., Goel, A., Gregersen, Ø.W. and Ramarao, B.V., "Comparison of 3D structural characteristics of high and low resolution X-ray microtomographic images of paper and board", I*nternational Paper Physics Conference*, Victoria BC, Canada, pp 65-69 (2003).
82. Goel, A., "Numerical methods and image analysis to predict the transport properties of porous media", Ph.D. thesis, University of Minnesota, USA (2003).
83. Rolland du Roscoat, S., Thibault, X., and Bloch, J.-F., "Image analysis of 3D structure: application to X-ray microtomography", *Progress in paper physics seminar*, Trondheim, Norway, p. 63 (2004).
84. Knackstedt, M.A., Arns, C.H., Holmstad, R., Antoine, C. and Gregersen, Ø.W., "Characterisation of 3D structure and transport properties of paper from

tomographic images", *Progress in paper physics seminar*, Trondheim, Norway, pp 64-66 (2004).

85. Holmstad, R., Goel, A., Arns, C.H., Knackstedt, M.A. and Gregersen, Ø.W., " Effect of papermaking variables on the detailed 3D paper structure assess by X-ray microtomography", *Progress in paper physics seminar*, Trondheim, Norway, pp 67-69 (2004).
86. Aaltosalmi, U., Kataja, M., Koponen, A., Timonen, J., Goel, A., Lee, G., and Ramaswamy, S., "Numerical analysis of fluid flow through fibrous porous materials", *International Paper Physics Conference*, Victoria BC, Canada, pp 247-251 (2003).
87. Reverdy-Bruas, N., Serra-Tosio J.-M., Bloch J.-F. and Boller, E., "Three-dimensional analysis of paper through X-ray microtomography", Rev. ATIP, 55(4):12-14, 16-19 (2001). (In french)
88. Thibault, X., Bloch J.-F. and Boller, E., "Felt structure characterised by synchrotron microtomography", *Appita J.*, 55(2):145-148 (2002).
89. Thibault, X., Chave, Y., Serra-Tosio J.-M. and Bloch J.-F., "Permeability measurements of press felts", The science of papermaking - 12th Fundamental research symposium, Oxford, UK, vol. 2, pp 947-974 (2001).
90. Vlaardingerbroek, M.T. and den Boer, J.A., *Magnetic resonance imaging: theory and practice,* Springer Verlag, Berlin, Germany (1996), ISBN 3-540-60080-9.
91. Graeff, W. and Engelke, K., "Microradiography and microtomography" in *Handbook on Synchrotron radiation*, ed. S. Ebashi, M. Koch and E. Rubinstein, North-Holland, Amsterdam, Netherlands, Chapter 11, vol. 4, pp 361-405 (1990). ISBN 0-444-87423-2
92. Weitkamp, T., "Imaging and tomography with high resolution using coherent hard synchrotron radiation", Doctoral thesis, University of Hamburg, Germany, Cuvillier Verlag, Göttingen (2002). (ISBN: 3-89873-609-1).
93. http://www.esrf.fr/exp_facilities/ID19/homepage/id19homepage.html (Homepage of beamline ID-19 at the ESRF).
94. Wilkins S.W., Gureyev T.E., Gao D., Pogany, A. and Stevenson, A.W., "Phase-contrast imaging using polychromatic hard X-rays", *Nature*, 384(6607):335-338 (1996).
95. Weitkamp, T., Rau, C., Snigirev, A.A., Benner, B., Günzler, T.F., Kuhlmann, M., and Schroer, C.G., "In-line phase contrast in synchrotron-radiation microradiography and tomography", *Developments in X-ray Tomography III*, edited by U. Bonse, Proceedings of SPIE Vol. 4503, pp 92-102 (2001).
96. http://www.skyscan.be/next/spec_1072.htm (Homepage of SkyScan - about the SkyScan 1072 model).
97. Antoine, C., Nygård, P., Gregersen, Ø.W., Weitkamp, T. and Rau, C., "3D images of paper obtained by phase-contrast X-ray micro tomography: image quality and binarisation", *Nucl. Instrum. Meth. A*, 490(1-2):392-402 (2002).
98. http://rsb.info.nih.gov/ij/plugins/index.html (ImageJ plugin site) and http://bij.isi.uu.nl/vr.htm (VolumeJ download and description).
99. Arns, C.H., Knackstedt, M.A., Pinczewski. W.V. and Mecke, K.R., "Euler-Poincare characteristics of classes of disordered media", *Phys. Rev. E*, 63(3), Art. No. 031112 (2001).

100. Hilpert, M. and Miller, C.T., “Pore-morphology-based simulation of drainage in totally wetting porous media”, *Adv. Water Resour.*, 24(3-4):243-255 (2001).

101. Thovert, J.F., Yousefian, F., Spanne, P., Jacquin, C.G. and Adler, P.M., “Grain reconstruction of porous media: Application to a low-porosity Fontainebleau sandstone”, *Phys. Rev. E*, 63(6), Art. No. 061307 (2001).

102. Lin, C.L. and Miller, J.D., “Pore structure analysis of particle beds for fluid transport simulation during filtration”, *Int. J. Miner. Process.*, 73(2-4):281-294 (2004).

103. Qian, Y., D'Humier'es, D. and Lallemand, P., “Lattice-BGK models for Navier-Stokes equation”, *Europhys. Lett.*, 17(6):479-484 (1992).

104. Benzi, R., Succi, S. and Vargassola, M., “The lattice-Boltzmann equation: theory and application”, *Phys. Rep.*, 222(3):145-197 (1992).

105. Koponen, Kataja, M. and Timonen, J., “Tortuous flow in porous media”, P*hys. Rev. E*, 54(1):406-410 (1996).

106. Ferr'eol, B. and Rothman, D.H., “Lattice-Boltzmann simulations of flow through Fontainebleau sandstone”, *Transport Porous Media*, 20(1-2):3-20 (1995).

107. Kandhai, D., Koponen, A., Hoekstra, A., Kataja, M., Timonen, J., and Sloot, P., “Implementation aspects of 3D lattice-BGK: Boundaries, accuracy and a new fast relaxation method”, *J. Comp. Phys.*, 150(2):482-501 (1999).

108. Qian, Y.-H. and Zhou, Y., “Complete Galilean-invariant lattice BGK models for the Navier-Stokes equation”, *Europhys. Lett.,* 42(4):359-364 (1998).

109. Martys, N.S., Hagedorn, J.G., Goujon, D. and Devaney, J.E., “Large scale simulations of single and multi component flow in porous media”, *SPIE,* 309:205-213, (1999).

110. Martys, N.S., and Chen, H, “Simulation of multicomponent fluids in complex three-dimensional geometries by the lattice Boltzmann method”, *Phys. Rev. E*, 53(1):743-750 (1996).

111. Schwartz, L.M. and Banavar, J.R.,”Transport properties of disordered continuum systems”, *Phys. Rev. B*, 39(16):11965-11970 (1989).

112. Massoquete, A., Lavrykov, S., Ramarao, S., Goel, A., and Ramaswamy, S., “Anisotropic moisture diffusion study on refined paper”, *International Paper Physics Conference*, Victoria BC, Canada, pp 253-257 (2003).

113. Reyes, S.C. and Iglesia, E., “Effective diffusivities in catalyst pellets - new model porous structures and transport simulation techniques”, *J. Catal.*, 129(2):457-472 (1991).

114. Lindquist, W.B., Lee, S.M., Coker, D.A., Jones, K.W. and Spanne, P., “Medial axis analysis of void structure in three-dimensional tomographic images of porous media”, *J. Geophys. Res. B Solid Earth Planets*, 101(B4):8297-8310 (1996).

115. Lindquist, W.B., Venkatarangan, A., Dunsmuir, J. and Wong, T.F., “Pore and throat size distributions measured from synchrotron X-ray tomographic images of Fontainebleau sandstones”, *J. Geophys. Res. B Solid Earth Planets*, 105(B9):21509-21527 (2000).

116. Baldwin, C.A., Sederman, A.J., Mantle, M.D., Alexander, P. and Gladden, L.F., “Determination and characterization of the structure of a pore space from 3D volume images”, *J. Colloid Interf. Sci.*, 181(1):79-92 (1996).

117. Liang, Z., Ioannidis, M.A. and Chatzis, I., “Geometric and topological analysis of three-dimensional porous media: Pore space partitioning based on morphological skeletonization”, *J. Colloid Interf. Sci.*, 221(1):13-24 (2000).
118. Zhao, H.Q., MacDonald, I.F. and Kwiecien, M.J., “Multiorientation scanning - a necessity in the identification of pore necks in porous-media by 3-D computer reconstruction from serial section data”, *J. Colloid Interf. Sci.*, 162(2):390-401 (1994).
119. Blum, H., “A Transformation for Extracting New Descriptors of Shape” in Models for Speech and Visual Form, ed. Weiant Whaten-Dunn, MIT Press, Cambridge, pp 362-381 (1967).
120. Delerue, J.P., Perrier, E., Yu, Z.Y. and Velde, B., “New algorithms in 3D image analysis and their application to the measurement of a spatialized pore size distribution in soils”, *Phys. Chem. Earth Solid Earth Geodes.*, 24 (7), pp 639-644, (1999).
121. http://www.ams.sunysb.edu/~lindquis/3dma/3dma.html (Homepage of 3D medial axis research at Stony Brook University).
122. Lorensen, W.E. and Cline, H.E. “Marching Cubes: A High Resolution 3D Surface Construction Algorithm”, *Computer Graphics (Proceedings of SIGGRAPH '87)*, 21(4):163-169 (1987).
123. Brunborg, H., Smørgrav, T., Blake, R. and Nygård, P., “Light propagation in pulp and paper research, *SIMS 2003 - 44th Conference on Simulation and Modelling, Västerås*, Sweden (2003).
124. Koponen, A., Kandhai, D., Hellen, E., Alava, M., Hoekstra, A., Kataja, M., Niskanen, K., Sloot, P. and Timonen, J., “Permeability of 3D random fibre webs”, *Phys. Rev. Letter*, 80:716-719 (1998).
125. Bentz, D.P., Quenard, D.A., Kunzel, H.M., Baruchel, J., Peyrin, F., Martys, N.S. and Garboczi, E.J., “Microstructure and transport properties of porous building materials part II: Three-dimensional X-ray tomographic studies”, *Mater. Struct.*, 33(227):147-153 (2000).
126. Raven, C., *Microimaging and tomography with high energy coherent synchrotron X-rays*, Shaker Verlag, Aachen, Germany (1999), ISBN 3-826-54520-6.
127. Perona, P., Shiota, A. and Malik, J., “Anisotropic diffusion”, *Geometry Driven Diffusion in Computer Vision,* Kluwer Academic Publ., Dordrecht, Netherlands, pp 73-92, 1994.
128. Smith, S.M., “A new class of corner finder”, *3rd British Machine Vision Conference*, pp 139-148 (1992).
129. Smith, S.M., “Flexible filter neighbourhood designation”, *13th International Conference on Pattern Recognition*, vol. 1, pp 206-212 (1996).
130. http://www.ica1.uni-stuttgart.de/Recent_publications/Papers/acp/node56.html (From web-based monograph on transport and relaxation in porous media)
131. Gupta, M., Goel, A., Ramaswamy, S., Pands, H. and Ramarao, B.V., “Analysis of Z-directional 3D structural characteristics of commercial paper and handsheets”, *International Paper Physics Conference*, Victoria BC, Canada, pp 247-251 (2003).
132. Box, G.E.P., Hunter, W.G. and Hunter, J.S., *Statistics for experimenters: an introduction to design, data analysis, and model building*, Wiley series in probability and mathematical statistics, John Wiley & Sons, New York, USA (1978).
133. http://www.esrf.fr/AboutUs/AboutSynchrotron/ (the ESRF homepage).

134. Hagen, M., Holen, R., Holmstad, R. and Blake, R., “Digital identification of connected paper fibres with cracks”, Progress in paper physics seminar, Trondheim, Norway, pp 164-166 (2004).

COLLECTION OF PAPERS

Papers are not included due to copyright.